ABSTRACT

Title of Document: AIR POLLUTANT CONCENTRATIONS AND TRENDS OVER THE EASTERN U.S. AND CHINA: AIRCRAFT MEASUREMENTS AND NUMERICAL SIMULATIONS

Hao He, Doctor of Philosophy, 2012

Directed By: Professor Russell R. Dickerson

Department of Atmospheric and Oceanic Science

In the last several decades, efforts have been made to mitigate air pollution all around the world. With surface observations showing substantial decrease of criteria pollutants, including O_3, NO_x, CO and SO_2, the long-term aircraft measurements over the eastern U.S. provide a unique opportunity to study the trend of the air pollutant column contents and the regional transport in the free troposphere. Analyses of the historical data indicated ~2.0 Dobson Unit/decade decrease in tropospheric O_3 columns over the eastern U.S. with a similar decreasing trend of CO. The statistical analysis also showed a significant decreasing trend for tropospheric SO_2. Analyses of the EPA CEMS emission data showed parallel reductions. A case study of tropospheric O_3 and SO_2 over downwind area of Baltimore showed that the regional

transport by westerly wind from Ohio and Pennsylvania play an important role in the local air quality issues.

As the second largest economy in the world, China's rapid economic growth in the last decade lead to a dramatic increase in energy demand, which relied heavily on coal burning. The enormous amount of SO_2 emissions caused severe environmental issues including acid deposition and particulate matter pollution. To mitigate these air quality problems, strict control measures and regulations were applied to abate sulfur emissions, especially before and during the 2008 Beijing Olympics. Aircraft measurements of tropospheric SO_2 were conducted over central China in spring 2008, where intense measurements are lacking. A substantial amount of SO_2 was observed in the free troposphere, which is important to regional transport and remote sensing. I successfully validated the SO_2 columns with satellite retrievals, and proved that the new OMI SO_2 algorithm performs better than the conventional algorithm. An emission inventory was evaluated through a combination of model simulations and satellite products. Between 2006 and 2008, the SO_2 emissions had been reduced substantially over middle and eastern China. I also analyzed the model simulations, and find the SO_2 lifetime is ~ 38 h during spring in China and that ~50% of Chinese emissions are exported to the western Pacific.

AIR POLLUTANT CONCENTRATIONS AND TRENDS OVER THE EASTERN U.S. AND CHINA: AIRCRAFT MEASUREMENTS AND NUMERICAL SIMULATIONS

By

Hao He

Dissertation submitted to the Faculty of the Graduate School of the

University of Maryland, College Park, in partial fulfillment

of the requirements for the degree of

Doctor of Philosophy

2012

Advisory Committee:

Professor Russell R. Dickerson, Chair/Advisor

Professor Zhanqing Li

Professor Robert D. Hudson

Professor Ross J. Salawitch

Dr. Nickolay A. Krotkov

Dr. Jeffrey W. Stehr

Dr. Shunlin Liang (Dean's Representative)

© Copyright by

Hao He

2012

Dedication

To My Family

Acknowledgements

Foremost, I would like to express my sincere gratitude to my advisor Professor Russ Dickerson for his continuous support of my Ph.D. study and research. With his inspiration and enthusiasm, he provided ideas and guidance for my research and helped me in the writing of this thesis. I would thank Professor Zhanqing Li for his support of the EAST-AIRC campaign, offering a unique opportunity for me to study air pollution for my motherland. Special thanks also go to Professor Ross Salawitch, Professor Robert Hudson, and Dr. Jeff Stehr for their intensive discussion and helpful suggestion on my research. I owe my sincere gratitude to Dr. Nick Krotkov for his help on OMI data and insightful discussion. I also wound like to thank Maryland Department of Environment for providing funding of this work.

In the last six years, I enjoyed my life in the AOSC department. I would like to thank my fellow labmates: Dr. Lackson Marufu, Dr. Jennifer Hains, Dr. Patti Castellanos, Dr. Chris Loughner, Dr. Dale Allen, Lacey Brent, Heather Arkinson, Dan Goldberg, for the days we were working together; and my classmates and friends: Matus Martini, Kristin Cummings, Jing Wang, Wen Mi, and other staff of AOSC. I also wish to thank my colleagues in China: Dr. Tianxue Wen of IAP, Dr. Qiang Zhang of Tsinghua Unviersity, Dr. Youfei Zheng of NUIST, Xiangdong Bao and Guoqiang Zhao of HMB, for their help for my research.

Last and most importantly, I owe my loving thank to my parents, my beloved wife Jessie Yang, and my daughter Kate. Their support and love made this thesis possible.

Table of Contents

Dedication ii
Acknowledgements iii
Table of Contents iv
List of Tables vi
List of Figures vii
Chapter 1: Introduction **1**
1.1 Background **1**
1.2 Important air pollutants **6**
1.2.1 Carbon monoxide **7**
1.2.2 Nitrogen oxides **9**
1.2.3 Ozone **11**
1.2.4 Sulfur dioxide **13**
1.2.5 Particulate Matter **14**
1.3 Air pollution in the eastern U.S. **18**
1.4 Air pollution in China **22**
1.5 Overview of the research **24**
Chapter 2: Experimental Methods and Data **27**
2.1 Instrumentation **27**
2.1.1 O_3 ..... **27**
2.1.2 CO **28**
2.1.3 SO_2 ..... **30**
2.1.4 Aerosols scattering **32**
2.2 Aircraft platforms **34**
2.2.1 RAMMP aircraft: Piper Aztec and Cessna 402B **34**
2.2.2 Y-7 aircraft in 2008 China campaign **36**
2.3 Emission data **38**
2.3.1 EPA NEI emission inventory of the U.S. **38**
2.3.2 INTEX-B emission inventory of East Asia **39**
2.4 Satellite data **41**
2.5 CMAQ model system **44**
Chapter 3: Long-term trends of air pollutants over the eastern U.S. **46**
3.1 Summary of RAMMPP research flights **46**
3.2 Trends of emissions and surface observations in the eastern U.S. **50**
3.3 Trends in O_3 and CO columns **58**
3.3.1 Evaluation of aircraft O_3 measurements and vertical distributions **59**
3.3.2 The climate penalty factor (CPF) **66**
3.3.3 Long-term trends of O_3 and CO column contents **69**
3.4 Trends of SO_2 and atmospheric optical depth (AOD) **72**
3.4.1 Isolated SO_2 plumes in the free troposphere **72**
3.4.2 Trends in atmospheric SO_2 column and AOD **76**
3.5 Cluster analysis **81**

3.5.1 Data and methods **81**
3.5.2 Results and discussion **86**
3.6 Summary of the long-range trend of air pollution in the eastern U.S. **95**
Chapter 4: 2008 aircraft campaign in central China **98**
4.1 Background and overview **98**
4.2 Results of airborne SO_2 measurements **101**
4.2.1 SO_2 altitude profiles **101**
4.2.2 Isolated SO_2 plumes in the FT **107**
4.2.3 Validation of OMI SO_2 products **109**
4.3 Summary of the 2008 EAST-AIRC aircraft campaign **115**
Chapter 5: Export and lifetime of SO_2 over central China **117**
5.1 Introduction **117**
5.2 CMAQ model simulations **118**
5.2.1 Model set-up **118**
5.2.2 Manipulation of emission input data **121**
5.2.3 Model modificaitons and sensitivity runs **125**
5.2.4 Preliminary CMAQ outputs **127**
5.2.5 Evaluation of CMAQ simulations with EAST-AIRC aircraft measurments **131**
5.3 SO_2 chemistry and lifetime **135**
5.4 Estimate of SO_2 emissions in central and eastern China **139**
5.5 Conclusions and discussion **144**
Chapter 6: Evalution of CMAQ-based aerosols properties with surface measurements and MODIS observations **147**
6.1 Introduction **147**
6.2 Evaluation of AOD measurements over Xinzheng **149**
6.3 Evaluation of CMAQ simulated aerosols over central and eastern China **153**
6.4 Conclusions and discussion **157**
Chapter 7: Conclusions and future work **160**
7.1 Summary of Results **160**
7.2 Recommendations for future work **163**
Appendix I Savitzky-Golay smoothing **167**
Appendix II Case studies on the emission rate of air pollutants from different type of power plants **168**
Appendix III NOAA HYSPLIT back trajectories of SO2 plumes in the FT observedduring the EAST-AIRC aircraft campaign **180**
Appendix IV Validation of OMISO2 PBL products vs. the integrated EAST-AIRC SO_2 column contents **183**
Appendix V. Evaluation of the WRF simulation **184**
Appendix VI Analyses of the SO_2 dry deposition calculated by MCIP and CMAQ **188**
Appendix VII Discussion on the SO_2 lifetime due to sinks and chemistry **192**
Appendix VIII Advection of SO_2 ans sulfate aerosols **196**
Bibliography **199**

List of Tables

Table 1.1. Typical extinction coefficients of different aerosols **18**
Table 1.2. U.S. national ambient air quality standards **20**
Table 1.3. National ambient air quality standards for some air pollutants in China **23**

Table 2.1. List of instruments on RAMMPP aircraft and implementation year **34**
Table 2.2. List of instruments on the Cessna 402B **36**
Table 2.3. Description on 5 emission categories of NEI **38**

Table 3.1. Major airports for RAMMPP research flights. **49**
Table 3.2. List of some major point sources **54**
Table 3.3. Summary of SO_2 plumes observed during RAMMPP research flights **75**
Table 3.4. Statistics of SO2 column and AOD over Harford Co. (0W3) and Easton (ESN) **80**
Table 3.5. Meteorological fields used for the HYSPLIT model runs **83**
Table 3.6. Characteristics and emission estimates of clusters. **85**
Table 3.7. Linear regression of CEMS emissions versus RAMMPP column contents for each cluster. **87**

Table 4.1. Summary of EAST-AIRC research flights in April 2008 ..... **103**
Table 4.2. Summary of ambient SO_2 concentrations observed during research flights. **105**
Table 4.3. Summary of SO_2 plumes observed in the FT. **105**

Table 5.1. Speciation of INTEX-B emission data for SAPRC-99 chemical mechanism. **123**

Table 6.1. Statistical analysis of differences (MODIS-CMAQ) of AOD and PM2.5 column mass **157**

Table AI.1. Weighting coefficients of "quadratic Savitzky-Golay smoothing". **167**
Table AII.1. Characteristics of Brand Shores, Brunot Island, and Rocksprings stations. **169**
Table AII.2. Summary of NO_x and SO_2 emission rate per unit mass of CO_2. **176**

List of Figures

Figure 1.1. Schematic diagram showing aerosol direct and indirect effects..... **5**
Figure 1.2. National trends of CO, O_3, SO_2 and NO_2 from 1980 to 2010. ..... **19**
Figure 1.3. National trends of PM_{10} and $PM_{2.5}$ from 1990 to 2010. ..... **20**
Figure 1.4. Map of the 8-hour O_3 nonattainment areas in the Mid-Atlantic states. **21**
Figure 1.5. Map of $PM_{2.5}$ nonattainment areas in Mid-Atlantic region. **22**

Figure 2.1. Flow diagram of the TEI O_3 analyzer..... **28**
Figure 2.2. Flow diagram of the modified CO analyzer. **29**
Figure 2.3. Flow diagram of the modified SO_2 analyzer. **30**
Figure 2.4. Flow diagram of the TSI 3563 Nephelometer. **32**
Figure 2.5. Pictures of trace gas and aerosol inlet. **35**
Figure 2.6. Figures of Y-7 aircraft and the trace gas inlet for 2008 China campaign. **37**
Figure 2.7. Distribution of CO from INTEX-B emission inventory..... **40**

Figure 3.1. Locations and statistics of RAMMPP flights over Mid-Atlantic region **48**
Figure 3.2. Flightroute map and SO_2 vertical profiles of 08/09/2008..... **49**
Figure 3.3. Monthly emission data of NO_x, SO_2 and CO_2 form the CEMS dataset **52**
Figure 3.4. Locations of NO_x sources, SO_2 sources, NO_x/CO_2 ratios, and SO_2/CO_2 ratios in MD, OH, PA, VW, and WV..... **53**
Figure 3.5. Trends of NO_x and CO emissions from mobile sources in the EPA NEI. **55**
Figure 3.6. Annual mean NO_x and CO emissions from NEI mobile sources and national toal CO, NO_x, SO_2, and VOC emissions. **56**
Figure 3.7. Map of EPA AQS stations for ground level O_3 and NO_x observations. **57**
Figure 3.8. Long-term trends of surface O_3 and NO_x observed in MD/DC/NOVA. **58**
Figure 3.9. Comparison of surface O_3 concentrations observed by RAMMPP aircraft and the EPA AQS site. **60**
Figure 3.10. Comparison of surface O_3 concentrations and the RAMMPP O_3 column contents between ground and 1500 m. **61**
Figure 3.11. Vertical distributions of tropospheric O_3 over the Mid-Atlantic region **62**
Figure 3.12. The mean CO profile from 2001. ..... **64**
Figure 3.13. Daily and monthly mean temperature at BWI. **68**
Figure 3.14. Number of days with $T_{mean} > 28$ ℃ at BWI from 1997 to 2011… **68**
Figure 3.15. Lumped upwind and downwind O_3 column contents..... **69**

Figure 3.16. Long-term trends of tropospheric O_3 and CO columns in the Mid-Atlantic region. **71**
Figure 3.17. Sample cases of isolated SO_2 plumes in the FT. **74**
Figure 3.18. SO_2 column contents over the five airports between 2000 and 2011. ..... **78**
Figure 3.19. SO_2 column contents after eliminating large plumes over the five airports between 2000 and 2011. ..... **79**
Figure 3.20. Trend in AOD over Harford Co. airport (0W3) from 2000 to 2011. ..... **80**
Figure 3.21. Location of coal power plants with tall smokestacks as of December 2010. ..... **82**
Figure 3.22. Sample of HYSPLIT 48-h back trajectory in 08/13/2005. ..... **83**
Figure 3.23. Results of clustering RAMMPP research flights over Harford Co.airport **85**
Figure 3.24. RAMMPP column contents versus CEMS emissions for all clusters. **86**
Figure 3.25. RAMMPP column contents versus CEMS emissions in MD. **88**
Figure 3.26. Trend of ground level NO_x observations, CEMS NO_x emissions and USEPA NEI mobile NO_x emissions. **88**
Figure 3.27. Scatter plot of CEMS NO_x emissions versus the EPA AQS NO_x observations. **89**
Figure 3.28. Scatter plots of CEMS daily NO_x emissions versus BWI dialy temperature. **92**
Figure 3.29. Linear regression trends of CEMS NO_x emissions versus surfacetemperature observations. **93**

Figure 4.1. Location of Henan province in China..... **100**
Figure 4.2. Flight routes with altitude for all EAST-AIRC aircraft campaign **103**
Figure 4.3. SO_2 altitude profiles form research flight on 04/15/2008..... **107**
Figure 4.4. *In situ* measurements and the mean SO_2 profiles for the aircraft campaign **106**
Figure 4.5. Altitude profile and HYSPLIT 72-hr back trajectory of SO_2 plume observed in 04/20/2008. ..... **108**
Figure 4.6. Evaluation of *in situ* measurements vs. the modified OMISO2 PBL (+ 0.4 DU) products. **111**
Figure 4.7. Evaluation of *in situ* measurements vs. the off-line OMI ISF SO_2 products. **114**

Figure 5.1. Domains of the WRF simulations. **119**
Figure 5.2. Emission maps of SO_2 for CMAQ simulations. **124**
Figure 5.3. Emission maps of CO, NO_x, sulfate aerosols, organic aerosols emissions in the coarse domain. **125**
Figure 5.4. CMAQ daily maps of major air pollutants of coarse domain in 04/18/2008 ..... **128**
Figure 5.5. CMAQ daily maps of major air pollutants of nested domain in 04/18/2008 ..... **129**

Figure 5.6. Vertical distribution of major air pollutants over Zhengzhou in 2 pm, 04/18/2008. ..... **129**
Figure 5.7. Daily NO_2 and SO_2 data from *in situ* measurements and CMAQ simulations **130**
Figure 5.8. Comparison of aircraft observations and CMAQ simulations **132**
Figure 5.9. Evaluation of *in situ* and CMAQ SO_2 column contents. **133**
Figure 5.10. Comparison of monthly mean SO_2 profiles of *in situ* measurements and CMAQ sensitivity runs **134**
Figure 5.11. Budget of sulfur compounds over the central China. **137**
Figure 5.12. SO_2 column maps of OMI PBL products and CMAQ simulations in04/05/2008 ..... **141**
Figure 5.13. Monthly average SO_2 column maps of the OMI PBL productsand CMAQ simulations **142**
Figure 5.14. Histogram of monthly average OMI-CMAQ SO_2 column difference with probability density. **143**

Figure 6.1. Comparison of surface AOD measurements with MODIS Level 2 AOD products **150**
Figure 6.2. Comparison of Angstrom Exponent values from surface sunphotometer measurements and MODIS observations. **151**
Figure 6.3. Comparison of AODs from surface sunphotometer measurements and CMAQ simulations.. ..... **152**
Figure 6.4. Monthly mean AOD and $PM_{2.5}$ column mass maps from MODIS aerosol products and CMAQ simulations **154**
Figure 6.5. Monthly mean Angstrom Exponent map from MODIS **155**
Figure 6.6. Scatter plot of AOD and $PM_{2.5}$ column mass.. ..... **156**
Figure 6.7. Histograms of MODIS-CMAQ AOD and $PM_{2.5}$ column mass differences. **157**

Figure AII.1. Google Earth images of Brand Shores, Brunot Island, and Rock Springs generating stations **170**
Figure AII.2. Scatter plot and linear regression of NO_x and CO_2 emissions of Brandon Shores generating station during JJA in 2000 and 2009.. ..... **172**
Figure AII.3. Trend of slope of air pollutant emissions versus CO_2 emissions of Brand Shores generating station in JJA. **173**
Figure AII.4. Scatter plot and linear regression of NO_x and CO_2 emissions of Brunot Island generating station in JJA before 2002 and after 2002..... **174**
Figure AII.5. Scatter plot and linear regression of NO_x and CO_2 emissions of Rock Springs generating station in JJA. **175**
Figure AII.6. Trends of linear regression analysis on CEMS NO_x data in MD/OH/PA/VA/WV during JJA. **177**
Figure AII.7. Trends of linear regression analysis on CEMS SO_2 data in MD/OH/PA/VA/WV during JJA. **178**

Figure AIII.1. Observations and back trajectories of plume 1 in Table 4.3. ... **180**
Figure AIII.2. Observations and back trajectories of plume 2 in Table 4.3. ... **180**

Figure AIII.3. Observations and back trajectories of plume 4 in Table 4.3.... **181**
Figure AIII.4. Observations and back trajectories of plume 5 in Table 4.3.... **181**
Figure AIII.5. Observations and forward trajectories of plume 3 in Table 4.3. ..... **182**

Figure AIV.1. Evaluation of *in situ* measurements vs. the co-located OMISO2 PBL products. **183**

Figure AV.1. Evaluation of WRF SLP and KMA surface analysis in 04/18/2008. ..... **185**
Figure AV.2. Evaluation of meteorological observations from WRF and Zhengzhou city. **186**
Figure AV.3. Comparison of WRf meteorological data and sounding observations **186**

Figure AVI.1. SO_2 dry deposition velocity map of 04/05/2008 and 04/18/2008. ..... **189**
Figure AVI.2. SO_2 dry deposition flux map of 04/05/2008 and 04/18/2008... **190**
Figure AVI.3. Terrain height of the nested domain..... **191**

Figure AVII.1. H_2O_2 and SO_2 concentrations from CMAQ simulations **194**

Figure AVIII.1. SO_2 and sulfate advections in and out of the nested domain. **196**

Chapter 1. Introduction

1.1 Background

Air pollution refers to any atmospheric condition with substances at concentrations higher than their normal ambient levels, producing a measurable effect on man, animals, vegetation, or materials [*Seinfeld*, 1986]. These substances, defined as air pollutants, can be introduced into the atmosphere from natural sources and anthropogenic sources. Natural sources of air pollution include volcanic eruptions, breaking waves, pollens, windblown dust, etc. [*Wayne*, 2000]. The major anthropogenic sources of air pollution encompass fossil fuel burning, industrial processes, biomass burning and soil cultivation [*Seinfeld and Pandis*, 2006]. Prior to the industrial era, smoke and fumes from sea coal burning in London were noticed as air pollution and attributed to mortality [*Tebrake*, 1975]. With the rapid industrialization and urbanization after the Industrial Revolution, human activities accentuated the degradation of air quality for the last several centuries. Severe air pollutant events drew public attention to the influences of air pollutants on human health, and epidemiological studies proved the effects on mortality and diseases [*Anderson*, 2009; *Brook et al.*, 2004; *Sunyer*, 2001].

The air pollutants can be categorized into two groups: primary pollutants are emitted directly from sources, and secondary pollutants are formed from primary pollutants (i.e., precursors) by chemical reactions. One case of the air pollution mainly

caused by primary pollutants is the notorious "London Smog". In the 18th century, the Industrial Revolution promoted the usage of steam power, which was primarily fueled by coal. The combustion of sulfur rich coal released large amounts of sulfur dioxide (SO_2) and particulate matter (PM), which caused the "London Smog" under foggy and stagnant meteorological conditions normally associated with strong temperature inversion [*Finlayson-Pitts and Pitts*, 1999]. The portmanteau "smog" was introduced to describe the smoky fog, containing mainly soot particulate and SO_2. The death rate in London was found to track high concentrations of air pollutants during the Great Smog of 1952 [*Bell and Davis*, 2001]. The "London Smog" called attention to the air pollution world wide, and the British Clean Air Act of 1956 implemented a number of control measures to reduce air pollutant emissions.

In the late 1940's, another type of air pollution was noticed in the Los Angeles area. In contrast to the "London smog", this type of smog was found under hot weather and bright sunshine, causing eye irritation and damages to plants. Under a temperature inversion and strong sunlight, nitrogen oxides (NO_x) and volatile organic compounds (VOC) generate ozone (O_3) through photochemical reactions [*Haagensmit*, 1952; *Haagensmit and Fox*, 1956]; the "Los Angeles smog" is also called "photochemical smog". As a secondary pollutant, O_3 production is determined by its precursors, NOx and VOC, byproducts from internal combustion engines (mainly automobiles) and industrial fuel burning processes. In southern California, new technology and strict control measures were taken to abate the NOx and VOC emissions, and O_3 concentrations declined significantly in the 1980s and hereafter [*Finlayson-Pitts and Pitts*,

1999]. With less coal burning and more cars, the "photochemical smog" replaced the "London smog" and became the prevalent air pollution in urban areas around the world.

Traditionally, air pollution is treated as local events to large urban centers and industrialized region; now it is believed that urban and industrial areas are just "hot spots" in the regional or global distributions of air pollutants. An example of the global air pollution is the stratospheric ozone problem. During the study of the stratospheric ozone layer, production and destruction mechanisms were proposed to investigate the stratospheric O_3 depletion [*Bates and Nicolet*, 1950; *Chapman*, 1930; *Crutzen*, 1970; *Johnston*, 1971]. Later, it was discovered that the photolysis of man-made chlorofluorocarbons (CFCs) in the stratosphere releases chlorine (Cl) atoms initiating catalytic cycles of O_3 destruction [*Molina and Rowland*, 1974; *Rowland and Molina*, 1975]. Stratospheric O_3 depletion drew great public attention especially after the extreme event of O_3 loss over the Antarctic region, the "ozone hole" observed in early 1980s [*Farman et al.*, 1985]. The formation of the "ozone hole" involved complicated heterogeneous reactions [*Anderson et al.*, 1989; *Anderson et al.*, 1991; *Salawitch et al.*, 1989; *Solomon et al.*, 1986], the general consensus was reached that the emissions of CFCs must be abated to avoid the stratospheric O_3 depletion. In 1987, the Montreal Protocol was signed to protect the O_3 layer by phasing out the production and usage of ozone depletion substances including CFCs [*Seinfeld and Pandis*, 2006]. The Montreal Protocol is not only effective [*Anderson et al.*, 2000; *Morgenstern et al.*, 2008], but also established a framework for international cooperation on global air pollution issues.

Man-made climate change has become a global issue and drawn public attention in the last several decades. The globally-averaged carbon dioxide (CO_2) concentration

has increased from a pre-industrial value of ~280 parts per million (ppm) to ~390 ppm in December 2011 (http://www.esrl.noaa.gov/gmd/ccgg/trends/). Global warming since late nineteenth century is estimated as 0.4-0.8 ℃ [*Seinfeld and Pandis*, 2006], and another 0.4 ℃ is projected in the next two decades [*IPCC*, 2007]. The impacts of climate change include the sea level rise, retreat of glaciers, increase of extreme weather, and loss of air quality [*IPCC*, 2007]. The interaction between the atmospheric chemistry and climate is a two way process [*Ramanathan et al.*, 1987], therefore the improvement of air pollution can benefit the climate change and vice versa.

Two most important air pollutants threatening public health and contributing to climate change are tropospheric O_3 and particulate matter. A correlation between elevated O_3 and temperature has been observed [*Wise and Comrie*, 2005], and the concept of climate change penalty factor was introduced to quantitatively describe the correlation [*Bloomer et al.*, 2009]. The radiative forcing of the tropospheric ozone is estimated as 0.35 ± 0.15 W/m^2. Tropospheric O_3 is considered to be the third most important anthropogenic contributor to radiative forcing (RF) of climate [*IPCC*, 2007], and tropospheric O_3 also influences the chemistry of greenhouse gases such as methane (CH_4) in the atmosphere [*Finlayson-Pitts and Pitts*, 1999].

Particulate matter (PM), commonly called aerosol, has both natural sources such as windborne dust, sea salt, and volcanic activities, and anthropogenic sources such as combustion of fossil fuels. PM pollution is estimated to have caused 22,000 to 52,000 deaths during 2000 in the U.S. [*Mokdad et al.*, 2004]. Aerosols have both direct and indirect effects on the RFs of climate. The direct effects include scattering and absorption of the shortwave and longwave radiation [*Haywood and Boucher*, 2000; *Stier*

et al., 2007], and the total influence is estimate as -0.5 ± 0.4 W/m^2 [*IPCC*, 2007]. The indirect aerosol effect is related to the aerosol effects on the cloud properties, including the "Twomey effect" [*Lohmann and Feichter*, 2005; *Twomey*, 1977] and the "cloud lifetime effect" [*Albrecht*, 1989] among others. Figure 1.1 presents the summary of aerosols radiative effects. There are great uncertainties on the estimate of aerosol indirect effects, and the best estimate is -0.7 [-0.3 to -1.8] W/m^2 [*IPCC*, 2007]. Most natural aerosol emissions are influenced by climatic parameters such as wind and temperature, therefore climate change also affects the chemistry and lifetime of natural aerosols.

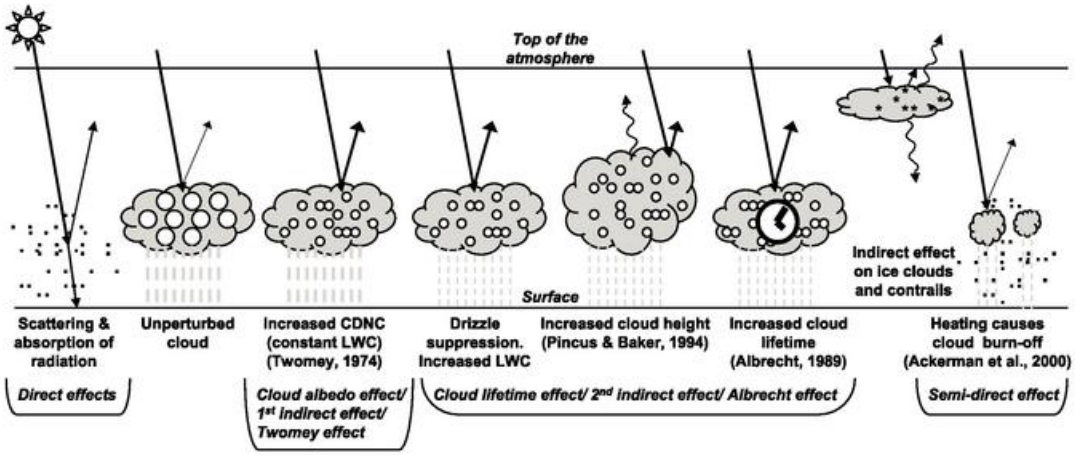

Figure 1.1 Schematic diagram showing aerosols direct and indirect effects (adapted from IPCC 2007 report on climate change: the physical science basics).

In the last several decades, public attention has been drawn to air pollution all over the world, and great efforts were taken to improve the ambient air quality. To investigate current air pollution issues, studies on air pollutant emissions, atmospheric chemistry, regional transport, chemical transformations, and sinks are needed simultaneously. We need to evaluate the benefits from mitigating the air pollution,

important for the policy decisions in the future. For this dissertation, I studied the air pollution in China and the eastern U.S.; the trend of air pollution is also discussed.

1.2 Important air pollutants

In this chapter, a brief discussion on the major air pollutants is introduced. To investigate the chemistry and evolution of one specific pollutant, we need to discuss the sources, lifetime, and sinks. The sources include natural and anthropogenic emissions for primary air pollutants, and the conversion from precursors to secondary air pollutants. Two major sinks encompass direct transfer of air pollutants to the Earth's surface (dry deposition) and removal of air pollutants in the aqueous form during precipitation (wet deposition); the conversion to another chemical species is also a sink for some air pollutants. The fundamental principle governing the behavior of an air pollutant is the conservation of mass [*Seinfeld and Pandis*, 2006]. If the total mass of a chemical within a specific air mass, mass flow in and out, are defined as Q, F_{in} and F_{out} respectively, and the rate of production and removal of this species are denoted as P and R. The conservation of mass is:

$$\frac{dQ}{dt} = (F_{in} - F_{out}) + (P - R) \qquad \text{(Equation 1.1)}$$

If the total mass of one chemical species in the air mass is constant, i.e., $dQ/dt = 0$, we can define this case as steady-state, so the mass balance expression is:

$$F_{in} + P = F_{out} + R \qquad \text{(Equation 1.2)}$$

When discussing this chemical species in the whole atmosphere, we have $F_{in} = F_{out} = 0$, then under the state-state condition, equation (1.2) becomes $P = R$. The lifetime τ is defined as:

$$\tau = \frac{Q}{P} = \frac{Q}{R} \qquad \text{(Equation 1.3)}$$

The lifetime calculation reveals how long a species can stay in the atmosphere, and how far it will be transported before deposited to the Earth's surface [*Seinfeld and Pandis*, 2006]. The prevalent wind at mid-latitudes is 10-30 m/s in the west-east direction in the free troposphere, and dominates the transport process. Slower transport happens in the north-south and vertical directions, with time-scale about one year for the global mixing through two hemispheres. Therefore, the long-range transport pattern of a chemical species depends on its lifetime. For instance, sulfur compounds (SO_2 + sulfate aerosols) with lifetime about one week can be transported couple hundred to thousand kilometers downwind; some greenhouse gases like nitrous oxide (N_2O) and CH_4 with lifetime much longer than one year are mixed thoroughly in the troposphere [*Wayne*, 2000].

1.2.1 Carbon monoxide

Carbon monoxide (CO) is a toxic trace gas and in high concentration can cause poisoning or irreversible effect on human health [*Seinfeld*, 1986]. The major natural source of CO is the oxidation of VOCs including CH_4; biomass burning and fossil fuel combustion are the main anthropogenic sources. It is estimate that about two-thirds of the CO emissions, ~1,350 teragram carbon (Tg C, 10^{12} grams) per year, are related to human activities [*IPCC*, 2007]. The reaction with hydroxyl (OH) radicals acts as the major sink of CO, ~800 Tg C/yr.

$$CO + OH + O_2 \rightarrow CO_2 + HO_2 \qquad \text{(reaction 1.1)}$$

The ambient tropospheric CO concentration ranges from 40 to 200 parts per billion by volume (ppbv), with a lifetime of 30~90 days on the global scale [*Seinfeld and Pandis*, 2006]. CO is one of the important precursors for tropospheric O_3 production in the remote regions, through the catalytic cycles with nitric oxide (NO) and nitrogen dioxide (NO_2).

$$HO_2 + NO \rightarrow NO_2 + OH \qquad \text{(reaction 1.2)}$$

$$NO_2 + h\upsilon \rightarrow NO + O \qquad \text{(reaction 1.3)}$$

$$O + O_2 + M \rightarrow O_3 + M \qquad \text{(reaction 1.4)}$$

The net reaction of reactions 1.1 to 1.4 is:

$$CO + 2O_2 + h\upsilon \rightarrow CO_2 + O_3 \qquad \text{(reaction 1.5)}$$

The production of O_3 is controlled by the relative concentrations of NO_x, and the details will be discussed later in the section 1.2.3.

1.2.2 Nitrogen Oxides (NO_x)

The primary source of NO_x (NO_2 + NO) is the combustion of fossil fuels, accounting for 33.0 Tg N/yr out of the total emission (51.9 Tg N/yr). Other important sources include biomass burning (7.1 Tg N/yr), soils (5.6 Tg N/yr) and lightning (5.0 Tg N/yr) [*Seinfeld and Pandis*, 2006]. In the daytime, the major chemistry of NO_x refers to the catalytic cycle (reaction 1.1 to 1.4) plus the termination step:

$$OH + NO_2 + M \rightarrow HNO_3 + M \qquad \text{(reaction 1.6)}$$

This cycle is critical for the ambient O_3 production, and the details will be discussed in the section 1.2.3. During the nighttime, the main reactions of NO_x refer to:

$$NO_2 + O_3 \rightarrow NO_3 + O_2 \qquad \text{(reaction 1.7)}$$

$$NO_2 + NO_3 + M \leftrightarrow N_2O_5 + M \qquad \text{(reaction 1.8)}$$

$$N_2O_5 + H_2O \rightarrow 2HNO_3 \qquad \text{(reaction 1.9)}$$

With high chemical reactivity, NO_x has relative short lifetime (in hours during summer time); the NO_x has large variations in its spatial distribution, with 5-20 ppbv in urban areas, ~1 ppbv in rural areas and 0.01-0.1 ppbv in remote areas [*Seinfeld and Pandis*, 2006]. The nitric acid (HNO_3) generated through these chemical reactions plays an important role in acid deposition, i.e., acid rain. Atmospheric HNO_3 can react with basic substance like ammonia gas (NH_3), forming the nitrate aerosols:

$$HNO_3(g) + NH_3(g) \leftrightarrow NH_4NO_3(s,aq) \qquad \text{(reaction 1.9)}$$

Reaction 1.9 is an equilibrium system, which is influenced by the ambient temperature and relative humidity (RH) [*Mozurkewich*, 1993]. Ammonium nitrate (NH_4NO_3) aerosol, one of the major anthropogenic aerosols, has the seasonal cycle with high concentrations during the winter.

NOx can react with organic compounds in the atmosphere to form alkyl nitrates and peroxyacyl nitrates (PANs) [*Seinfeld and Pandis*, 2006]. Alkanes in the atmosphere can react with OH to form alkyl radicals through the following reaction:

$$RH + OH \cdot \rightarrow R \cdot + H_2O \qquad \text{(reaction 1.10)}$$

Then alkyl radicals react rapidly with O_2 molecules to yield alkyl peroxy radicals (RO_2) and alkyl nitrates late

$$R \cdot + O_2 + M \rightarrow RO_2 \cdot + M \qquad \text{(reaction 1.11)}$$

$$RO_2 \cdot + NO \rightarrow RONO_2 \qquad \text{(reaction 1.12)}$$

PANs mainly include peroxyacetyl nitrate ($CH_3C(O)OONO_2$) and peroxypropionyl nitrate ($CH_3CH_2C(O)OONO_2$) through oxidation of aldehydes. For instance, OH radicals react with acetaldehyde through the following steps:

$$CH_3CHO + OH \rightarrow CH_3CO + H_2O \qquad \text{(reaction 1.13)}$$

$$CH_3CO + O_2 \rightarrow CH_3C(O)O_2 \qquad \text{(reaction 1.14)}$$

Then the peroxyl radicals react with NO_2 to form PAN

$$CH_3C(O)O_2 + NO_2 + M \leftrightarrow CH_3C(O)O_2NO_2 + M \qquad \text{(reaction 1.15)}$$

The thermal decomposition of PANs can release NO_2 back to the atmosphere; during the ambient temperature around 15 ℃, the lifetime of PANs with respect to the thermal decomposition is ~15 hr. When lifted to the relatively cooler free troposphere, PANs is stable and serves as NO_x reservoir. After long-range transport, PANs can decompose and release NO_x in the downwind area.

1.2.3 Ozone (O_3)

After the "photochemical smog" was discovered in 1950s, tropospheric O_3 became the most predominant air pollution for urban centers all over the world. O_3 is a secondary air pollutant, mainly produced through photochemical reactions between VOCs and NO_x, while troposphere-stratosphere air exchange also contributes a small amount of tropospheric O_3. The total production of tropospheric O_3 is estimated as 3420 $\pm$ 770 Tg/yr; the major sinks include chemical reactions and dry deposition to the Earth's surface with lifetime as 24 $\pm$ 2 days [*IPCC*, 2007].

In the clean marine atmosphere, the production of O_3 refers to the oxidation of CO (reactions 1.1 to 1.5) with NO_x as catalyst. In the polluted atmosphere, VOCs (noted as RH in the following reactions) contribute more to the photochemical production:

$$RH + OH + O_2 \rightarrow RO_2 + H_2O \qquad \text{(reaction 1.16)}$$

$$RO_2 + NO + O_2 \rightarrow R'CHO + HO_2 + NO_2 \qquad \text{(reaction 1.17)}$$

$$HO_2 + NO \rightarrow OH + NO_2 \qquad \text{(reaction 1.18)}$$

$$NO_2 + h\upsilon \rightarrow NO + O \qquad \text{(reaction 1.3)}$$

$$O + O_2 + M \rightarrow O_3 + M \qquad \text{(reaction 1.4)}$$

The net reaction is

$$RH + 3O_2 \rightarrow R'CHO + O_3 + H_2O \qquad \text{(reaction 1.19)}$$

And these chain reactions can be stopped through:

$$HO_2 + HO_2 \rightarrow H_2O_2 + O_2 \qquad \text{(reaction 1.20)}$$

$$RO_2 + HO_2 \rightarrow ROOH + O_2 \qquad \text{(reaction 1.21)}$$

There are two types mechanism terminating the O_3 photochemical production: reaction 1.20 in the low NO_x conditions, named NO_x-sensitive conditions; reaction 1.21 in the high NO_x conditions, called NO_x-saturated conditions or VOC-sensitive conditions [*Seinfeld and Pandis*, 2006]. The understanding of different O_3 production mechanism is crucial to regulate O_3 precursor emissions for different chemical sensitive regions [*Seinfeld,* 1991].

Ozone is the precursor of hydroxyl (OH) radicals through the photolysis:

$$O_3 + h\upsilon\ (280\text{-}310\ nm) \rightarrow O(^1D) + O_2 \qquad \text{(reaction 1.22)}$$

$$O(^1D) + H_2O\ (vapor) \rightarrow 2OH \qquad \text{(reaction 1.23)}$$

OH radicals dominate the tropospheric chemistry, through initiating radical chain oxidation [*Finlayson-Pitts and Pitts*, 1999]. Therefore, the mitigation of tropospheric O_3 not only improves the air quality, but also can change the regional atmospheric chemistry.

1.2.4 Sulfur Dioxide (SO_2)

Natural sources of SO_2 encompass volcanic activity (~7 Tg S/yr), and oxidization from biogenic sulfur compounds such as dimethyl sulfide (DMS) and carbonyl sulfide (COS) [*Wayne*, 2000]. The main anthropogenic sources of SO_2 are the combustion of sulfur-containing fuels; the global emissions are about 140 Tg S/yr [*Smith et al.*, 2011]. Dry deposition is a main sink of tropospheric SO_2 [*Chin et al.*, 2000b], and the conversion to other sulfur compounds is the other important sink. In this study, I only focus on the anthropogenic SO_2 emissions to the troposphere. The basic chemistry of tropospheric SO_2 is the oxidation from the lower oxidation state S(IV) to higher oxidation state S(VI) [*Finlayson-Pitts and Pitts,* 1999].

In the gas phase, SO_2 is oxidized by OH radicals:

$$SO_2 + OH + M \rightarrow HOSO_2 + M \qquad \text{(reaction 1.24)}$$

The further oxidation of sulfurous acid ($HOSO_2$) can form the sulfuric acid aerosols:

$$HOSO_2 + O_2 \rightarrow HO_2 + SO_3 \qquad \text{(reaction 1.25)}$$

$$SO_3 + H_2O \rightarrow H_2SO_4 \qquad \text{(reaction 1.26)}$$

SO_2 gas is slightly soluble in the water; aqueous oxidation happens

$$SO_2 + H_2O \leftrightarrow H_2SO_3 \qquad \text{(reaction 1.27)}$$

$$H_2SO_3(aq) + H_2O_2(aq) \rightarrow H_2SO_4(aq) + H_2O(aq) \qquad \text{(reaction 1.28)}$$

Sulfuric acid is neutralized reacting with alkaline substances like NH_3 and mineral limestone dust in the atmosphere, forming sulfates (SO_4^{2-}).

$$H_2SO_4 + 2NH_3 \rightarrow (NH_4)_2SO_4 \qquad \text{(reaction 1.29)}$$

The sulfate aerosol, consisting of sulfuric acid and sulfates, is the major component of tropospheric aerosols from anthropogenic emissions. The study of sulfate aerosols is important to improve our knowledge on acid deposition and global climate change [*Finlayson-Pitts and Pitts*, 1999].

1.2.5 Particulate Matter (PM)

Particulate matter refers to any substance existing in the atmosphere, which can be in liquid or solid phase except pure water [*Seinfeld and Pandis*, 2006]. Though technically aerosol includes particles and/or liquid droplets and the gas together, the term aerosol is commonly used to describe particulate matter in the atmosphere. Aerosols have natural sources such as wind-borne dust, sea spray, and volcanic activities, and anthropogenic sources like combustion of fossil fuels and industrial processes [*Seinfeld*, 2004]. In this study, I only focus on the anthropogenic aerosols. The man-made PM can arise from direct emissions from sources and from nucleation through gas-phase reactions, which are named as primary aerosol and secondary aerosol respectively. For instance, soot particles produced from diesel engines are directly emitted aerosols; the oxidation of SO_2 discussed in section 1.2.4 shows an example of homogeneous nucleation.

The properties of aerosols are determined by their chemical composition and size distribution. From the chemical composition, tropospheric aerosols include sulfate, nitrate (NO_3^-), ammonium (NH_4^+), sodium (Na^+), chloride (Cl^-), trace metals, crustal elements, elemental carbon (EC, also called black carbon or soot), organic carbon (OC),

water (H_2O), biogenic organic particles, etc. The size of ambient atmospheric aerosols ranges from ~0.002 micrometer (μm) to ~10.0 μm, which can be grouped into several modes: 1) Aitken mode (<0.1μm), typically for fresh particles; 2) accumulation mode (0.1-2.5μm), typically for aged particles; 3) coarse mode (2.5-10.0μm) [*Finlayson-Pitts and Pitts*, 1999]. The aerosols in Aitken and accumulation mode, usually called fine mode, are generated through gas-phase nucleation and coagulation of anthropogenic air pollutants; the coarse mode particles are mainly crustal materials (mineral dust, fine soil particles, etc.) and biogenic organic aerosols (pollens, bacteria, etc.) from natural sources. In the study of air quality, another two categories are introduced: PM_{10}, total mass of aerosols with diameter less than 10μm; $PM_{2.5}$, total mass of aerosols with diameter less than 2.5μm. Therefore, PM_{10} is the sum of Aitken, accumulation and coarse mode aerosols, and $PM_{2.5}$ is the sum of Aitken and accumulation mode aerosols. PM_{10} and $PM_{2.5}$ aerosols are also called coarse particles and fine particles.

The major sinks of atmospheric aerosols are dry and wet deposition. Aerosols in coarse mode with size larger than 2.5 μm, which are easily removed from the atmosphere by gravitational sedimentation, have a shorter lifetime than fine particles [*Seinfeld and Pandis*, 2006]. But during some episodes, large particles can be transported long distance such as during Asian dust storms [*DeBell et al.*, 2004; *Tsai and Chen*, 2006; *Yumimoto et al.*, 2010]. Fine particles, with sufficiently small size, undergo Brownian diffusions instead of gravitational settling. Without convection, the motions of particles with diameter smaller than ~0.1μm are dominated by random Brownian movement [*Finlayson-Pitts and Pitts*, 1999]. In the real world turbulence exists ubiquitously within the atmosphere, therefore the transport of fine particles is more complex. Wet deposition

includes precipitation scavenging, in-cloud scavenging, and snow scavenging [*Seinfeld and Pandis*, 2006]. Therefore, the removal of aerosols is mainly controlled by wet deposition; the lifetime is about one week, the same as the lifetime of water in the atmosphere.

Epidemiologic studies reveal the effects of fine particles on the human health, such as aggravating respiratory and cardiovascular diseases, and causing premature mortality [*Seinfeld*, 2004]. For any climate change scenario, aerosols are crucial to investigate the global radiative budget through complicated direct and indirect effects [*IPCC*, 2007]. However, a discussion of these topics is outside the scope of this study. Here I will focus on the air pollution issues caused by tropospheric aerosols, and one prominent case is visibility impairment [*Hand and Malm*, 2007; *Watson*, 2002].

Solar radiation within the atmosphere is scattered and absorbed by the gas molecules and particles. The intensity of attenuation can be expressed in:

$$\frac{I}{I_0} = e^{-bextL} \qquad \text{(Equation 1.4)}$$

as Beer-Lambert law, where I and I_0 are the incident and transmitted light intensities, b_{ext} is the extinction coefficient and L is the path length. The b_{ext} can be grouped by the scattering and absorption from gas molecules and particles respectively,

$$b_{ext} = b_g + b_p = b_{ag} + b_{sg} + b_{ap} + b_{sp} \qquad \text{(Equation 1.5)}$$

In the visible spectrum, the magnitude of gas absorption and scattering is much smaller than the extinction caused by particles, which is further dominated by fine particle scattering [*Finlayson-Pitts and Pitts*, 1999], therefore Equation 1.5 can be expressed in:

$$b_{ext} \approx b_{ap} + b_{sp} \qquad \text{(Equation 1.6)}$$

The particle scattering can be categorized into three groups based on the relative relationship between particle size (D, diameter) and light wavelength (λ): Rayleigh scattering [*Bates*, 1984], $D << \lambda$; Mie scattering [*Hansen and Travis*, 1974; *Van de Hulst*, 1957], $D \sim \lambda$; Geometric scattering, $D >> \lambda$. The visible and near ultraviolet radiation at the Earth's surface has the spectrum from ~290-750 nm, so particles with size from 0.3-0.8 μm, in the fine mode, are predominantly in the Mie scattering range. In the atmosphere, the scattering is caused by sulfate aerosols, nitrate aerosols, organic carbon (OC), fine soil particles, and coarse aerosols; black and brown carbon are the major contributor to aerosol absorption. The aerosol extinction coefficient (e, with units of m^2/g) is introduced to link the aerosol extinction to aerosol concentration. The Equation 1.6 is expressed:

$$b_{ext} = e_{sulfate}[sulfate] + e_{nitrate}[nitrate] + e_{OC}[OC] + e_{soil}[soil] + e_{coarse}[coarse] + e_{BC}[BC]$$

(Equation 1.7)

Table 1.1 summarizes the typical ranges of different aerosols. To mitigate the visibility impairment, control measures on sulfate, nitrate, OC and BC are cost effective. With moisture in the atmosphere, hygroscopic growth of sulfate and nitrate aerosols significantly enhances the aerosols extinctions [*Hand and Malm*, 2007], while the less

Table 1.1, Typical Extinction Coefficients of Different Aerosols

Aerosol Species	Sulfate	Nitrate	OC	FineSoil	Coarse	BC
Extinction Coef. (m^2/g)	1.5~4	2.5~3	1.8~4.7	1~1.25	0.3~0.6	8~12

Adapted from [Seinfeld, 2004]

insoluble OC, BC, and dust are less influenced by the ambient humidity. For humid areas, reductions of sulfate and nitrate aerosols are more important for improving the visibility.

1.3 Air Pollution in the eastern U.S.

As discussed in section 1.1, public concern on air pollution issues occurred after the "Los Angeles Smog" was discovered in 1950s. In 1970, the first Clean Air Act was passed by the U.S. congress, and the U.S. Environment Protection Agency (USEPA) was established to regulate emissions from point and mobile sources. The USEPA also set the National Ambient Air Quality Standards (NAAQS) with six criteria air pollutants: carbon monoxide (CO), lead, NO_x, O_3, sulfur dioxide (SO_2) and particulate pollution (PM_{10} and $PM_{2.5}$). The Clean Air Act was substantially amended in 1977 and 1990. The EPA estimates that in 2020 the Clean Air Act and its amendments will prevent over 230,000 early deaths, and create about $2 trillion in economic benefits. The total cost of clean air act amendments is about $65 billion, and the estimated benefits exceed costs by a factor of 30 to 1 [*EPA*, 2011].

During the last several decades, the continuous monitoring of criteria air pollutants demonstrated the benefits from the clean air act and its amendments. Figure 1.2 presents the long-term trends of ambient CO, O_3, SO_2 and NO_2 from 1980 to 2010 (figures from http://www.epa.gov/airtrends/). Figure 1.3 presents the trends for PM_{10} and $PM_{2.5}$ mass concentrations. With large reductions of CO, SO_2, NO_x and PM emissions, the national ambient concentrations of CO, SO_2, NO_2 and PM_{10} are generally lower than the NAAQS standards, while O_3 and $PM_{2.5}$ have become the predominant sources of air pollution exceedance in the U.S. With the improved information on health effects, the

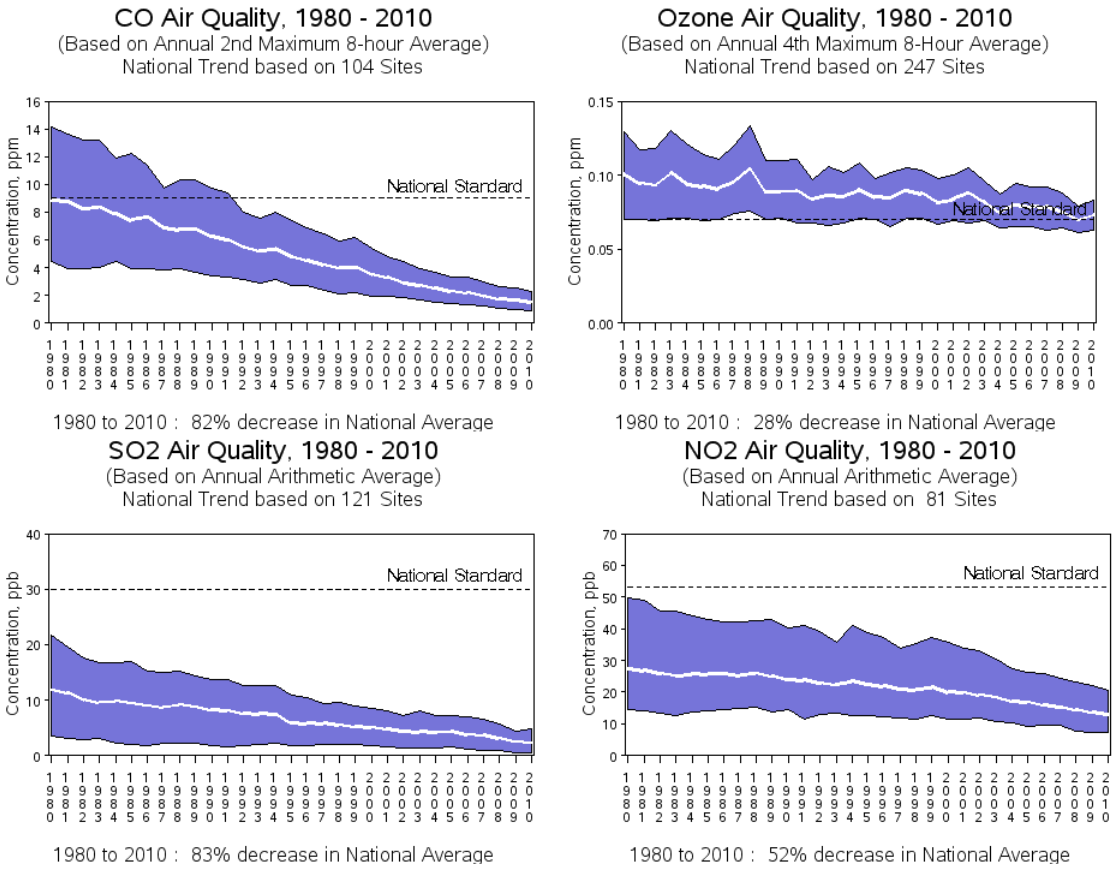

Figure 1.2 National Trends of CO, O_3, SO_2 and NO_2 from 1980 to 2010.

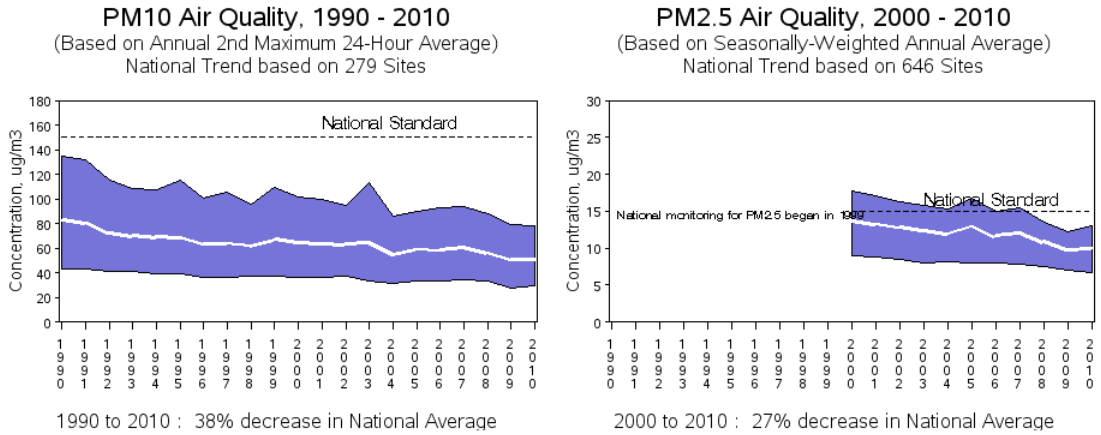

Figure 1.3 National Trends of PM_{10} and $PM_{2.5}$ from 1990 to 2010.

NAAQS standards have been becoming stricter during the last several decades. For instance, the ambient O_3 standard changed from 1-hour average of 120 ppb in 1979 to 8-hour average of 80 ppb in 1997, and finally to an 8-hour average of 75 ppb in 2008. Table 1.2 presents the current standards for each air pollutant.

Table 1.2. U.S. National Ambient Air Quality Standards.

Pollutant	Primary/Secondary	Averaging Time	Level
CO	Primary	8-hour	9 ppm
		1-hour	35 ppm
Lead	Primary and Secondary	3-month	0.15 $\mu g/m^3$
NO_2	Primary	1-hour	100 ppb
	Primary and Secondary	Annual	53 ppb
O_3	Primary and Secondary	8-hour	75 ppb
$PM_{2.5}$	Primary and Secondary	Annual	15 $\mu g/m^3$
		24-hour	35 $\mu g/m^3$
PM_{10}	Primary and Secondary	24-hour	150 $\mu g/m^3$
SO_2	Primary	1-hour	75 ppb
	Secondary	3-hour	0.5 ppm

Source: EPA website: http://www.epa.gov/air/criteria.html. Primary standards provide public health protection, including protecting the health of 'sensitive' populations such as asthmatics, children, and the elderly. Secondary standards provide public welfare protection, including protection against decreased visibility and damage to animals, crops, vegetation, and buildings. Units: ppm = parts per million, $\mu g/m^3 = 10^{-6}$ g/m^3

In the eastern U.S., O_3 and particulate matter are the major air pollution problems. Figure 1.4 and 1.5 presents the nonattainment areas for 8-hour O_3 and annual $PM_{2.5}$ standards (adapted from http://www.epa.gov/reg3artd/airquality/nonattain.htm) in the Mid-Atlantic region. In this study, I focus on the air pollution issues in this region including Maryland (MD), Virginia (VA), and Pennsylvania (PA). To investigate the regional transport of air pollutant, the upwind states Ohio (OH) and West Virginia (WV) are also incorporated here.

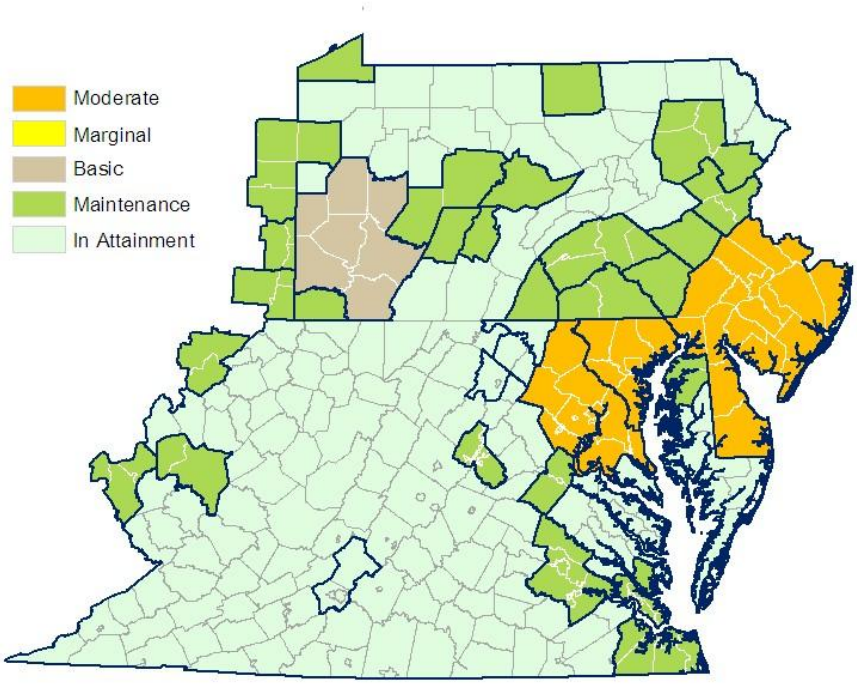

Figure 1.4 Map of the 8-hour O_3 nonattainment areas in the Mid-Atlantic States (adapted from http://www.epa.gov/reg3artd/airquality/nonattain.htm).

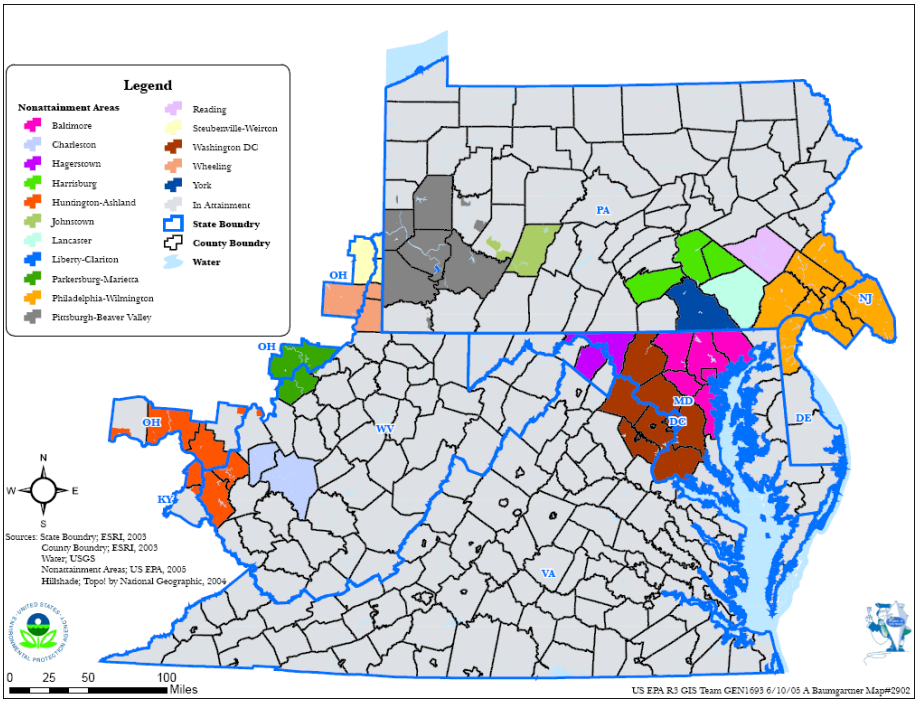

Figure 1.5 Map of $PM_{2.5}$ Nonattainment areas in Mid-Atlantic region (adapted from http://www.epa.gov/reg3artd/airquality/nonattain.htm).

1.4 Air Pollution in China

Nowadays China is the world's second largest economy, and considered the engine of the world's economic growth. With the rapid economic development, the demand for energy and raw material increased drastically in the last several decades. Coal burning accounts for 70% of the total energy consumption in China [*CESY*, 2005], and the total number of passenger vehicles in China is about 100 million in 2011. The air quality is deteriorating in China, especially in the megacities [*Chan and Yao*, 2008]. Table 1.3 presents the Chinese National Ambient Air Quality Standards (CNAAQS) and values recommended by the World Health Organization (WHO). The version of

CNAAQS was established in 1996, now outdated to accommodate the change of emissions in the last decade. In the 1990s, the major concerns on air quality were floating dust and dust storm, so the total suspended particulates (TSP) and PM_{10} were incorporated in the CNAAQS. With great efforts to defend against the expansion of deserts in northeast China, the frequency and intensity of dust storms have been substantially decreased in the last 20 yr [*Wang et al.*, 2004; *Wang et al.*, 2010d]. With significantly increased coal burning and vehicles numbers, SO_2 and $PM_{2.5}$ have become major air pollution issues in urban areas

Table 1.3 National Ambient Air Quality Standards for some air pollutants in China.

Pollutant	Averaging Time	China I[a]	China II[a]	China III[a]	WHO[b]
	1-hour	150	500	700	
	24-hour	50	150	250	125
SO_2	Annual	20	60	100	50
	1-hour	120	120	240	
	24-hour	80	80	120	
NO_x	Annual	40	40	80	
	1-hour	120	120	240	200
	24-hour	80	80	120	
NO_2	Annual	40	40	80	40
	1-hour	10000	10000	20000	30000
	8-hour				10000
CO	24-hour	4000	4000	6000	
	1-hour	120	160	200	
O_3	8-hour				120
	24-hour	50	150	250	
PM_{10}	Annual	40	100	150	
	24-hour	120	300	500	
TSP[c]	Annual	80	200	300	

Data are from the GB 3095-1996, Unit: $\mu g/m^3$

[a] China I: residential Areas; China II: commercial areas; China III: industrial areas

[b] WHO values are guideline values

[c] TSP: total suspended particulate matter, with diameter less than 100 μm

[*Chan and Yao,* 2008]. Therefore, control measures have been established individually from different areas of China [*Hu et al.,* 2010], and especially for the Beijing area during 2008 Olympics [*Schleicher et al.,* 2011; *Shen et al.,* 2010; *Wang et al.,* 2010c].

Recently, the $PM_{2.5}$ pollution emerged in megacities such as Beijing and Guangzhou. In Beijing, the total number of passenger vehicles increased from 2 million in 2003, to 3 million in 2007, 4 million in 2010, and reached around 5 million in late 2011. The increase of automobiles not only created traffic jams, but also drastically elevated the emissions of air pollutants such as NO_x and CO. In Beijing, weekly average $PM_{2.5}$ concentrations were observed as 37-357 $\mu g/m^3$ with the highest concentration in the winter [*He et al.*, 2001]; the daily value for 2005-2006 was 118.5 ± 40.6 $\mu g/m^3$ [*Yang et al.*, 2011]. The annual value of $PM_{2.5}$ was 101 $\mu g/m^3$, about 6 times higher than the USEPA $PM_{2.5}$ standard [*Zheng et al.,* 2005]. Several episodes in 2011 drew public attentions to the air pollution caused by fine particles; the incorporation of $PM_{2.5}$ standard into CNAAQS is under development [*Yang,* 2012]. In this study, I will focus on the SO_2 pollution, the primary pollution and an important precursor for anthropogenic aerosols.

1.5 Overview of the research

The University of Maryland (UMD) Regional Atmospheric Measurement Modeling and Prediction Program (RAMMPP) has performed aircraft measurements during the O_3 season (June to September) for the last 15 years. The research flights were

mainly conducted near the Washington DC-Baltimore (MD) region. I analyzed the long-term data of vertical distribution of air pollutants such as O_3, SO_2, CO and aerosols, and to investigate the long-term trend of air pollution in the Mid-Atlantic region. I also utilized the USEPA Continuous Emission Monitoring System (CEMS) data, SO_2 and NO_x emissions from the point sources like power plants and industrial boilers, to investigate the long-term trend of air pollutant emissions. The long-term surface observations of NO_x and O_3 in MD, DC and northern VA (NOVA) were analyzed to track the response to change of emissions. The local air quality in DC-Baltimore region is determined not only by the local emissions, but also by the regional transport of air pollutants and their precursors from the upwind states such as OH and PA. I conducted a cluster analysis of back trajectories to study the effects of regional transport.

The study of air pollution in China focused on sulfur compounds including SO_2 and sulfate aerosols. I participated in the East Asian Study of Tropospheric Aerosols and Impact on Regional Climate (EAST-AIRC) campaign, and conducted aircraft measurements of ambient SO_2 over central China. I used the integrated SO_2 columns to evaluate the remotely sensed SO_2 products by NASA's Ozone Monitoring Instrument (OMI). A new retrieval algorithm for OMI SO_2 products was also tested. To study the regional SO_2 pollution over central and eastern China, I conducted numerical simulations using the Community Multiscale Air Quality (CMAQ) model. The CMAQ model system was modified for improved calculation of SO_2 dry deposition velocity and by adding the function of horizontal advection calculation. I evaluated the NASA Intercontinental Chemical Transport Experiment Phase-B (INTEX-B) emission inventory through the comparison of OMI SO_2 products and numerical simulations. The export and lifetime of

atmospheric SO_2 were also discussed. At last, the MODIS aerosol products were applied to evaluate the aerosol simulations from CMAQ.

In section 2, I briefly describe the experiment methods and data used including aircraft platform, emission data, numerical model, and satellite products. Section 3 presents the study of long-term trends of trace gas over the eastern U.S., and the clustering analysis is introduced. In section 4, I summarize the results from aircraft campaign over central China, discuss the SO_2 plumes observed in the free troposphere (FT), and validate the OMI SO_2 products. Section 5 illustrates the CMAQ model set up for numerical simulations, and I evaluate the emission inventory for China constrained by aircraft observations and satellite measurements. I also conduct a case study on properties of atmospheric aerosols using the numerical simulations in section 6. Finally, I explain the conclusions of this work, and discuss the work in future.

Chapter 2. Experimental Methods and Data

2.1 Instrumentation

2.1.1 O_3

In situ measurements of ambient O_3 were conducted using a commercially available analyzer (Thermo Environmental Instruments, Model 49/49C, Franklin, Massachusetts). The analyzer measures the O_3 absorption at 254 nm and calculates the absolute O_3 concentration based on the Beer-Lambert Law. Figure 2.1 presents the flow diagram of TEI 49C analyzer. Ambient air enters the instrument and splits to two parts; one portion flows directly into the optical cells, and the other portion flows through the O_3 scrubber creating "zero O_3" air. Two cells (Cell A and Cell B) sample ambient air and "zero O_3" air alternately. Radiation released from the UV lamp enters two optical cells and two detectors measure their intensities. The absorption measured with the "zero O_3" air is used as the reference intensity I_0 and the value obtained from the ambient air is the measurement I. Applying the Beer-Lambert Law, we have

$$\frac{I}{I_0} = e^{-C[O_3]} \qquad \text{(Equation 2.1)}$$

where C is the instrument constant (the absorption cross-section times path length), and $[O_3]$ is the ambient O_3 concentration. Controlled by two solenoids, the ambient air and "zero O_3" air alternate every 10 seconds, i.e., the two optical cells work simultaneously,

but out of phase. Through averaging readings from these two optical cells, the fluctuations of lamp intensity are cancelled out [*TEI*, 2004a]. The precision of TEI 49C can reach 1 ppb for 10 s data.

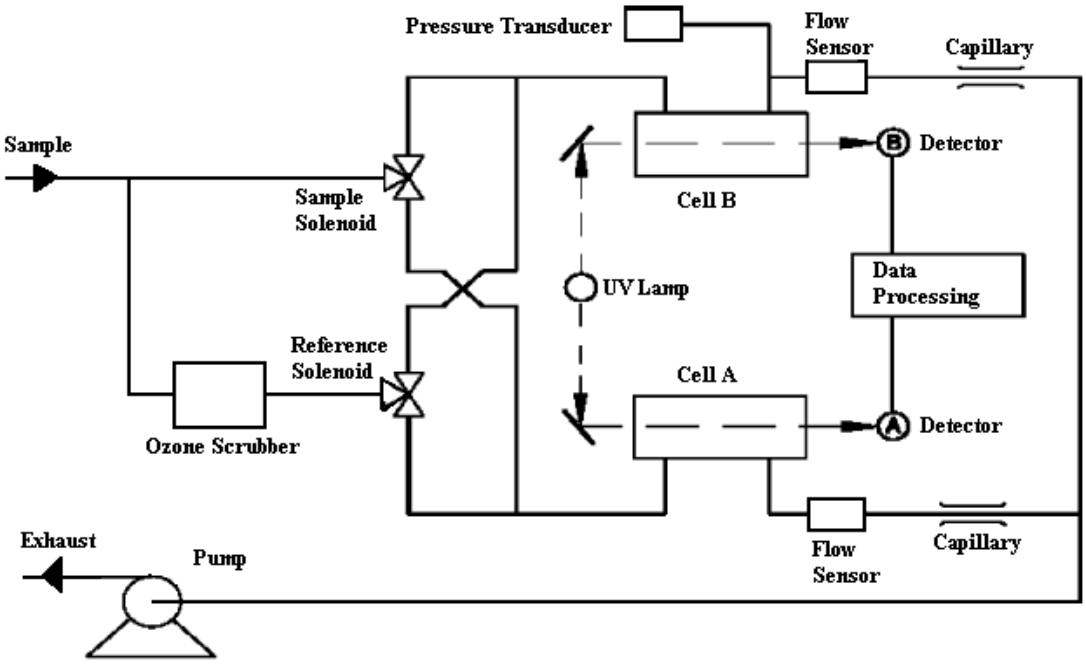

Figure 2.1 Flow diagram of the TEI O_3 analyzer (adapted from TEI 49C manual).

2.1.2 CO

CO is measured by a modified commercial analyzer (Thermo Environmental Instruments, 48S, Franklin, Massachusetts) [*Dickerson and Delany*, 1988]. The operational mechanism is a non-dispersive infrared (NDIR) gas filter correction (GFC) algorithm. Figure 2.2 demonstrates the flow diagram of this instrument. A lamp emitting 4.67 μm radiation works as the IR source. The radiation is chopped by a rotating gas filter; half of the filter is filled with high concentration of CO gas, and the other half of

filter is filled with pure N_2 gas. The N_2 gas does not absorb IR radiation, so the beam passing through it is considered to be the sample beam; the IR radiation passing through the CO gas is the reference beam, which is optically thick. Both beams enter the optical cell with the about 30-m optical path, and the detector measures the intensities after absorption. The difference between the sample and reference beam is used to calculate the absolute concentration of ambient CO gas [*TEI*, 2004b].

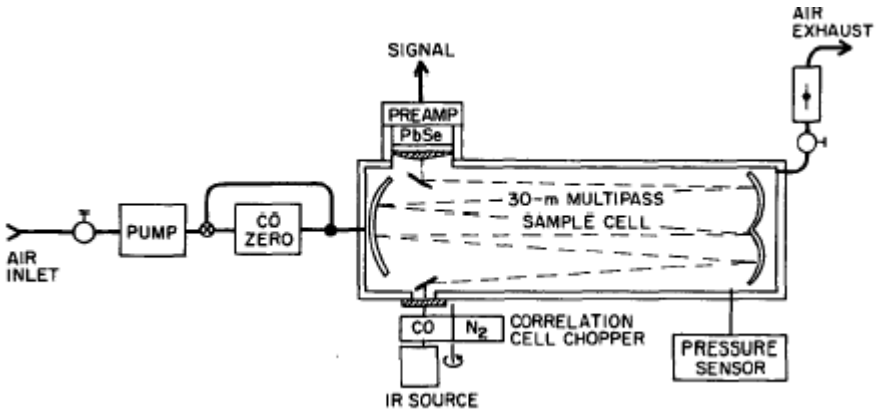

Figure 2.2 Flow diagram of the modified CO analyzer (adapted from [*Dickerson and Delany*, 1988]).

The baseline of 48S analyzer drifts with respect to the ambient temperature and pressure change. To correct for background drift, a "chemical zero" is added to the instrument, as "CO zero" labeled in Figure 2.2. The device is packed with molecule sieves, gamma alumina coated with 5% palladium (Pd), and heated to 250 ℃, which works as catalyst converting the ambient CO to CO_2. The gas flow is controlled by a solenoid. When the sample air passes through the catalyst, the reading is considered as

reference in "zero mode"; when the sample air bypasses from the catalyst, the signal is measurements in "sample mode". During a research flight, the instrument is frequently set in "zero mode" to track baseline shifts, and the baseline CO is subtracted from the measurement to retrieve the ambient CO concentration. The CO analyzer has about 40 ppb precision (95% confidence interval) for one minute moving averages of 10 s data [*Dickerson and Delany*, 1988]

2.1.3 SO_2

The ambient SO_2 concentration is observed using a modified commercial analyzer (Thermo Environmental Instruments 43C, Franklin, Massachusetts) [*Luke*, 1997]. The analyzer uses a pulsed fluorescence technique, and the flow diagram is shown in Figure

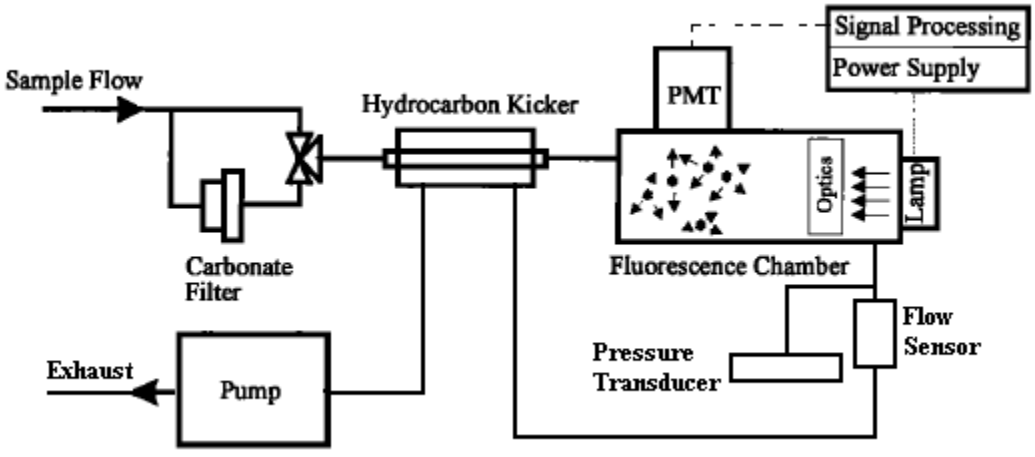

Figure 2.3 Flow diagram of the modified SO_2 analyzer (adapted from [*TEI*, 2004c]).

2.3. Ambient air is pumped into the instrument at a flow rate of 0.5 L/min. The pulsed fluorescence technique has significant interferences from organic compounds. Therefore the sample air passes through a "hydrocarbon kicker", a semi-permeable membrane that removes VOCs such as polycyclic aromatic hydrocarbons (PAH) but does not affect SO_2. Then the sample air enters the optical chamber, and is exposed to a pulse of shortwave radiation near 180-230 nm emitted by the UV lamp [*Calvert and Stockwell*, 1984]. The SO_2 molecules are excited by the UV radiation, then decay to a lower energy state by fluorescence at a different wavelength [*TEI*, 2004c].

$$SO_2 + h\upsilon_1 \rightarrow SO_2^* \rightarrow SO_2 + h\upsilon_2 \qquad \text{(reaction 2.1)}$$

To reduce interferences from the incident UV radiation, the photomultiplier (PMT) detector is located perpendicular to the optical chamber. The intensity of emitted fluorescence is proportional the SO_2 concentration [*Hains*, 2007].

A filter soaked with potassium carbonate (K_2CO_3) and glycerin is placed in the flow system before the optical chamber for scrubbing SO_2, and acts as the "chemical zero". A solenoid is installed to switch the air between flowing through the "chemical zero" in zero mode and bypassing this device in sample mode. During aircraft measurements, the SO_2 analyzer is set frequently to zero mode in order to determine the analyzer's baseline. In the post flight data processing, the value of baseline is interpolated and subtracted from measurements in sample mode to calculate the absolute SO_2 concentration. The detection limit of this instrument is 0.25-0.3 ppb for 10 second data [*Hains*, 2007].

2.1.4 Aerosols Scattering

A commercial Trust Science Innovation (TSI) Nephelometer (Model 3563, TSI, St. Paul, MN) is used to measure the light scattering of atmospheric aerosols at three wavelength: 450, 550, and 700 nm. Figure 2.4 presents the flow diagram of this instrument. The main body of the Nephelometer is a 10-cm diameter aluminum tub as sensing volume. Along the axis there are several aperture plates, ranging from 7-170 °on the horizontal range of the lamp. The backscatter shutter blocks the angles from 7-90 °so that only backscattering is measured. The light trap provides a dark reference against which to measure the scattered light. Three PMTs are located behind the reference chopper to measure the intensity of scattering at three wavelengths individually. A reference chopper is utilized to calibrate the scattering measurement. The chopper is divided into three parts: the dark zone, the calibration zone, and the view zone. The dark zone blocks out all light, and works as a "zero" to test the background noise; the calibration zone allows about 0.1% of the light passing through, to monitor the lamp's

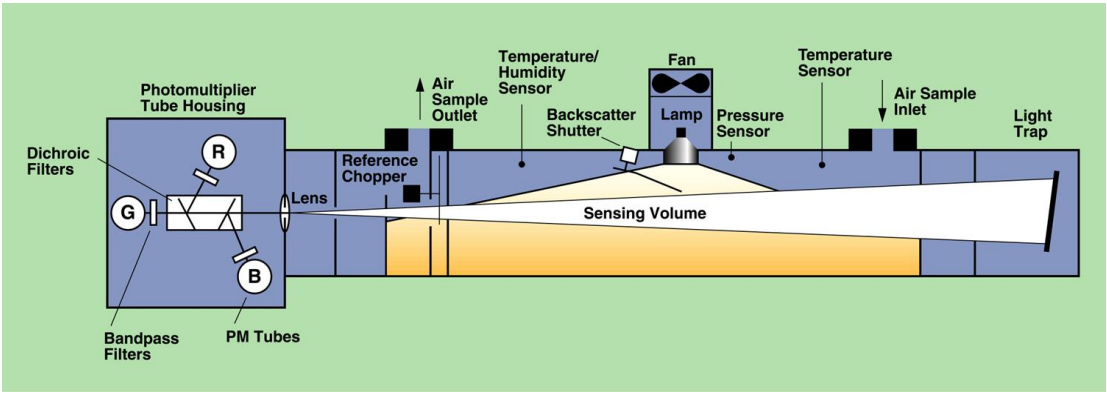

Figure 2.4 Flow diagram of the TSI 3563 Nephelometer (adapted from [*TSI*, 1997]).

stability; the view zone passes light through unchanged as the signal. After the beam is chopped by the rapidly rotating chopper, data processing devices retrieve the information from the resulting signal [*TSI*, 1997].

The light flux (B) detected by the PMTs is derived as [*Anderson et al.*, 1996]:

$$B = \frac{I_0}{y}\int_{\phi_1}^{\phi_2} \beta(\phi)\sin(\phi)d\phi \qquad \text{(Equation 2.2)}$$

Where I_0 is the intensity of incident light, y is the optical path length, ϕ is the angle between the source and the incident light, and $\beta(\phi)$ is the angular scattering function. Through integrating from $\phi_1 = 0$ to $\phi_2 = \pi$, the equation 2.2 becomes

$$B = \frac{I_0}{y} \times \frac{b_{scat}}{2\pi} \rightarrow b_{scat} = \frac{2\pi By}{I_0} \qquad \text{(Equation 2.3)}$$

It is worth noting that the instrument heats the airstream, drying the ambient air to a relative humidity (RH) less than 20%. Therefore the hygroscopic growth or, in this case, shrinking of aerosol particles should be incorporated to correct this influence. The hygroscopic growth factor f(RH) is expressed in:

$$f(RH) = \frac{b_{scat,RH}}{b_{scat,RH_{ref}}} = \left(\frac{100 - RH}{100 - RH_{ref}}\right)^{-\gamma} \qquad \text{(Equation 2.4)}$$

where RH is the ambient relative humidity, and RH_{ref} is the relative humidity inside the Nephelometer. The coefficient γ must be empirically measured, and depends on the chemical composition of the aerosols sampled. An empirical value is 0.35 for γ in the

eastern U.S. [*Remer et al.*, 1997]. The detection limits are 0.44, 0.17 and 0.26 Mm^{-1} (10^{-6} m^{-1}) for scattering at 450, 550, and 700 nm respectively.

2.2 Aircraft Platform

2.2.1 RAMMPP aircraft: Piper Aztec and Cessna 402B

Light aircraft are employed by the UMD RAMMPP program to conduct the airborne measurements: a Piper Aztec (before 2009) and a Cessna 402B (2010 to 2011). Both aircraft have twin engines, and the instruments are installed inside the fuselage. Table 2.1 lists the implementation of selected instruments with data used in this study.

Table 2.1 List of instruments on RAMMPP aircraft and implementation year.

Instrument	O_3	CO	SO_2	Nephelometer	NO_2
Data from	1996	1999	2000	2001	2011

The instruments sample the ambient atmosphere through separating trace gas and aerosol inlets. Figure 2.5 demonstrates the inlets on the Aztec and Cessna. The inlets on the Aztec are located on top of the fuselage; the aerosol inlet faces forward and the trace gas inlet faces aft. Even though the curve of sampling tubing is designed to be isokinetic, the shape of aerosol inlet limits the sampling range of aerosols to those below 1.0 μm in diameter. Compared to the Aztec, the Cessna has more space to carry more instruments, and on its nose is a specially designed, shrouded, aerosol inlet positioned 46 cm forward of the nose cone. The shrouded inlet has been characterized in two different aerosol inlet

characterization experiments [*Huebert et al.*, 2004; *McNaughton et al.*, 2007], and is currently used on NOAA's Cessna T206, and NASA's P3 aircraft. The inlet's blunt edges and aerodynamic shape conform to aircraft sampling requirements of isoaxial sampling, isokinetic sampling, and positioning of the inlet outside of the boundary layer of the aircraft. The new inlet has improved the RAMMPP aerosol collection capability from sub-micron particles only to a 50% passing efficiency of particles up to 5 μm in diameter (spherical) or 3.0 μm in diameter (geometric).

Figure 2.5 Pictures of trace gas and aerosol inlet (left: Aztec; right: Cessna).

The meteorological information is collected through an RH/Temperature/Pressure probe, and the location and altitude information is retrieved from an aviation Global Positioning System (GPS) device. Other aerosol instruments such as an Aethalometer and a Particle Soot Absorption Photometer (PSAP) are also onboard. Table 2.2 presents the list of the instruments installed in the Cessna during the 2011 flight season. More

information about the RAMMPP aircraft program can be found at the RAMMP website (http://www.atmos.umd.edu/~RAMMPP).

Table 2.2 List of Instruments on the Cessna 402B.

Parameter	Temporal Resolution	Detection Limit	Technique/Instrument
Position	10 s	15 m	Garmin GPS90
Pressure	10 s	0.2 hPa	Vaisala PTU 300
Temperature	10 s	0.2 ℃	Vaisala PTU 300
RH	10 s	1.00%	Vaisala PTU 300
O_3	10 s	1 ppb	UV O_3 Analyzer (TEI 49C)
CO	10 s	40 ppb	Modified NDIR/GFC CO Analyzer (TEI 48S)
SO_2	10 s	0.3 ppb	Modified UV Fluorescence SO_2 Analyzer (TEI 43C)
NO_2	10 s	60 ppt	Cavity Ringdown Spectroscopy (LGR[a] RMT-200)
Aerosol Absorption	2 min	0.1 μg/m^3	7 Wavelength[b] Aethalomter (Magee Scientific AE31)
Aerosol Scattering	30 s	0.17-0.44 Mm^{-1}	3 Wavelength[c] Integrating Nephelometer (TSI 3563)
Particle Counts	1 s	0.01 um	Condensation Particle Counter (TSI 3007)
Aerosol Size	10 s	N/A	Laser based optical (MetOne 9012)

[a] LGR: Los Gatos Research, Mountain View, CA

[b] 7 wavelengths: 380, 470, 520, 590, 660, 880, and 950 nm

[c] 3 wavelengths: 450, 550, and 700 nm

2.2.2. Y-7 aircraft in 2008 China campaign

In the U.S.-China joint aircraft campaign during spring 2008, a Y-7 turboprop transport airplane (the Chinese version of the Antonov An-26) was employed as the airborne measurement platform. The aft-facing trace gas inlet was installed on a rack to

the left of fuselage along with a T/RH probe. Figure 2.6 presents the aircraft and the T/RH probe.

Figure 2.6 Figures of Y-7 aircraft and the trace gas inlet for 2008 China campaign.

The modified TEI 42C fluorescence SO_2 analyzer was located inside the fuselage, and generated 10 s data of the ambient SO_2 concentration. The T/RH probe and an onboard GPS device provided measurements of ambient temperature, RH, location and altitude. Compared with the light aircraft used in the eastern U.S., Y-7 is a larger airplane with a payload about 5 tons and cruise speed of ~400 km/h. For safety concerns, the airplane is forbidden to fly below 1000 m above ground level (AGL) except on takeoff and landing. The details of flight planning are discussed later in section 4.1.

2.3 Emission data

2.3.1 EPA NEI Emission Inventory of the U.S.

For a comprehensive study of air pollution trend in the eastern U.S., two emission datasets were applied: the USEPA National Emission Inventory (NEI) and the USEPA Continuous Emission Monitoring System (CEMS) data for states of Maryland (MD), Virginia (VA), West Virginia (WV), Pennsylvania (PA) and Ohio (OH) (hereafter named the five states). The NEI emission inventory, a comprehensive and detailed estimate of emissions of both criteria and hazardous air pollutions from all sources, is prepared every three years and is based on emission measurements and emission model results (available

Table 2.3 Description on 5 emission categories of NEI.

Emission Category	Descriptions	Examples
Point	emission sources individually inventoried and usually located at a fixed location	industrial facilities and power plants
Nonpoint	individual emission sources too small in magnitude or too numerous to inventory as point sources	residential heating and consumer solvent use
On-road	estimates from MOBILE6[a] model for highway vehicles, aircraft, locomotives, marine vessels, etc	highway vehicles
Non-road	estimate from NONROAD[b] model for internal combustion engine emissions	railroad equipment, off highway vehicles
Event	random sources of air pollution emissions	wildfires and prescribed burns

Information from NEI description (http://www.epa.gov/ttnchie1/net/2008inventory.html)

[a] MOBILE6 Vehicle Emission Modeling Software, an emission factor model to predict gram per mile emissions of VOCs, CO, NO_x, CO_2, PM and toxics from cars, trucks, and motorcycles under various conditions. (model website http://www.epa.gov/otaq/m6.htm)

[b] NON-ROAD model, estimate the emission inventories for all non-road equipment with different fuel types, including VOCs, CO, NO_x, PM, SO_2, and CO_2. (Model website http://www.epa.gov/otaq/nonrdmdl.htm#model)

http://www.epa.gov/ttnchie1/net/2008inventory.html). In the NEI, emissions are grouped into five data categories: point, nonpoint, on-road, non-road, and event. Table 2.3 lists the description of each categories of the latest 2008 NEI. In this study, NEI data from 2002, 2005, and 2008 and annual national data were utilized to investigate the trends of criteria air pollutants from point sources and automobiles over the last decade.

Because the NEI has only annual emission data and is updated every three years, it is not practical to investigate the daily change of emissions. The CEMS program was developed by the USEPA, which is continuously monitoring the emissions of point sources for the USEPA Clean Air Market (http://www.epa.gov/airmarkets/). CEMS data include the emissions of criteria air pollutants such as NO_x and SO_2, with hourly resolution of each point source. Point sources are important for some air pollutants; for instance, almost all the anthropogenic SO_2 emissions are from point sources. In this study, the daily CEMS data from the five states from 1997 to 2011 (3^{rd} quarter) are used.

2.3.2 INTEX-B emission inventory for East Asia

During the EAST-AIRC campaign, an aircraft campaign was carried out in spring 2008 over central China, to measure the distribution of ambient SO_2. As well as the *in situ* measurements, I also used the OMI SO_2 satellite products to evaluate the tropospheric SO_2 column contents over the campaign area (section 4.2). Numerical model simulations of tropospheric SO_2 were also conducted using the CMAQ model (section 5.2), to provide supplementary information on the study of sulfur pollutants. To

drive the model and evaluate the SO_2 export and lifetime (section 5.2), I used the latest East Asian emissions dataset, the NASA INTEX-B emission inventory.

The INTEX-B emission inventory was developed based on the year of 2006, to support global chemical transport models (CTMs) such as the Goddard Chemistry Aerosol Radiation and Transport (GOCART) model [*Chin et al.*, 2000a]. The INTEX-B emission inventory followed the NASA Transport and Chemical Evolution over the

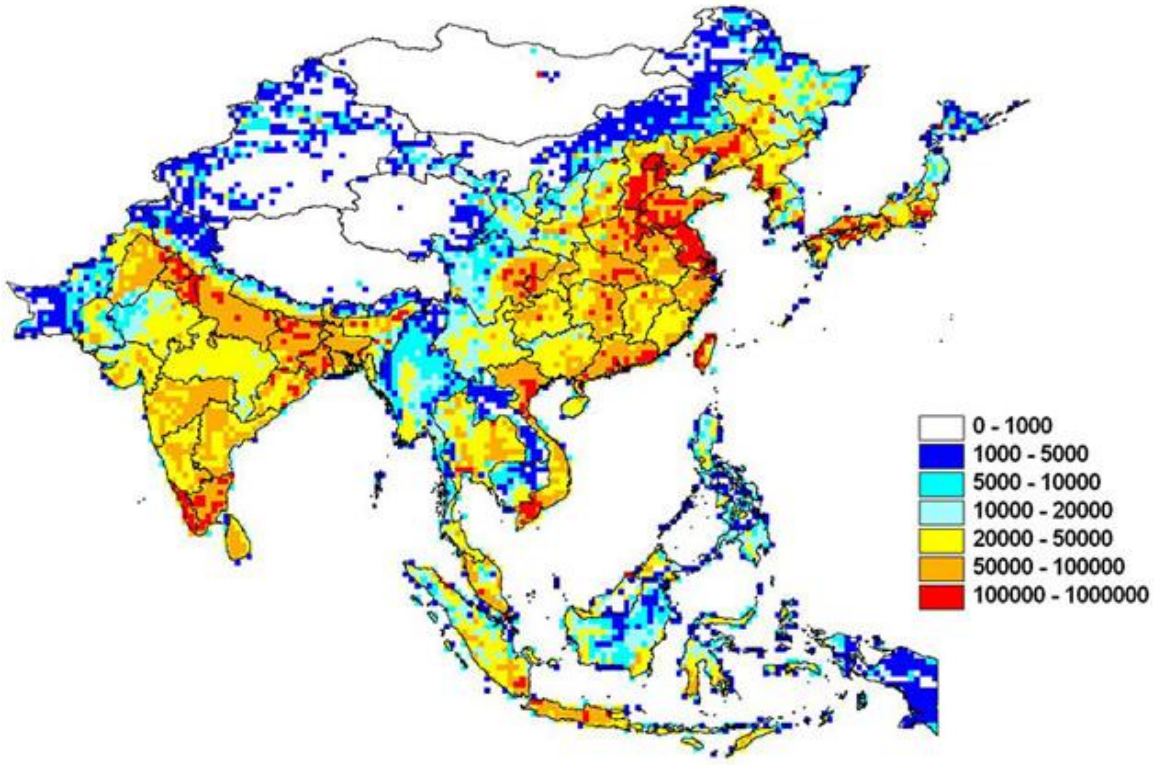

Figure 2.7 Distribution of CO from INTEX-B emission inventory (Unit: tons/year per grid, adapted from http://www.cgrer.uiowa.edu/EMISSION_DATA_new/index_16.html).

Pacific (TRACE-P) emission inventory for year 2000 [*Streets et al.*, 2003]. The INTEX-B emission inventory (available at http://mic.greenresource.cn/intex-b2006) contains emissions estimates for major pollutants (SO_2, NO_x, CO, PM_{10}, $PM_{2.5}$, BC and OC) and 30 lumped VOC species from the SAPRC-99 chemical mechanism; the spatial resolution is $0.5° \times 0.5°$. For an example, Figure 2.7 illustrates the spatial distribution of CO emissions. It is notable that central and eastern China, where the majority of population and industry are located, accounts for a large part of the total emissions of China. Distributions of other air pollution emissions have a similar pattern with central and eastern China as hot spots. I applied this emission inventory to investigate tropospheric SO_2 chemistry through combination of *in situ* measurements, satellite observations, and numerical simulations. Details are discussed in section 5.

2.4 Satellite data

Satellites are effective at monitoring large areas for conducting long-term global observations of the land surface, biosphere, atmosphere, and ocean of the Earth, and the NASA's Earth Observing System (EOS) is one of the best-known satellite programs (EOS website http://eospso.gsfc.nasa.gov/). Large amounts of EOS satellite data have been collected, processed, and stored for public usage such as the NASA Goddard Earth Sciences Data and Information Service Center (GES DISC, home page http://disc.sci.gsfc.nasa.gov/data-holding). In this study, OMI tropospheric SO_2 products are used. OMI is an ultraviolet/visible (UV/VIS) nadir solar backscatter spectrometer

built under the cooperation between the Netherlands Agency for Aerospace Programs (NIVR) and Finnish Meteorological Institute (FMI), onboard of NASA Aura satellite. OMI provides nearly daily global coverage with spatial resolution of 13 km × 24 km and measures trace gases including O_3, NO_2, SO_2, HCHO, as well as aerosol characteristics, and cloud properties [*Levelt et al.*, 2006].

The OMI SO_2 retrievals followed previous SO_2 remote sensing products from the Total Ozone Mapping Spectrometer (TOMS) [*Bluth et al.*, 1992; *Bluth et al.*, 1993; *Krueger*, 1983; *Krueger et al.*, 1995], the Global Ozone Monitoring Experiment (GOME) [*Burrows et al.*, 1999; *Eisinger and Burrows*, 1998], and the Scanning Imaging Absorption Spectrometer for Atmospheric Cartography (SCIAMACHY) [*Bovensmann et al.*, 1999]. The Band Residual Difference (BRD) algorithm was developed for SO_2 retrievals [*Krotkov et al.*, 2006] by the NASA/GSFC Global Sulfur Dioxide Monitoring group (http://so2.gsfc.nasa.gov/). OMI SO_2 products have proven useful for measurements of volcanic sulfur emissions [*Carn et al.*, 2009; *Yang et al.*, 2007], industrial processes [*Carn et al.*, 2007] and anthropogenic emissions [*Krotkov et al.*, 2008]. There are four estimates of SO_2 column densities; planetary boundary layer (PBL) SO_2 column, lower tropospheric (TRL) SO_2 column, middle tropospheric (TRM) SO_2 column, and upper tropospheric and stratospheric (STL) SO_2 column, with center of mass altitudes (CMA) of 0.9 km, 2.5 km, 7.5 km, and 17 km respectively (description at http://so2.gsfc.nasa.gov/Documentation/OMSO2Readme_V111_0818.htm).

Because this study focuses on the SO_2 in the lower atmosphere, the OMI daily gridded products (SO2L2G, named OMISO2 product hereafter) are used (available on http://disc.sci.gsfc.nasa.gov/Aura/data-holdings/OMI/OMISO2g_v003.shtml). The daily

data are downloaded and pre-processed for future use. The details are discussed in section 4.2. To improve the detection limit and quantification of SO_2 from OMI, an advanced algorithm, the Iterative Spectral Fitting (ISF) algorithm was tested for this study. The ISF algorithm was utilized previously for detecting volcanic clouds [*Yang et al.*, 2009a; *Yang et al.*, 2009b; *Yang et al.*, 2010], to take advantage of the large amount of spectral measurement information from hyper-spectral instruments, such as OMI and GOME-2. The ISF algorithm provides less noisy and potentially more accurate column estimates under the diverse range of conditions encountered in global observations, and has been extended to extract the height of volcanic SO_2 layers in the atmosphere [*Yang et al.*, 2010]. Off-lines ISF products over eastern Asia were generated specifically for the EAST-AIRC aircraft campaign.

To evaluate the aerosol simulations, I used the spaceborne observations of tropospheric aerosols from the Moderate Resolution Imaging Spectroradiometer (MODIS) sensor aboard the EOS Aqua and Terra satellites [*King et al.*, 2003]. MODIS is a multiple-wavelength sensor (36 wavelength bands from 0.415 μm to 14.5 μm), and has moderately high resolution (0.25 km, 0.5 km, or 1 km, depending on wavelength band). A finite look-up table (LUT) is utilized to match the observed spectral reflectance to the simulated spectral reflectance for special aerosol condition [*Kaufman et al.*, 1997]. The MODIS aerosol products are processed for three cases: 1) dark-surface (far from sun glint) ocean target [*Remer et al.*, 2005]; 2) dark-surface (vegetation, soils) land target [*Levy et al.*, 2007]; 3) bright surface (desert) land targets [*Hsu et al.*, 2004]. In this study, I selected the level 2 Aqua aerosol 'dark-target' aerosol products [*Levy et al.*, 2009] (MYD04_2, http://modis-atmos.gsfc.nasa.gov/MOD04_L2/index.html). The MYD04_2

AOD products have been evaluated and compared with the surface AERONET AOD measurements globally [*Levy et al.*, 2010] and in China [*Mi et al.*, 2007]. This daily product has a resolution of 10 × 10 km at nadir, with global coverage every day. There are 144 separate files created each day, and I selected the files over East Asia collected during the EAST-AIRE aircraft campaign period.

2.5 CMAQ model system

Chemical transport models are widely used in research of air pollution and pollution regulations [*Brasseur et al.*, 1998; *Dennis et al.*, 1996; *Muller and Brasseur*, 1995; *Rotman et al.*, 2004]. To conduct numerical simulations for the 2008 EAST-AIRC campaign, I used the USEPA CMAQ modeling system. This system includes the Weather Research and Forecasting (WRF) model (Version 3.1), the Meteorology-Chemistry Interface Processor (MCIP, version 3.5), and the CMAQ model (version 4.6) [*CMAS*, 2007]. WRF is a mesoscale numerical weather prediction system, which digests the meteorological data and generates high resolution meteorological fields for driving CMAQ [*NCAR*, 2010]. The MCIP model is used to convert the WRF outputs to CMAQ-ready meteorological fields with essential parameters such as wet and dry deposition velocities of chemical species [*Byun et al.*, 2007]. I applied the NASA INTEX-B emission inventory to provide emission information for the CMAQ model. The CMAQ model was run 45 days with the first 15 days as spin-up, and hourly outputs were stored

and analyzed. Modifications were also conducted to improve the CMAQ model system; details are discussed in section 5.2.

Chapter 3. Long-term trends of air pollutants over the eastern U.S.

3.1 Summary of RAMMPP research flights

The UMD RAMMPP program was established to conduct atmospheric chemistry related studies on air quality issues in the Mid-Atlantic region through in situ measurements, air quality forecasting, mesoscale modeling and chemical transport modeling [*Castellanos et al.*, 2009; *Castellanos et al.*, 2011; *Dickerson et al.*, 1995; *Doddridge et al.*, 1998; *Hains et al.*, 2008; *Loughner et al.*, 2011; *Ryan et al.*, 1998; *Taubman et al.*, 2004a; *Taubman et al.*, 2004b; *Taubman et al.*, 2006; *Zhang et al.*, 2009a]. As one important component, aircraft measurements of trace gases and aerosol properties have been performed every O_3 season (May to September) for the last 15 years. With an updated air sampling platform and incorporation of new instruments, nowadays the RAMMPP aircraft has the ability to measure CO, O_3, SO_2, NO_2, aerosol absorption, aerosol scattering, particle counts, aerosol size distribution, temperature, pressure, relative humidity, and other parameters (detailed information available on webpage http://www.atmos.umd.edu/~RAMMPP/Instruments.html). The processed flight data and flight statistics are archived at the RAMMPP homepage (available at http://www.atmos.umd.edu/~RAMMPP/archives/ArchiveFlightData.html).

In the last 15 years, about 1000 research profiles (defined as a spiral measuring the vertical distribution of air pollutants, named as research spirals hereafter) have been carried out over more than 100 airports from Georgia to Vermont. During one flight day, several spirals are performed to observe the vertical distribution of air pollutants; most of the flights occur in the O_3 season. Here I only select the flights conducted within the Mid-Atlantic regions during the O_3 season; Figure 3.1 shows the location and statistics of these spirals. On average, there are about 40 spirals conducted each year (except 2006). These research spirals focus on the upwind and downwind areas of the DC-Baltimore region. There are mainly two types of flight plans: the westerly transport flight plan and the southerly transport plan, to investigate the influence of long-range transport. A typical flight day is divided into two parts, a morning flight and an afternoon flight. The morning flight usually covers the upwind region: western MD such as Cumberland, MD for the westerly transport flight pattern and southern VA such as Williamsburg, VA for the southerly transport flight pattern. The afternoon flight usually covers the eastern MD region such as Churchville, MD, downwind of the DC-Baltimore region, to measure the maximum O_3 in the afternoon.

The flight plan is chosen based on the air quality forecast from the Maryland Department of Environment (MDE); a research flight is usually conducted with a forecast of bad air quality. Therefore, most of the research flights occurred on hot summer days with weak surface winds and stagnation. Before 2000, the airports selected for research spirals were changed year by year; after 2000, five airports have been fixed for the westerly transport pattern, which is the major flight pattern. Table 3.1

a)

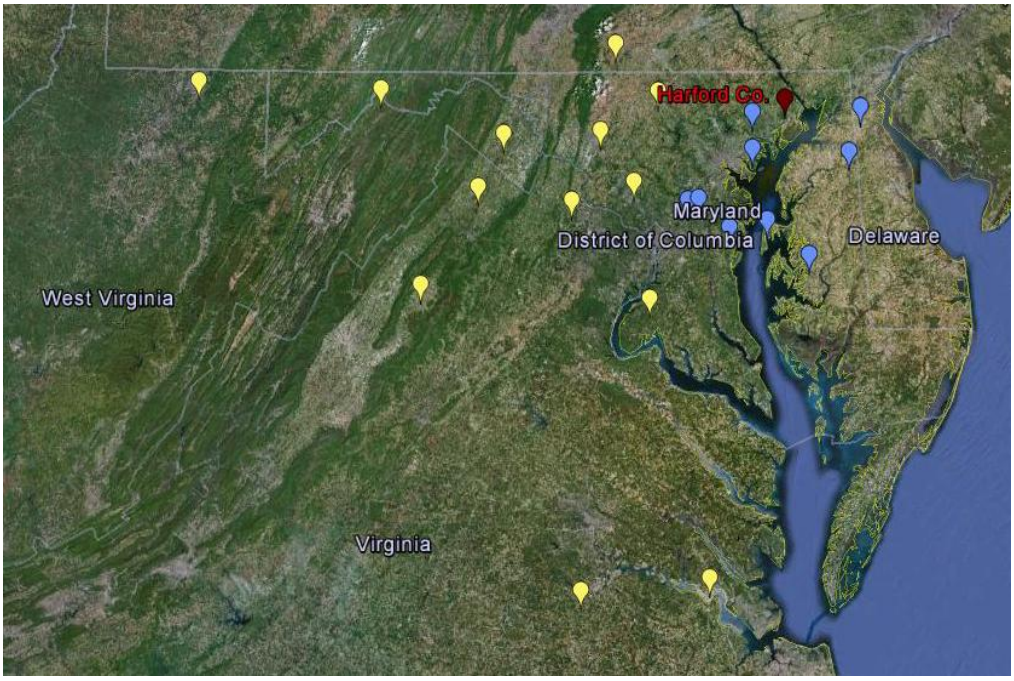

(Yellow pins: morning spirals; blue pins: afternoon spirals; red: Harford Co. airport)

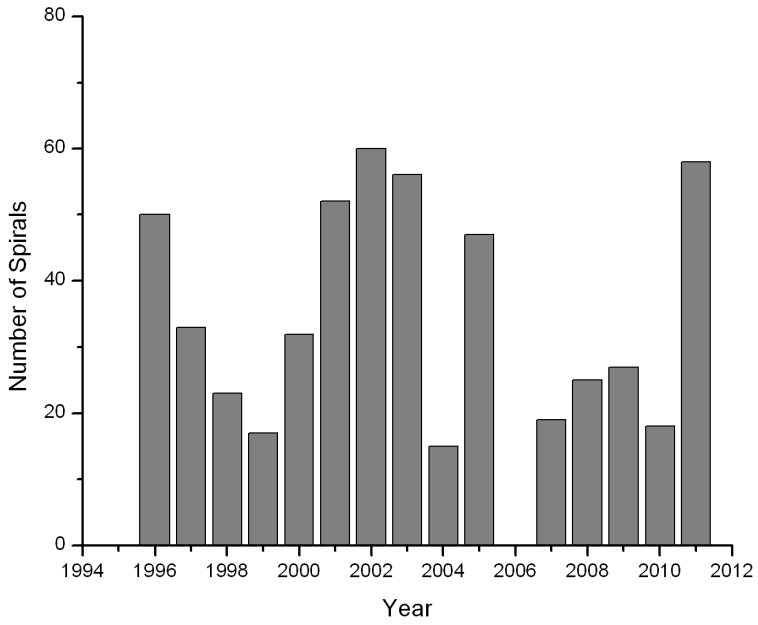

b)

Figure 3.1 Locations and statistics of RAMMPP flights over Mid-Atlantic region.

presents the information about these five airports; Figure 3.2 shows an example of a westerly transport flight with vertical SO_2 profiles for each spiral.

Table 3.1 Major airports for RAMMPP research flights.

Airport Code	Town	Latitude	Longitude	Elevation *	# of Spirals
W45	Luray, VA	38.6671 ºN	78.5006 ºW	275.4	65
OKV	Winchester, VA	39.1436 ºN	78.1444 ºW	221.4	57
CBE	Cumberland, MD	39.6155 ºN	78.76082 º W	236.4	71
0W3	Churchville, MD	39.5668 ºN	76.2022 ºW	124.7	64
ESN	Easton, MD	38.8042 ºN	76.069 ºW	22.0	72

* meters MSL

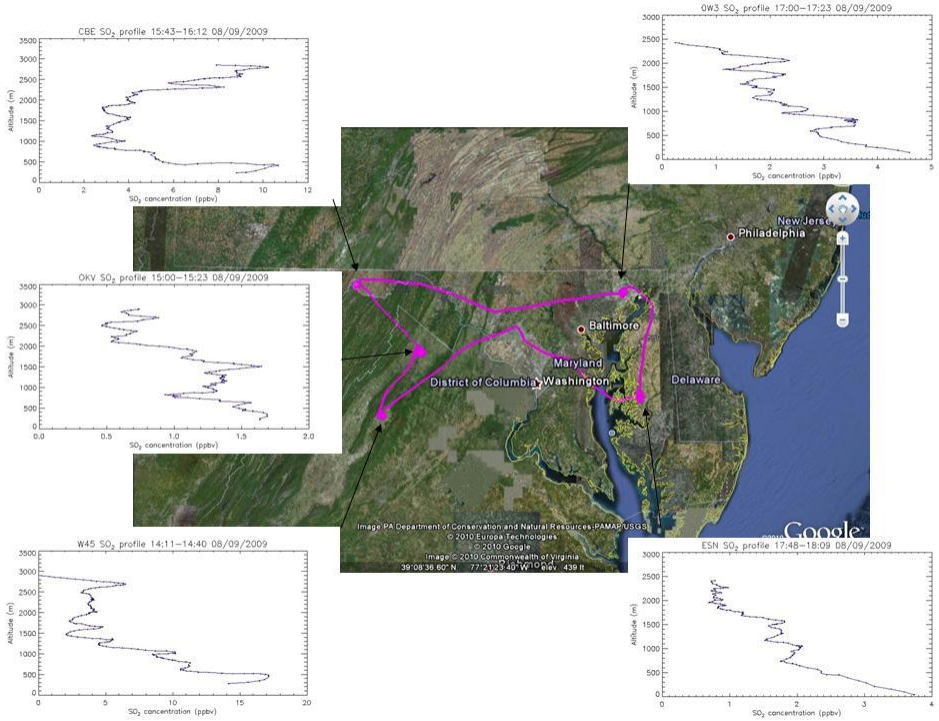

Figure 3.2 Flight route map and SO_2 vertical profiles of 08/09/2008 (data from the surface to 1500 m AGL for calculating air pollutant column contents).

To investigate the trends of air pollutants considering their vertical distributions, the column contents are necessary. As well as the flight pattern, the spiral pattern has been changed gradually. For instance, the maximum height of each spiral was restricted to 1500 m before 2000, and increased to 3000/2500 m for the morning/afternoon flight respectively. Therefore, to study the long-term trend, I integrated the altitude profiles from the surface to 1500 m above ground level (AGL) to calculate the air pollutant column contents.

3.2 Trends of emissions and surface observations in the eastern U.S.

How do emission controls affect air quality? Figure 3.3 presents the monthly CEMS emission data from MD, OH, PA, VA and WV from 1997 to 2011 (3^{rd} quarter). The point sources in the CEMS program mainly include the electric power plants and other large combustion sources. CO_2 emissions stay at the similar levels for the five states, while the NO_x and SO_2 emissions have been reduced significantly through several phases:

1) 1997-2002 with slow decrease of air pollutants;

2) 2003-2004, due to the EPA State Implementation Plan (SIP) call, NO_x emissions decreased substantially, but sometimes only during the summer O_3 season;

3) 2005-2008, post the SIP call with gradual decrease of SO_2 emissions;

4) 2009-2011, substantial decrease of SO_2 emissions especially in MD, PA and WV.

In 2003, the USEPA began to implement the NO_x SIP call and the NO_x Budget Trading Program (BTP), market-based cap and trade program in order to reduce NO_x emissions and mitigate ground-level O_3 pollution in the eastern U.S. A similar market-based cap and trade program, the Acid Rain Program, was utilized to reduce both SO_2 and NO_x emissions to protect the environment and public health. Progress reports on these two programs are published and available on the USEPA website (http://www.epa.gov/airmarkets/progress/progress-reports.html). From 2005 to 2009, NO_x emissions from point sources in PA, OH and WV were only scrubbed during the O_3 season, and a further decrease was observed after 2009.

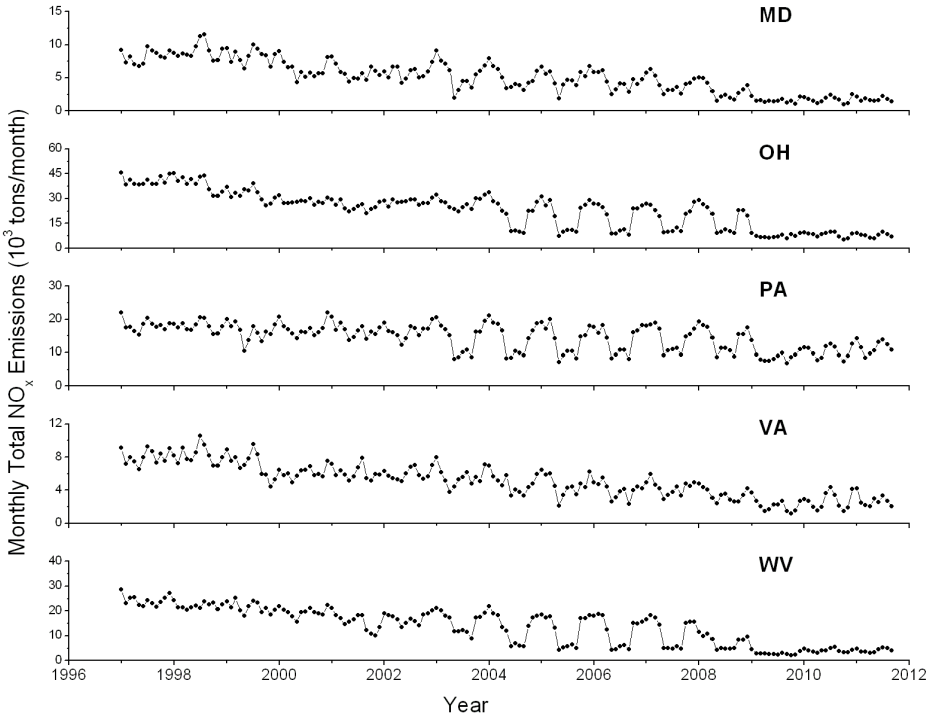

a)

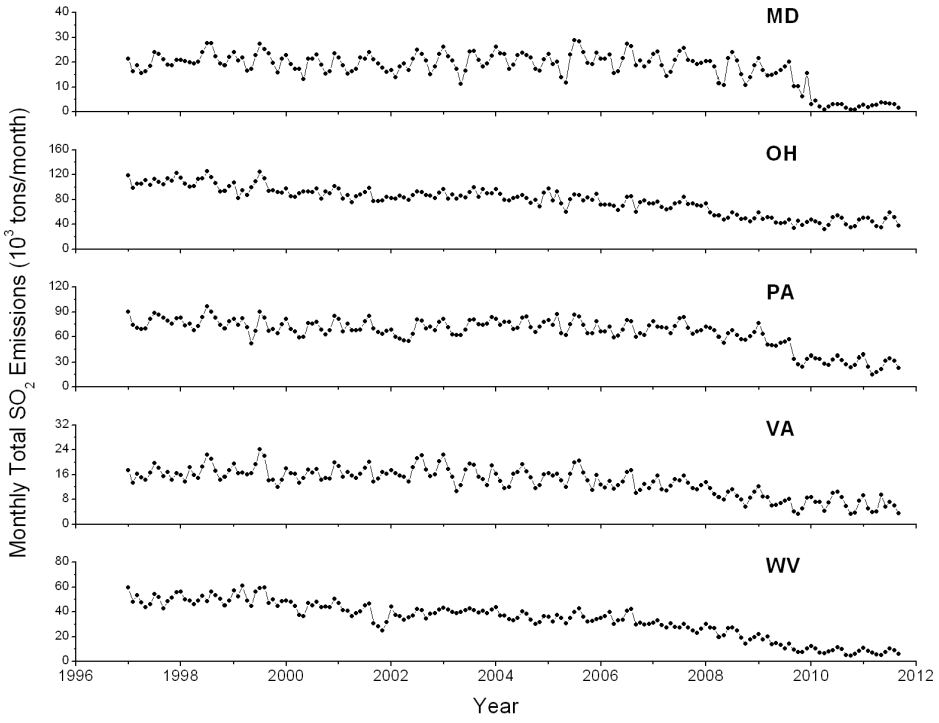

b)

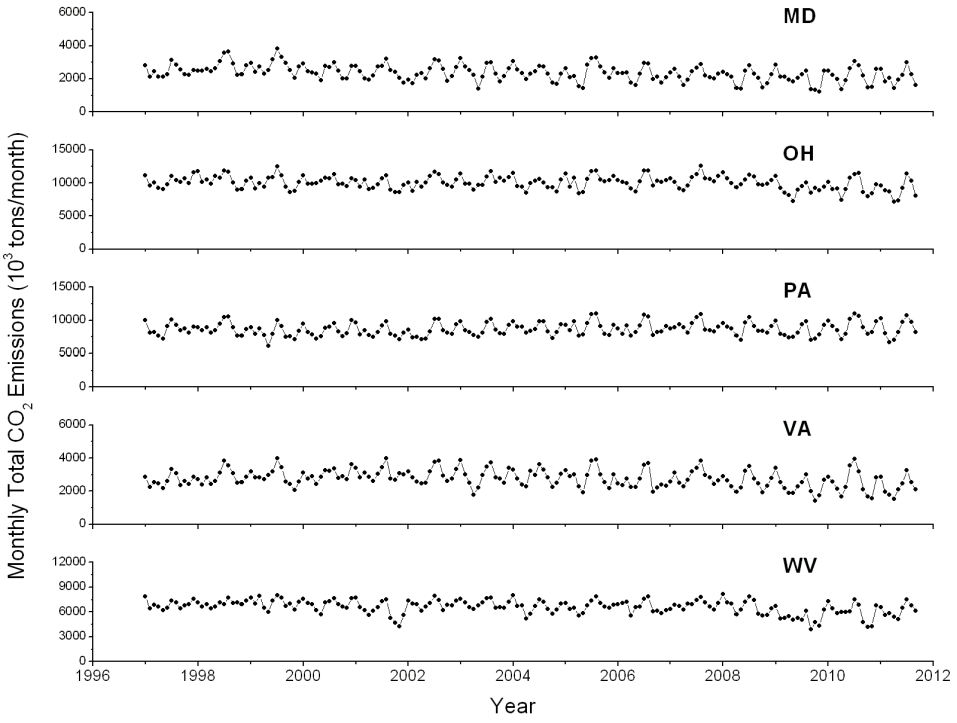

c)

Figure 3.3 Monthly emission data of NO_x, SO_2 and CO_2 from the CEMS dataset.

For the state of MD, another milestone for air pollution regulation, the "Healthy Air Act" (HAA), was passed by the Maryland General Assembly in 2005, aimed at eliminating Maryland nonattainment regions the federal deadline of 2010. The first phase of HAA regulates power plant emissions, reducing NO_x emissions by ~70%, SO_2 emissions by ~80%, and mercury by ~80% from 2002 level. The second phase (http://www.mde.md.gov/programs/Air/ProgramsHome/Pages/air/md_haa.aspx) is under implementation, aiming at reduce NO_x emissions by ~75%, SO_2 emissions by ~85%, and mercury by ~90% of 2002 level. The long-term emission trend of SO_2 reveals a large

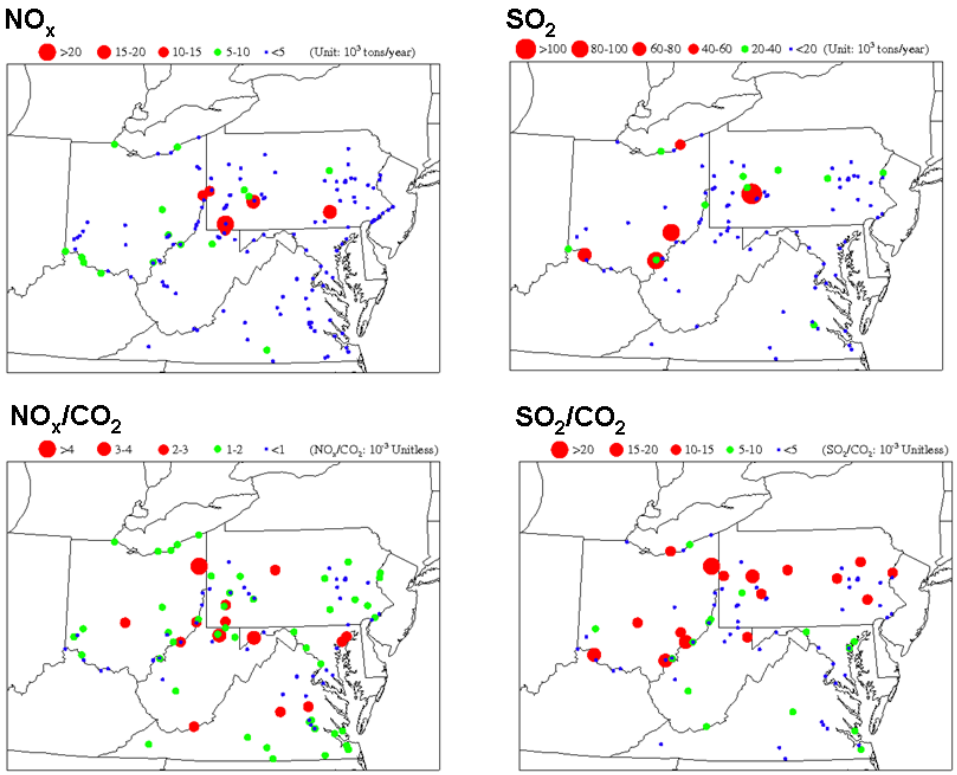

Figure 3.4 Locations of NO_x sources, SO_2 sources, NO_x/CO_2 ratios, and SO_2/CO_2 ratios in MD, OH, PA, VA, and WV. (size of dot is proportional to the amount of emissions).

Table 3.2 List of some major point sources. (Point sources with annual SO_2 emissions > 6×10^3 tons/year, SO_2/CO_2 ratio > 1.0×10^{-2}, NO_x emissions > 1×10^3 tons/year, and NO_x/CO_2 ratio > 3.0×10^{-4})

State	Facility Name	Latitude	Longitude
OH	Avon Lake Power Plant	41.50	-82.05
OH	Kyger Creek	38.92	-82.13
OH	Muskingum River	39.59	-81.68
OH	Niles	41.17	-80.75
OH	Richard Gorsuch	39.37	-81.52
OH	Walter C Beckjord Station	38.99	-84.30
PA	Armstrong Power Station	40.93	-79.47
PA	Homer City	40.51	-79.20
PA	New Castle	40.94	-80.37
PA	Portland	40.91	-75.08
PA	Shawville	41.07	-78.37
PA	Sunbury	40.84	-76.83
PA	Titus	40.31	-75.91
WV	Albright Power Station	39.49	-79.64

drop of point source SO_2 emissions after 2010. Figure 3.4 (upper panels) presents the emission map of major point sources with CEMS annual emissions from 2010. The largest NO_x emission sources are located in southern PA; the largest SO_2 sources are in the Ohio River Valley region. This diagram indicates that large amounts of air pollutants have been released in upwind regions of the DC-Baltimore area, exerting a significant influence on the downwind air quality under the prevailing westerly winds during the O_3 season. The ratios of NO_x and SO_2 emissions to CO_2 emissions are presented in Figure 3.4 (lower panels). These 'hot spots', listed in Table 3.2, are the low-hanging fruit for the future regulations on air pollution emissions.

CEMS data only cover the point sources, but more than half of the NO_x and almost all the CO is emitted by the mobile sources, including on-road and non-road vehicles with internal combustion engines. For instance, for MD, the NO_x emissions

from point sources and vehicles were ~40,000 tons and ~90,000 tons in 2008 respectively. It is necessary to take the mobile emissions into account; I used the EPA NEI emission inventory and calculated the annual CO and NO_x emissions for the five states in 2002, 2005, and 2008. Gradual decreasing trends are observed for both on-road and non-road mobile sources in the five states (Figure 3.5). Therefore, during the EPA SIP call during 2003-2004, the emissions of mobile sources decreased uniformly compared with the sharp decrease of point source emissions.

The EPA NEI provides a comprehensive and detailed estimate of air pollutant

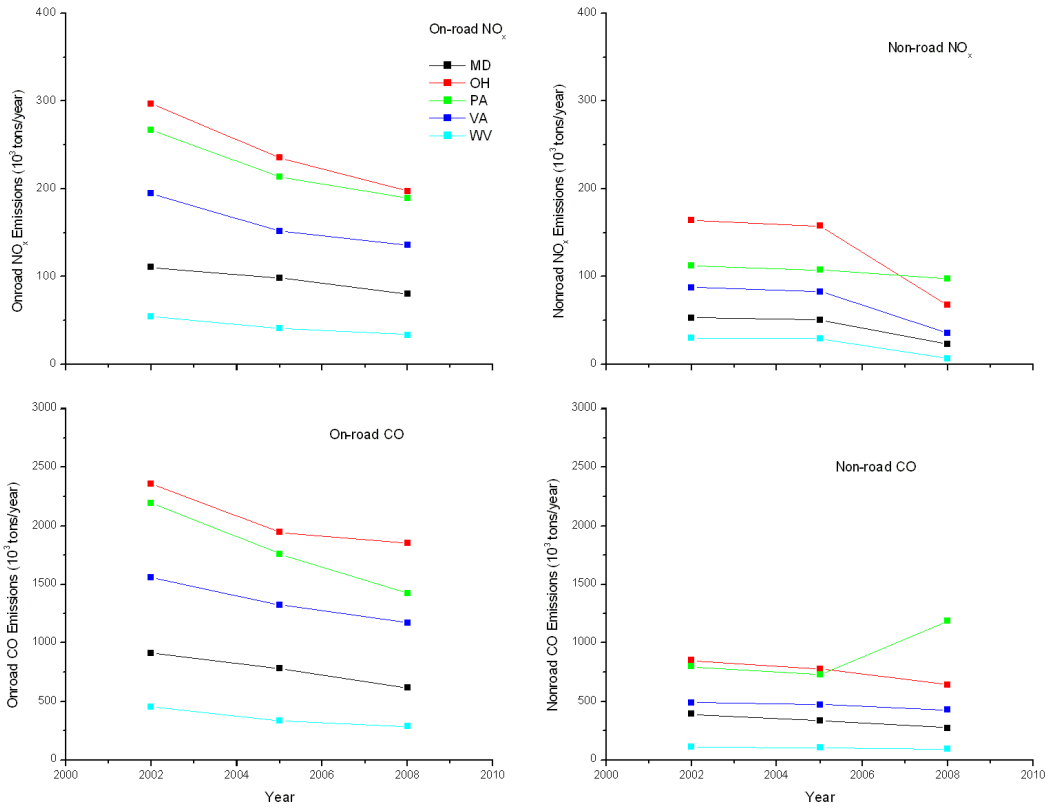

Figure 3.5 Trends of NO_x and CO emissions from mobile sources in the EPA NEI.

a)

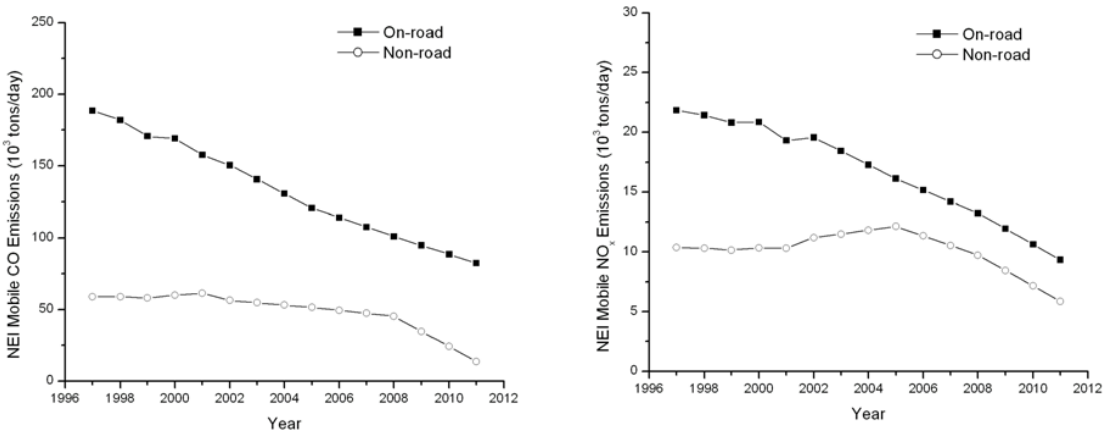

b)

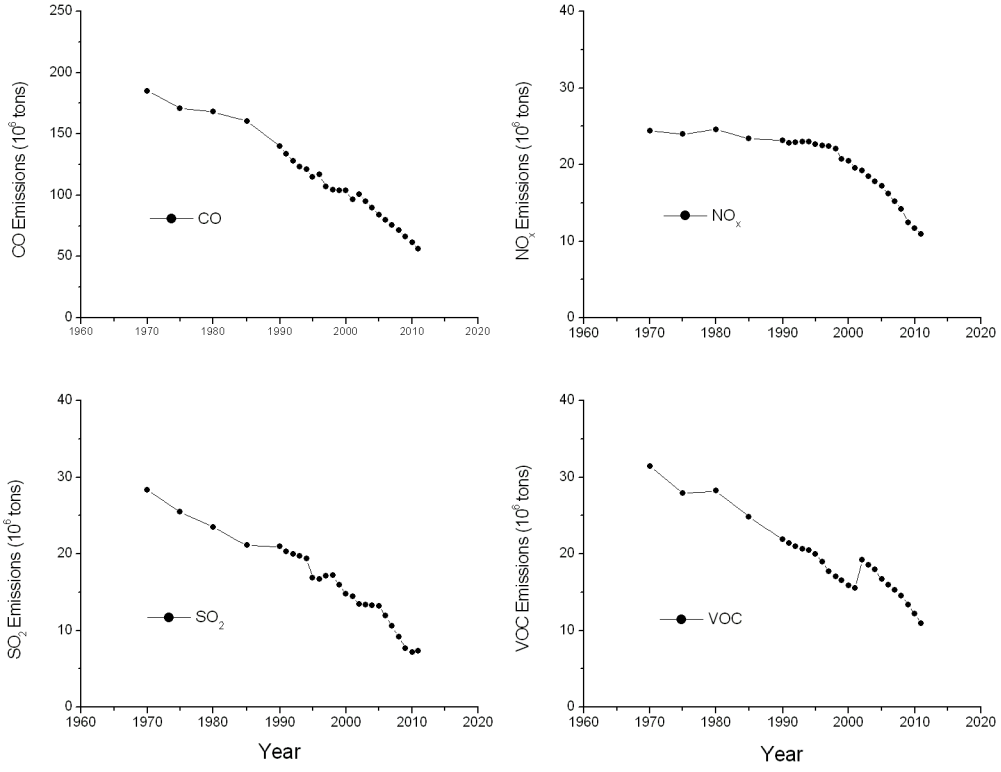

Figure 3.6 Annual mean NO_x and CO emissions from NEI mobile sources (Figure a) and national total CO, NO_x, SO_2, and VOC emissions (Figure b).

emissions from different sectors at county level, which requires considerable effort for collecting and processing data, so they are only available every three years. To illustrate the long-term trend, I present the NEI air pollutant emissions trend data (1970–2011 average annual emissions, http://www.epa.gov/ttn/chief/trends/index.html) in Figure 3.6. These national emissions from mobile sources also demonstrate a gradual decreasing trend, without showing a sharp decrease between 2002 and 2003 as the cap was implemented during the NO_x SIP call. These characteristics provide a unique opportunity to evaluate the effects of the SIP call on the air quality in the DC-Baltimore region.

Air quality in the DC-Baltimore region benefited from these substantial reductions in air pollutant emissions. The surface observation data (courtesy of EPA and Kyle Hosley from UMD) of ground level O_3 and NO_x of MD, DC, and northern VA were investigated here. Figure 3.7 depicts the location of these surface observations. Hourly

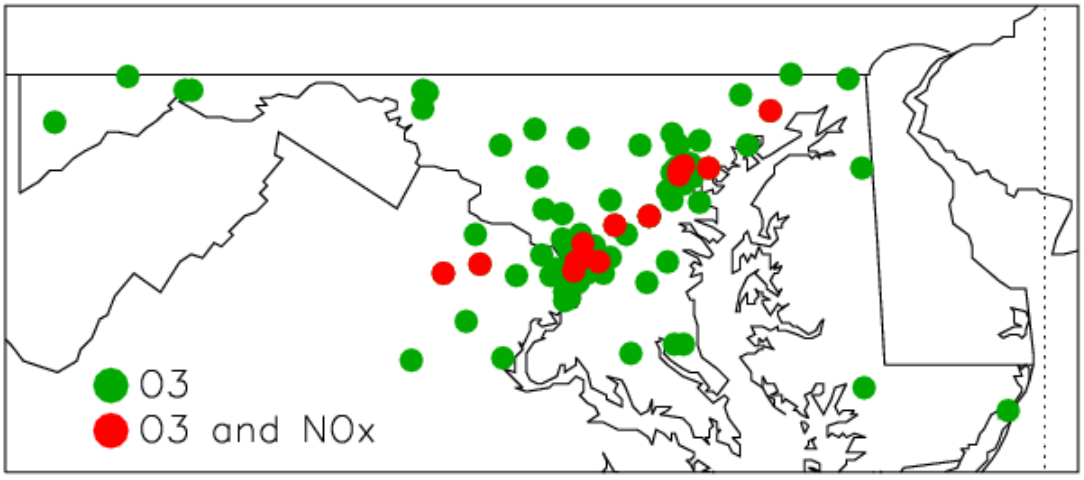

Figure 3.7 Map of EPA AQS stations for ground level O_3 and NO_x observations (courtesy of Linda Hembeck from UMD, lhembeck@atmos.umd.edu).

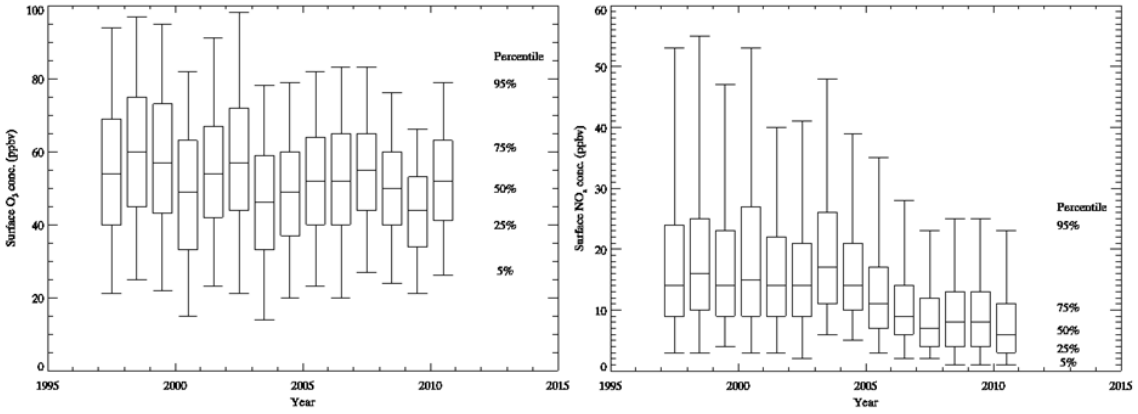

Figure 3.8 Long-term trends of surface O_3 and NO_x observed in MD/DC/NOVA.

trace gases observations were analyzed; the statistics are presented in the Figure 3.8. The O_3 and NO_x observations are sampled for afternoon values (12 pm to 6 pm) in the ozone season (June to September) because afternoon values correspond to the time of the deepest boundary layer and better reflect the large-scale atmospheric composition; 5^{th}, 25^{th}, 50^{th}, 75^{th}, 95^{th} percentiles were calculated. Compared with the median values, 95^{th} percentiles of O_3 and NO_x, i.e., bad air quality days, show dramatic decreasing trends, suggesting that high O_3 events have been improved substantially. Because the relationship between O_3 production and the NO_x precursors is influenced by the ambient temperature [*Finlayson-Pitts and Pitts*, 1999], the O_3 trend data should be corrected to compensate for the temperature differences (discussed in section 3.3).

3.3 Trends in O_3 and CO columns

3.3.1 Evaluation of aircraft O_3 measurements and vertical distributions

The USEPA and State governments established a national network to monitor the ground level concentration of air pollutants, but there is limited information on the concentrations of air pollutants aloft. To link the surface observations to aircraft measurements, I compared our aircraft O_3 measurements with the EPA network. I selected the spirals over Harford County airport (0W3) as a case study, where the USEPA/MDE Aldino site is located at the end of runway. A typical spiral over 0W3 starts with a low pass (about 3 m above the runway), followed by an ascent to 2500 m with a rate of climb of 100 m/min. The measurements during low pass are considered as the "aircraft surface O_3". The hourly EPA AQS O_3 measurements are sampled corresponding to the time of research flights, see Figure 3.9. Aircraft measurements are correlated to the EPA AQS observations (*r = 0.64*), and the slope of linear regression is close to unity (*slope = 0.93*). EPA AQS data are hourly averaged values, while the "aircraft surface measurements" are snapshots (a couple of minutes) of the O_3 near the ground, therefore discrepancies between the surface and aircraft measurements are to be expected. The accuracy of aircraft measurements of O_3 is of research quality, and tied to the NIST O_3 standard.

A simple approach is applied here to link surface observations to the air pollutant column content, assuming the air pollutants are well mixed within the lowest atmosphere (surface to 1500 m) under constant temperature (25 ℃). The relationship between the surface concentration and the O_3 column contents can be derived as:

$$Column_{O_3} = \int_{p_{sfc}}^{p_{1500}} [O_3]dp \approx (p_{sfc} - p_{1500}) \times [O_3]_{sfc} = 0.15 \times [O_3]_{sfc} \qquad \text{(Equation 3.1)}$$

where 0.15 is the conversion factor from surface O_3 concentration to O_3 column content, in units of DU/ppb.

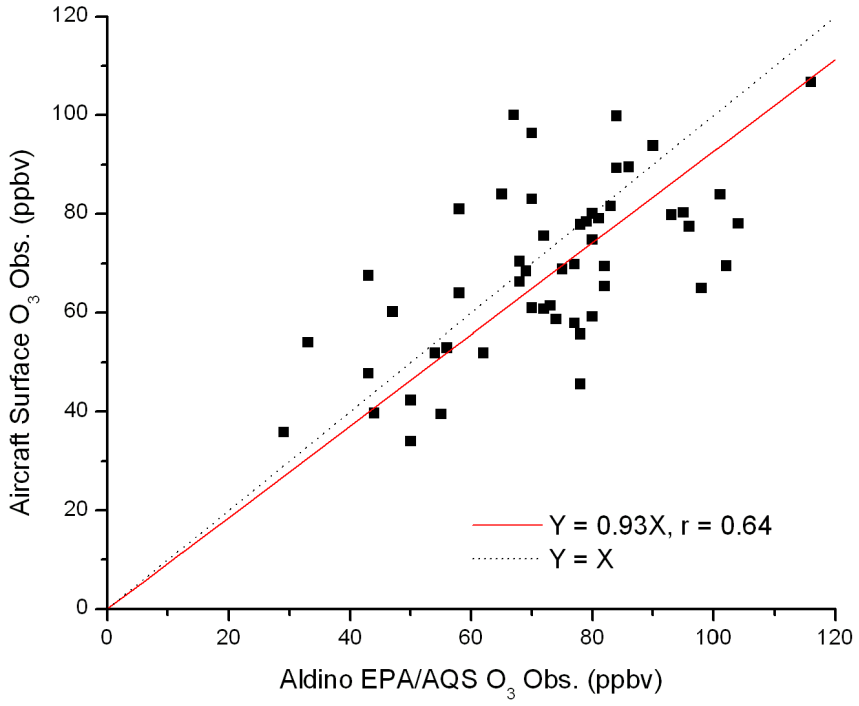

Figure 3.9 Comparison of surface O_3 concentrations observed by RAMMPP aircraft and the EPA AQS site. EPA/AQS measurements: hourly data, Red line: linear regression forced through zero, Black line: 1:1 ratio line.

I present the evaluation of "aircraft surface O_3" with respect to the O_3 column contents from afternoon flights in Figure 3.10. The good correlation ($r = 0.62$) and slope close to theoretical value (best linear fit *slope* = *0.14* vs. *0.15* in Equation 3.1) show that O_3 is reasonably well-mixed in early afternoon in the lower atmosphere. This finding is

valuable for estimating tropospheric O_3 column contents based on the surface observations.

The RAMMPP research flight pattern during the O_3 season is designed to observe the upwind O_3 in the morning and the downwind O_3 in the afternoon, so I lumped the spirals into two categories: the upwind group and the downwind group, following a similar approach used in other RAMMPP studies [*Castellanos et al.*, 2009; *Castellanos et al.*, 2011; *Hains et al.*, 2008; *Taubman et al.*, 2006]. A statistical analysis was performed to study the vertical distribution of tropospheric O_3, and results from the 2001 data are

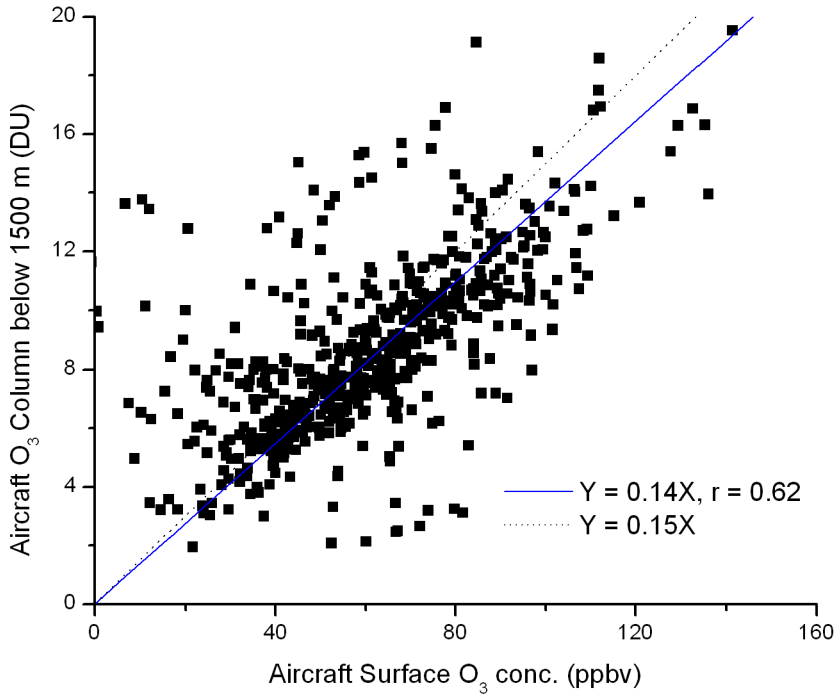

Figure 3.10 Comparison of surface O_3 concentrations and the RAMMPP O_3 column contents between ground and 1500 m. Blue line: linear regression forced through zero, Black dotted line: $Y = 0.15\ X$, well-mixed assumption.

demonstrated in the Figure 3.11. I observed high variations in the vertical distribution of tropospheric O_3. In the morning upwind flights (Figure 3.11 middle), O_3 concentrations near the surface are relatively low compared with the values in the FT (higher than 1000 m), indicating chemically active O_3 is lost due to dry deposition and reactions with NO_x during nighttime. In the morning with the low photochemical production at ground level and slow mixing, the O_3 concentration stays low until about noon. The relatively high O_3 observed in the lower FT is in the residual layer from previous days, which works as an O_3 reservoir. The O_3 and other pollutants in the residual layer have longer lifetimes there and can be transported farther than trace gases in the PBL. With the build up of the PBL during daytime, the residual layer will be mixed with contents of the new

a)

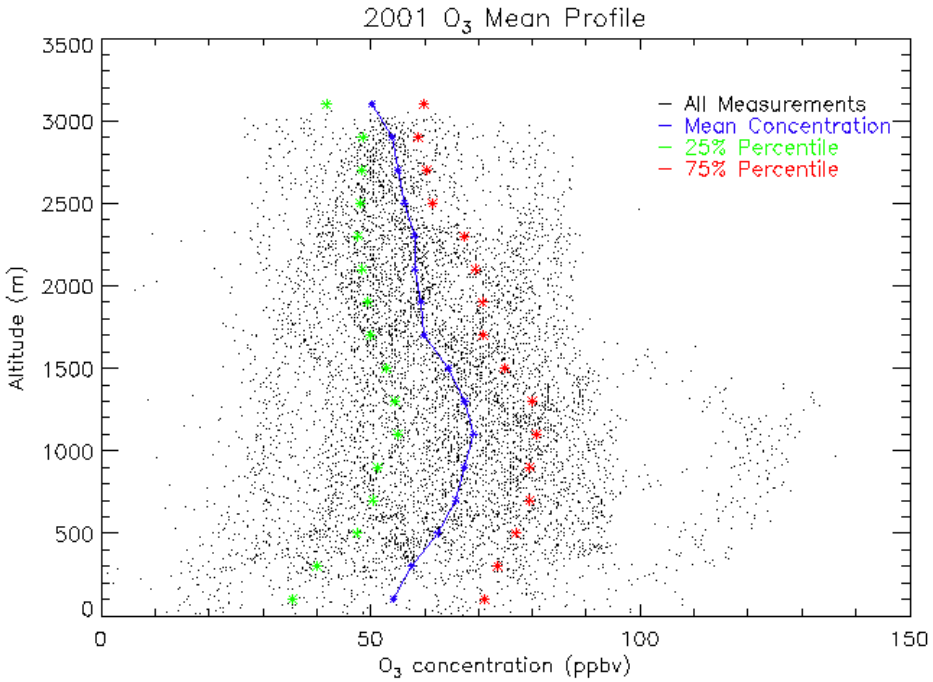

b)

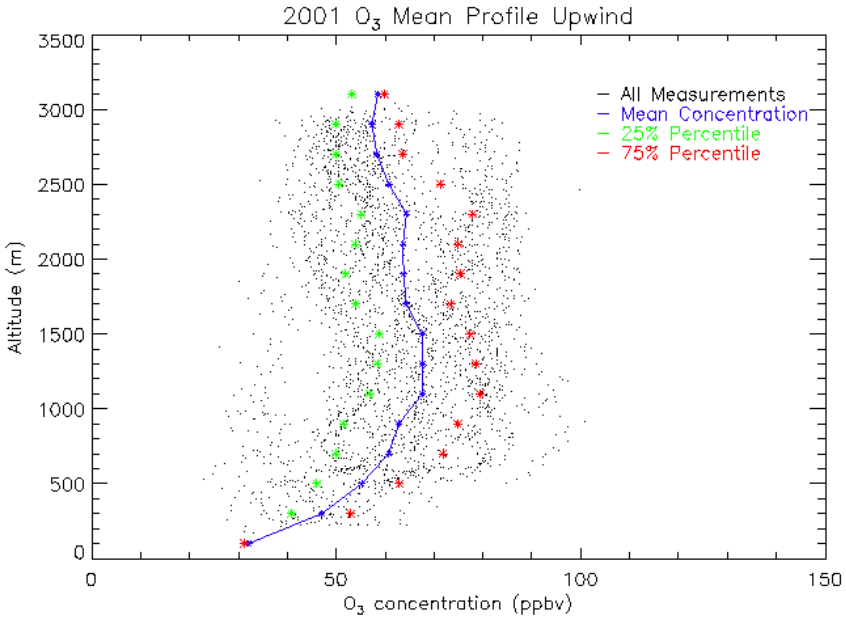

c)

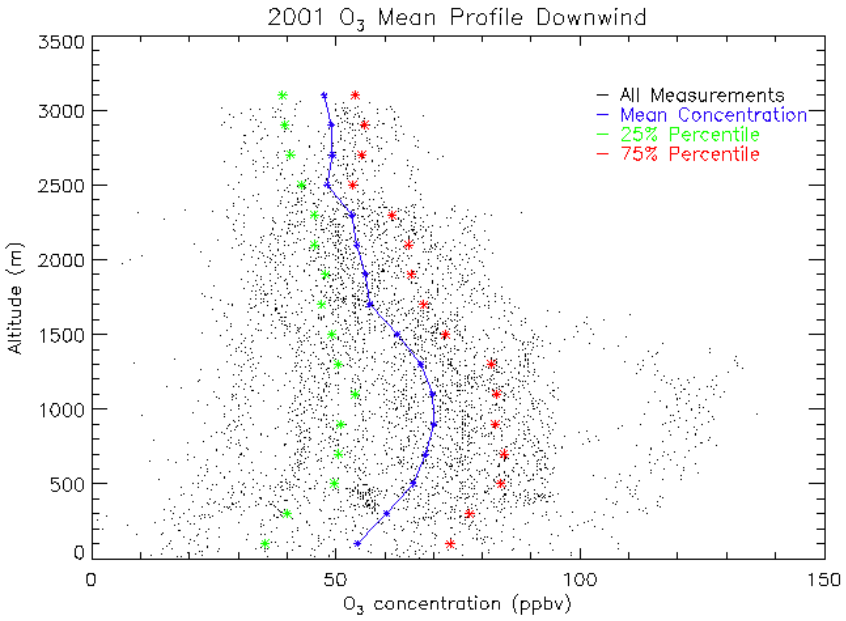

Figure 3.11 Vertical distributions of tropospheric O_3 over the Mid-Atlantic region (a: all spirals; b: only the upwind spirals; c: only the downwind spirals).

PBL, transporting the residual-layer pollutants downward. In the afternoon, downwind flights (Figure 3.11 c), O_3 is formed through photochemical production and transported downwind due to mixing. These mean O_3 vertical profile shows a quasi-uniform concentration, which supports the hypothesis of quasi well-mixed PBL discussed above. The afternoon mean profile has a secondary maximum at ~1000 m, with ~18 ppb O_3 higher than the surface concentration. These pollutants aloft do not immediately influence the local air quality, but the long range transport of these pollutants exert significant effects on downwind air pollution.

Figure 3.12 a presents the mean CO profile of 2001, which has a uniform concentration of ~250 ppb in the FT and the highest concentration near the surface. It reveals that atmospheric CO comes from the sources on the Earth's surface; with a lifetime of one month, CO can be transported upward to the FT and well mixed there. So CO is a good chemical tracer to investigate advection in the lower atmosphere [*Castellanos,* 2009; *Loughner,* 2011]. The mean CO profiles from upwind and downwind spirals exhibit similar vertical distributions (Figure 3.11 b and c), indicating that CO pollution is a regional problem. CO is concentrated within the PBL, as is NO_x, so the production of O_3 is enhanced in the lower atmosphere.

To summarize, I evaluated the aircraft measurements by comparing them with the USEPA AQS surface observations, and found that the airborne measurements are correlated with ground level O_3 concentrations. A simple hypothesis on O_3 vertical distribution has been evaluated, indicating that O_3 is quasi-well mixed in the lower atmosphere during hot summer afternoons. The reason for this mixing could be that the layer from surface to 1500 m is generally within summertime PBL [*Seidel et al.*, 2010],

a)

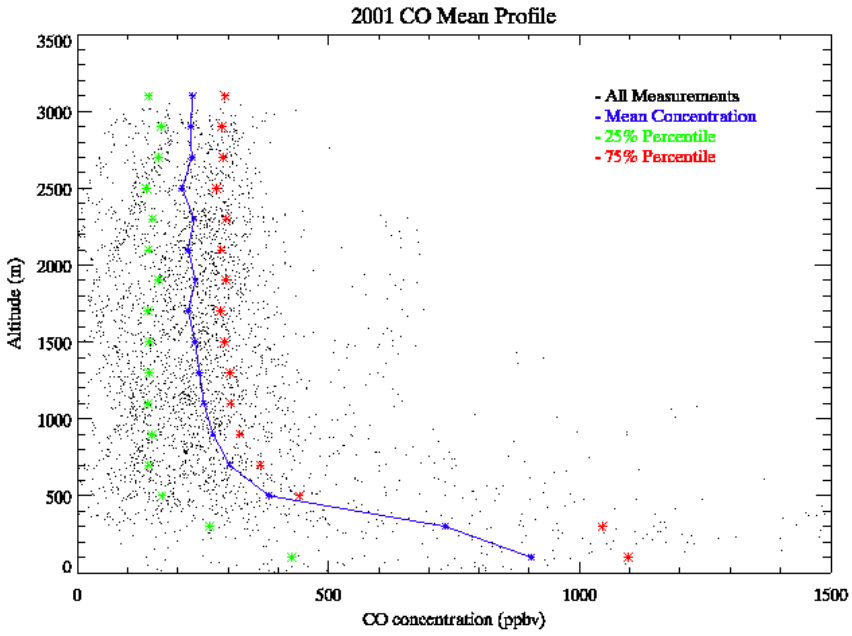
2001 CO Mean Profile
- All Measurements
- Mean Concentration
- 25% Percentile
- 75% Percentile
Altitude (m)
CO concentration (ppbv)
0
500
1000
1500
2000
2500
3000
3500

b)

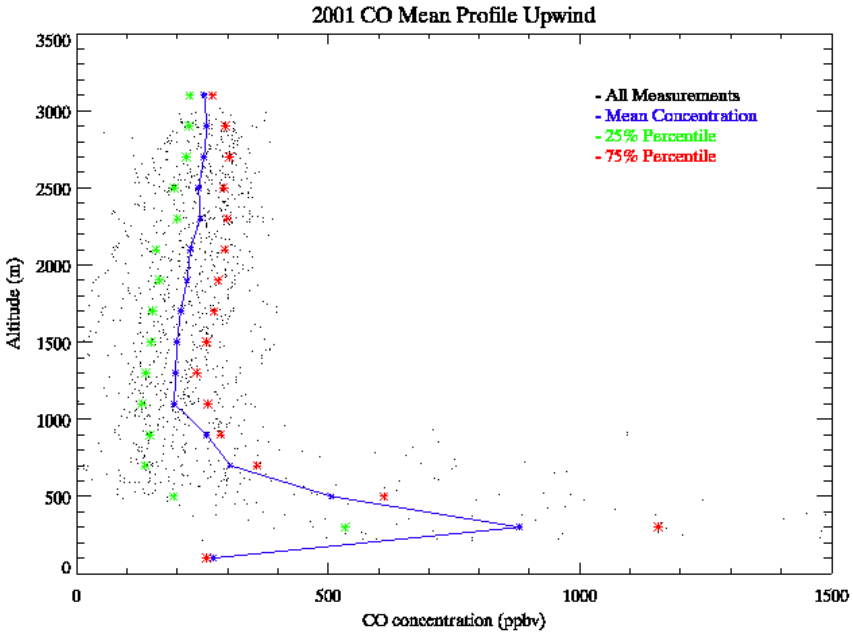
2001 CO Mean Profile Upwind
- All Measurements
- Mean Concentration
- 25% Percentile
- 75% Percentile
Altitude (m)
CO concentration (ppbv)
0
500
1000
1500
2000
2500
3000
3500

c)

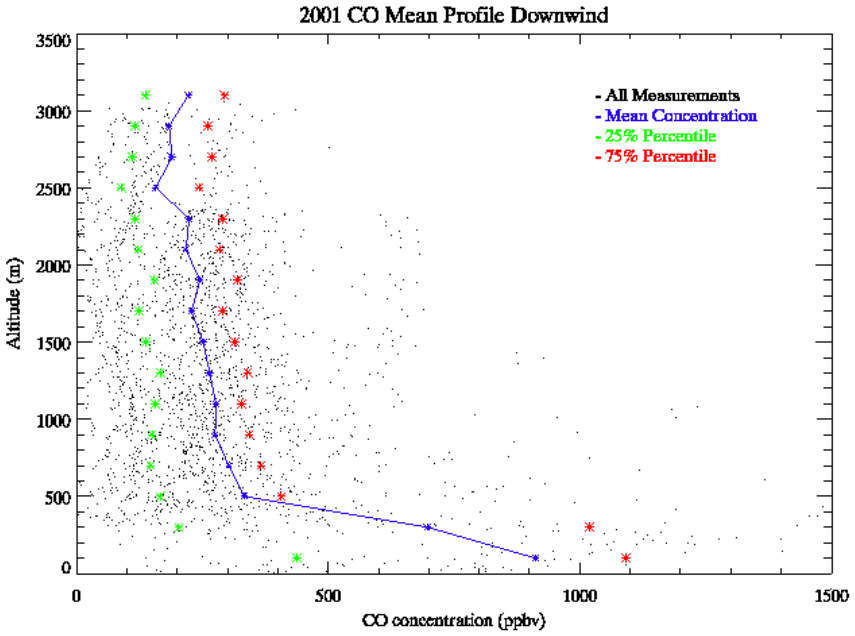

Figure 3.12 Mean CO profiles from 2001 (a: all spirals; b: only the upwind spirals; c: only the downwind spirals).

which means that the convection caused by the radiative heating of the land surface is capable of mixing the air pollutants such as O_3 in this thin layer. These upward motions are effective in lifting air pollutants to the FT, where stronger winds are prevalent. Air pollutants such as O_3 and SO_2 have a longer lifetime in the FT [*Finlayson-Pitts and Pitts*, 1999; *Seinfeld and Pandis*, 2006], playing an important role in the long regional transport and causing regional air pollutant problems.

3.3.2 The climate penalty factor (CPF)

The global warming since late 19th century is estimated as 0.4-0.8 ℃, and another 0.4 ℃ increase is projected for the next two decades [*IPCC*, 2007]. Since temperature is

one of the most important meteorological factors affecting O_3 formation in the lower atmosphere [*Camalier et al.*, 2007; *Finlayson-Pitts and Pitts*, 1999; *Jacob and Winner*, 2009]. The increase of ambient temperature is likely to boost the ambient O_3 concentration [*EPA*, 2006], and 1-10 ppbv increase of the ground level O_3 due to climate change is estimated by a coupled Global Climate Model (GCM) and CTM [*Jacob and Winner*, 2009]. How can we quantify the effects of climate change on local/regional O_3 pollution? The climate penalty factor (CPF) is defined as $\frac{d[O_3]}{dT}$, describing the increase of O_3 concentration with enhanced ambient temperature. Bloomer et al. [2009] reported the CPF from a statistical analysis, and calculated the CPF as ~3.2 ppbv/℃ prior to 2002 and ~2.2 ppbv/℃ after 2002. Bloomer's study is based on the ground level O_3 and surface temperature at rural sites in the eastern U.S., where the O_3 photochemical production is NO_x-sensitive.

Daily and monthly mean surface temperature at Baltimore-Washington International Airport (BWI) is presented in Figure 3.13. Because high O_3 episodes are normally correlated with the high temperature, I focus on hot summer days. Figure 3.14 presents the number of days with daily mean surface temperature higher than 28 ℃ at BWI. Some years are statistically warmer such as 2002, 2010, and 2011, so it is important to correct the O_3 aircraft measurements with respect to ambient temperature in order to investigate the long-term trend of O_3. Here, a mean CPF value of 2.0 ppbv/℃ is used to adjust the O_3 measurements; with the quasi-well mixed assumption, the equation 3.1 can be expressed as:

$$O_{3,adjusted} = O_{3,measured} + O_{3,correction} \qquad \text{(Equation 3.2)}$$

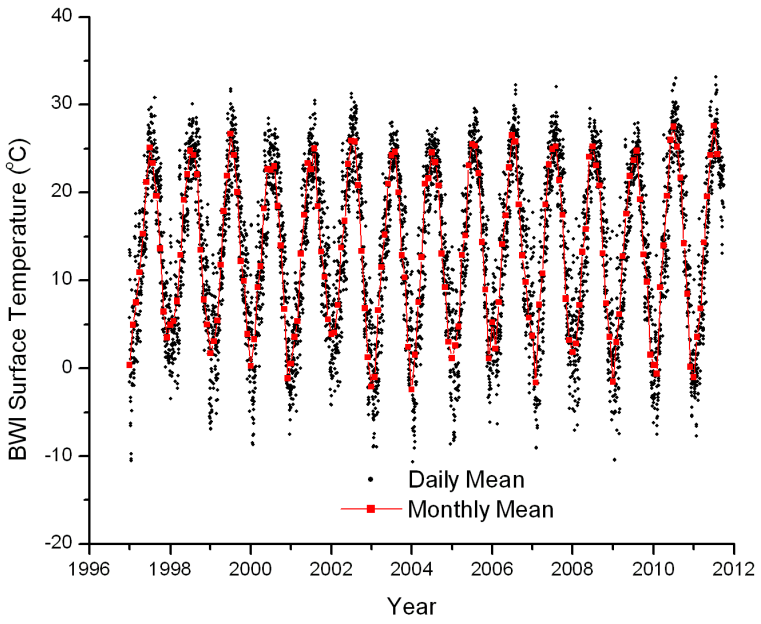

Figure 3.13 Daily and monthly mean temperature at BWI from 1997 to 2010.

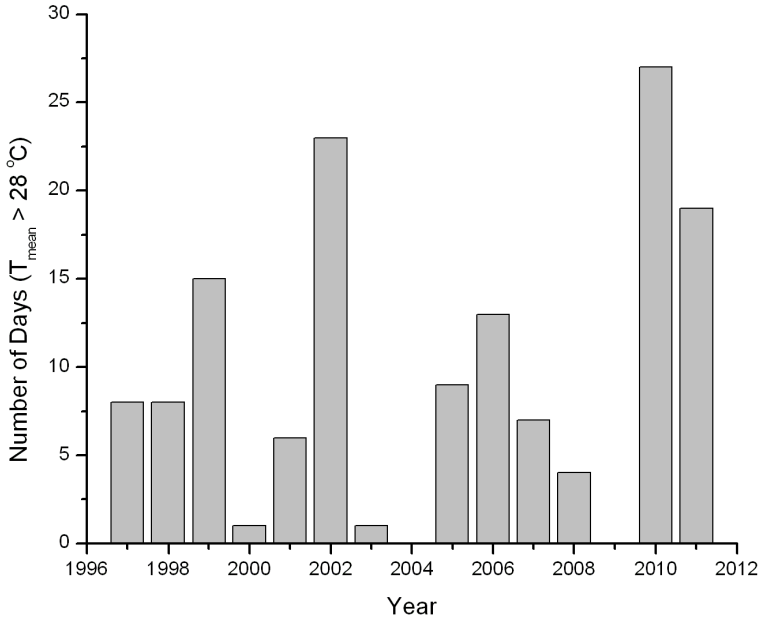

Figure 3.14 Number of days with T_{mean} > 28 ℃ at BWI from 1997 to 2011.

where $O_{3,correction} = 0.15\Delta_{[O_3]} = 0.15 \times 2.0 \times \Delta T = 0.3\Delta T$. This correction was applied to O_3 column contents observed by the RAMMPP aircraft, and the results are discussed in section 3.3.3.

3.3.3 Long-term trends of O_3 and CO column contents

O_3 column contents (after corrected with CPF) and CO column contents are calculated through integrating the altitude profiles from the surface to 1500 m AGL. I lumped the O_3 column contents into upwind and downwind groups (Figure 3.15). Large uncertainties are observed for 1999 and 2008, when limited research flights were conducted. The upwind O_3 column contents are considered to be background air entering

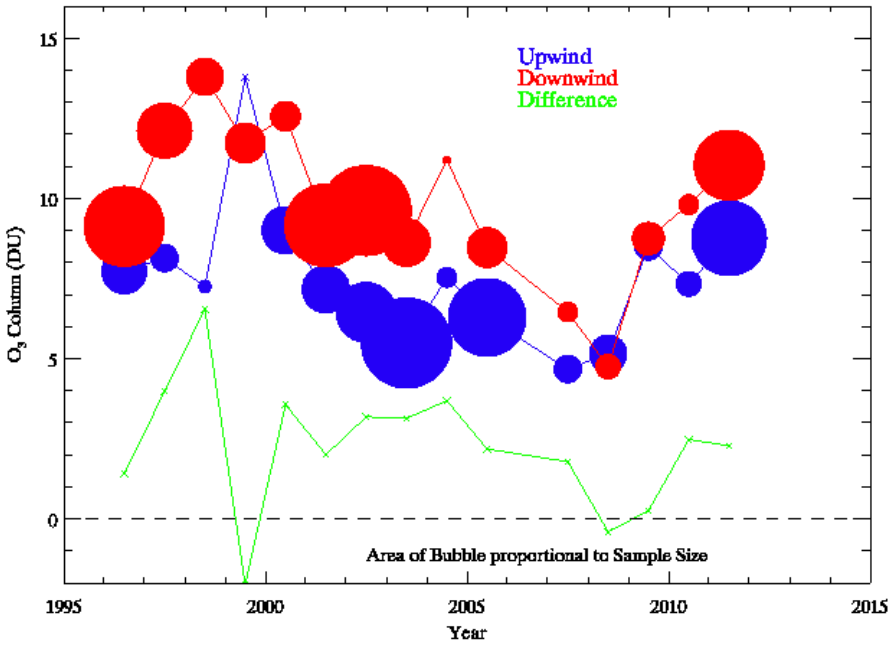

Figure 3.15 Lumped upwind and downwind O_3 column contents (the size of bubble is proportional to the number of spirals).

the DC-Baltimore region, with O_3 mainly existing in the residual layer; the downwind contents represent the total of background O_3 plus O_3 generated by photochemical reactions. The afternoon flights are usually finished before 4pm when the maximum ground level O_3 is observed, so the difference between morning and afternoon flights accounts for the daily production of tropospheric O_3 in the DC-Baltimore region, which is estimated to be 2.3 ± 2.0 Dobson Units (DU, $1\ DU = 2.69 \times 10^{16}\ molecules/cm^2$). Under the quasi-well mixed assumption, this value equals a ~15 ppb O_3 increase in the lower atmosphere.

As one of the precursors for O_3 production, CO column contents (below 1500 m) are calculated. The O_3 and CO columns for each year are plotted showing the long-term trend in Figure 3.16. Savitzky-Golay Smoothing is used, which is described in Appendix I [*Bromba and Ziegler*, 1981; *Gorry*, 1990; *Savitzky and Golay*, 1964]. This smoothing technique preserves the features of the data while reducing the influences of noise and missing data. Figure 3.16 shows ~2.0 DU/decade and ~20.0 DU/decade decrease of O_3 and CO column contents respectively. Since O_3 in the lower atmosphere is quasi-well mixed, the decrease in column content is equivalent to ~13 ppb/decade decrease in ground level O_3. This value is much higher than the 4~6 ppb/decade decrease observed at ground level in the eastern U.S. [*Bloomer et al.*, 2010]. The reason could be that RAMMPP research flights are usually conducted on high O_3 days, suggesting that air quality action days, i.e., bad air quality events, have been improved more than normal days in the O_3 season.

Based on the vertical profiles of CO in Figure 3.12, CO concentrations decay exponentially going away the surface within the lowest 500 m to near constant values

aloft. So the 20.0 DU/decade decrease in CO column contents can be interpreted as an ~800 ppb/decade decrease, about half of the nationwide decrease shown in Figure 1.3. One possible explanation is that the national trend is calculated based on the 2nd maximum of annual 8-hour average, i.e., the values from CO episodes, which usually

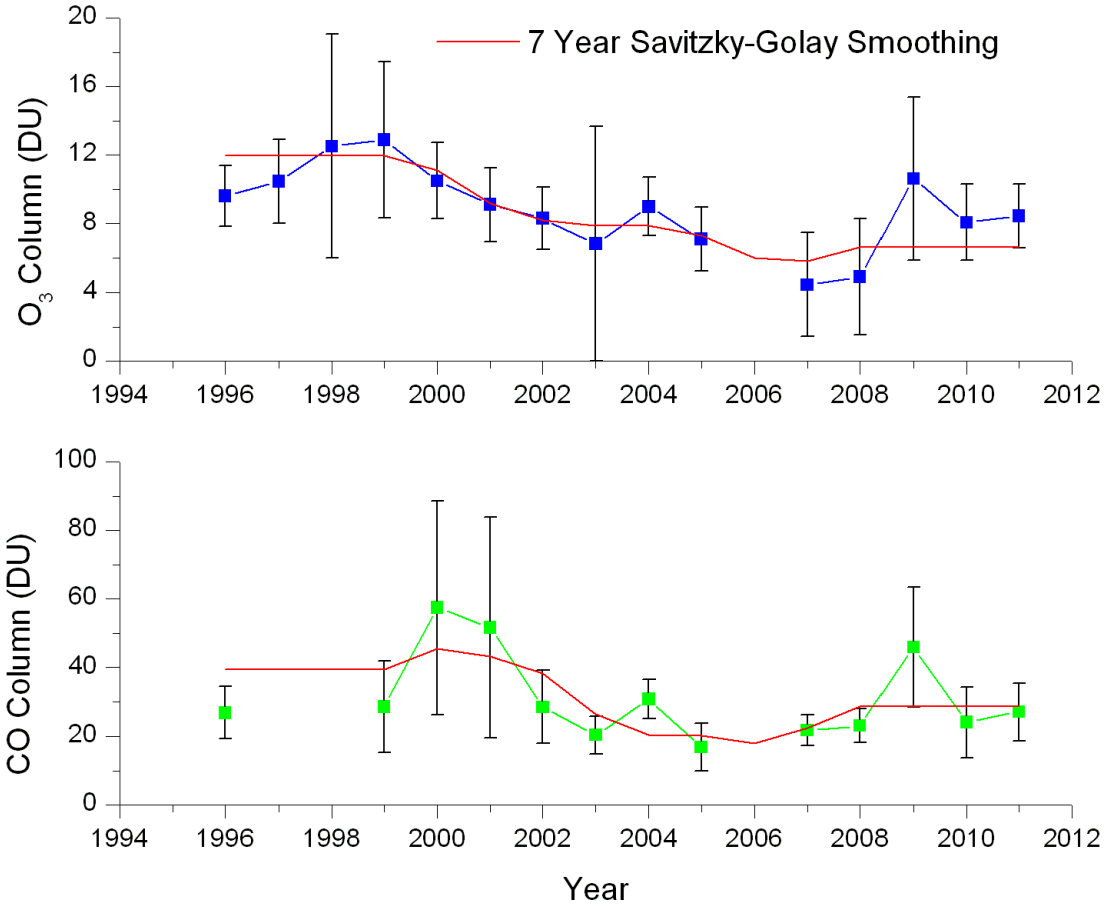

Figure 3.16 Long-term trends of tropospheric O_3 and CO columns in the Mid-Atlantic region (error bars are 1 standard deviation σ).

happen on cold winter days with a temperature inversion. RAMMPP research flights are normally carried out during the O_3 season, when CO pollution is not severe and strong

convection exists ubiquitously to transport CO upward from surface sources. As shown in figure 3.6, the national emissions of CO decreased from ~120 $\times 10^6$ tons in 1997 to ~60 $\times 10^6$ in 2011, with a reduction of ~50%. This value is close to the decrease observed in Figure 3.16, from ~30 DU to ~20 DU, which is close to the background CO concentration (~150 ppbv in the northern hemisphere).

Figure 3.16 also shows that the O_3 and CO column contents are correlated, in particular after the EPA SIP call. For instance, in 2009, high CO columns are observed as well as high O_3 columns. The major sources of CO are on-road and non-road vehicles, whose emissions have decreased substantially in recent years (Figure 3.5). So the abnormally high CO column contents in 2004 and 2009 could be related to other sources such as wildfires, and further studies are needed to illustrate these events. CO normally coexists with NO_x from biomass burning and automobile emissions; at the same time, VOC emissions (Figure 3.6 b) feature a monotonic decreasing trend instead of fluctuations. Therefore, a high concentration of CO might be an indicator of high NO_x, which would also boost the production of O_3. But airborne NO_2 measurements were not available before 2011, so this hypothesis of intercepting automobile exhausts can not be verified in this study.

3.4 Trends of SO_2 and atmospheric optical depth (AOD)

3.4.1 Isolated SO_2 plumes in the free troposphere

$PM_{2.5}$ pollution is also a problem pollutant in the Mid-Atlantic region (Figure 1.5), and sulfate aerosols with SO_2 as precursors are important especially in the summer, the O_3 season. In contrast to the regional nature of O_3 and CO pollution, SO_2 has a relatively short lifetime at 19 ± 7 hrs in summer over the Mid-Atlantic region [*Hains*, 2007]. SO_2 exists in plumes instead of broadly distributed regional pollutants, so airborne measurements of SO_2 are significantly influenced by the stochastic probability of hitting or missing these plumes. During RAMMPP research flights, isolated SO_2 plumes are observed frequently in the FT [*Hains*, 2007; *Taubman et al.*, 2006]. In this section, a statistical study of these plumes is conducted.

Figure 3.17 presents several examples of these isolated SO_2 plumes. These plumes were mainly observed above 1000 m, in the FT. The maximum SO_2 concentrations in these plumes are usually several times higher than the values near the Earth's surface. Table 3.3 summarizes the characteristics of all SO_2 plumes observed in the last 10 years. As seen in this summary, most of these plumes are observed in the upwind areas such as Winchester (OKV), Cumberland (CBE), and Luray (W45) (locations illustrated in Table 3.1). The plumes observed over Luray and Winchester are usually found in the FT. Because these two airports are located in rural areas with few local sources, the results suggest that these plumes are transported from upwind regions such as power plants in the Ohio River Valley. Over Cumberland, plumes are observed both aloft in the FT and near the surface. Like Luray and Winchester, Cumberland is also influenced by the long range regional transport of air pollutants from the upstream sources, mainly in the FT. But there is a local source: the Warrior Run facility

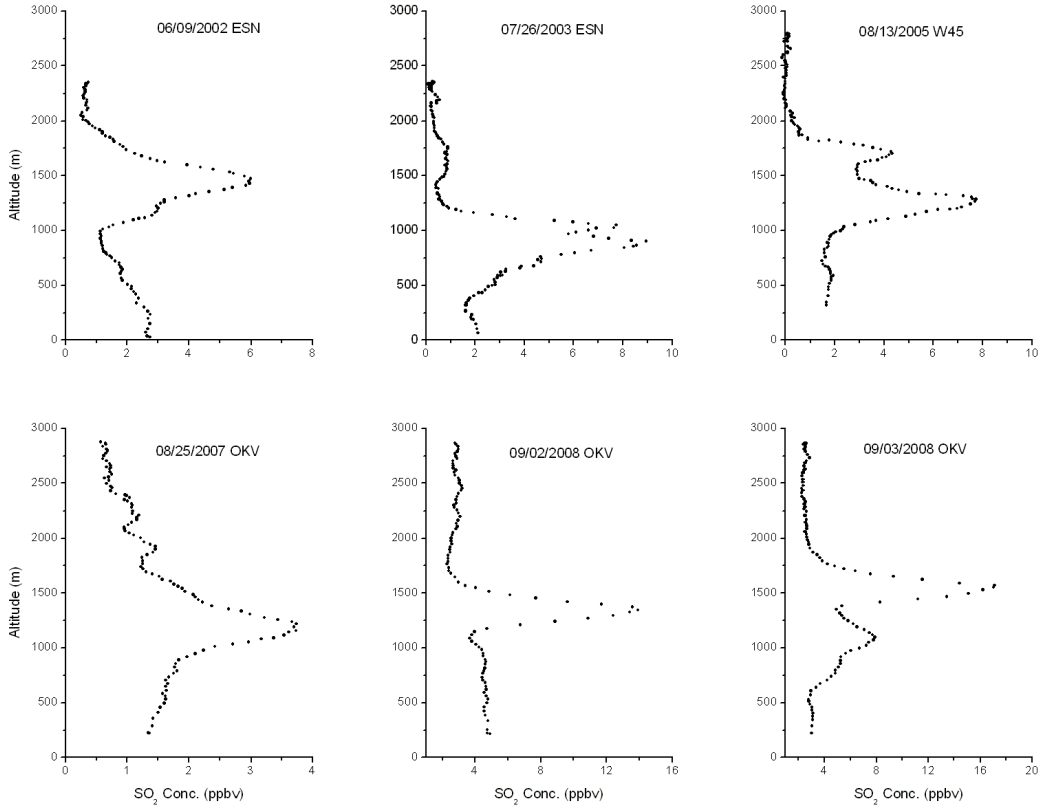

Figure 3.17 Sample cases of isolated SO_2 plumes in the FT (ESN airport in Easton, MD; OKV airport in Winchester, VA, details in Table 3.1).

(http://www.sourcewatch.org/index.php?title=AES_Warrior_Run_Generation_Plant) in Cumberland, MD. The annual SO_2 emission from the Warrior Run facility in 2010 was 1246.5 tons based on EPA CEMS data. The high SO_2 concentrations near the surface in profiles over Cumberland are likely explained by local emissions. In 2011, the research flight pattern was changed (from Luray-Winchester-Cumberland to Cumberland-Luray-Frederick in the morning). So Cumberland was visited earlier in the morning, and substantial amounts of SO_2 were observed by the RAMMPP aircraft.

Table 3.3 Summary of SO_2 plumes observed during RAMMPP research flights.

Flight Date	Time (UTC)	Location	Notes
07/09/00	14:07	OKV	15 ppb at 1200 m, 18 ppb at 450 m
06/27/01	14:34	CBE	7.5 ppb at 400 m
06/28/01	14:13	OKV	12 ppb at 800 m
06/09/02	18:01	0W3	13 ppb at 1000 m
06/09/02	18:50	ESN	6 ppb at 1500 m
06/24/02	14:04	OKV	50 ppb 1600 m
06/24/02	14:47	CBE	>8 ppb from surface to 2000 m
06/25/02	13:55	OKV	5 ppb at 800 m
06/25/02	14:38	CBE	8 ppb at 300 m
06/26/02	14:58	CBE	5 ppb at 1700 m, 9 ppb at 500 m
07/13/03	14:30	W45	5 ppb at 1200 m
07/26/03	20:32	0W3	6.5 ppb at 600 m
07/26/03	21:34	ESN	9 ppb at 900 m
08/15/03	14:00	W45	37 ppb at 1000 m
08/15/03	15:25	CBE	20 ppb at 600 m
08/21/03	15:56	CBE	>8 ppb from surface to 800 m
08/21/03	20:21	ESN	8 ppb at 800 m
08/28/03	14:24	W45	8 ppb at 1200 m
08/28/03	15:06	OKV	13 ppb at 800 m
08/28/03	15:48	CBE	40 ppb at 500 m
07/21/04	13:36	W45	23 ppb at 1000 m
10/07/04	13:51	W45	26 ppb at 800 m
10/07/04	14:36	OKV	20 ppb at 800 m
10/07/04	15:15	CBE	33 ppb at 500 m
08/13/05	14:12	W45	8 ppb at 1300 m
08/13/05	14:54	OKV	11 ppb at 1200 m
08/02/07	15:45	CBE	14 ppb at 1800 m, 14 ppb near the surface
08/03/07	15:38	CBE	10 ppb at surface
08/03/07	18:55	0W3	10 ppb at 700 m
08/24/07	18:59	CBE	>5ppb between 500 and 1500 m
08/24/07	21:39	0W3	>15 ppb below 500 m
08/25/07	16:24	CBE	5 ppb below 600 m
09/02/08	14:59	OKV	14 ppb at 1400 m
09/03/08	14:51	OKV	17 ppb at 1600 m
09/03/08	15:26	CBE	>9 ppb from surface to 1500 m
09/04/08	14:59	OKV	16 ppb at 1100 m
09/04/08	15:36	CBE	>9 ppb from surface to 1500 m
08/04/09	19:02	ESN	>20 ppb from surface to 2000 m
09/01/10	21:31	0W3	5 ppb at 500 m
06/09/11	15:42	CBE	>7 ppb below 800 m
07/11/11	15:19	CBE	10 ppb at 700 m
07/18/11	13:08	CBE	13 ppb at 700 m
07/20/11	13:52	CBE	23 ppb at 1200 m
07/21/11	14:10	CBE	>15 ppb below 500 m
07/22/11	14:42	CBE	>10 ppb below 1000 m
07/29/11	13:14	CBE	25 ppb at 1500 m, >10 ppb below 900 m

The statistics on SO_2 plumes over Harford Co. and Easton in the downwind region show relatively low values compared with the plumes over Cumberland, Winchester, and Luray; the altitudes of SO_2 plumes are also lower. Unlike the upwind region, the SO_2 loading over the downwind region is likely influenced by Maryland emissions, considering the short SO_2 lifetime during the summer. The maximum SO_2 concentration in these plumes (Table 3.3) decreased substantially in the last decade, in particular, after 2009 when the Healthy Air Act was implemented. In July 2011, in cooperation with the NASA DISCOVER-AQ campaign, an intensive aircraft campaign was carried out, which enhanced the likelihood of measuring these isolated plumes, but these SO_2 plumes were not observed by the RAMMPP aircraft in this campaign.

Since atmospheric SO_2 has such a short lifetime in the summer [*Hains*, 2007], observations of SO_2 plumes usually indicate fresh emissions. Atmospheric SO_2 disperses during the transport processes, and is also converted to other sulfur compounds through oxidation at the same time. There are about 50 spirals with distinguishable SO_2 plumes (Table 3.3) out of the total number of SO_2 measurements (~500), suggesting the probability of intercepting a SO_2 plume is around 10%. Even though the chance of observing SO_2 plumes is pretty low, these plumes are important for estimating atmospheric SO_2 column contents. Remote sensing techniques such as OMI SO_2 products, using the UV scattering to retrieve the trace gas information, are more sensitive to these SO_2 plumes in the FT.

3.4.2 Trends in atmospheric SO_2 column and AOD

Based on the discussion of SO_2 plumes, I find that the atmospheric SO_2 pollution is substantially influenced by the local or regional sources. Therefore unlike the O_3 and CO study, the long-term trend of SO_2 should be investigated individually at each location. Figure 3.18 presents the yearly mean average SO_2 column contents (below 1500 m) for the five airports. It is difficult to determine the long-term trend in the last decade, but I observe that isolated high SO_2 measurements (i.e., intercepting SO_2 plumes) normally dominates the yearly-mean value, resulting in high standard deviations of the mean, as happened in 2010 at Luray, Harford Co., and Easton. These low frequency events contribute a lot to the yearly mean SO_2 loading, so an approach was developed to filter out their influence. Surface observations demonstrate that the hourly SO_2 concentrations approximately follow a lognormal distribution [*Smith et al.*, 1989; *Winner et al.*, 1986]. So the values outside the 3-σ range are filtered out in pairs, i.e., ruling out the highest and lowest values at the same time, which keeps the geometric mean of a lognormal distribution unchanged. The data remaining after using this approach are illustrated in Figure 3.19. At the five airports, Cumberland has consistently high SO_2 column contents, which is very likely due to the nearby Warrior Run facility. The background SO_2 loadings over Luray and Winchester are low, except for a few large values influenced by transport from upwind sources (discussed in 3.4.1). Therefore, I selected Harford Co. and Easton airports to investigate atmospheric SO_2 trends. In a DC-Baltimore area summer, sulfate aerosols account for a significant portion of the particulate matter in the atmosphere [*Hains*, 2007], and create hazy days with low visibility. The Nephelometer onboard the RAMMPP aircraft provides information on the vertical distribution of aerosol scattering, and through integrating scattering from the surface to 1500 m I calcu-

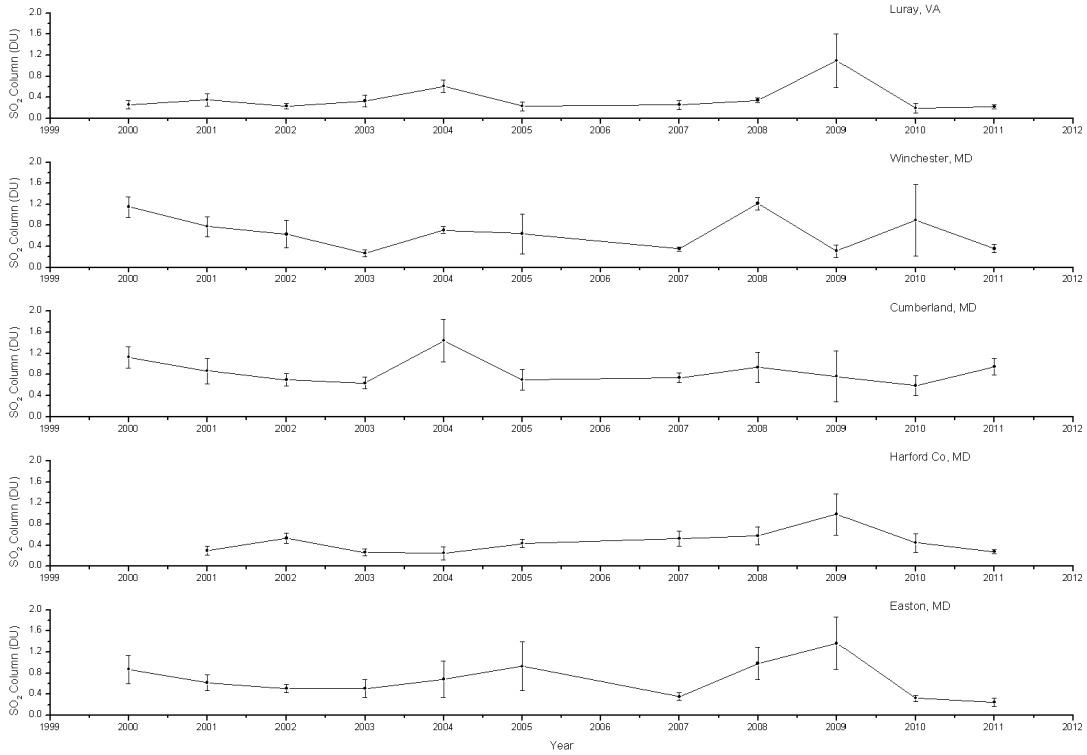

Figure 3.18 SO_2 column contents over the five airports between 2000 and 2011 (error bar shows the 1 standard deviation normalized by the flight number).

lated AODs for the lower atmosphere. The case study of Harford Co. is presented in Figure 3.20. Unlike atmospheric SO_2, the AODs are greatly influenced by ambient meteorological parameters, in particular RH [*Hand and Malm*, 2007], and tend to represent regional signatures. So directly using AOD values to evaluate the sulfate aerosol loading is not quantitative without compensating for hygroscopic growth. But one can qualitatively investigate the trend over the last decades.

Here I selected the SO_2 and AODs over the downwind areas (Harford Co. and Easton) for a statistical analysis because they are well within the Sate of Maryland, and

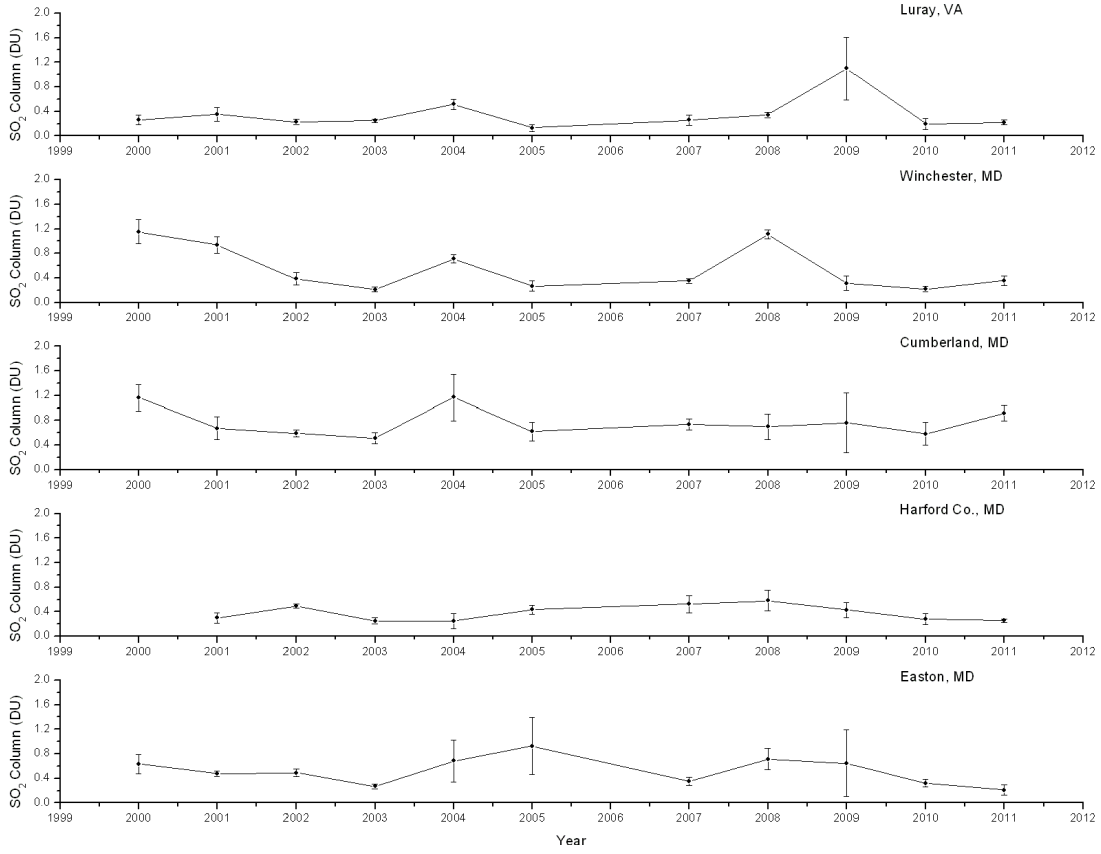

Figure 3.19 SO_2 column contents after eliminating large plumes over the five airports between 2000 and 2011 (error bars are one standard deviation of the mean normalized by the flight number).

the effects of the Healthy Air Act, especially on SO_2, are most likely to be represented. Based on CEMS data, local MD emissions fell substantially as the Healthy Air Act was fully implemented after 2009, so I calculated the mean values for 2000-2009 and 2010-2011 (Table 3.4). It is notable that after the Healthy Air Act, SO_2 column contents over both Harford Co. and Easton have shown significant reductions of ~40%, while the AOD data only demonstrate a moderate decrease of ~8%. The results confirm that SO_2

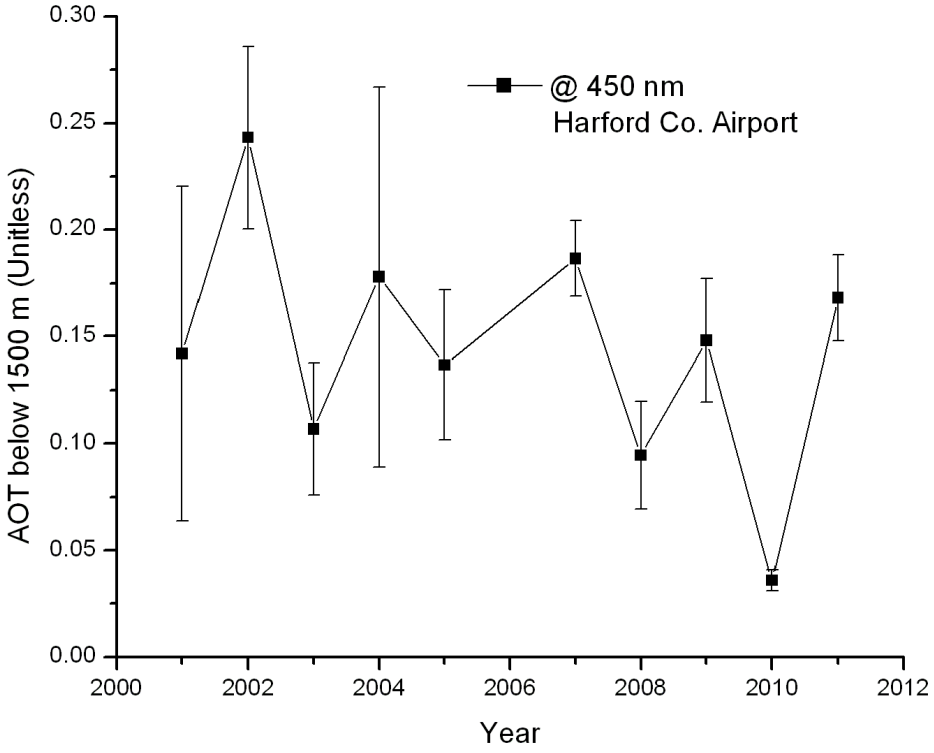

Figure 3.20 Trend in AOD over Harford county airport (0W3) from 2000 to 2011 (error bars are the one standard deviation of the mean, normalized by the flight number).

pollution in the downwind regions of the DC-Baltimore corridor is more related to emissions in MD, and that PM pollution tends to be more a regional issue.

Table 3.4 Statistics of SO_2 column and AOD over Harford Co. (0W3) and Easton (ESN).

	0W3 SO_2 (DU)	0W3 AOD	ESN SO_2 (DU)
2000-2009	0.42 (0.04*)	0.156 (0.015)	0.49 (0.05)
2010-2011	0.27 (0.04)	0.144 (0.023)	0.26 (0.05)
Decrease#	-36%	-8%	47%

* Standard Deviation of the mean (std/sqrt(n))

2000-2009 data as baseline

3.5 Cluster Analysis

3.5.1 Data and methods

Numerous studies have shown that back trajectory calculations are capable of representing the general wind flow under specific synoptic conditions [*Stohl et al.*, 1995; *Stohl*, 1998; *Stunder*, 1996]. A clustering study on the RAMMPP research flights in the Mid-Atlantic region from 1997 to 2003 has been conducted [*Hains et al.*, 2008]. Here I performed a similar case study, which incorporates long-term measurements over Harford Co. airport (0W3) and the CEMS data discussed in section 2.3. The CEMS program monitors point sources equipped with tall smokestacks such as power plants and industrial boilers For instance, a study conducted by the U.S. Government Accountability Office (U.S. GAO) tracked 284 smokestacks at 172 coal power plants in 34 states, of which 205 are 62.5 to 213 m tall, 63 are 213 to 305 m tall, and 12 are higher than 305 m [*G.A.O.*, 2011]. About one-third of these tall stacks are located in five states along the Ohio River Valley. Such stacks can disperse air pollutants over greater distances (Figure 3.21) than normal stacks. As well as the stack height, the height of plume rise is determined by the amount, temperature and velocity of emissions and meteorological conditions such as wind speed and wind velocity.

Since the DC-Baltimore region is downwind of the Ohio River Valley, the power plants' emissions are expected to exert effects on the air pollution in Maryland. As demonstrated in section 2.3, the emission data were aggregated by state, because these point sources are regulated by each state with its own implementation plan such as the Healthy Air Act of MD. Airborne measurements from 63 RAMMPP research flight over

Harford Co. from 1998 to 2011 were selected for this case study. I utilized the National Oceanic and Atmospheric Administration (NOAA) Air Resource Laboratory (ARL) Hybrid Single-Particle Lagrangian Integrated Trajectory (HYSPLIT) model (version 4, http://www.arl.noaa.gov/ready/hysplit4.html) to calculate 48-h back trajectories. The time of each aircraft spiral was utilized to initialize the model with release heights of 500,

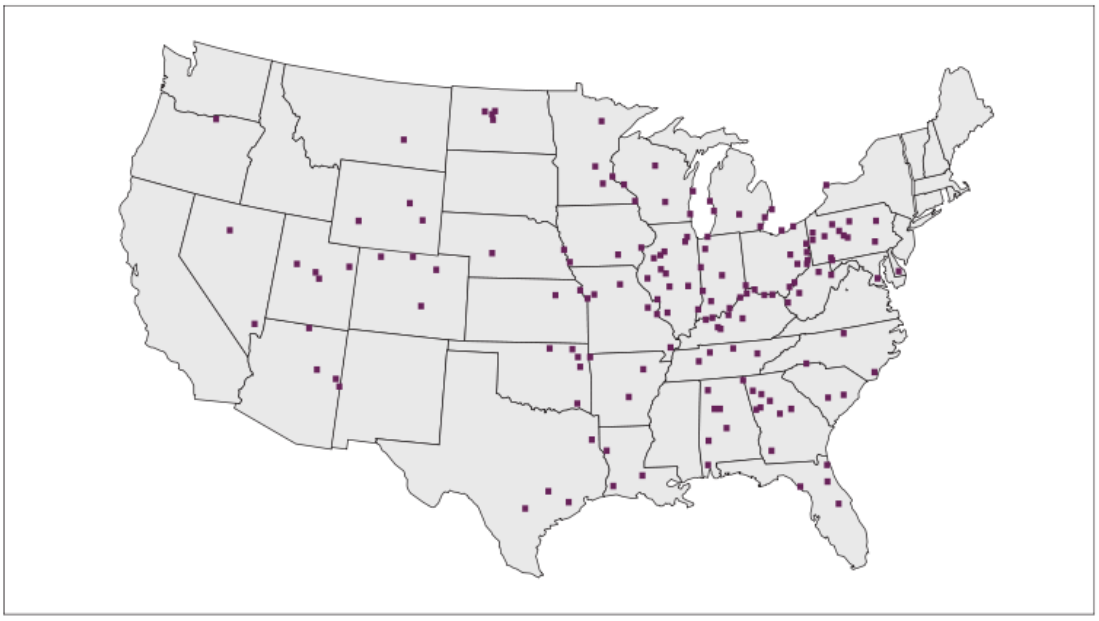

Sources: GAO and Map Resources (map).

Note: Alaska and Hawaii are not included because they do not have tall stacks.

Figure 3.21 Location of coal power plants with tall smokestacks as of December 2010 (Adapted from the U.S. GAO report [*G.A.O.*, 2011]).

1000, and 1500 m AGL respectively; one back trajectory is shown as an example in Figure 3.22. Different meteorological fields are used to drive the model, and the details are in Table 3.5. The accuracy of these trajectories is adequate to track the general circulation patterns that transport these air pollutants [*Stohl et al.*, 1995; *Stohl*, 1998].

Table 3.5 Meteorological fields used for the HYSPLIT model runs.

Year	Meteorology	Resolution	Layer
1997-2004	Eta Data Assimilation System (EDAS)	80 km	26
2004-2006	Eta Data Assimilation System (EDAS)	40 km	26
2007-2011	North America Mesoscale (NAM)	12 km	26

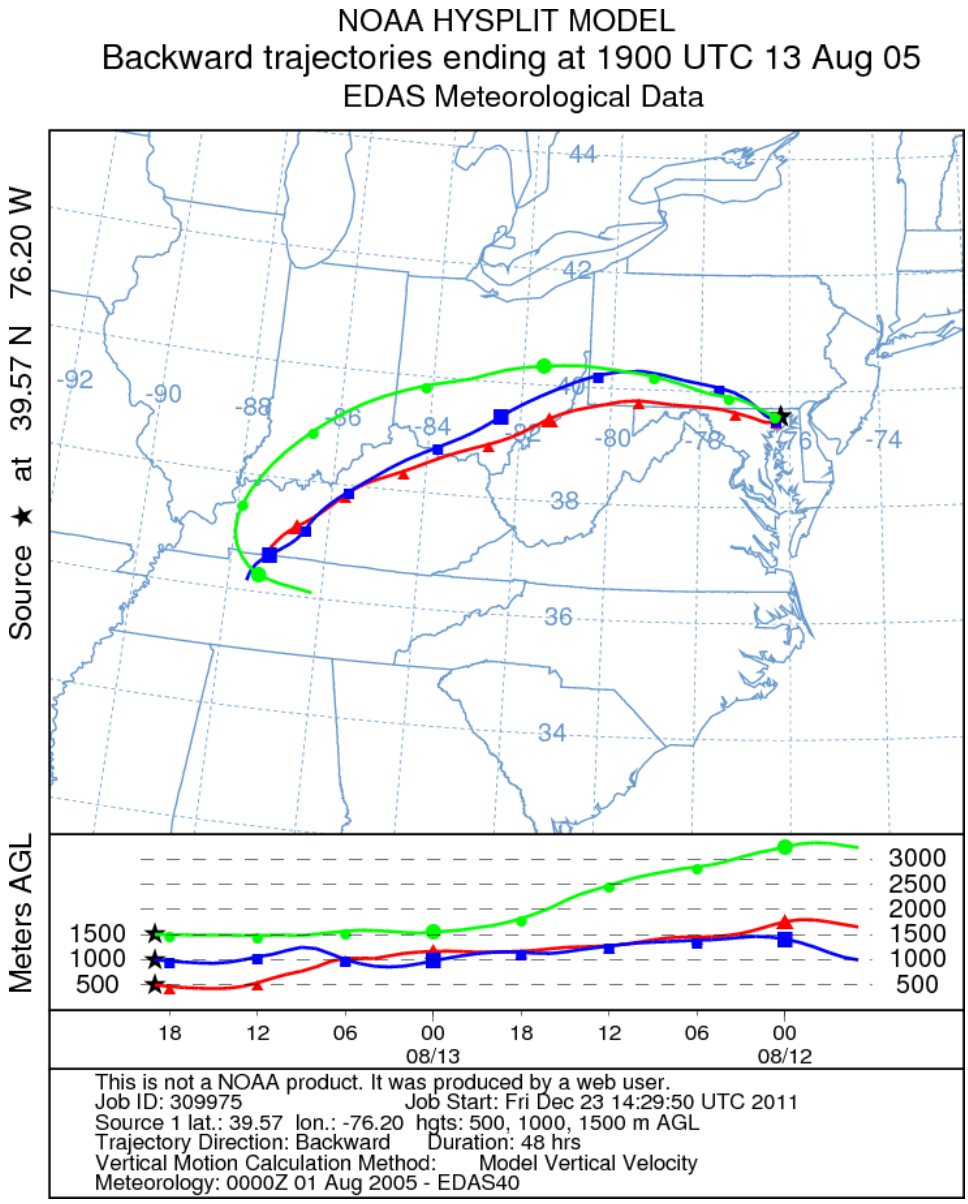

Figure 3.22 Sample of HYSPLIT 48-h back trajectory in 08/13/2005.

Location and altitude information of each HYSPLIT back trajectory is archived and the back trajectories ending at 1000 m over Harford Co. are selected to investigate the transport processes. Generally, the transport of air pollutant can be estimated by the product of wind speed and pollutant concentration, with maximum value at about 1000 m AGL. Unlike the previous study [*Hains*, 2007; *Hains et al.*, 2008], these trajectories were grouped into clusters by identifying which state it passes. For instance, the 1000 m trajectory in Figure 3.22 is indentified as passing over OH and PA, and grouped into the OH/PA cluster. Figure 3.23 presents the result of clustering; there are three clusters labeled by different colors, and two uncommon clusters are embedded in black underneath these spaghetti-like clusters. A simple approach was developed to evaluate the influences of upwind emissions: if the back trajectory passes by OH and PA, and ends at MD, the emission is expressed as:

$$Emission_{total}=Emission_{MD,i}+0.5Emission_{PA,i-1}+0.25Emission_{OH,i-1} \quad \text{(Equation 3.3)}$$

Where the subtitle *i* represents the flight date, and *i-1* represents upwind emissions data from the day before the flight day. Table 3.6 summarizes the characteristics of each cluster and the equation to calculate the total emissions. The coefficients of 0.5 and 0.25 are used under a simple assumption based on the distance between the upwind sources and air pollutants over eastern MD, i.e., PA is next to MD so half of the CEMS emissions are assumed to be transported into MD; OH is farther away from MD, so the coefficient is assumed to be 0.25. It is worth noting that these coefficients were created based on a simple conceptual model for qualitative study, and better parameterization is needed for future research.

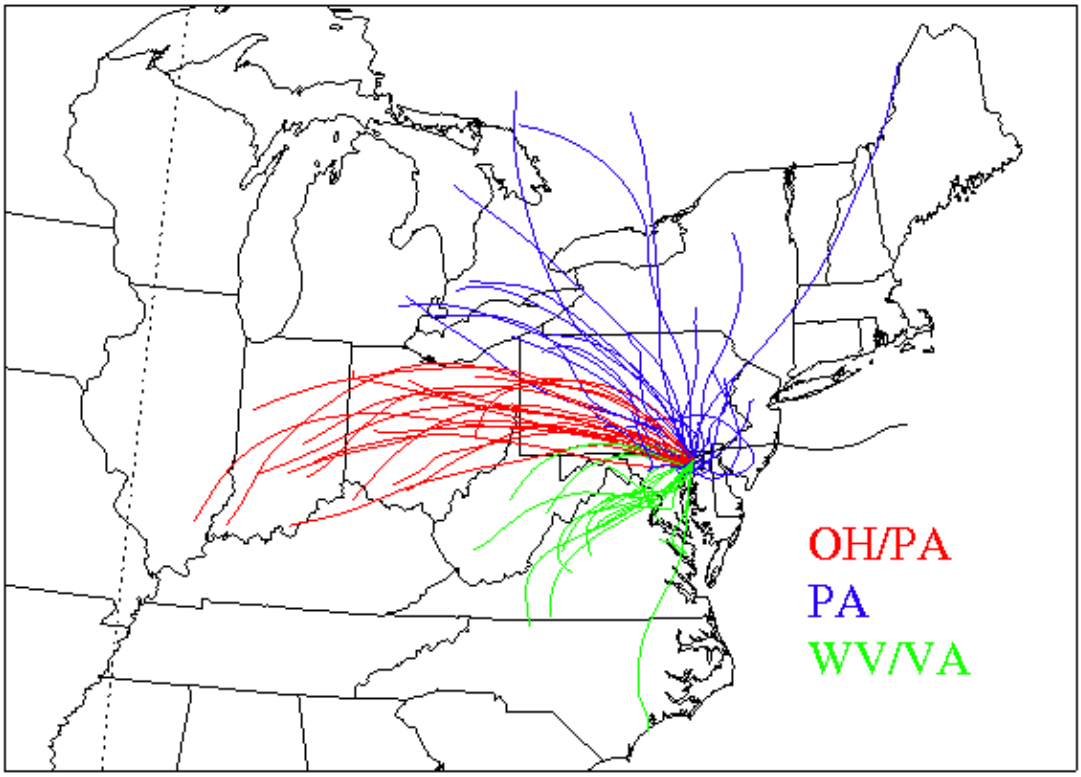

Figure 3.23 Results of clustering RAMMPP research flights over Harford county airport (black line shows the background flight on 09/09/03).

Table 3.6 Characteristics and emission estimates of clusters.

cluster	upwind states	Emission estimate
1	OH and PA	$MD_i + 0.5PA_{i-1} + 0.25PA_{i-1}$
2	PA	$MD_i + 0.5PA_{i-1}$
3	WV or VA	$MD_i + 0.5VA_{i-1}$ or $MD_i + 0.5VA_{i-1}$
4	Recirculation	$MD_i + 0.5\ VA_{i-1} + 0.5\ PA_{i-1}$
5	Stagnation*	MD_i

*The background flight was incorporated into the stagnation cluster because it shares the same estimate of upwind emissions.

3.5.2 Results and discussion

CEMS data only contains continuous measurements of SO_2 and NO_x (a precursor of O_3), so the RAMMPP SO_2 and O_3 column contents below 1500 m are utilized here to identify the effects of upwind emissions. Figure 3.24 shows CEMS emissions versus the column content measurements. Linear regressions are conducted for each cluster and the results are presented in Table 3.7. The OH/PA cluster shows strong correlation between

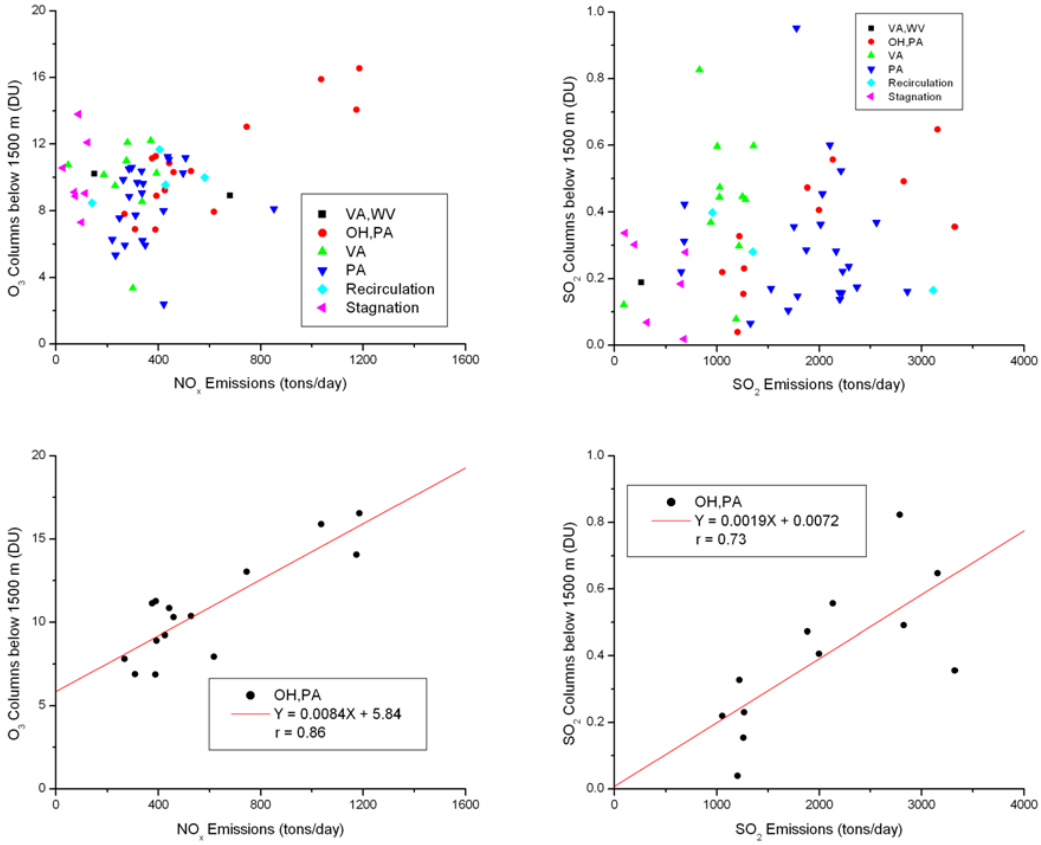

Figure 3.24 RAMMPP column contents versus CEMS emissions for all clusters (upper panel: all clusters; lower panel: OH/PA cluster only).

the upwind emissions and downwind air pollution. Similar plots with only MD CEMS emissions are presented in Figure 3.25, and the low correlation reveals that air pollutants are not controlled exclusively by local emissions in MD, and the long-range transport should be taken into account.

As illustrated in section 3.2, NO_x emissions from mobile sources account for about half of the total NO_x emissions. The high correlation between upwind CEMS NO_x emissions and local O_3 column contents could be a coincidence that if power plant emissions are correlated with mobile emissions during hot summer days when RAMMPP research flights are conducted. Unfortunately, daily mobile emissions are not available to test this hypothesis, so instead a simple case study on examining the long-term trend was performed here. I plot the average ground level NO_x observations in MD/DC/NOVA during O_3 season (section 3.2) versus both the daily CEMS emissions and national mobile

Table 3.7 Linear Regression (*Y = A + BX, r as correlation coefficient*) of CEMS emissions versus RAMMPP column contents for each cluster (only the OH/PA transport pattern has impact on the downwind air pollution, highlighted in **Bold**).

		O_3 columns vs CEMS NO_x			SO_2 columns vs CEMS SO_2		
Cluster	Num.*	slope	intercept	r	slope	intercept	r
VA/WV	2	-0.02	10.58	N/A	N/A	N/A	N/A
OH/PA	**16**	**0.0076**	**5.84**	**0.86**	**0.00017**	**0.0072**	**0.73**
VA	10	-0.0018	10.39	-0.08	0.000144	0.26	0.26
PA	22	0.0024	7.47	0.16	-0.000012	0.32	-0.04
Recirculation	4	0.0034	8.43	0.53	-0.000087	0.45	-0.94
Stagnation	7	0.0022	9.91	0.04	-0.00021	0.3	-0.47

* Number of HYSPLIT back trajectories.

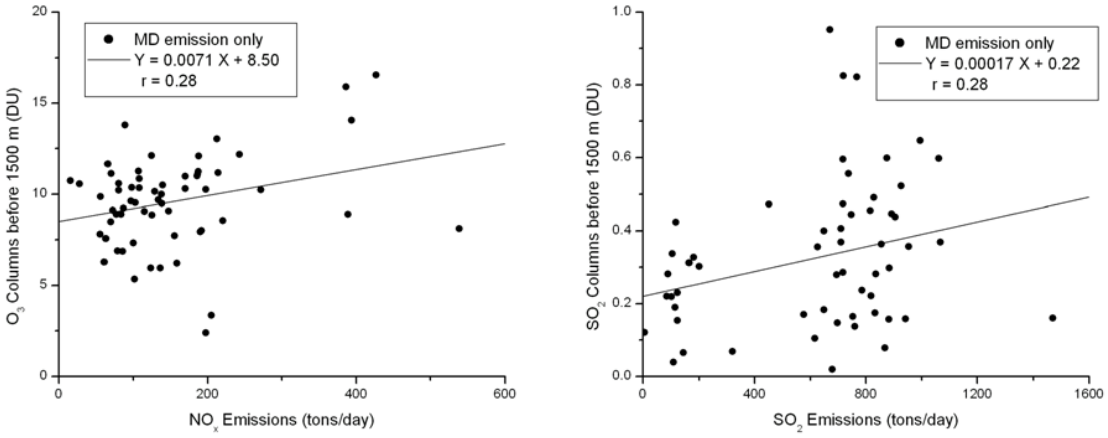

Figure 3.25 RAMMPP column contents versus CEMS emissions in MD.

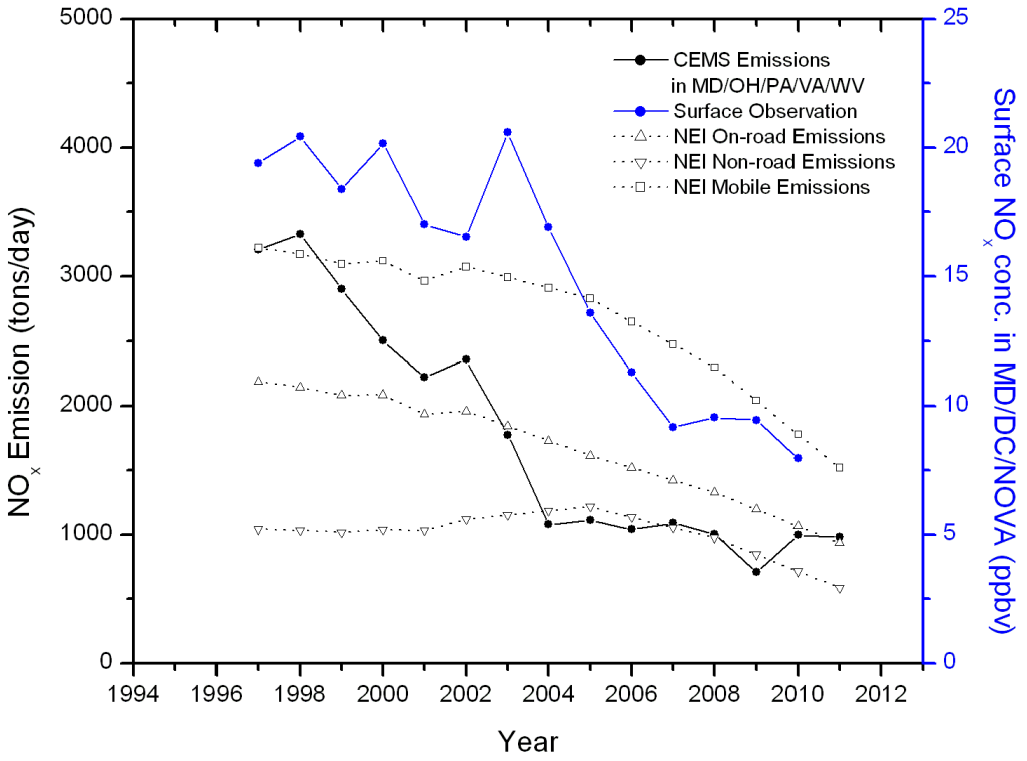

Figure 3.26 Trend of ground level NO_x observations, CEMS NO_x emissions and USEPA NEI mobile NO_x emissions (all values are daily mean values, and national NEI mobile emissions divided by 10 to approximate emissions from the five states).

emission data (Figure 3.26). A sharp decrease of ground level NO_x concentrations is observed from 2003 to 2007, which followed the EPA NO_x SIP call (2003-2004). During the same time period, the emissions from mobile sources show a gradual decrease. Figure 3.27 presents the linear regression of NO_x emissions from both CEMS emissions and CEMS plus NEI emissions versus EPA AQS NO_x observations. Both of the emission data show good correlation with the surface NO_x observations. Because the daily emissions of mobile sources are not available from measurements, the CEMS data provide a unique opportunity to investigate their effects on the surface NO_x observations. Considering that ground level NO_x concentrations are controlled by other parameters

a)

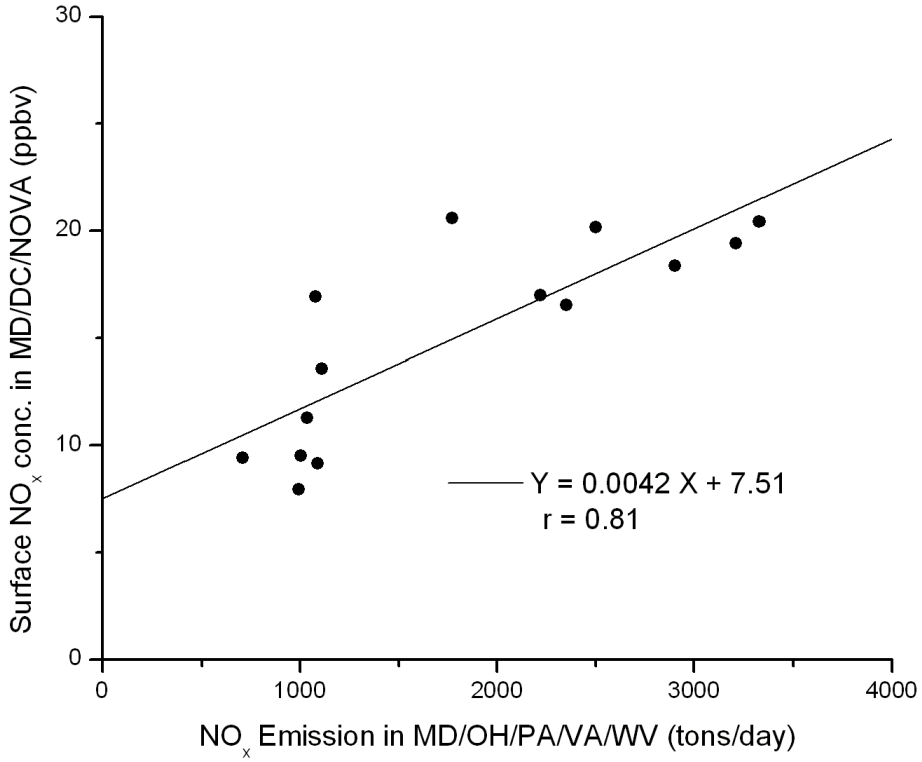

b)

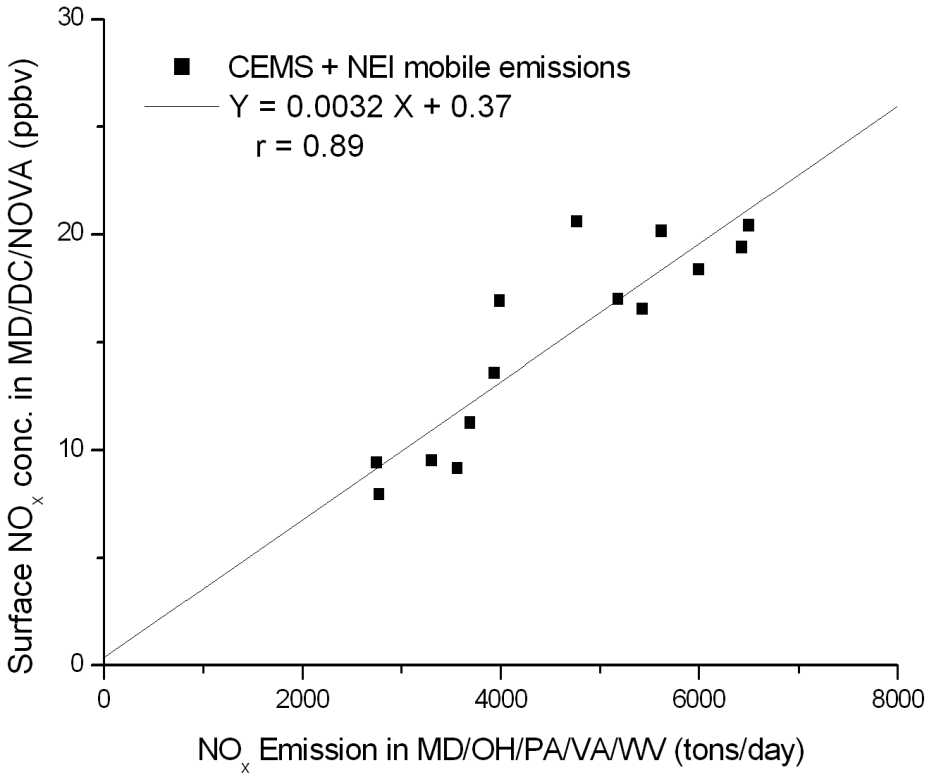

Figure 3.27 Scatter plots of NO_x emissions versus the EPA AQS NO_x observations (daily mean value sampled for afternoons during the O_3 season), a) CEMS emissions only; b) CEMS plus the scaled NEI mobile emissions.

such as temperature, turbulence, and concentration of VOCs, the CEMS data are surprisingly a good proxy to evaluate the ground level NO_x concentration. Total daily CEMS NO_x emissions in the five states decreased from ~3500 tons/year in 1998 to ~1000 tons/year (Figure 3.25 a), which approximately equal to a ~7.5 ppb decrease or ~5.0 ppb/decade of the ground level NO_x concentrations. In Mid- Atlantic, O_3 photochemistry production is largely NO_x-sensitive, so the decrease in NO_x concentration is expected to

reduce O_3 pollution. Due to the complicated chemical mechanism of tropospheric O_3, quantifying this effect is beyond the scope of this thesis.

CEMS data are expected to reflect the ambient temperature change since they are dominated by power plant emissions, especially on the hot summer days when electricity demand surges dramatically. High O_3 episodes are also frequently linked to high temperature days in the Mid-Atlantic region, when the Bermuda high is strong enough to create stagnation and sunny weather over MD. So it is important to study the relationship between power plant emissions and surface temperature (Figure 3.28). The blue points in Figure 3.28 represent the data during the EPA NO_x SIP call. The slope of NO_x emissions versus surface temperature decreased significantly after the SIP call. Since CEMS NO_x emissions are a good proxies for evaluating ground level NO_x concentration, $\frac{dEmission_{NO_x}}{dT}$ has been calculated for last 15 years by each state (Figure 3.29). High correlation (except for 2003 WV) was observed, and the value of $\frac{dEmission_{NO_x}}{dT}$ decreased from ~15 tons/℃ before 2002 to ~8 tons/℃ after 2002. The mean daily NO_x emissions are ~1000 tons/day in the five state (Figure 3.26), so if the ambient temperature in the Mid-Atlantic area increased 1 ℃ the total NO_x emissions would increase ~40 tons, resulting in ~4% increase. By applying the relationship between surface NO_x and CEMS NO_x data illustrated in Figure 3.27 a, $\frac{d[NO_x]}{dT}$ is calculate as ~0.30 ppb/℃ before 2002 and ~0.15 ppb/℃ after 2002.

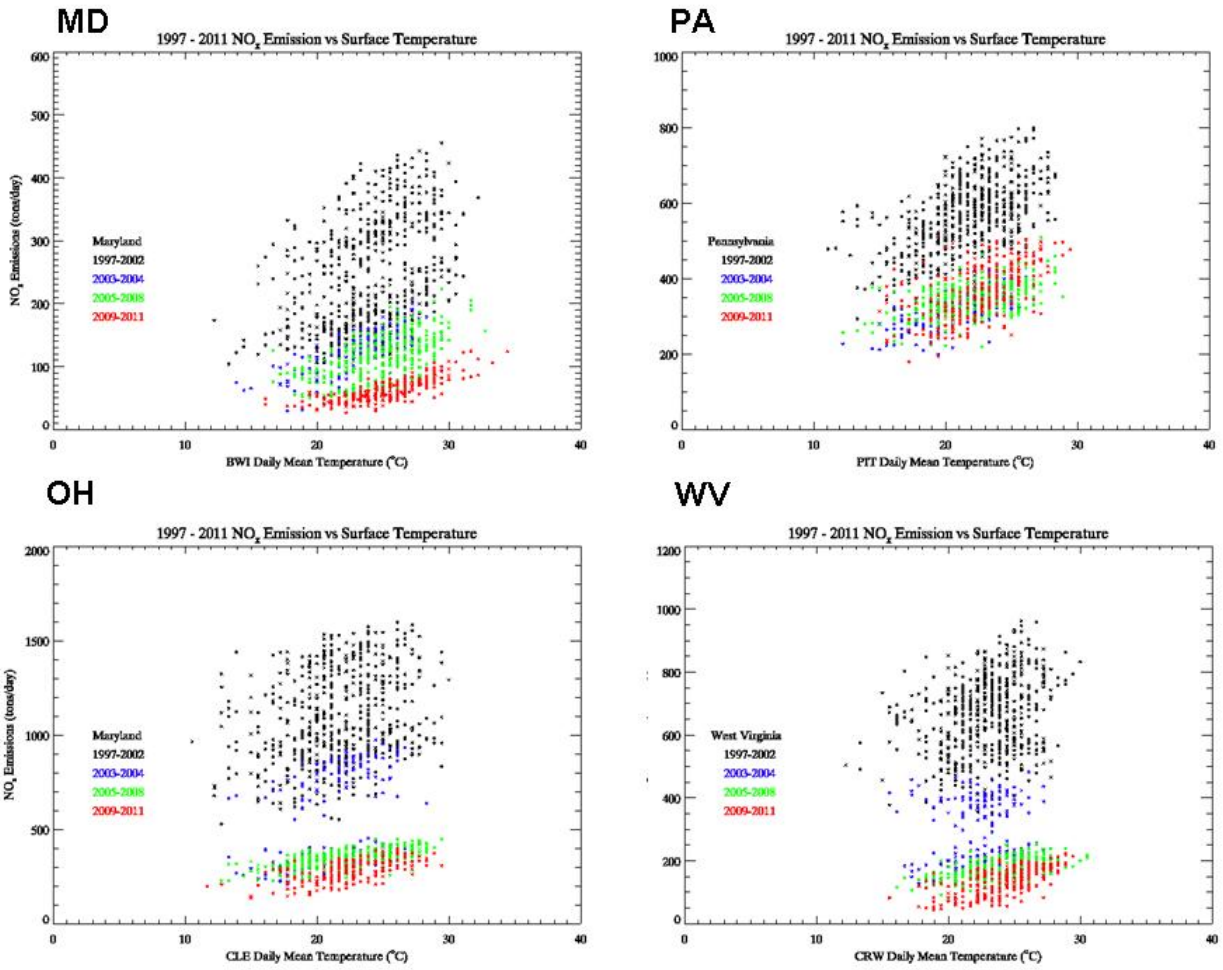

Figure 3.28 Scatter plots of CEMS daily NO_x emissions versus BWI daily temperature (all data are selected during the O_3 season, May to September). Black, Blue, Green, and Red dots represent the data in 1997-2002, 2003-2004, 2005-2008, and 2009-2011 respectively.

Here I introduced the O_3 production efficiency (OPE), which is defined as the net number of O_3 molecules produced per molecule of NO_x in NO_x-sensitive regions [*Hirsch et al.*, 1996; *Jacob*, 2000; *Liu et al.*, 1987]. Tropospheric O_3 production is a nonlinearsystem, which is influenced by parameters such as VOC concentrations, ambient temperature, locations and altitudes [*Lin et al.*, 1988; *Nunnermacker et al.*, 2008; *Shon et al.*, 2008; *Sillman*, 1995; *Walcek and Yuan*, 1995; *Wood et al.*, 2009]. The value

a)

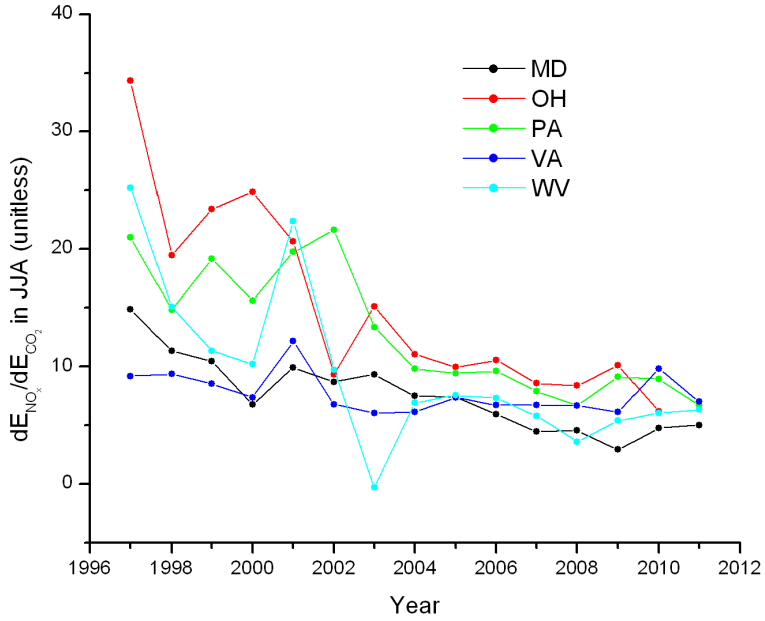
40
30
20
10
0
1996
1998
2000
2002
2004
2006
2008
2010
2012
Year
dE$_{NO_x}$/dE$_{CO_2}$ in JJA (unitless)
MD
OH
PA
VA
WV

b)

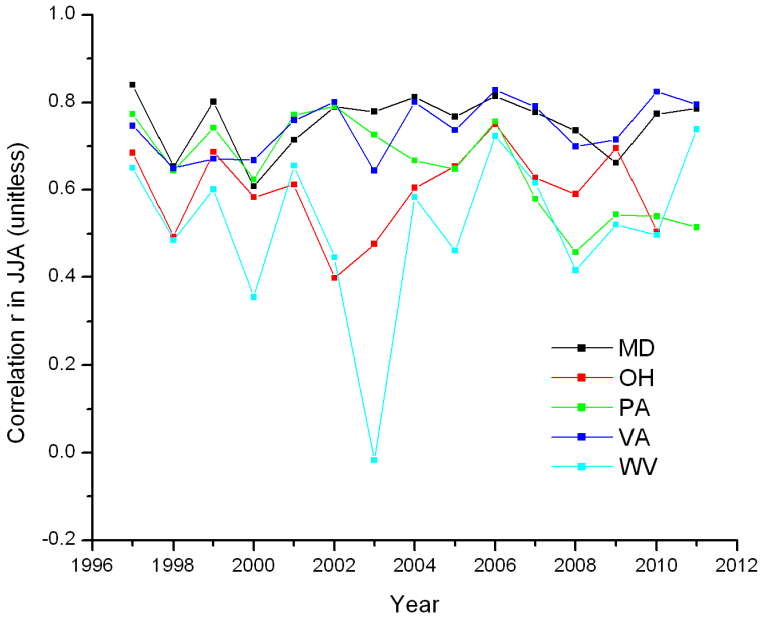
1.0
0.8
0.6
0.4
0.2
0.0
-0.2
1996
1998
2000
2002
2004
2006
2008
2010
2012
Year
Correlation r in JJA (unitless)
MD
OH
PA
VA
WV

c)

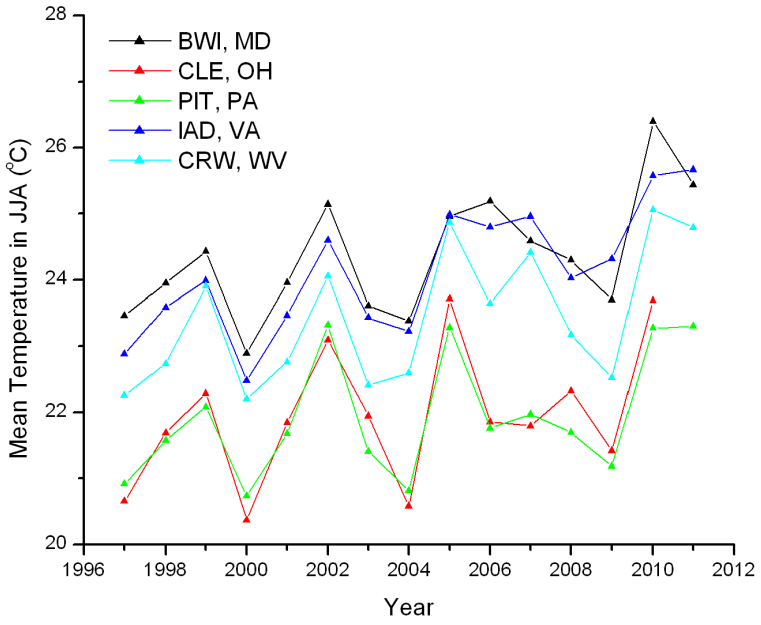

Figure 3.29 Linear regression trends of CEMS NO_x emissions versus surface temperature observations. Linear fit ($Y = A + BX$, r) has been conducted for all CEMS data (in Figure 3.27) during JJA. Slope (B), correlation (r) and mean temperature are showed in the a), b), and c) plots respectively. Comparison of slope (B) and JJA mean temperature demonstrated that the slope (B) is not correlated to the ambient temperature.

of OPE can range from 5 mol/mol in urban areas [*Kleinman*, 2000; *Nunnermacker et al.*, 2000] to ~50 mol/mol in the clean marine atmosphere [*Wang et al.*, 1998]. In this study, a value of 2-8 mol/mol was used for the Mid-Atlantic area [*Kleinman et al.*, 2002]. When utilizing OPE to $\frac{d[NO_x]}{dT}$, the $\frac{d[O_3]}{dT}$ is estimated as 0.6-2.4 ppb/℃ before 2002 and 0.3-1.2 ppb/℃ after 2002, contributing around half of the CPF reported (3.2 ppb/℃ before 2002 and 2.2 ppb/℃ after 2002 in the Mid-Atlantic [*Bloomer et al.*, 2009].

During hot summer days, the demand for electricity increases with increasing usage of air conditioners, so peaking units, electricity generating units running only when there is a high demand in the power grid, kick in to provide more electricity. Peaking units in the five states usually emitted more NO_x than conventional coal-fired power plants equipped with NO_x scrubbers (Case studies on peaking units are presented in Appendix II). With the installation of NO_x scrubbers especially during 2002 and 2003, the value of $\frac{dEmission_{NO_x}}{dT}$ decreased substantially. In conclusion, both bulk NO_x emissions and the value of $\frac{dEmission_{NO_x}}{dT}$ were reduced under the EPA NO_x SIP call. The decreasing NO_x emissions might have changed the photochemistry of O_3 production in the Mid-Atlantic area by varying the NO_x to VOC ratios. The decrease of $\frac{dEmission_{NO_x}}{dT}$, followed by the decrease of $\frac{d[NO_x]}{dT}$ and $\frac{d[O_3]}{dT}$ (from 0.6-2.4 ppb O_3/℃ before 2002 to 0.3-1.2 ppb O_3/℃ after 2002), can explain the CPF change from 3.2 ppb/℃ to 2.2 ppb/℃ observed in the eastern U.S. [*Bloomer et al.*, 2009].

3.6 Summary of the long-term trend of air pollution in the eastern U.S.

In this chapter, I investigated the long-term trend of air pollution in the Mid-Atlantic through a comprehensive study using emission data, aircraft measurements, and a clustering technique. The EPA CEMS program is continuously monitoring the emissions from major point sources including power plants and industrial boilers, and the

data for five states (MD, OH, PA, VA, and WV) were used to investigate the interstate transport of air pollutants. The long-term trend in CEMS emissions demonstrates significant decreases of NO_x and SO_2 emissions in the last 15 years, in agreement with the national trends of ambient air pollutants. The EPA NO_x SIP call (2003-2004) was proven effective in reducing the NO_x emissions from point sources, which helped improve local and regional air quality, especially for O_3 production. The SO_2 trend presents a gradual decrease, and the local Healthy Air Act (implemented in 2010) drastically reduced sulfur emissions in MD. Mobile sources such as highway vehicles also contributed to the NO_x emissions, so I investigated NEI mobile emissions in 2002, 2005, and 2008, which showed a gradual decrease. The surface NO_x observations in MD, DC, and northern VA captured the decreasing trend of CEMS emissions well, with a sharp decrease after the EPA NO_x SIP call. Therefore, I find that the CEMS emissions can work as proxy for ground level NO_x concentrations, which is useful for a study on CPF.

The aircraft measurements of O_3, CO, SO_2, and aerosol scatterings were integrated to column contents (AOD for aerosols scattering) from surface to 1500 m, and categorized into upwind group and downwind groups. The difference of O_3 column contents in these two groups was considered to be the net photochemical production of ambient O_3, which is a 2.3 ± 2.0 DU increase in column contents or a ~15 ppb increase evenly within the lowest 1500 m. The decreasing trends of CO and O_3 were found to be ~20.0 DU/decade and ~2.0 DU/decade respectively, which are equivalent to ~800 ppb/decade and ~13 ppb/decade decreases in the lowest 1500 m. Because RAMMPP research flights are mostly conducted on the air quality action days, the substantial O_3

decreasing trend illustrates that O_3 pollution on the bad air quality days has improved significantly. In contrast to regional O_3 and CO pollution, atmospheric SO_2 exists in the form of plumes with short lifetimes in summer, and the SO_2 column contents are substantially influenced by the locations of research spirals. I select the spirals to the east of the DC-Baltimore area, where the SO_2 loadings come predominantly from MD. In 2010, the Healthy Air Act required about a 90% reduction of power plant SO_2 emissions in MD, and a 30~40% decrease of SO_2 column contents was observed. A similar approach was applied to aerosol scattering, and the AOD showed only a ~10% decrease after the Healthy Air Act. This finding suggests that SO_2 pollution is a local problem, while aerosol pollution and visibility impairment are more regional issues.

To study the effects of long-range transport of air pollutants, in particular from power plants with high smokestacks, back trajectories were calculated using the NOAA HYSPLIT model. And these trajectories were grouped into several clusters, depending on the locations passed. Emissions were estimated by combining MD emissions with upwind state emissions, and I performed the linear regression analysis for each cluster, finding that transport from OH and PA has significant effects on MD air pollution. Power plant emissions are approximately determined by electricity demand, which is related to ambient temperature. So I studied NO_x emissions with respect to temperature observations, and found $\frac{dEmission_{NO_x}}{dT}$ (correlated with $\frac{d[NO_x]}{dT}$) has been reduced significantly in the last decade. By utilizing the OPE, I estimated the value of $\frac{d[O_3]}{dT}$ caused by $\frac{dEmission_{NO_x}}{dT}$ as 0.6-2.4 ppb/℃ before 2002 and 0.3-1.2 ppb/℃ after

2002, contributing around half of the CPF reported from observations in Mid-Atlantic area.

Chapter 4. 2008 aircraft campaign in central China

4.1 Background and overview

In 2008, a joint U.S.-China campaign, the East Asian Study of Tropospheric Aerosols and their impact on Regional Climate (EAST-AIRC), was conducted to study the aerosols in China and their effects on and interactions with the regional climate [*Li et al.*, 2011]. In addition to field experiments at four locations in southern and north China, an airborne campaign on ambient SO_2 was carried out in Henan province, central China. During the rapid economic development in the past decades, the consumption of energy and raw material in China increased dramatically, and 70% of the total energy consumption relied on coal burning [*CESY*, 2005]. The total anthropogenic SO_2 emissions were ~31.3 Tg (Teragram, 10^{12} g) [*Lu et al.*, 2010], and atmospheric SO_2 is oxidized to form sulfate aerosols [*Finlayson-Pitts and Pitts*, 1999; *Seinfeld and Pandis*, 2006]. The sulfur compounds can cause environment problems [*He et al.*, 2002], such as acid deposition [*Hao et al.*, 2000; *Larssen et al.*, 2006], visibility degradation [*Chang et al.*, 2009; *Che et al.*, 2007; *Deng et al.*, 2008], and pose a hazard to public health [*Chen et al.*, 2011; *Kan et al.*, 2010], and long-range transport of these pollutants are observed [*Dunlea et al.*, 2009; *Prospero et al.*, 2003; *van Donkelaar et al.*, 2008].

A number of studies on the sulfur pollution in China have been conducted. Surface observations of ambient SO_2 were made in and near Beijing [*Li et al.*, 2007a; *Sun*

et al., 2009], Yangtze River Delta (YRD) [*Costabile et al.*, 2006], Pearl River Delta (PRD) [*Zhang et al.*, 2008], and rural areas [*Meng et al.*, 2010]. Vertical distribution of ambient SO_2 are studied through aircraft measurements in the Northeast [*Dickerson et al.*, 2007], South [*Wang et al.*, 2008], and East of China [*Geng et al.*, 2009; *Xue et al.*, 2010]. During these *in situ* measurements, large variations were observed in spatial and temporal distributions of ambient SO_2. For instance, ten background and rural sites revealed low concentration ($\pm \sigma$) of 0.7 $\pm$ 0.4 ppb at Waliguan on Qinghai Plateau and high concentration of 67.3 $\pm$ 31.1 ppb at Kaili in southwest China [*Meng et al.*, 2010]; over the PRD, Wang et al. reported 18.5 ppb SO_2 at 2100 m and up to 107.5 ppb SO_2 within the PBL during one research flight [2008]; over northeast, 5-20 ppb SO_2 in the PBL and < 1 ppb SO_2 were observed [*Dickerson et al.*, 2007]. However, most of the studies focused on the highly industrialized regions such as eastern China, and here emerged the importance of investigating the sulfur pollution in the developing areas of central and western China.

The Y-7 transport airplane was located in the Zhengzhou Xinzheng International Airport (IATA: CGO, 34.52°N, 113.84°E) in suburban Zhengzhou, a megacity with ~7 million residents. Zhengzhou is the capitol city of Henan province, the most populous region of China with ~100 million residents in 160,000 km^2 areas (Figure 4.1) Coalmines and power plants are concentrated in western and southern Henan, and coal burning is ubiquitous for domestic cooking and heating. In 2007, 2.3 Tg SO_2 was emitted in Henan, ~7% of the total SO_2 emissions of China; the power plants in Henan released 1.1 Tg SO_2, ranking 3rd by province [*Lu et al.*, 2010]. These emission data suggest that Henan in central China is a major source of anthropogenic SO_2 emissions, which has not

been thoroughly investigated. The aircraft campaign was conducted in April 2008, when the long-range transport is predominant [*Tan et al.*, 2002].

Figure 4.1 Location of Henan province in China (adapted from wikipedia webpage, http://en.wikipedia.org/wiki/Henan).

One incentive of this campaign was to validate or evaluate the OMI SO_2 products, so the research flights were synchronized with OMI over passing time (~1:30 pm local time). The aircraft took off ~1 pm local time, and the spirals were conducted between 1 and 2 pm; the total length of one research flight was ~2 hrs within 200 km radius of the CGO airport. Flight routes were selected based on the near real-time OMI SO_2 maps (http://so2.gsfc.nasa.gov/pix/daily/0408/china_0408z.hmtl), but forbidden over western and northern Henan with mountains higher than 1000 m. Synoptic circulation patterns were tracked through satellite images, surface analyses and forecasts from the Korea

Meteorological Administration (KMA, http://web.kma.go.kr/eng/index/jsp). Different locations were selected for research flights in order to measure ambient SO_2 over both strong and weak OMI SO_2 signals. Because Y-7 is a large airplane, with cruise speed of ~400 km/hr and a payload of 5 tons, the spirals were restricted between 900 to 4500 m AGL for safety concerns. The typical height of PBL in spring China is around 1000 m, where ambient SO_2 is concentrated, so I retrieved the information of PBL SO_2 during the descents over the CGO airport.

A handheld sunphotometer (Microtops II, Solar Light Company, Glenside, PA) was also deployed in the Xinzheng Meteorological Observatory (34.38 ºN and 113.72 ºE, 116.6 m AGL) from April 2 to 22, 2008. Measurements were taken every 15 minutes from 13:00 to 14:30 (local time). The hand held instrument measured the AOD in 5 wavelengths 340, 380, 440, 500, and 870 nm, and was widely used for the previous 2005 East Asian Study of Tropospheric Aerosols and their Impact on Regional Climate (EAST-AIRE) [*Li et al.*, 2007b; *Xin et al.*, 2007]. The instrument was serviced and calibrated by the NASA Goddard Space Flight Center (GSFC) Aerosol Robotic Network (AERONET) team, and the data was processed with the AERONET Version 2 algorithm. The data were sampled to remove the cloud-contaminated observations based on the observer's records.

4.2 Results of airborne SO_2 measurements

4.2.1 SO_2 altitude profiles

During the aircraft campaign, seven research flights were conducted on April 4, 5, 15, 16, 18, 20, and 22, 2008. Table 4.1 presents the summary of research flights and locations of spirals. All the flights were carried out under cloud-free weather conditions, except flight of 04/20/08, a cloud seeding experiment. I summarized the flight route with the altitude information in Figure 4.2. These flights were evenly distributed on the east, south and west of Zhengzhou except north where mountains are located, and within ~150 km radius of the CGO airport. Strong OMI SO_2 signals were observed over Changyuan (35.20 °N, 114.68 °E), while weak signals were over Yexian (33.62 °N, 113.35 °E). In this study, the region covered by these flights (33.0 to 35.5 °N, 112.5 to 115.5 °E) is selected for study and named the campaign area hereafter.

SO_2 altitude profiles from a research flight on 04/15/2008 are presented in Figure 4.3. The spiral location, Shangcai (33.25 °N, 114.26 °E) had a moderate OMI SO_2 signal, and relatively high SO_2 concentration (up to 1.5 ppb) was observed at high altitudes, ~4000 m. I conducted a statistical analysis of all SO_2 measurements averaged in 500 m layers from the surface to 4000 m in Table 4.2 to show the variations. For instance, over Changyuan (April 4th and 5th), up to 7 ppb SO_2 at 2000 m, while over Yexian (April 18th and 22nd) the ambient SO_2 concentration was below the detection limit (~0.3 ppb). And these results were consistent with the OMI SO_2 maps. During descents over the CGO airport, substantial amounts of SO_2 were observed consistently, suggesting the urban area of Zhengzhou is a major source of SO_2 pollution; relatively high SO_2 concentrations were found below 500 m, implying the majority of anthropogenic SO_2 was concentrated in the PBL.

Table 4.1 Summary of EAST-AIRC research flights in April 2008.

Date	Flight Type	Flight Time (UTC)	Spiral Location
04/04/08	Air Sampling	6:04-7:24	Changyuan (35.20 °N, 114.68 °E)
04/05/08	Air Sampling	5:38-6:50	Changyuan (35.20 °N, 114.68 °E)
04/09/08	Air Sampling	N/A*	Huojia (35.27 °N, 113.63 °E)
04/15/08	Air Sampling	6:10-6:56	Shangcai (33.25 °N, 114.26 °E)
04/16/08	Air Sampling	6:10-7:38	Suiping (33.15 °N, 113.95 °E)
04/18/08	Air Sampling	6:05-7:14	Yexian (33.62 °N, 113.35 °E)
04/20/08	Cloud Seeding	3:20-4:35	Weishi (34.41 °N, 114.17 °E)
04/22/08	Air Sampling	6:11-7:32	Yexian (33.62 °N, 113.35 °E)

* Power failure during the flight.

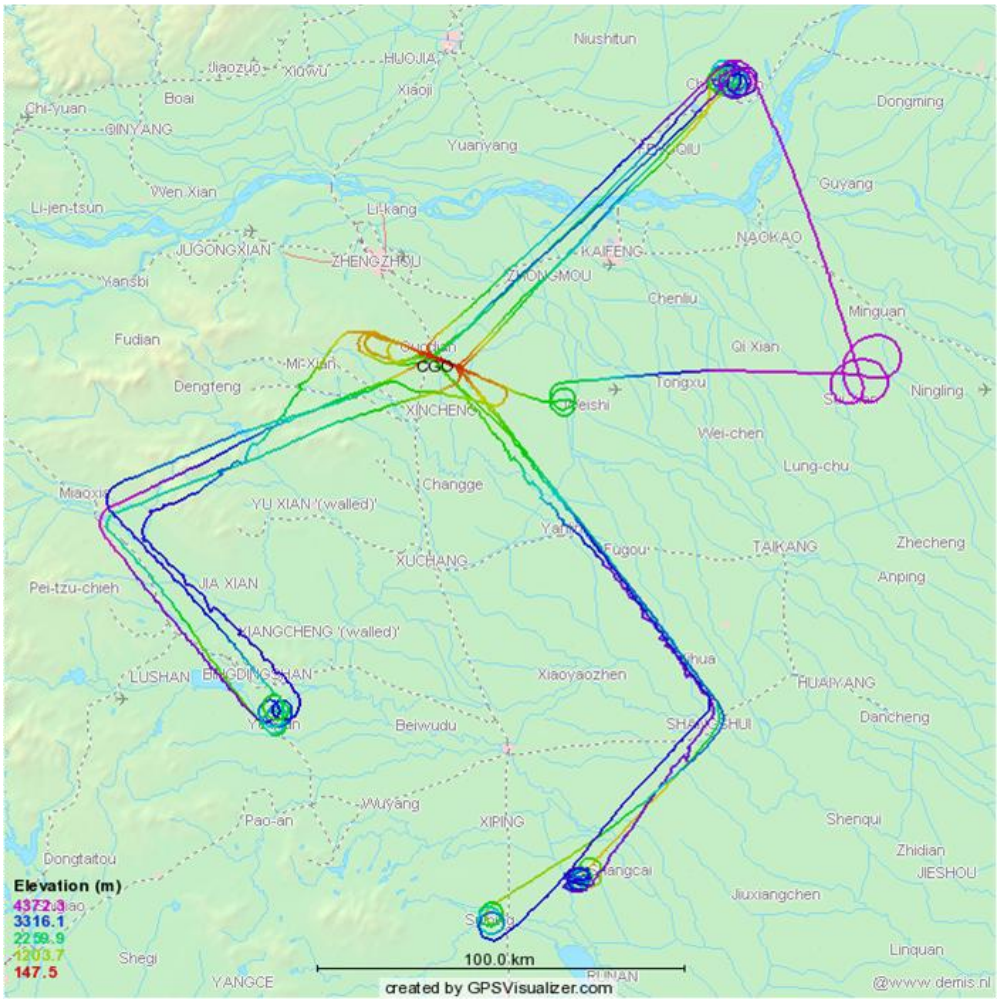

Figure 4.2 Flight routes with altitude for all EAST-AIRC aircraft campaign.

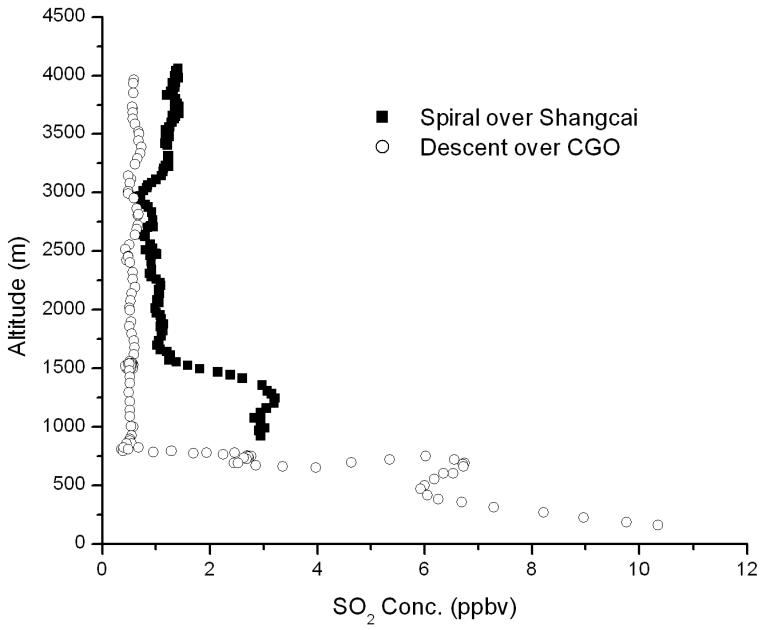

Figure 4.3 SO_2 altitude profiles from research flight on 04/15/2008.

Figure 4.4 shows the summary of all SO_2 measurements observed during this campaign, and the statistical analysis. The mean profile was calculated by averaging every 200 m from the surface to 4500 m. The vertical distribution of ambient SO_2 exhibited large variability, especially between 1000 and 3000 m, above the typical PBL height during spring in central China. The majority of SO_2 was found within the PBL and in the lower atmosphere with an effective scale height of ~800 m, from the surface to ~1800 m. The mean profile also depicts that higher SO_2 concentrations exist within the PBL. Compared with the RAMMPP aircraft observations from 1996 to 2005 in the Mid-Atlantic [*Hains*, 2007], the shape of mean SO_2 altitude profile is similar but the measurements in China

Table 4.2 Summary of ambient SO_2 concentrations observed during research flights.

Flight	Spiral				Descent (over CGO)			
		SO_2 Conc. (ppbv)				SO_2 Conc. (ppbv)		
Date	Altitude (m)	Mean	Stdev*	Median	Altitude (m)	Mean	Stdev	Median
4/4/2008	1000	4.67	0.29	4.67	500	7.16	0.87	7.02
	1500	3.74	0.27	3.84	1000	5.14	3.38	3.13
	2000	2.71	0.34	2.63	1500	1.31	0.33	1.25
	2500	1.72	0.26	1.65	2000	1.00	0.06	1.01
	3000	1.79	0.32	1.81				
	3500	1.23	0.22	1.21				
	4000	0.87	0.06	0.89				
4/5/2008	1000	4.81	0.32	4.93	500	9.48	4.18	8.51
	1500	6.08	0.75	5.94	1000	2.07	1.42	1.29
	2000	7.31	0.13	7.34	1500	0.97	0.52	1.24
	2500	5.96	1.06	6.26	2000	0.20	0.06	0.21
	3000	2.29	0.83	2.00				
	3500	1.50	0.07	1.49				
	4000	1.08	0.16	1.07				
4/15/2008	1000	3.00	0.12	2.95	500	4.99	1.86	6.00
	1500	1.86	0.79	1.58	1000	0.88	0.72	0.52
	2000	1.07	0.04	1.08	1500	0.51	0.05	0.50
	2500	0.91	0.07	0.91	2000	0.54	0.03	0.53
	3000	0.93	0.18	0.92				
	3500	1.28	0.09	1.24				
	4000	1.34	0.05	1.35				
4/16/2008	1500	0.29	0.12	0.31	500	3.62	1.52	4.35
	2000	0.18	0.05	0.19	1000	0.42	0.05	0.41
	2500	0.23	0.03	0.23	1500	0.16	0.23	0.11
	3000	0.21	0.10	0.22	2000	0.15	0.08	0.19
	3500	0.32	0.09	0.35				
4/18/2008	1500	-0.06	0.06	-0.04	500	3.30	0.35	3.40
	2000	-0.08	0.04	-0.07	1000	1.38	1.08	1.63
	2500	-0.11	0.08	-0.10	1500	0.00	0.03	-0.01
	3000	0.04	0.11	0.09	2000	0.03	0.05	0.02
	3500	0.25	0.13	0.19				
4/20/2008	3000	0.98	0.05	0.98	500	4.14	1.71	4.65
	3500	1.08	0.17	1.12	1000	0.29	0.15	0.22
	4000	1.98	0.44	1.79	1500	0.22	0.02	0.21
					2000	0.70	0.31	0.58
4/22/2008	1500	-0.14	0.02	-0.14	500	3.82	0.10	3.83
	2000	-0.11	0.07	-0.06	1000	1.04	1.13	0.41
	2500	-0.14	0.09	-0.19	1500	0.35	0.09	0.38
	3000	-0.09	0.09	-0.04	2000	0.38	0.07	0.36
	3500	-0.03	0.04	-0.03				
	4000	-0.05	0.05	-0.04				

* stdev: standard deviation

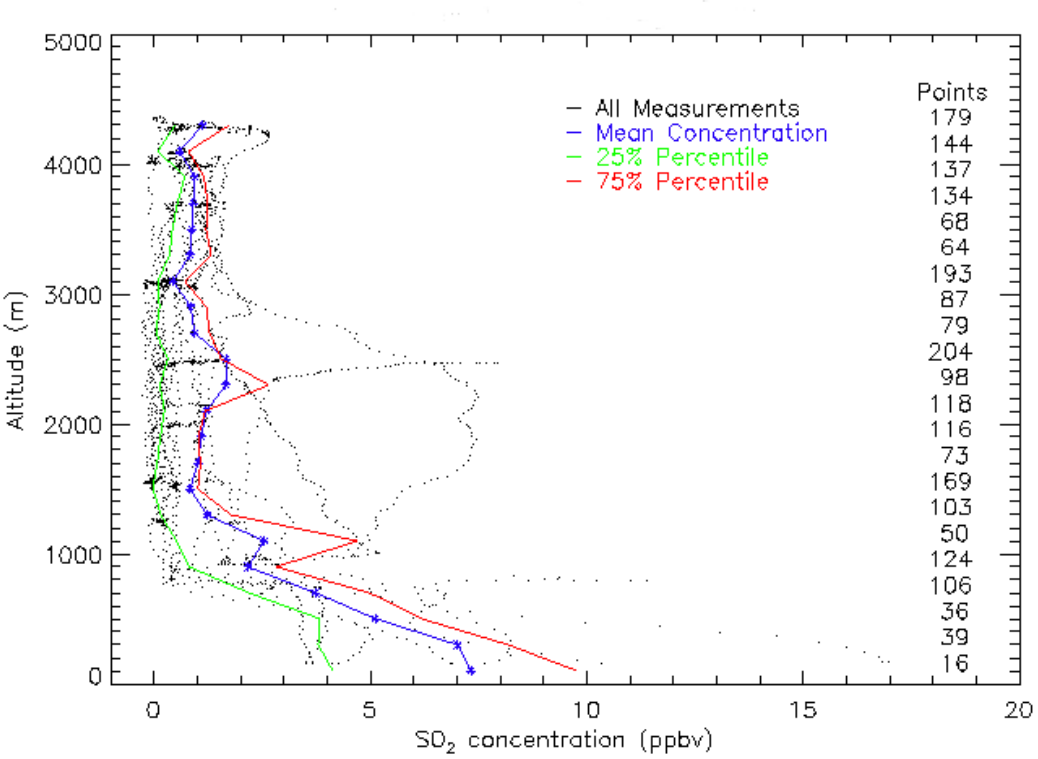

Figure 4.4 *In situ* measurements and the mean SO_2 profiles for the aircraft campaign (Green, Blue, and Red represent the 25th, 50th, and 75th percentile; figures listed on the right depict the number of SO_2 data points within the 200 m layer).

are about 50% higher. It is necessary to point out that the RAMMP flights were mostly conducted during summer time with high SO_2 emissions from power plants related to large electricity demands, while the 2008 EAST-AIRC aircraft campaign occurred in the early spring with low SO_2 emissions from electricity generation facilities. Therefore, the ambient SO_2 loadings during the summer in China are expected to be much higher than depicted in Figure 4.4. On the other hand, ambient SO_2 has longer lifetime in spring due to low concentrations of OH radicals in relatively cool weather, and the long-range transport is predominant.

4.2.2 Isolated SO_2 plumes in the FT

During the EAST-AIRC aircraft campaign, isolated SO_2 plumes were detected frequently in the FT, similar to observations of RAMMPP program in the eastern U.S. [*Hains*, 2007; *Taubman et al.*, 2006]. All of the research flights were performed under calm and stable weather conditions without strong convection, so the SO_2 plumes in the FT were likely related to up wind or large-scale vertical transport. These substantial amounts of SO_2 aloft have profound effects on the long-range transport of sulfur compounds due to relatively strong winds and long lifetime in the FT, exerting great impacts on large-scale air quality and climate. I summarized all the SO_2 plumes observed during the aircraft campaign in Table 4.3. The HYSPLIT model, driven by the Global Data Assimilation System (GDAS) meteorological fields, was employed to calculate the 72-hr back trajectory. Time and height of the observed SO_2 plumes were utilized as release time and release height (plume height ± 500 m). Figure 4.5 illustrates the altitude profile and back trajectory of plume 3, and other plumes are presented in Appendix III.

Table 4.3 Summary of SO_2 plumes observed in the FT.

Plume	Date	Time (UTC)	Location	Conc. (ppbv)	Altitude (m)	Size (km)	RH* (%)
1	4/15/2008	6:05 - 6:13	114.50E, 33.85N	2.0-8.0	2500	30	47
2	4/16/2008	7:00 - 7:07	114.31E, 34.36N	1.3	3700	26	75
3	4/20/2008	3:34 - 3:42	114.70E, 35.26N	2.6	4200	22	90
4	4/20/2008	4:00 - 4:13	115.20E, 34.54N	2.2	4300	18	100
5	4/22/2008	6:53 - 7:03	113.11E, 33.93N	1.6	3700	22	20

*RH: Relative Humidity

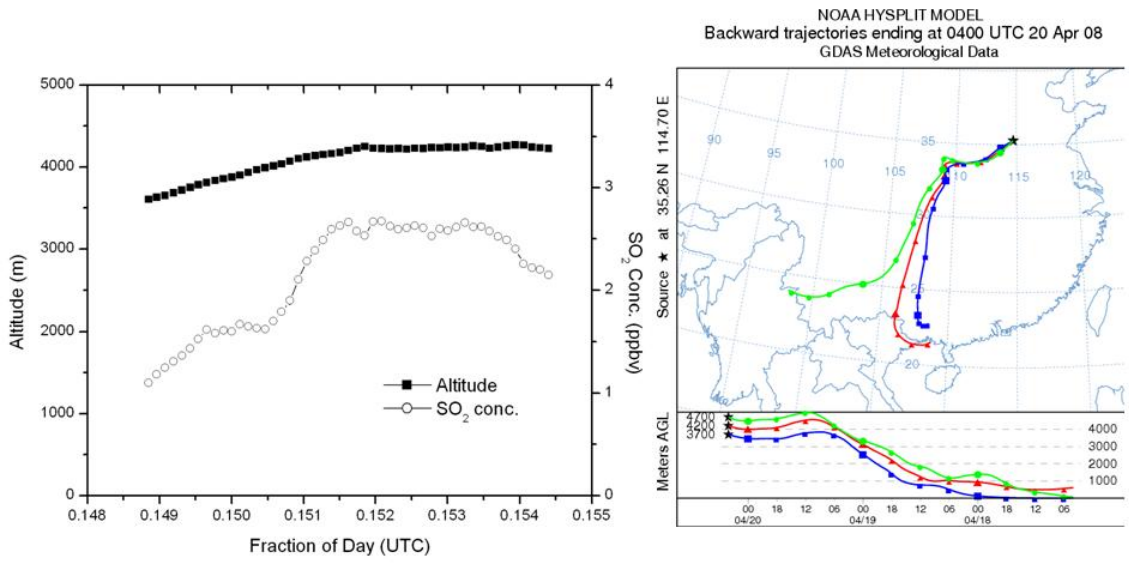

Figure 4.5 Altitude profile and HYSPLIT 72-hr back trajectory of SO_2 plume observed in 04/20/2008.

Plume 1 demonstrates a local stagnation case with air circulating within a radius of ~400 km. The SO_2 concentration is relatively high at 2500 m, ~8 ppb, revealing the substantial vertical mixing of air pollutants. No isentropic lifting was observed for plumes 2, 4, and 5, suggesting sub-grid convection could be important. The back trajectory of plume 3 presents a case of long-range transport with isentropic upward motion from southern China. Within 72 hrs, the air mass was lifted from the surface to 4200 m and transported about 1500 km. Plume 3 had about 2.6 ppb SO_2 and high RH of 90%; the horizontal width and depth are estimated as ~22 km and ~1 km based on GPS data. Assuming the mean SO_2 concentration within the plume as 2 ppbv, I estimated the SO_2 mass as ~1.5 tons. Forward trajectory (Appendix III) of plume 3 illustrates that the SO_2 plume, as well as its oxidation products, will be exported eventually to high altitude. The sulfur pollutants transported to high altitude can contribute to the formation of arctic

haze in the polar region [*Barrie et al.*, 1981; *Kahl et al.*, 1989; *Quinn et al.*, 2007; *Rahn et al.*, 1977; *Shaw*, 1995].

With the limited research flights over central China, the chance of intercepting SO_2 plumes in the FT is much higher. We observed 5 plumes on 7 flights. And these plumes existed in higher altitude (> 2500 m AGL). There are two possible reasons: first, in spring China, strong westerly winds enhance the long-range transport such as the case of plume 3; second, SO_2 emissions in China are in large scale compared with emissions in the U.S. These plumes contribute substantially to the high concentration of SO_2 in the mean altitude profile (Figure 4.4), leading to ~2.0 ppb SO_2 at 2500 m AGL. Future research efforts are needed to better understand the vertical distribution of sulfur pollutants, such as utilizing global chemical transport model simulations [*Lee et al.*, 2011].

4.2.3 Validation of OMI SO_2 products

The OMI SO_2 retrieval has been evaluated based on the EAST-AIRE aircraft campaign results in northeastern China during 2008 [*Krotkov et al.*, 2008], and the EAST-AIRC campaign provided a unique opportunity to revisit the validation processes and test a new algorithm. In the previous section, I found that the near real-time OMI SO_2 products are useful for designing the flight plans, and here I quantitatively evaluate the products. Because OMI provides vertical column estimates of PBL SO_2, the *in situ* SO_2 column contents are necessary for evaluation. The mean center of mass altitudes (CMA) of the EAST-AIRC flights is close to 1200 m, and the ceiling of these research

spirals is about ~4500 m, well into the troposphere. The mean vertical profile also shows substantial amount of SO_2 existing within the PBL, while the lowest altitudes of spirals were restricted to ~900 m AGL, so the information of SO_2 below the spiral is retrieved from the descents over the CGO airport. Because the spiral and descent were not at the same location, this approach generated uncertainties, which will be discussed later. So the integration of SO_2 vertical altitudes represents the vertical column contents of PBL SO_2, which are used to validate the co-located OMI SO_2 products.

Following the comparison approach utilized earlier [*Krotkov et al.*, 2008], the average values of the nearest 30 km radius of spiral locations were compared with the corresponding vertically integrated *in situ* SO_2 columns. The uncertainties of the satellite measurements were estimated as the largest value of the OMI average background noise, i.e., 0.62 DU for 8 pixel mean error for the PBL products [*Krotkov et al.*, 2008], and the standard deviation of the 8 nearest pixels. It is worth noting that this error estimate approach yields an upper limit, because it includes the natural variability of SO_2 spatial distribution as part of the error. The uncertainty of integrated *in situ* SO_2 columns mainly comes from the ambient SO_2 missed below the lowest altitude of spirals, ~900 m. It is reported that this part of SO_2 column usually accounts for 10-30% of the total SO_2 column contents [*Lee et al.*, 2009], which makes the largest contribution to the error budget of aircraft measured total columns. As discussed above, to compensate these missing columns, I used the SO_2 measurements obtained during the landing at the CGO airport in the same flight day. Even though the locations are different; the distance is less than 200 km so a certain degree of correlation of PBL columns between these two locations is expected. I assumed that SO_2 in the lowest part of the atmosphere is

homogeneous with the same value as the mean concentration observed during the descent. Under this assumption, I estimated the upper limit of SO_2 column uncertainty as half of the added partial column.

I compared the SO_2 column estimates using *in situ* measurements and OMISO2 PBL products through linear regression (Figure 1 in Appendix IV). The slope of linear regression is pretty low (*slope = 0.16*), while the correlation is high (*r = 0.84*). It

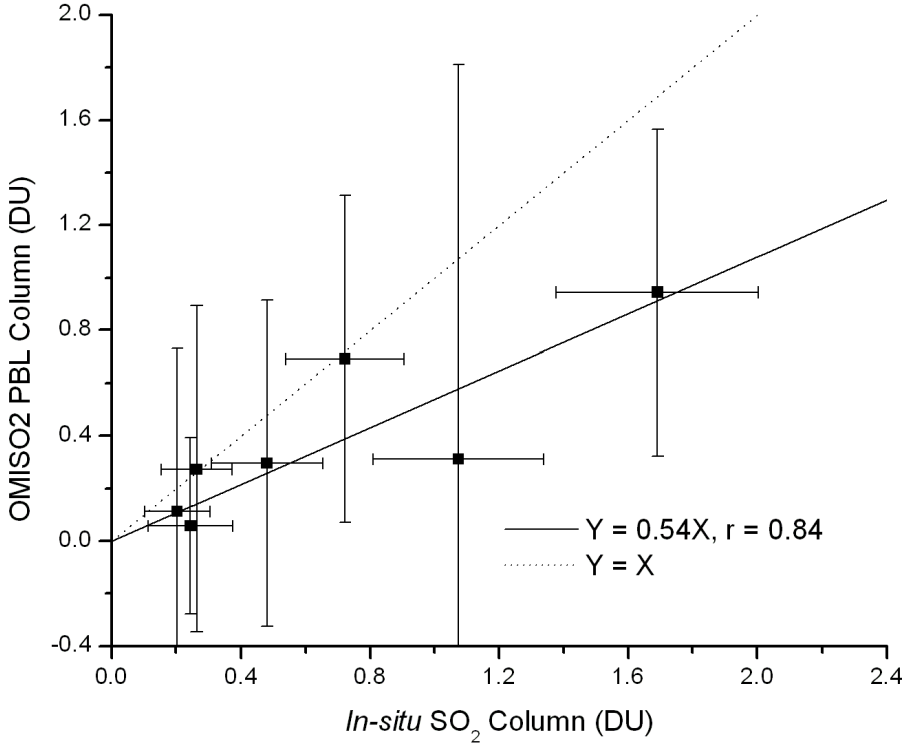

Figure 4.6 Evaluation of *in situ* measurements vs. the modified OMISO2 PBL (+ 0.4 DU) products. The dotted line represents the Y = X line. X and Y error bars describe the uncertainties of aircraft observations and OMI PBL column estimates. Solid line is linear regression passing through zero.

suggests that the OMI data capture the ambient SO_2 column consistently but with a significant underestimate. Fioletov et al. reported that the OMISO2 products have variable biases, which need to be removed or compensated empirically [*Fioletov et al.*, 2011]. Here I added 0.4 DU to all OMISO2 PBL products to keep the data physically meaningful, and re-plot the comparison in Figure 4.6. The comparison shows a strong correlation ($r = 0.84$), which is higher than that obtained from validation studies over the North America, but the slope (slope = 0.54) is still lower than the previously reported in the comparison of improved OMI products during INTEX-A and INTEX-B campaigns [*Lee et al.*, 2009]. In that study, OMI data were post-corrected applying the local air mass factor (AMF) calculated through using monthly SO_2 profiles and aerosols climatology from the global Goddard Earth Observing System chemical transport (GEOS-Chem) model. The correction resulted in typically reduced SO_2 values over oceans, which includes INTEX-A and INTEX-B regions. However, over China the local AMFs [*Lee et al.*, 2009] are close to the operational value ~0.4 [*Krotkov et al.*, 2008], so no local AMF compensation was applied in this study. The OMI PBL products underestimated the tropospheric SO_2 columns by ~50% likely due to: 1) systematic negative biases in OMISO2 PBL values when the satellite field of views were cloud contaminated; 2) reduced satellite measurement sensitivity to SO_2 in the lowest levels due to the presence of aerosols; 3) spatial averaging of local SO_2 plumes over large OMI pixel size. Low visibility (i.e., high tropospheric aerosol loadings) conditions were commonly observed during the aircraft campaign, especially in the morning. Visibility observations (available at www.underground.com) at the CGO airport at 9 am local time from March

28 to April 26, 2008 show that most of flight days had visibility lower than 5 km. OMI has lower sensitivity to the SO_2 close to the surface, compared with SO_2 in the upper atmosphere, and the aircraft measurements illustrate that substantial amount of ambient SO_2 exists in the PBL. Therefore, the presence of heavy aerosol loading above or co-located with the ambient SO_2 further reduce the sensitivity, leading to a substantial underestimate, when the aerosols effects are not accounted for in the operational OMI SO_2 PBL products. Evaluation based on the 2005 EAST-AIRE aircraft campaign found that the local AMFs could be reduced to ~0.2, only half of the operational value, due to dust aerosols [*Krotkov et al.*, 2008]. Similar situation might also exist for the 2008 EAST-AIRC, while no correction of AMFs has been conducted, in which case the OMISO2 PBL products could be doubled to compensate the underestimate of AMFs.

I also compared the integrated SO_2 columns with off-line OMI ISF retrievals in Figure 4.7. The ISF products demonstrate similar correlation ($r = 0.87$) as the OMISO2 PBL products, while less noise and better evaluation (*slope = 0.86*) are noticed. Background noise has not been observed, though the comparison indicates that current ISF retrievals still have low bias with respect to the airborne observations over central China. The underestimates could be caused by the similar reasons discussed above, indicating the importance to improve the ISF algorithm through incorporation of tropospheric aerosol information in future.

To reduce the random uncertainties of OMISO2 PBL products, a good strategy is averaging the noisy daily SO_2 measurements over long time and large area. I selected the campaign area and calculated the monthly average SO_2 column, which is 0.63 ± 0.26 DU. In April 2008, the monthly mean daily average temperature in Zhengzhou is 16.0 ± 5.0

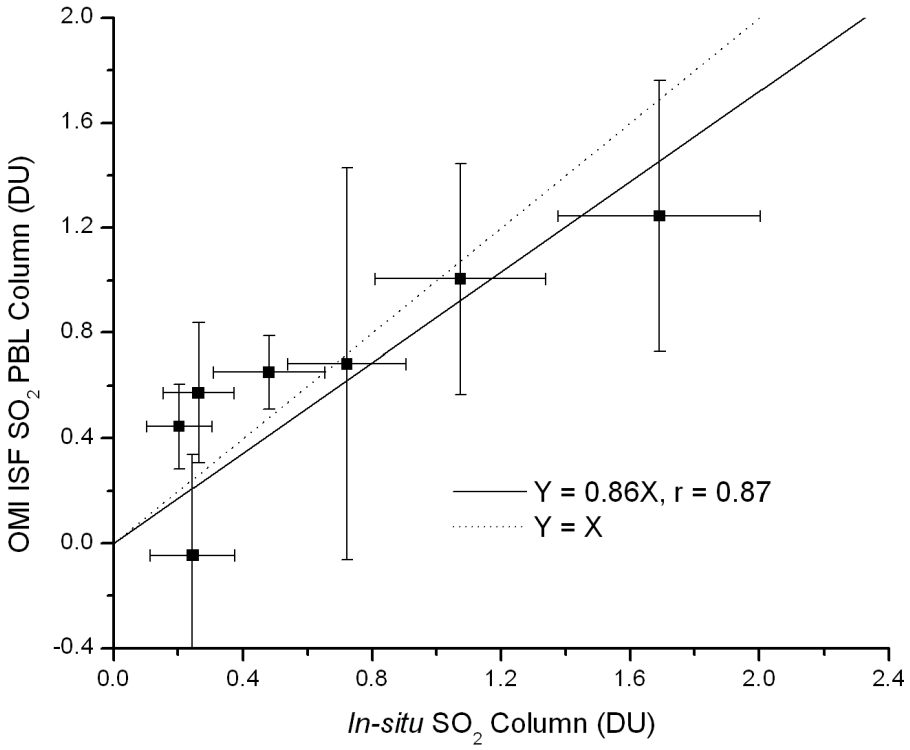

Figure 4.7 Evaluation of *in situ* measurements vs. the off-line OMI ISF SO_2 products. The dotted line represents the Y = X line. X and Y error bars describe the uncertainties of aircraft observations and OMI column estimates. Solid line is linear regression passing through zero.

℃ (data from www.wunderground.com), relatively stable. It is reasonable to assume that the sulfur emissions from coal burnings for electricity generation, domestic heating, and cooking did not change dramatically during the campaign, so the integrated column content from mean SO_2 altitude profile (Figure 4.4) may be considered to represent the monthly mean tropospheric SO_2 loading over the campaign area, with the value of 0.73 DU. Therefore, the monthly mean OMISO2 PBL column is ~15% lower than the monthly mean SO_2 loading from aircraft measurements. This underestimation is much

lower than the validation over several scattered observations (Figure 4.6), suggesting that after averaging over a month and a large region, the operational OMISO2 PBL products can capture the tropospheric SO_2 column contents better than for isolated measurements in individual days.

4.3 Summary of the 2008 EAST-AIRC aircraft campaign

The aircraft campaign during spring 2008 provided a unique opportunity to study the tropospheric SO_2 in the lower atmosphere over central China. Research flights were confined within Henan province, where large amount of anthropogenic sulfur emissions exists. The near real-time OMI SO_2 products were employed to design the flight plans. Research spirals started from ~900 m to 4500 m AGL, and the information of SO_2 within the PBL was retrieved from the descent on the same flight data over the CGO airport. During the research flights, I frequently observed the isolated SO_2 plumes in the FT, and the HYSPLIT back trajectory calculation showed the case of rapid long-range transport. The mean SO_2 vertical profile also demonstrated the existence of substantial SO_2 between 2500 m and 3000 m AGL. The monthly mean SO_2 loading is estimated using the mean SO_2 altitude profile, with the value of 0.73 DU.

For safety concerns, the lowest altitude of research flights was restricted to ~900 m AGL, which can not provide the information of vertical SO_2 in the PBL. To compensate for the missing port of tropospheric SO_2, I utilized the SO_2 measurement during the descent in the same day to the CGO airport. Integration of this modified SO_2

vertical profiles results in the tropospheric SO_2 column content, with half of added SO_2 column as uncertainty. Scattered *in situ* measurements were compared with co-located OMI SO_2 products. The OMISO2 PBL products demonstrate good correlation but significant underestimation, revealing the existence of systematic low biases. I added 0.4 DU to the satellite observations, to make these measurements physically meaningful. The improved OMISO2 products show better performance, but still have substantially underestimation, ~50%. A new OMI SO_2 retrieval, ISF algorithm, was produced off-line for this campaign. ISF products show good correlation and ~15% underestimation, with respect to the aircraft measurements. With further improvements, the ISF algorithm will replace the operational BRD algorithm, and be used to produce operational OMI SO_2 products. Therefore, better performance is expected after the ISF algorithm is implemented. To reduce the daily noise of OMISO2 products, I averaged the data over the campaign area for April 2008. The monthly mean OMISO2 PBL column is close to the mean SO_2 column obtained from airborne observations, suggesting averaging over large area and long time is necessary to apply the OMISO2 retrievals. The discrepancies between the *in situ* measurements and remotely sensed products, both operational OMISO2 and operational ISF products, show the importance to improve the retrieval algorithm for China, where high loadings of atmospheric aerosols are located.

Chapter 5. Export and lifetime of SO_2 over central China

5.1 Introduction

As discussed in section 1, tropospheric SO_2 and its oxidation products, such as sulfuric acid and sulfate aerosols, pose hazards to both environment and public health [*Anderson*, 2009; *Peled*, 2011; *Seinfeld*, 2004]. For instance, ~30% of the SO_2 can be removed directly from the atmosphere through dry deposition [*Wesely and Hicks*, 2000], and sulfuric acid accounts for the major part of aqueous acid deposition in the form of acid rain and acid fog [*Wayne*, 2000]. The deposition of these sulfur compounds contributes to the acidification of soil and water. Sulfate aerosols can cause visibility impairment [*Hand and Malm*, 2007; *Watson*, 2002], hazards to human health [*EPA*, 2004; *Schlesinger and Cassee*, 2003], and change the global radiative balance [*Haywood and Boucher*, 2000; *IPCC*, 2007; *Stier et al.*, 2007]. Because SO_2 has a lifetime in days [*Berglen et al.*, 2004; *Chin et al.*, 1996; *Koch et al.*, 1999; *Pham et al.*, 1995], inter- and intra- continent long-range transport from Asia is observed [*DeBell et al.*, 2004; *Igarashi et al.*, 2006; *Jaffe et al.*, 1999; *Kim et al.*, 2001; *Tu et al.*, 2004]. The lifetime of sulfate aerosols is about 7 days, so these sulfur compounds can travel longer range, like lifted by the Asian dust storms [*DeBell et al.*, 2004; *Husar et al.*, 2001; *Shen et al.*, 2007; *Tsai and Chen*, 2006]. Numerical models have been developed and applied to investigate the chemistry and transport of sulfur compounds [*Chin et al.*, 2000a; *Chin et al.*, 2000b; *Feichter et al.*, 1996; *Langner and Rodhe*, 1991; *Pham et al.*, 1995], but uncertainties

with respect to observations were found [*Barrie et al.*, 2001; *Haerter et al.*, 2009; *Lohmann and Feichter*, 2005].

In this study, I applied the WRF-CMAQ model system to simulate the SO_2 chemistry for the EAST-AIRC campaign. Previous studies demonstrated the capability of studying sulfur chemistry in eastern Asia through CMAQ simulations [*Lin et al.*, 2008a; *Liu et al.*, 2010a; *Liu et al.*, 2010b; *Wang et al.*, 2010a; b]. The latest NASA INTEX-B emission inventory is utilized to provide emission input data for CMAQ. Modifications on the CMAQ model system have been conducted to investigate the SO_2 sinks and transport. This chapter is organized as following: first, the CMAQ model simulations are described in section 5.2, including model set-up, manipulation of emissions, model modifications, conclusions, and discussion on SO_2 chemistry; then I utilize the OMISO2 PBL products to evaluate the model performance in a large area, over central and eastern China, in section 5.3. This comprehensive study of SO_2 and sulfur compounds through combination of aircraft measurements, satellite retrievals, and numerical simulations provides the capability to evaluate the SO_2 concentrations and chemistry for the 2008 EAST-ARIC aircraft campaign.

5.2 CMAQ model simulations

5.2.1 Model set-up

In this study, I used the WRF V3.1 model [*NCAR*, 2010] to generate meteorological fields for the CMAQ model. Figure 5.1 presents the WRF domains in a Lambert projection. The coarse domain (30 km grid cells) covers the central and eastern part of China, where most of the population and industry are located; the nested domain (10 km grid cells) focuses on the aircraft campaign region. The U.S. Geological Survey (USGS) 24-category data were used to determine the terrain and land use. I used the National Center for Environment Prediction (NCEP) Final Operational Model Global Tropospheric Analyses (FNL) (http://dss.ucar.edu/datasets/ds083.2) as initial and boundary conditions. The NCEP FNL data are on 1 °× 1 °grids with 26 vertical levels

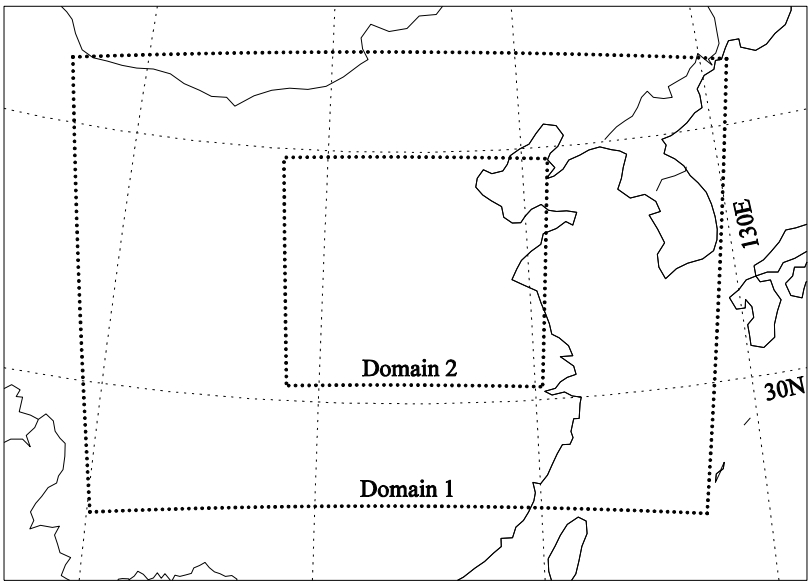

Figure 5.1 Domains of the WRF simulations. Both the coarse and nested domains are centered at Zhengzhou city (34.8 °N, 113.7 °E). The coarse domain (Domain 1) has 97 × 67 grids and 30 km horizontal resolution, and the nested domain (Domain 2) has 117 × 102 grids and 10 km horizontal resolution. The CMAQ domains are 2 grid cells smaller on each side of the WRF domains to eliminate lateral effects.

from 1000 to 10 hPa with a time step of 6 hours. The major physics options applied in the WRF simulation included Thompson microphysics scheme [*Thompson et al.,* 2006], YSU boundary-layer scheme [*Hong and Lim,* 2006], Kain-Fritsch (new Eta) cumulus scheme [*Kain*, 2004], and Noah land-surface scheme [*Ek et al.*, 2003]. The model was run with 35 vertical layers from the surface to 50 hPa with the first 12 layers in the PBL, and re-initialized every 5 d to reduce simulation errors. Hourly WRF output data were stored in the IOAPI/netCDF format, which contained fields such as U/V/W winds, surface pressure, skin temperature, cloud vapor mixing ratio and so on [*NCAR*, 2010]. More details of the CMAQ simulations are discussed in Appendix V.

MCIP model V3.5 was applied to convert the WRF outputs to CMAQ-ready IOAPI format data [*Byun and Ching*, 1999], which contains the necessary meteorological and chemical parameters for CMAQ simulations. For instance, the MCIP model also provides important meteorological parameters such as PBL height and soil temperature [*Byun et al.*, 2007]; deposition velocities (both dry and wet deposition) of chemical species such as CO and SO_2 are calculated in the MCIP model, which affects the dry deposition calculations in CMAQ. In this study, the MCIP model has been modified to correct the calculation of SO_2 dry deposition velocity, and the details will be discussed later.

CMAQ V4.6 (released in September 2006) [*Byun and Schere*, 2006] was utilized to conduct a 45-d simulation from 03/13/2008 to 04/26/2008, with the first 15 days as spin-up. CMAQ was run with a coarse and nested domain with the same horizontal and vertical resolutions as the WRF simulation. Chemical initial conditions for the coarse domain were obtained from Regional Acid Deposition Model version 2 (RADM2)

concentration profiles [*CMAS*, 2007; *Stockwell et al.*, 1990]. The Statewide Air Pollution Research Center-99 (SAPRC-99) scheme and the 4th generation aerosol scheme (AE4) were selected as the gas-chemistry mechanism and aerosol modules respectively. The Regional Acid Deposition Model (RADM) based cloud processor with the asymmetric convection model (ACM) was used for the aqueous/cloud chemical mechanism. For the calculation of horizontal advections, CMAQ employed the Yamartino (HYAMO) in the default setting. In this study, to compute the horizontal advection of air pollutants, the new Piecewise Parabolic Method (HPPM) scheme was applied. The effects of this modification will be discussed later. The CMAQ output files including hourly 3-D fields of gaseous and aerosol species concentrations were stored for further analyses.

5.2.2. Manipulation of emission input data

Emission data for eastern Asia, the NASA INTEX-B emission inventory [*Zhang et al.*, 2009b], were utilized to provide emission fields for the CMAQ model, although there is evidence that emissions of China have decreased between 2006 and 2008 [*Witte et al.*, 2009]. The INTEX-B emission inventory (data available at the website http://mic.greensource.cn/intex-b2006) is based on the study of anthropogenic emissions in 2006, including major pollutants (SO_2, NO_x, CO, PM_{10}, $PM_{2.5}$, BC, and OC) and 30 lumped VOC species for SAPRC-99 chemical mechanism with a resolution of $0.5° \times 0.5°$. Compared with USEPA's National Emission Inventory (NEI) database, INTEX-B only contains estimates in format of area emissions, lacking point sources, mobile sources, and other geographic information. Therefore, emission processing software such as the

Sparse Matrix Operator Kernel Emission (SMOKE) can not be applied to create the 3-D emission input data for CMAQ. I developed an approach to create the emission input data through the following steps:

1) As supplement to INTEX-B, I incorporated the 2008 NH_3 emission prediction from the Regional Emission Inventory in Asia (REAS) program (data available at http://www.jamstec.go.jp/frsgc/research/d4/emission.htm). The REAS emission inventory was developed by the Atmospheric Composition Research Program (ACRP) at Frontier Research Center for Global Change. REAS emission data have the same horizontal resolution ($0.5° \times 0.5°$) as INTEX-B.

2) INTEX-B emission inventory has each pollutant calculated individually for four sectors: Electricity Generation, Industry, Residential Emission, and Transportation. I allocated them into two groups, Electricity Generation and Others. Since stack parameters such as plume exit velocity and plume exit temperature were not available, emissions from the Electricity Generation were located ~200 m above the surface as an approximation of average stack height and plume rise.

3) Allocate the emission data of NO_x and $PM_{2.5}$ into NO_2, NO, sulfate and nitrate aerosols to accommodate the SAPRC-9 chemical mechanism. The manipulation of the speciation approach is summarized in Table 5.1 (based on personal communication with the P.I. of INTEX-B emission inventory, Dr. Qiang Zhang qiangzhang@tsinghua.edu.cn).

4) The yearly emission values from the INTEX-B emission inventory were averaged into hourly values arithmetically. Then the hourly data were allocated into the CMAQ grid

cells through bilinear interpolation, creating a 3-D emission input data with constant values for all chemical species.

Table 5.1 Speciation of INTEX-B emission data for SAPRC-99 chemical mechanism.

INTEX-B SPECIES	SAPRC-99 category	Conversion factor
Black Carbon (BC)	Particlulate Element Carbon (PEC)	*[BC] = [PEC]*
Carbon Monoxide (CO)	Carbon Monoxide (CO)	*[CO] = [CO]*
Nitrogen Oxides (NO_x)	Nitrogen Dioxide (NO_2)	*$[NO_2] = 0.05[NO_x]$*
	Nitric Oxide (NO)	*$[NO] = 0.95[NO_x]$*
Sulfur Dioxide (SO_2)	Sulfur Dioxide (SO_2)	*$[SO_2] = [SO_2]$*
Organic Carbon (OC)	Particulate Organic Aerosol (POA)	*[POA] = 1.2[OC]*
Particulate Matter (PM_{10})	Coarse Particulate Matter (PMC)	*$[PM_{10}] = [PMC]$*
Particulate Matter ($PM_{2.5}$)	Fine Particulate Matter (PMFINE)	*$[PMFINE] = [PM_{2.5}] - [BC] - [OC] - [PSO_4] - [PNO_3]$*
	Sulfate Aerosol (PSO_4)	*$[PSO_4] = 0.119[PM_{2.5,industry}] + 0.0187[PM_{2.5,transportation}]$*
	Nitrate Aerosol (PNO_3)	*$[PNO_3]=0.00395[PM_{2.5,transportation}]$*

The INTEX-B emission inventory estimated total emission of SO_2 for China was 31.0 Tg per year with ±12% reported uncertainty, and the arithmetical mean daily SO_2 emission was 84.9 kT. This value is close to 84.8 kT and 78.9 kT from the arithmetic mean from March and April emissions, respectively [*Zhang et al.*, 2009b]. These values implied that the seasonality of SO_2 emissions was small during spring in China. The diurnal cycle of emissions is ignored by assuming constant emission rates since there was no available information on diurnal variation. For demonstration, I present the resulting SO_2 emission maps (Figure 5.2). These maps correspond well to the locations of cities, populations and industrial centers in China such as YRD region, and spatial accuracy is

crucial to CMAQ simulations. The spatial distribution of other air pollutants is presented in Figure 5.3. Large CO and NO_x emissions are observed in Beijing area and YRD region; large aerosols emissions exist in eastern China and Sichuan basin.

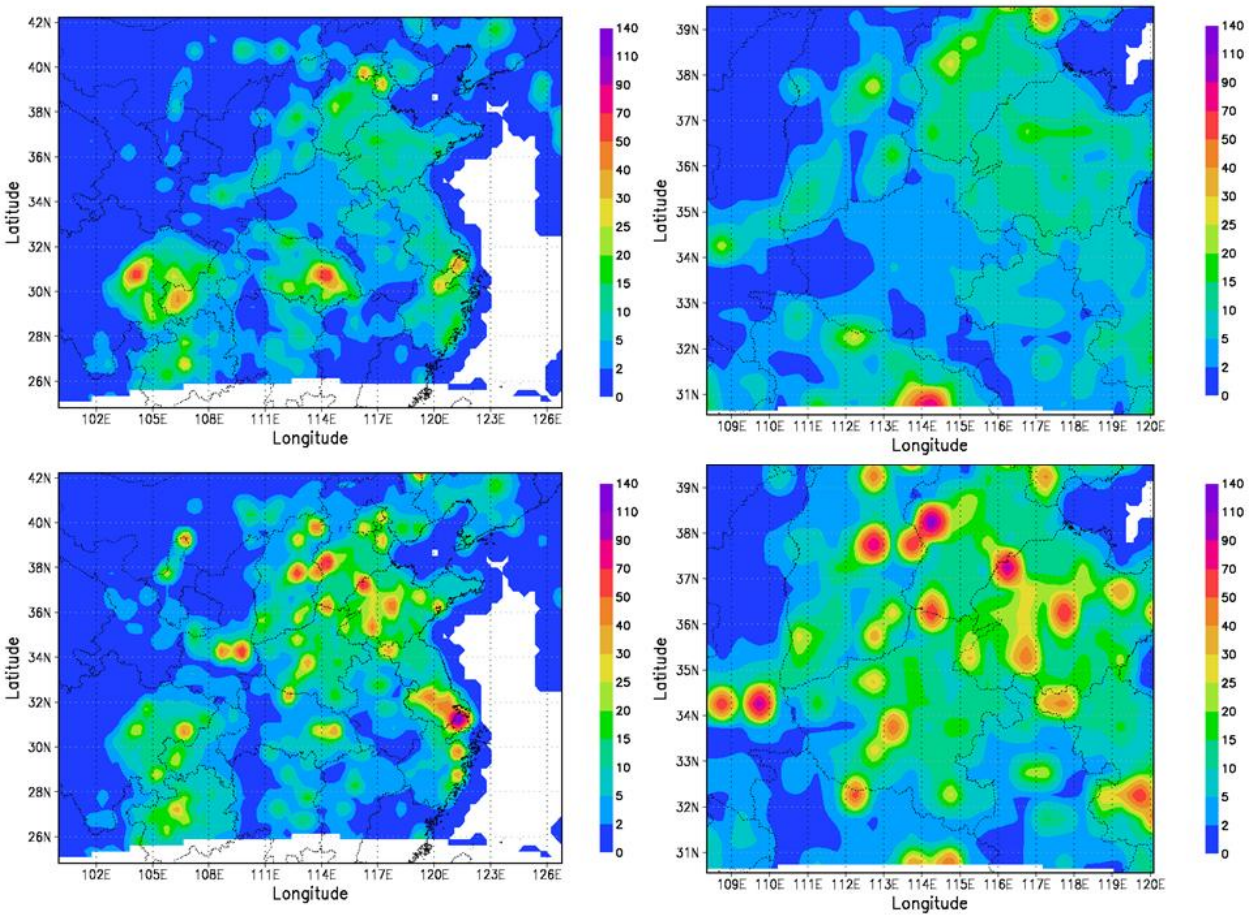

Figure 5.2 Emission maps of SO_2 for CMAQ simulations (Unit: mole/km^2 day). The left/right column demonstrates the SO_2 emission map for coarse/nested domain, and the upper/lower row presents the emission from Other (Industry, Residential and Transportation)/Power Sector respectively.

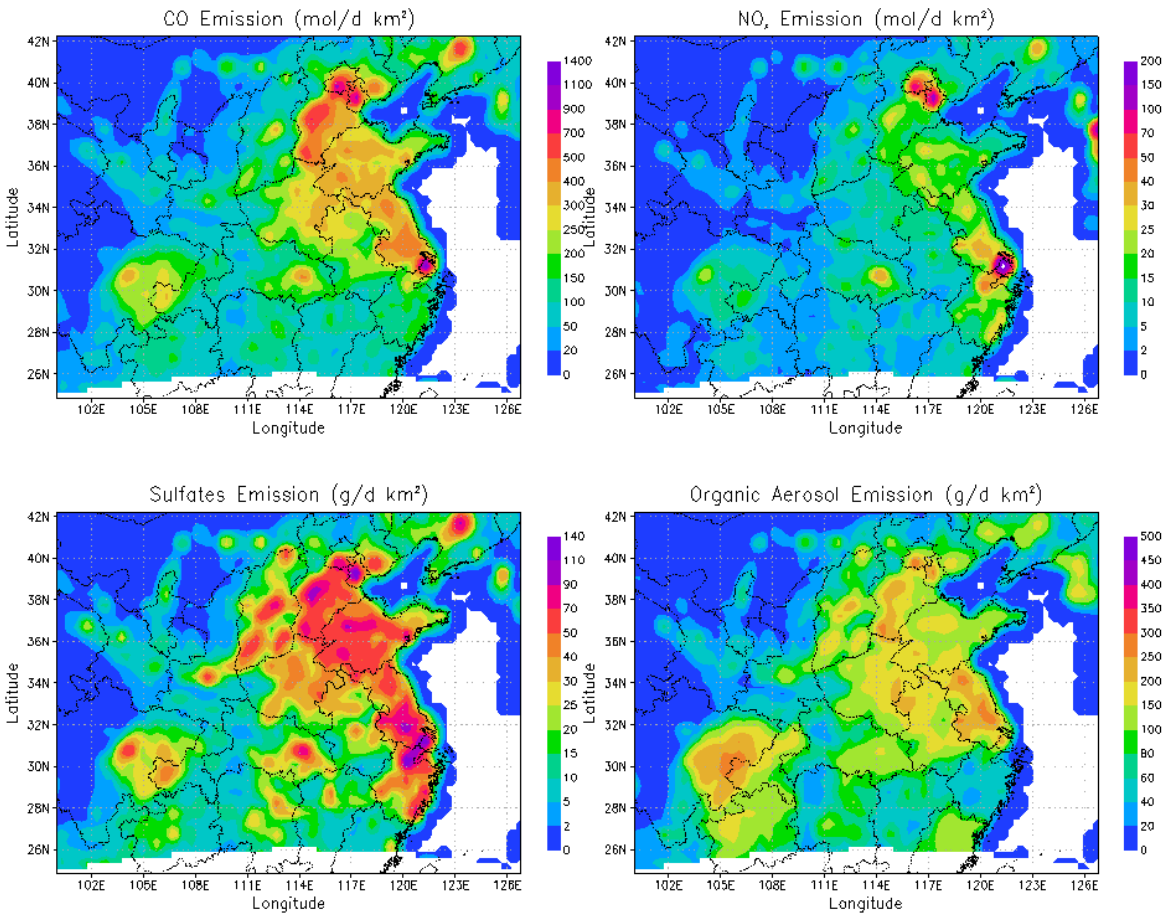

Figure 5.3 Emission maps of CO, NO_x, sulfate aerosols, organic aerosol emissions in the coarse domain (Unit mol/d km^2 for trace gases, and g/d km^2 for aerosols). Large sulfate and organic aerosol emissions are observed in the east coast and Sichuan basin (centered around 30 ℃N and 106 ℃E).

5.2.3 Model modifications and sensitivity runs

MCIP version 3.5 was applied to ingest the WRF output and create meteorological input files for the CMAQ model. For better performance, MCIP was modified to write out the percentage of each WRF grid cell that is urban, and new urban fraction variable was used to calculate vertical diffusion in CMAQ [*Castellanos*, 2009]. The SO_2 dry deposition velocity was computed in the MCIP program. In the default

MCIP setting, the mean SO_2 dry deposition velocity ($\pm\sigma$) was 0.58 ± 0.07 cm/s over the campaign area, which is substantially higher than 0.2-0.4 cm/s measured over northern China [*Sorimachi et al.*, 2003; *Sorimachi and Sakamoto*, 2007] and other areas [*Clarke et al.*, 1997]. Details of the analysis are summarized in Appendix VI. To correct the simulated dry deposition rate, I changed the mesophyll resistance of SO_2 from 0 (default value) to 8000 s/m [*Pfanz et al.*, 1987] in the MCIP model. Similar modification decreased the CO dry deposition velocity from ~0.4 cm/s to ~0.1 cm/s [*Castellanos et al.*, 2011].

To investigate the transport of S (sulfur) and sulfur budget, the CMAQ model was modified to calculate the horizontal advection of air pollutants. I changed the horizontal advection scheme in CMAQ from the HYAMO scheme to the HPPM scheme [*Loughner*, 2011; *Loughner et al.*, 2011], which enable tracking the pollutants transported entering and leaving the model domains. This improvement allowed pollutant fluxes, deposition, and emissions to be studied collectively, which enabled the quantification of sulfur budget and export. With the modifications of both MCIP and CMAQ, I conducted three sensitivity runs to study their influences: 1) default mesophyll resistentance (MR), and the HYAMO advection scheme; 2) default MR and the HPPM scheme; 3) updated MR and the HPPM scheme. They are named as NoMR_HYAMO, NoMR_HPPM, and MR_HPPM in this study respectively.

To isolate effects of modifying SO_2 mesophyll resistance, the difference between results from NoMR_HPPM and MR_HPPM was calculated. I selected data over the campaign area (mostly grassy plain with good vegetation coverage), on days with calm weather and no precipitation to minimize the effects of SO_2 wet deposition. The monthly

average dry deposition velocity (±σ) of the MR_HPPM run is 0.24 ± 0.06 cm/s, ~60% lower than the NoMR_HPPM run with the value of 0.58 ± 0.07 cm/s. I also investigated the SO_2 dry deposition flux, which is calculated in the CMAQ model. The monthly mean value (± σ) decreased from 0.093 ± 0.039 μg/m^2 s with NoMR_HPPM to 0.045 ± 0.031 μg/m^2 s with MR_HPPM, a 52% reduction. Discussion on the SO_2 dry deposition rate is included in Appendix VI. The MR_HPPM value is around 50% less than a lab experiment conducted in northern China, but the SO_2 dry deposition process is influenced by other factors such as soil type and meteorological conditions [*Sorimachi and Sakamoto*, 2007]. These results show that a better parameterization of SO_2 dry deposition is needed for future development of the CMAQ model. Hereafter in the following sections, we use results from MR_HPPM run and discuss the details of the three sensitivity runs in section 5.2.4.

5.2.4 Preliminary CMAQ outputs

CMAQ maps of selected pollutants (O_3, CO, SO_2 and sulfate) are presented with daily average surface value (Figure 5.4) in 04/18/2008. The locations of hot spots of pollutants agreed well with the major megacities such as Beijing area and YRD region. When zooming-in to the nested domain, more details of the pollutant distribution are revealed (Figure 5.5). The comparison between Figure 5.4 and Figure 5.5 reveals that the aircraft campaign area has moderate pollution with respect to other hot spots in China. The vertical distribution of these air pollutants is presented in Figure 5.6 from surface to the 50 hPa (~20 km AGL). These model profiles suggest that the majority of air

pollutants are concentrated in the lower troposphere (below 5 km). For instance, as primary pollutants, both CO and SO_2 concentrations are related to surface sources; quasi exponential decay is observed within the PBL (below 2 km), and relatively low concentrations are observed in the FT (above 2 km).

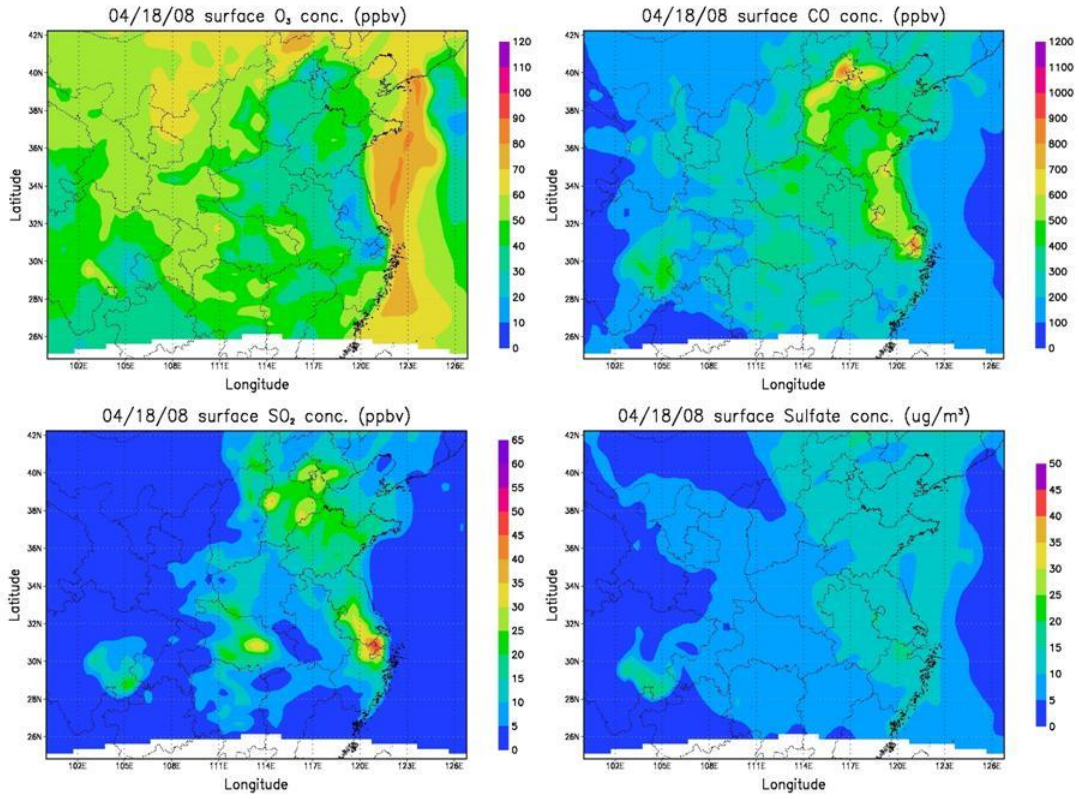

Figure 5.4 CMAQ daily maps of major air pollutants (O_3, CO, SO_2, and sulfate aerosols) of coarse domain in 04/18/2008.

The local air quality monitor network of Henan Meteorological Bureau (http://www.hnqx.cn/yubaoyujing/kongqiwuran/) supported daily measurements of ambient SO_2 and NO_2 in Zhengzhou. To evaluate the numerical simulation, I present the

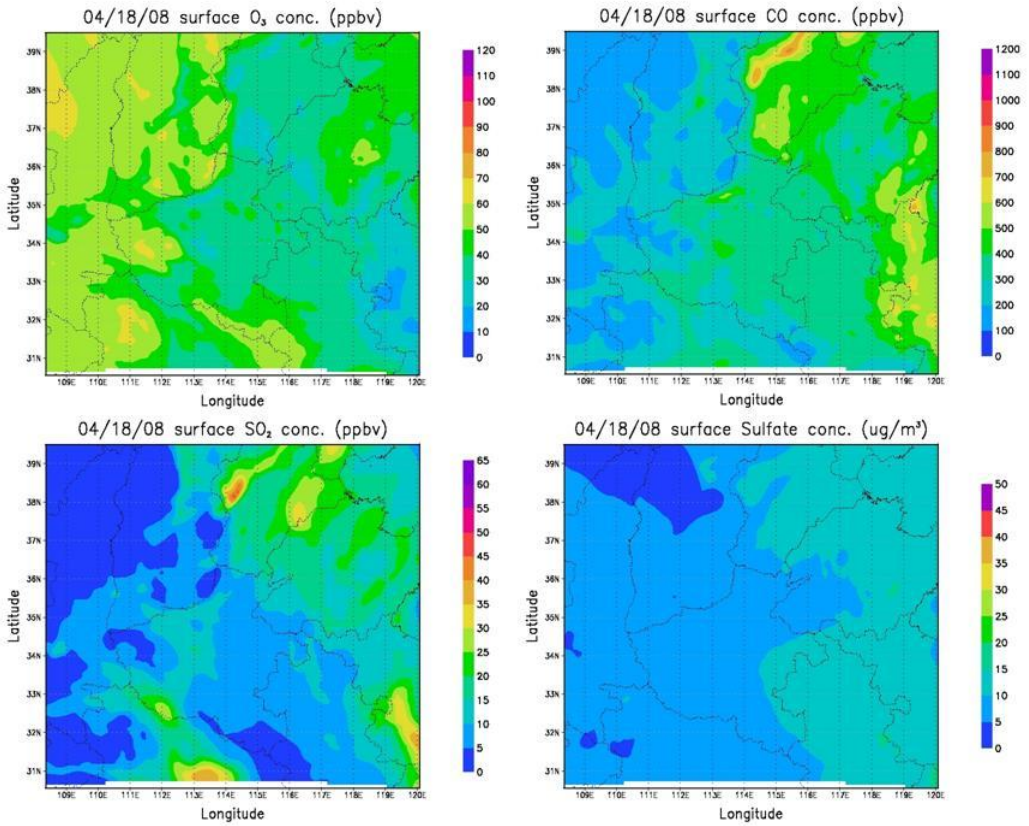

Figure 5.5 CMAQ daily maps of major air pollutants (O_3, CO, SO_2, and sulfate aerosols) of nested domain in 04/18/2008.

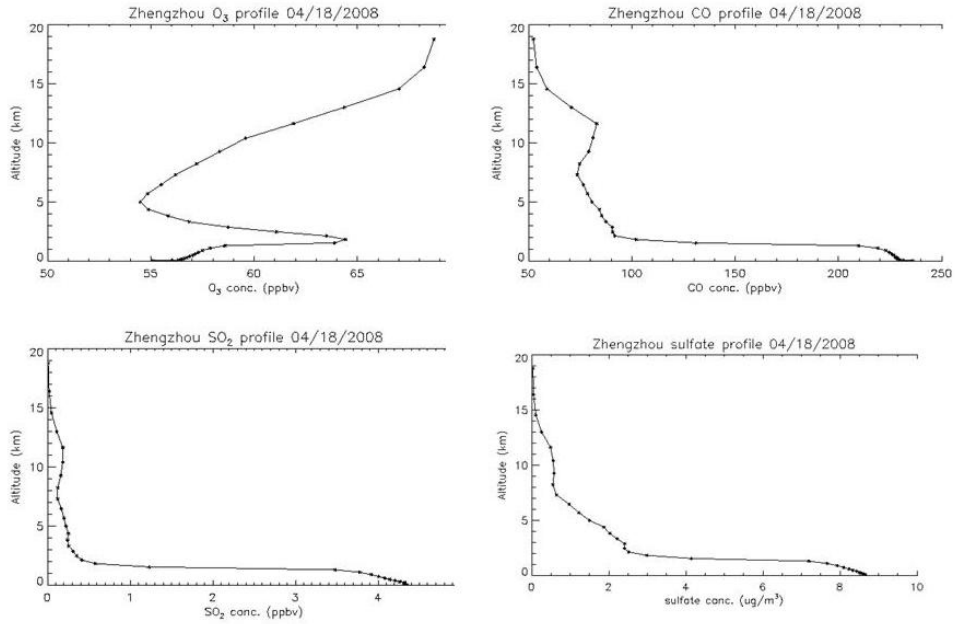

Figure 5.6 Vertical distributions of major air pollutants (O_3, CO, SO_2, and sulfate aerosols) over Zhengzhou in 2 pm (local time), 04/18/2008.

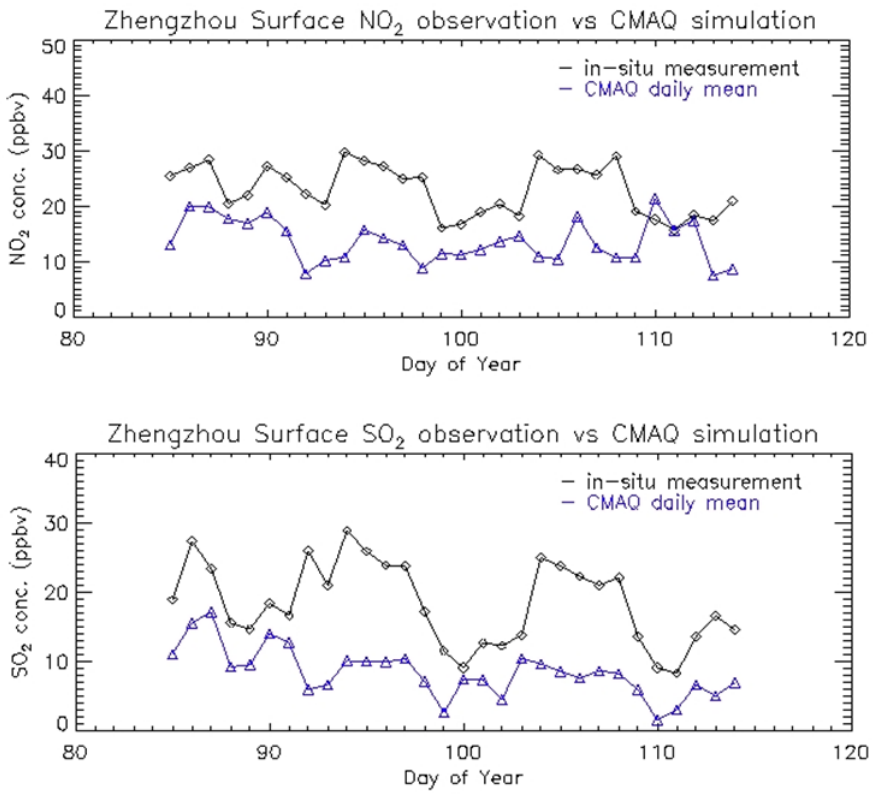

Figure 5.7 Daily NO_2 and SO_2 data from *in situ* measurements and CMAQ simulations.

comparison in Figure 5.7. Daily fluctuations of SO_2 and NO_2 in these 30 days were captured well by CMAQ, but CMAQ underestimated the value of both SO_2 and NO_2 by 30-50%. The HMB observation sites were located in the urban area of this megacity, so the measurements were greatly influenced by the surrounding local point sources while the INTEX-B emission inventory only has area source emission data to drive CMAQ.

In summary, the WRF-CMAQ system is successfully set up and numerical simulations have been conducted. The WRF simulations demonstrate the ability to precisely reproduce the meteorology to feed the chemical transport model (Appendix V). CMAQ provides 4D information about the spatial and temporal distributions of air pollutants. The nested domain, focused area of the EAST-AIRC aircraft campaign, is

observed with moderate loading of critical air pollutants. Vertical distributions suggest the majority of air pollutants existing in the PBL. Numerical simulations with high resolution (1 hour interval in 10 km grid cell), are essential to the evaluation of aircraft measurements and satellite observations.

5.2.5 Evaluation of CMAQ simulations with EAST-AIRC aircraft measurements

I compared two days' flight data with the CMAQ results, and found that the SO_2 profiles were not precisely simulated especially within the PBL (Figure 5.8). We also checked CMAQ simulations for the FT SO_2 plumes discussed in Table 4.3, and the model did not reproduce these plumes well. This implies that CMAQ (with 10 km resolution) had difficulty reproducing the vertical SO_2 altitude profiles at specific times and locations. Other studies have shown that CMAQ has similar problems with vertical profiles of trace gases over the eastern U.S. [*Castellanos et al.*, 2011; *Lee et al.*, 2011]. These issues were probably due to sub-grid scale convective lifting, and the model resolution of 10 km was apparently inadequate to simulate the vertical mixing [*Loughner et al.*, 2011].

Other sources of uncertainty include the precision of winds. Due to limited resource, we did not use Four-Dimensional Data Assimilation (FDDA) in WRF simulations. Without FDDA, wind errors were expected resulting in uncertainty of CMAQ simulations [*Otte*, 2008]. SO_2 emissions from power plants were estimated at 200 m AGL, however these plumes could rise to several hundred meters under certain weather conditions. Therefore, we focused on comparisons of SO_2 column contents of

each research flight to the corresponding SO_2 columns from CMAQ simulations in Figure 5.9. The CMAQ simulations had a moderately strong correlation (r = 0.62) with the

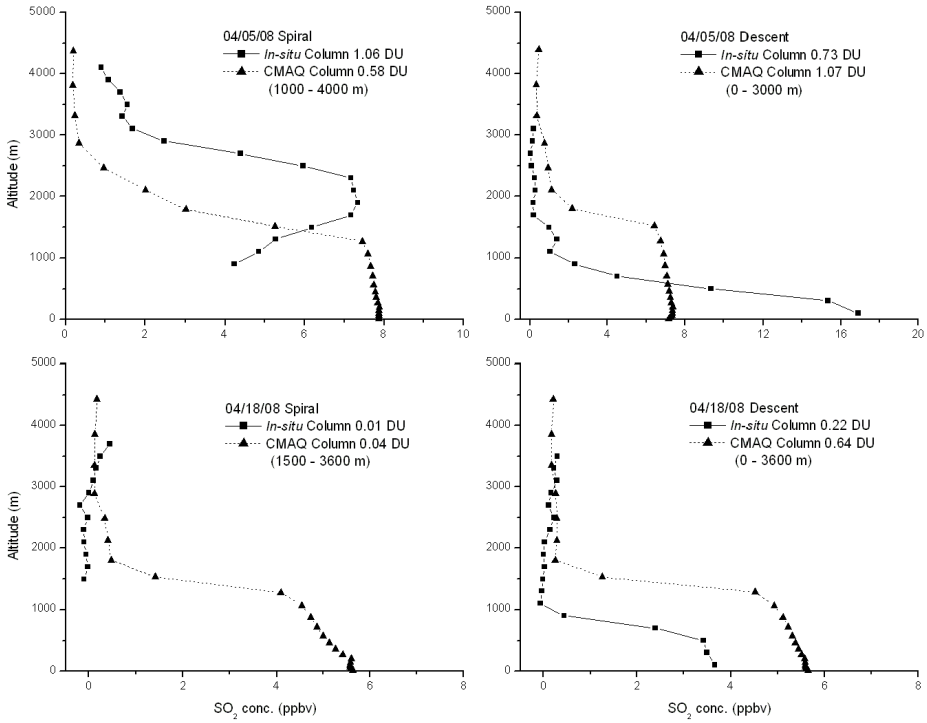

Figure 5.8 Comparison of aircraft observations and CMAQ simulations. The *in situ* measurements are calculated by averaging the aircraft SO_2 altitude profiles every 200 m from surface to 4500 m. The CMAQ SO_2 column contents are computed by integrating SO_2 in the same altitudes as aircraft measurements.

integrated aircraft measurements, with a slope of 1.33. This indicated that CMAQ provided a reasonable representation of the spatial/temporal variation of total SO_2 loading over the campaign area and period, and ~30% overestimate was observed.

Figure 5.10 compares CMAQ monthly mean SO_2 profile from different sensitivity runs over the campaign region, with the mean aircraft campaign profile. The monthly mean MR_HPPM profile underestimated the ambient SO_2 near the surface, overestimated

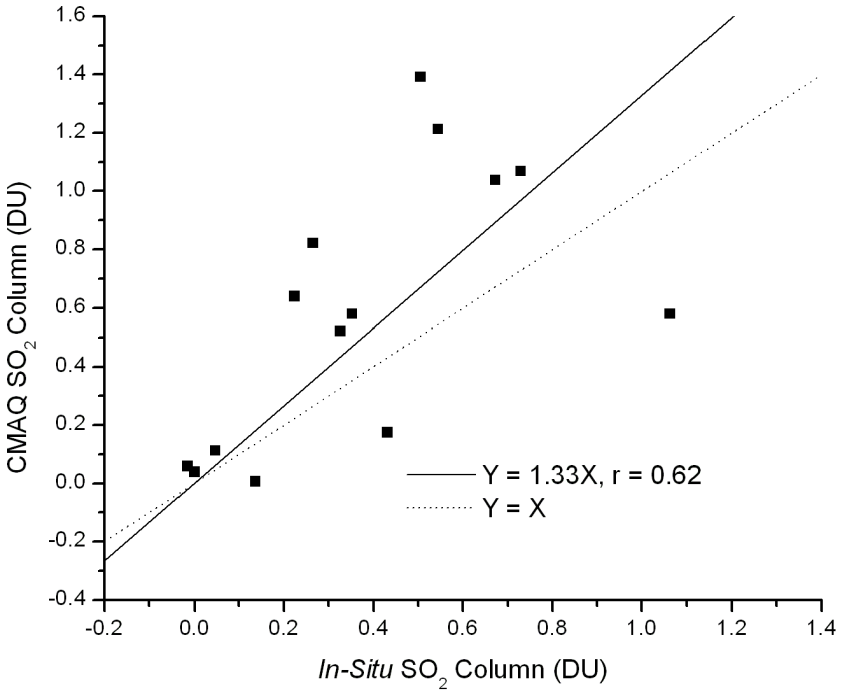

Figure 5.9 Evaluation of *in situ* and CMAQ SO_2 column contents. The CMAQ SO_2 column is calculated over corresponding altitudes of research flights. The dotted line represents the $Y = X$ line. The solid line shows the linear regression.

the SO_2 between 600 and 2200 m, and underestimated the SO_2 above 2500 m. The total SO_2 column was ~38% higher than the value obtained during the aircraft campaign. All the three sensitivity runs overpredicted the SO_2 columns. Based on differences of the NoMR_HPPM and MR_HPPM cases, it was confirmed that decrease of the SO_2 dry deposition increased the ambient SO_2 column content. Due to little SO_2 emission in upwind western China, the comparison between the NoMR_HYAMO and NoMR_HPPM

cases implied that the HPPM advection scheme transported less SO_2 out of the domain. The default CMAQ setup (NoMR_HYAMO case) demonstrated the best estimate of total SO_2 column content, while the modified case (MR_HPPM) had the best estimate of

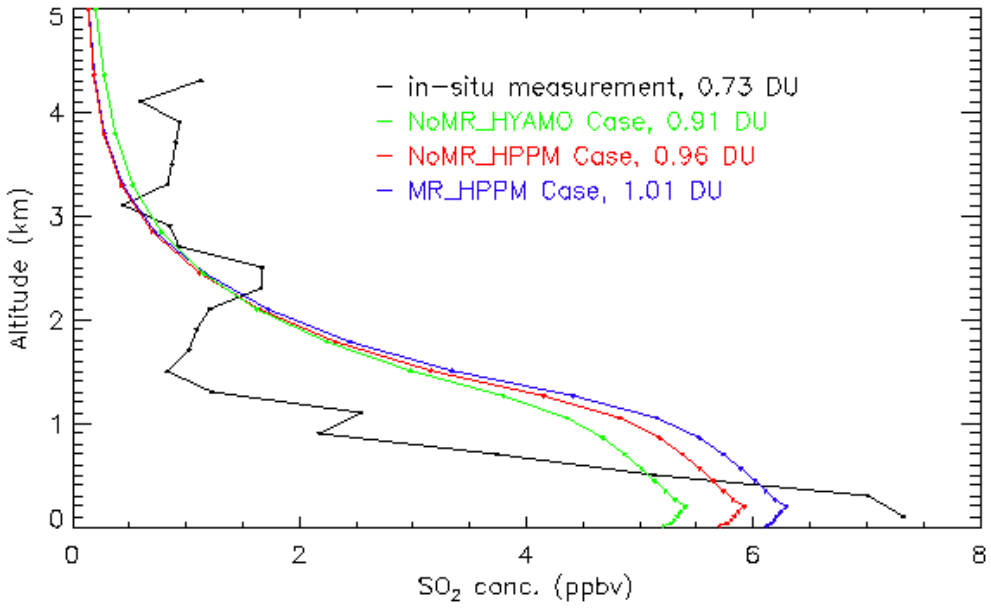

Figure 5.10 Comparison of monthly mean SO_2 profiles of in situ measurements and CMAQ sensitivity runs. The CMAQ SO_2 vertical column amount is the integral from the surface to 5000 m.

SO_2 concentration near the surface. Besides uncertainties in meteorological and emission data, the underestimate/overestimate within/above the PBL implied that the CMAQ model might mix the lower atmosphere too fast to transport the pollutants out of the PBL, also observed in the eastern U.S. [*Castellanos et al.*, 2011].

To summarize, the CMAQ simulations demonstrated reasonable accuracy (~30% overestimate) in reproducing the SO_2 column content observed during the research flights, but the SO_2 model profiles had substantial differences with respect to the measured SO_2 vertical distributions. More accurate model representation of pollutant vertical

distribution will require better parameterization of vertical transport and mixing in future. The comparison of monthly mean SO_2 profiles from sensitivity runs showed that the CMAQ model overestimated the SO_2 column content by 25-40% in difference sensitivity runs. The discrepancies are probably caused by the decrease from the 2006 emission inventory used in this CMAQ simulation. The recent decreasing trend, ~30% in Chinese SO_2 pollution has been reported by a number of studies [*Li et al.*, 2010b; *Lu et al.*, 2010; *Witte et al.*, 2009], which can be attributed to wide installation of Flue Gas Desulfurization (FGD) equipment on coal burning power plants.

5.3 SO_2 chemistry and lifetime

To investigate the conversion of SO_2 to other sulfur-compounds such as sulfate aerosols, I estimated lifetime of tropospheric SO_2. A simple box model was applied to the nested domain (area with ~1.25×10^6 km^2), and the SO_2 lifetime was calculated as $\tau_{SO_2} = \frac{Loading}{Emission}$. The average SO_2 emission was 4.3×10^{-3} mol/km^2 s based on the INTEX-B emission inventory. The campaign mean SO_2 loading from the aircraft campaign was 326 mol/km^2, and the SO_2 lifetime with respect to all losses from the domain (deposition, chemical transformation, and advection) was 21.0 hr. The lifetime was shorter than the result from a global model simulation [*Lee et al.*, 2011]. In summer over the Mid-Atlantic, the observed lifetime for chemical removal and deposition was 19 ± 7 hr [*Hains*, 2007]. April in China is cooler and drier than summer over the Mid-

Atlantic resulting in low photochemical reactivity, and a longer SO_2 lifetime is expected. The effects of sinks and chemistry on the SO_2 lifetime, like oxidation due to H_2O_2, are discussed in Appendix VII, which can not explain the discrepancy discussed above. The possible cause is that the ambient SO_2 is assumed being emitted within the box model region. The size of nested domain is only ~1000 × 1000 km, so an air mass with the typical wind speed of 10 m/s can move through it within one day. Therefore, substantial transport of sulfur-compounds in and/or out of the domain is expected.

Modification of the CMAQ advection scheme provided the ability to calculate the advection of pollutants through the boundaries; therefore I can investigate the budget of sulfur-compounds (SO_2 and sulfate aerosols). To simplify the computation, all sulfur-compounds are described in units of kT S. The reacted SO_2 amount, calculated as $SO_2(reactive) = Emission - Deposition - Advection$, assumed that the SO_2 oxidation product was 100% sulfate aerosols, i.e., 1 mole SO_2 is equivalent to 1 mole of sulfate. Figure 5.11 presents the monthly mean budget of sulfur-compounds of the nested domain, in units of kT/day. The daily SO_2 emission was 14.9 kT S and the monthly average SO_2 content in the domain was 14.7 kT S. The major sinks of SO_2 include daily dry deposition of 5.2 kT S and advection of 5.8 kT S out of the domain. The average rate of oxidation of SO_2 was assumed as 4.0 kT S/d, which generated the same amount of S in sulfate aerosols. The direct sulfate input from the emission inventory was small, 0.3 kT S. The discrepancy of sulfate budget (*sources* – *sinks*) is 0.5 kT S, accounting for less than 3% of the total daily S emission (14.9 kT S), which could be caused by: 1) assuming the 100% conversion from SO_2 to sulfate aerosols and ignoring the pathways to form other sulfur-compounds such as sulfuric acid vapor (H_2SO_4); and 2) neglecting minor

deposition processes such as SO_2 wet deposition and sulfate dry deposition. I re-calculated the lifetime of SO_2 as $\tau_{SO_2} = \frac{Loading}{Emission - Export}$. Based on Figure 11, the total amount of exported SO_2 was 5.8 kT/d, which accounts for ~39% of the total emitted SO_2. Including error analyses, the CMAQ simulated SO_2 budget and lifetime was computed for each day of the campaign, and the average lifetime ($\pm \sigma$) was 38 $\pm$ 7 hr. Due to significant advection, the oxidation rate was substantially decreased and the SO_2 lifetime is consistent with results from global model simulations [*Lee et al.*, 2011], and the case study in northern China with a SO_2 lifetime of ~2 d [*Li et al.*, 2010].

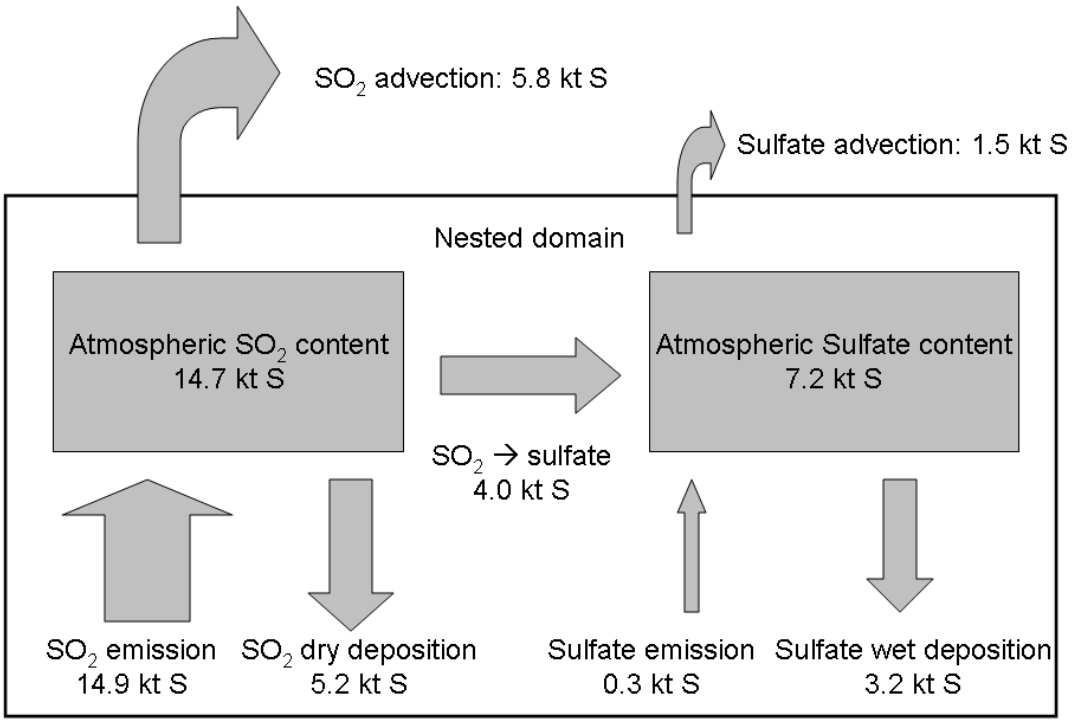

Figure 5.11 Budget of sulfur compounds over central China. The units for reservoirs are kT (1 kT = 10^6 kg), or kT/d for fluxes. All the data are the average daily value from the month-long simulations.

I further investigated the sinks and transport of sulfur-compounds. The daily total deposition (wet + dry) was 8.4 kT S, accounting for 55% of the total sulfur emission. This suggested the importance of controlling sulfur emissions for mitigating the soil and water acidification in central China [*Larssen et al.*, 2006]. Daily, 7.3 kT S were transported out of the domain, and the monthly mean ($\pm\sigma$) S of daily export was 48 $\pm$7% of the total sulfur emission.

The estimate of atmospheric sulfur export from central China is subject to random and systematic errors. The random uncertainty can be estimated from the standard deviation of daily sulfur export, 7%. A systematic bias is incurred if the month was atypical with respect to pollutant exports. April 2008 was observed as a generally wet month, with more precipitation than normal, 54 mm in April 2008 compared with 43 mm for long-term monthly average precipitation (data from www.wunderground.com). The WRF-CMAQ model also reproduced the wet month, therefore our approach using CMAQ simulations would overestimate the average sulfur wet deposition and underestimate export. I assumed conservatively the overestimation as half of the mean sulfate wet deposition: 1.6 kT S/d, or 10.5% of total S emissions (14.9 kT/d). Finally, errors in the simulated vertical distribution of SO_2 (Figure 5.10) affected the horizontal flux. I calculated the difference of average SO_2 concentration between *in-situ* measurements and CMAQ as +0.5 ppbv, -2.0 ppbv and +0.5 ppbv for layers 3000-4500 m, 500-2000 m, and surface to 500 m respectively. The wind speeds for these layers were estimated at 15 m/s, 8 m/s and 5 m/s respectably, based on statistics of zonal mean flow from long term observations. The SO_2 export was proportional to the product of SO_2 concentration and wind speed. So the CMAQ model had biases of +1.0 kT S, -3.0

kT S and +0.3 kT S for these three layers, which resulted in a net overestimate of 1.7 kT S in export, i.e., +11% of the total sulfur-compound emission. Adding these three uncertainties (±7% and ±11%) in quadrature provided an estimate of the total uncertainty for our estimate of S export. I concluded that 48% (±13%) of the S emitted into the atmosphere over central China was exported. The uncertainties were not Gaussian distributions, but we estimated the range of 35-61% with 90% confidence interval.

The nested domain is located in central China, and there are limited sulfur emissions in the upwind region of less developed western China. This study of pollutant transport demonstrated that most of the exported sulfur-compounds were transported through the northern and eastern boundary to the western Pacific coast (showed in Appendix VIII). Prior studies on S budgets through airborne measurements [*Koike et al.*, 2003] and model simulations [*Tan et al.*, 2002] also reported that around half of the sulfur-compounds were exported to the ocean. Quantifying long-range transport is crucial for understanding regional/global air quality and climate change due to emissions from East Asia.

5.4 Estimate of SO_2 emissions in central and eastern China

In section 4.2.3, I calculated the monthly mean OMI SO_2 column content over the campaign region as 0.63 ± 0.26 DU, which agrees with the observed aircraft average SO_2 column. CMAQ overestimated the monthly mean SO_2 column over the campaign region with a column content of 1.01 DU. The CMAQ high bias could be due to SO_2 being transported from nearby regions into the small campaign region. Because of small size,

the OMI instrument had only ~150 pixels per day within the campaign region. To reduce the noise and eliminate the influence of SO_2 transport, I selected CMAQ results of coarse domain (Figure 5.1) to study the total SO_2 burden over central and eastern China. The coarse domain (~4.6×10^6 km^2) covered most of the industrialized regions in China, and emitted ~25 Tg SO_2/year, ~80% of the total SO_2 emission in China [*Zhang et al.*, 2009]. I sampled CMAQ and OMISO2 PBL columns over the region with OMI reactive cloud fraction less than 0.3 (hereafter named cloud-free condition), in order to reduce cloud effects on the satellite retrievals.

A single-day comparison was conducted on the CMAQ SO_2 and OMISO2 columns for 04/05/2008 (Figure 5.12). The CMAQ simulations captured the large-scale SO_2 plumes in the northeast and southeast of China, but missed the plume in the northwest. We found the daily OMI SO_2 map had large variability due to both uneven coverage (sparse data on the east and west side of the domain) and instrument noise (negative value up to -2.0 DU). The CMAQ model overestimated the SO_2 burden by 10% compared with the OMISO2 product for 04/05/2008. To reduce the uncertainties of daily data, I present the monthly average SO_2 column map for both datasets (Figure 5.13). The CMAQ model captured the hot spots of SO_2 well over land, but missed the plumes off the coast. Column differences (OMI – CMAQ) were calculated resulting in a mean difference of -0.16 DU, and the histogram and probability density was analyzed (Figure 5.14) indicating a negative bias. So the CMAQ simulations systematically overestimated the SO_2 column by ~0.16 DU compared with OMISO2 PBL data. The monthly mean SO_2 loadings ($\pm \sigma$) were 54 ± 22 kT and 42 ± 26 kT for CMAQ simulations and OMISO2 PBL products respectively. Because both the OMISO2 products and CMAQ simulations were sampled

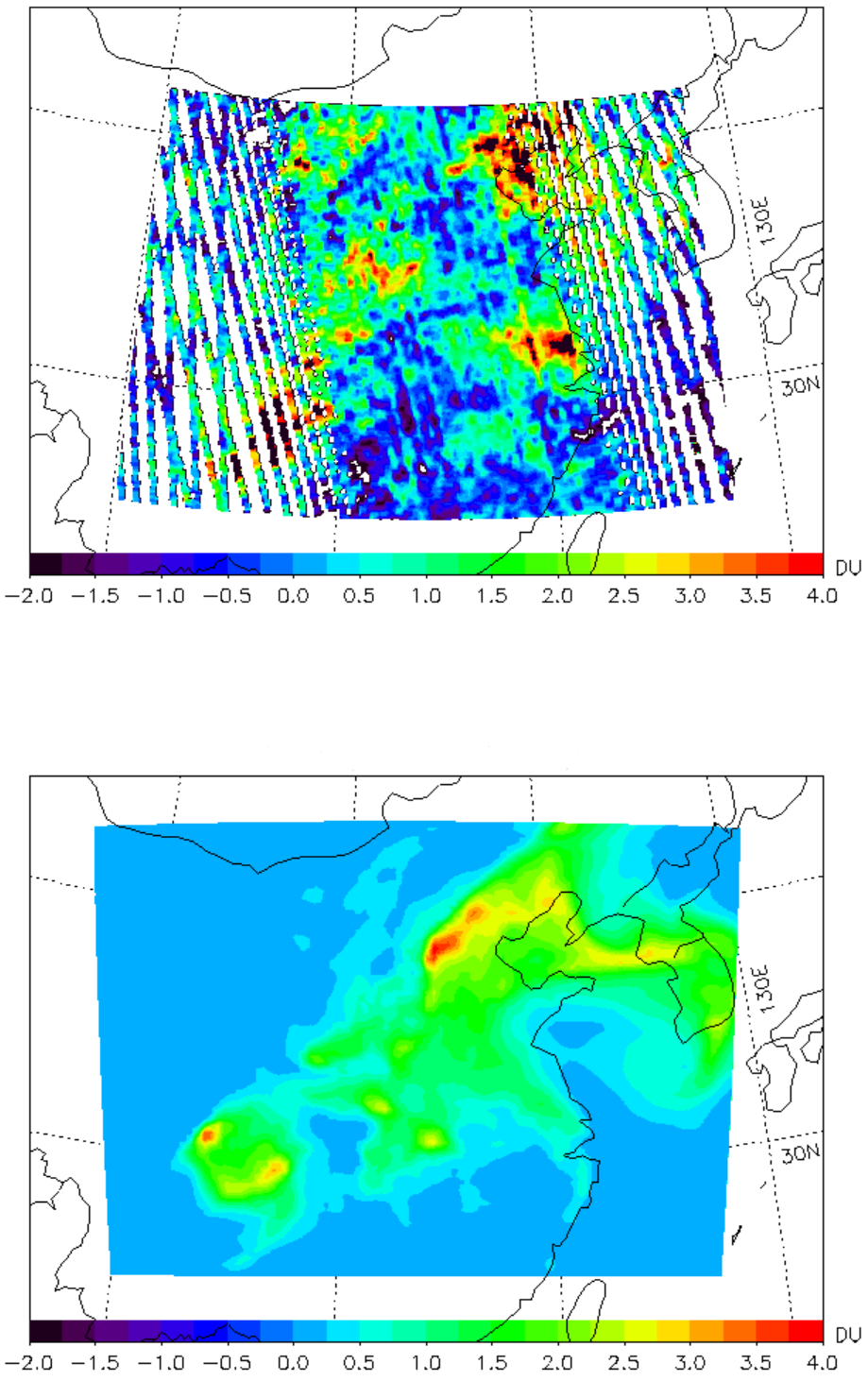

Figure 5.12 SO_2 column maps of OMI PBL products and CMAQ simulations in 04/05/2008. Upper panel: OMI SO_2 PBL column, 83.0 kT in 4.5 $\times 10^6$ km^2; lower panel: CMAQ SO_2 column, 92.0 kT in 4.6 $\times 10^6$ km^2.

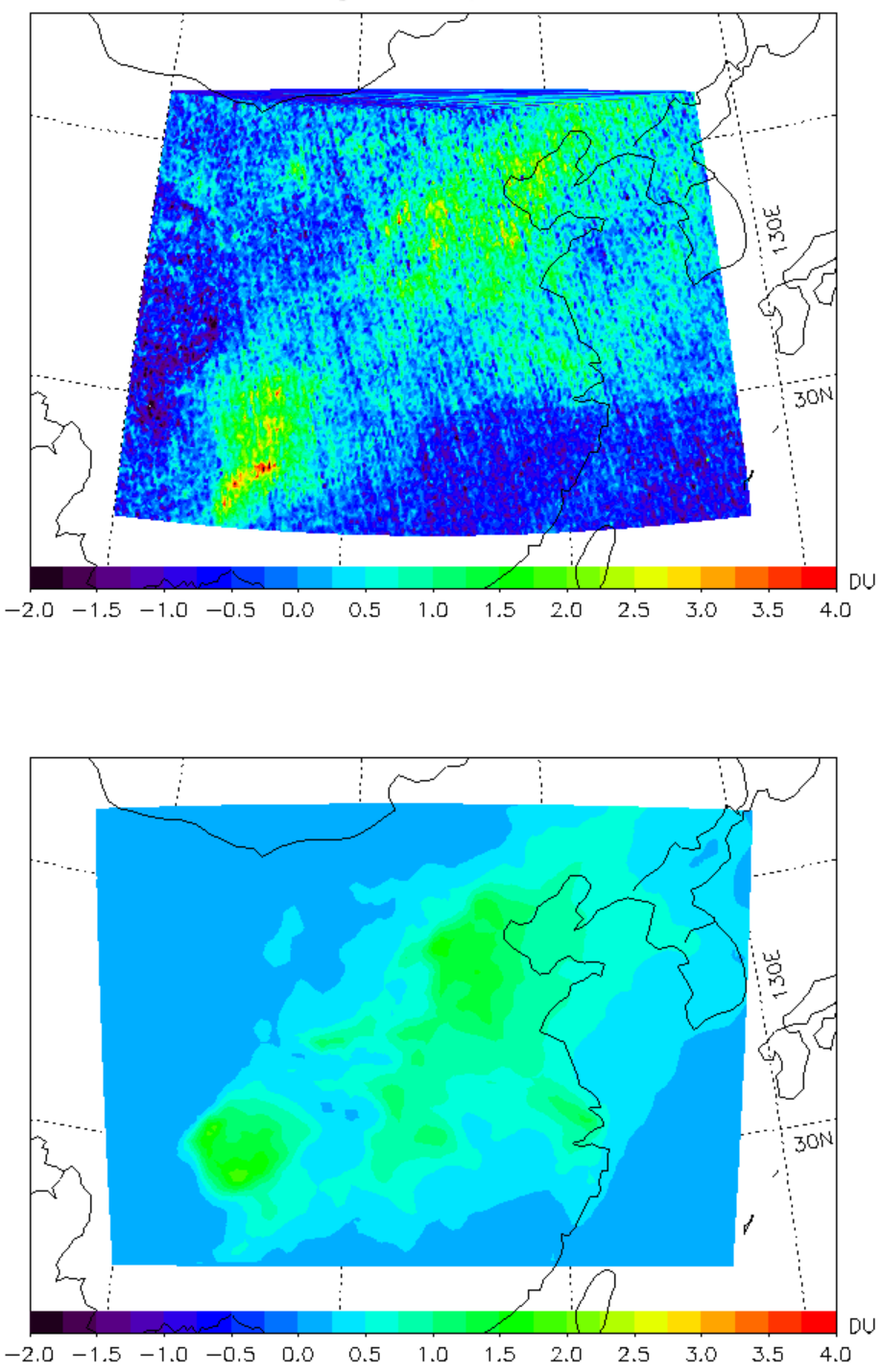

Figure 5.13 Monthly average SO_2 column maps of the OMI PBL products and CMAQ simulations. Upper panel: OMI SO_2 PBL column, 42 kT in 4.5×10^6 km^2; lower panel: CMAQ SO_2 column, 54 kT in 4.6×10^6 km^2.

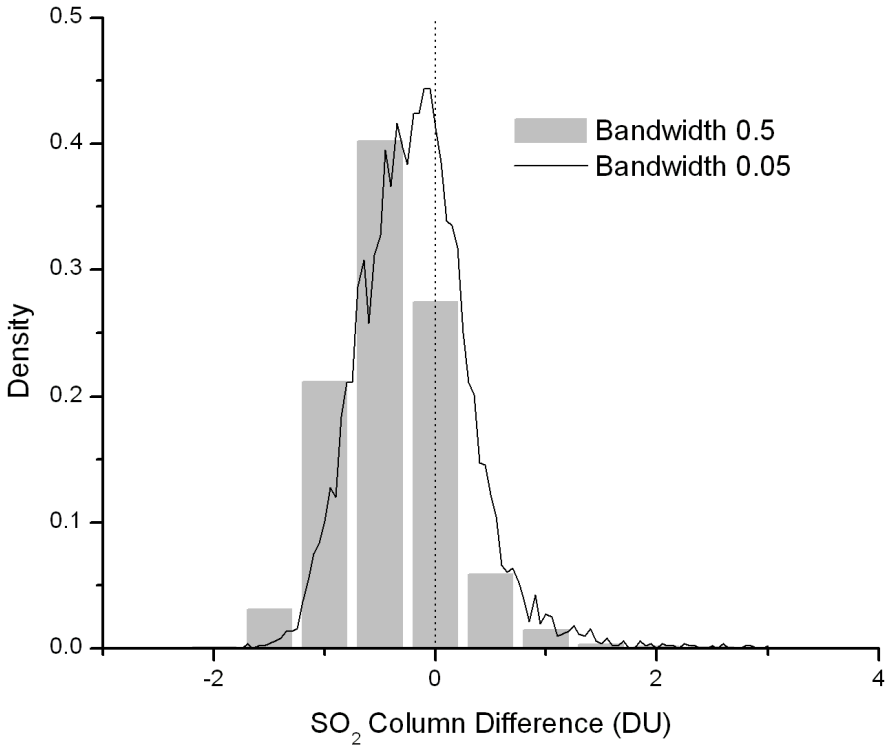

Figure 5.14 Histogram of monthly average OMI-CMAQ SO_2 column difference with probability density. (The curve density is multiplied by 10 for better visualization).

under cloud-free conditions using OMI radiative cloud fraction, these absolute low bias were expected in daily OMISO_2 and CMAQ SO_2 loadings. The monthly mean cloud-free fraction ($\pm \sigma$) was 56 $\pm$ 15%. The same approach of sulfur export error analysis was adopted here, i.e., underestimation is defined as half of SO_2 loading filtered out. The systematic low bias was estimated as +21 kT and +16 kT for CMAQ simulations and OMISO2 PBL products respectively, therefore the mean SO_2 loadings with all uncertainties were 54 (55-97) kT and 42 (37-89) kT. The result revealed that CMAQ simulations overestimated OMI SO_2 column contents by ~30%. The magnitude of

overestimation is consistent with the relative change in SO_2 emissions in China recently [*Lu et al.*, 2010].

As a summary, CMAQ simulations with the INTEX-B emission inventory demonstrated reasonable performance in describing the intensity and spatial distribution of sulfur-compound emissions in China. Both statistical analyses and total SO_2 loading computation indicated that CMAQ overestimated the SO_2 column contents compared with OMI products. This overestimation could be caused by the use of 2006 emission inventory, which is higher than 2008 emissions. Our results are consistent with reported decreasing trends of sulfur emission from 2006 to 2008 in China [*Lu et al.*, 2010; *Witte et al.*, 2009].

5.5 Conclusions and Discussion

SO_2 in central China was measured *in-situ* from an aircraft and remotely using the Ozone Monitoring Instrument (OMI) from the Aura satellite; results were used to develop a numerical tool for evaluating the tropospheric sulfur budget - sources, sinks, transformation and transport. In April 2008, measured ambient SO_2 concentrations decreased from ~7 ppbv near the surface to ~1 ppbv at 1800 m altitude (an effective scale height of ~800 m), but distinct SO_2 plumes were observed between 1800 and 4500 m, the research flights' ceiling. These free tropospheric plumes play a major role in the export of SO_2 and in the accuracy of OMI retrievals. The mean SO_2 column contents from aircraft measurements (0.73 DU, Dobson Units) and operational OMI SO_2 products (0.63

± 0.26 DU) were close. The OMI retrievals were well correlated with *in-situ* measurements (r = 0.84), but showed low bias (slope = 0.54). A new OMI retrieval algorithm was tested and showed improved agreement and bias (r = 0.87, slope = 0.86). The CMAQ model was used to simulate sulfur chemistry, exhibiting reasonable agreement (r = 0.62, slope = 1.33) with *in situ* SO_2 columns. The mean CMAQ SO_2 loading over central and eastern China was 54 kT, ~30% more than the estimate from OMI SO_2 products, 42 kT. These numerical simulations, constrained by observations, indicate that ~ 50% (35 to 61%) of the anthropogenic sulfur emissions were transported downwind, and the overall lifetime of tropospheric SO_2 was 38 ± 7 hr.

Using the combination of *in-situ* and remotely sensed measurement along with numerical simulation, it is possible to evaluate the SO_2 concentration and chemistry over central China – one of the most densely populated regions in the world. The CMAQ simulations served as a powerful tool to investigate tropospheric sulfur pollutants. Among the most important sources of uncertainties in the numerical simulations was the emission inventory, which was developed for the year 2006. The campaign was conducted in 2008, and from 2006 to 2008, especially in order to improve the air quality for the 2008 Beijing Olympics, sulfur emissions in China were reduced through stricter regulations on the usage of high sulfur coal and installations of FGD equipment in power plants. The decreasing trend has been observed [*Lin et al.*, 2012; *Okuda et al.*, 2011; *Witte et al.*, 2009], so the 2006 INTEX-B emission inventory probably has high bias, resulting in overestimated anthropogenic SO_2 emissions in the CMAQ simulations for spring 2008. A comparison with campaign SO_2 column contents demonstrated that CMAQ overestimated the tropospheric SO_2 columns over Henan by ~30%, and a similar

overprediction, also ~30%, was obtained through comparing monthly CMAQ and OMI SO_2 column contents over central and eastern China. These results are consistent with the reduction of sulfur emissions observed in China between years 2006 and 2008.

During the campaign, the aircraft instrument frequently observed SO_2 plumes in the FT, important for satellite retrieval and long-range transport. I found the SO_2 concentrations had high temporal and spatial variability during spring in China. Comparisons of *in-situ* measurements, the operational OMISO2 PBL products revealed good agreement, and the new ISF algorithm demonstrated better performance and will be employed operationally in the future. The CMAQ model didn't capture the SO_2 vertical distribution well, probably due to inadequate model resolution for computing vertical mixing. But the CMAQ simulations agreed with the mean aircraft measurements, with a ~30% overestimation. With a modified CMAQ advection scheme, I investigated the budget and transport of SO_2 and sulfate. The lifetime of SO_2 with respect to all reactions and removal from the atmosphere was 38 ± 7 hr, relatively long for spring. Due to the slow removal and strong winds in spring, ~ 50% (35-61%) of the total S emitted into the atmosphere in central and eastern China was transported out of the domain. Further research in East Asia will help to improve our knowledge on the effects on regional air quality and large-scale climate downstream.

Chapter 6. Evaluation of CMAQ-based aerosol properties with surface measurements and MODIS observations

6.1 Introduction

The increase of particulate matter in China has exerted significant impact on regional climate and air quality [*Chan and Yao*, 2008], and $PM_{2.5}$ pollution has emerged as a major issue in megacities [*He et al.*, 2002]. Chemical transport models such as CMAQ and WRF-Chem are used to conduct numerical simulations of tropospheric aerosols in China [*Lin et al.*, 2008a; *Lin et al.*, 2008b; *Matsui et al.*, 2009; *Matsui et al.*, 2010; *Wang et al.*, 2010a; b]. As part of the EAST-ARIC campaign, the CMAQ simulations for spring 2008 provide an opportunity to investigate tropospheric aerosols over China. In section 5 the discussion on the CMAQ sensitivity runs indicate that the MR_HPPM run shows the optimal simulations of sulfur compounds including sulfate aerosols, one of the major components in tropospheric aerosols, therefore the results of MR_HPPM simulations are applied here.

AOD was selected as surrogate to evaluate the aerosol simulations with respect to the surface photometer measurements and spaceborne MODIS observations. AOD is defined as the integrated extinction coefficients over the vertical column as:

$$\tau(z,\lambda) = \int_{z}^{z_{TOA}} b(z',\lambda)dz' \qquad \text{(Equation 6.1)}$$

Where z is the altitude, z_{TOA} is the top of atmosphere, $b(z',\lambda)$ is the extinction coefficient at altitude z' and wavelength λ [Seinfeld and Pandis, 2006]. AOD is useful to derive the aerosol mass concentration based on the following equation:

$$\tau = \alpha_a m_a H \qquad \text{(Equation 6.2)}$$

where α_a, is the light-scattering mass efficiency of the aerosol in units of m^2/g, m_a is the mass concentration in units of g/m^3, and H is the path length [*Seinfeld and Pandis*, 2006]. It is worth noting that the growth of hygroscopic aerosols such as sulfates is strongly determined by the ambient relatively humidity (RH), so it is practical to define the hygroscopic growth factor *f(RH)* as:

$$\alpha_{SO_4^{2-}} = \alpha_{SO_4^{2-}}^{RH} f(RH) \qquad \text{(Equation 6.3)}$$

f(RH) is crucial to reconstruct the AOD values from the simulated aerosols mass concentrations. A semi-empirical mass extinction (CMAQ-RM) method based on the Interagency Monitoring of Protected Visual Environments (IMPROVE) network observations was applied to reconstruct the mass extinction from simulated aerosol mass and ambient RH [*Malm et al.*, 1994]. The atmospheric AOD was calculated by integrating the mass extinction form the surface to top of the atmosphere.

As shown in Equation 6.1, the AOD is also a function of wavelength. The Angstrom Exponent (AE) is introduced to describe the wavelength dependence of the aerosol extinction coefficient:

$$\dot{\alpha} = -\frac{d \log b_{ext}}{d \log \lambda} \approx -\frac{\log(b_{ext1} / b_{ext2})}{\log(\lambda_1 / \lambda_2)} \qquad \text{(Equation 6.4)}$$

The Angstrom Exponent is inversely proportioned to the average size of aerosol particles, i.e., the smaller the value, the larger the particles. Therefore, AE is a useful tool to assess the particle size of atmospheric aerosols or cloud droplets. For instance, cloud droplets, with larger size than aerosols usually have small AE values (nearly zero); anthropogenic aerosols generated through nucleation have larger values (greater than 1). Angstrom exponents can be calculated from the AOD measurements at different wavelengths. In this study, I calculated them from a handheld sunphotometer and MODIS measurements.

During the aircraft campaign, surface AOD observations were monitored from a handheld sunphotometer, widely used and validated during previous campaigns in China [*Xin et al.*, 2007]. The observations were conducted every 15 minutes from 13:00 to 14:30 (local time), to encompass the OMI overpass time (13:30 local time). Data were processed by removing the cloud-contaminated conditions, and hourly mean AODs were obtained.

6.2 Evaluation of AOD measurements over Xinzheng

AODs from the handheld sunphotometer were processed and averaged for cloud-free days during the EAST-AIRC aircraft campaign period, and the MODIS Level2 data were selected over Xinzheng in the same days. The comparison of handheld AOD at 500 nm and MODIS AOD at 550 nm is presented in Figure 6.1. Good correlation (r = 0.89) was observed, but MODIS underestimated the surface AOD by ~30% (linear regression *slope = 0.71*), and the positive intercept (*intercept = 0.27*) indicated that the MODIS

products had a systematic high noise for central China in spring 2008. The underestimation is larger than the previous study over north and south China using the AERONET data [*Mi et al.*, 2007]. The explanation could be that few valid AOD data (8 out of 20 days during the deployment) were collected, while Mi et al. [2007] utilized AERONET data from 2005 and 2006. Another reason is that low visibility conditions were frequently observed during the campaign, possibly caused by heavy fog and low cloud, which prevented the surface observations or caused invalid observations in the surface site.

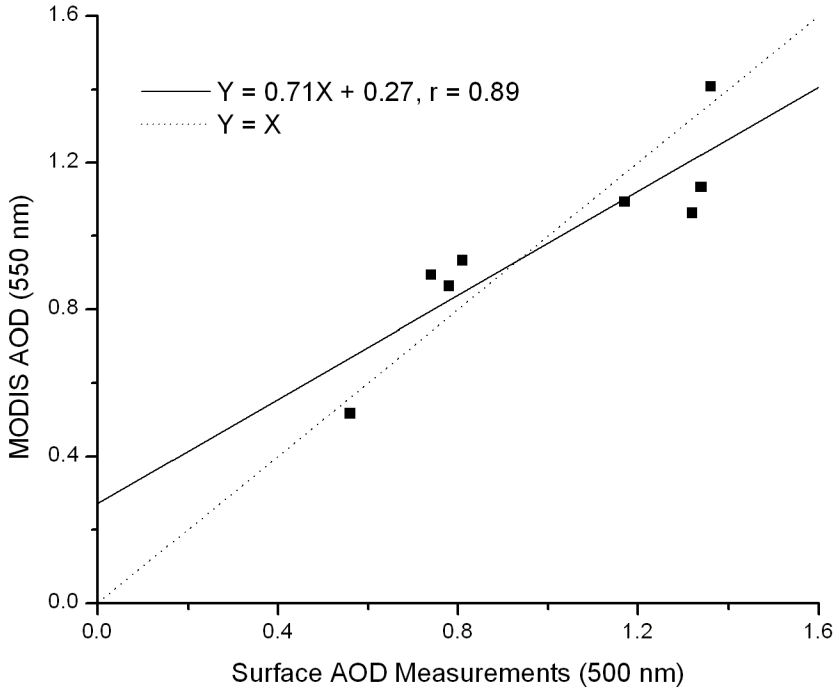

Figure 6.1 Comparison of surface AOD measurements (500 nm) with MODIS Level 2 AOD products (550 nm). Surface AOD measurements were measured by the handheld sunphotometer. black line presents the linear regression, dot line presents the 1:1 line.

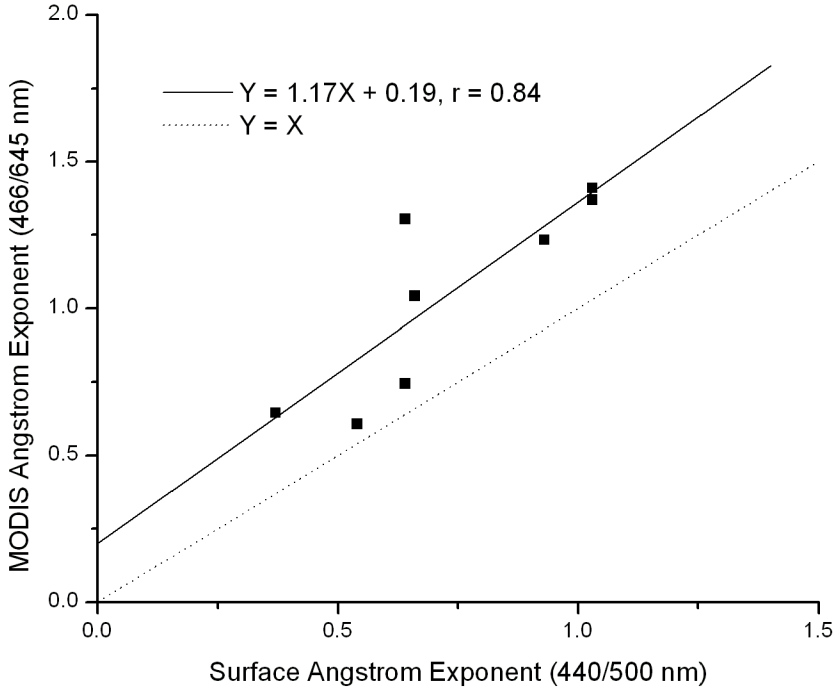

Figure 6.2 Comparison of Angstrom Exponent values from surface sunphotometer measurements and MODIS observations. Black line presents the linear regression; dot line presents the 1:1 line.

To investigate the size of observed aerosols, I calculated the AE based on the AODs measured at 440 nm and 500 nm from the handheld sunphotometer, and compared these with the MODIS AE at 550 nm band (466-645 nm) in Figure 6.2. Both the surface sunphotometer and the MODIS instrument observed occasional low AE days (value less than 1.0), indicating the existence of large particles, mainly dust, over central China. More than half of the days showed large AE values (greater than 1.0), related to small anthropogenic aerosols formed by *in situ* chemical reaction and nucleation. I selected the days with MODIS AOD greater than 1.0, and the mean MODIS AOD (550 nm) and

MODIS $PM_{2.5}$ column mass were 1.08 and 47.0 μg/cm^2 respectively. The cloud-free and dust-free cases revealed that high anthropogenic aerosol loadings existed over central China in spring 2008.

The CMAQ simulations of sulfur compounds demonstrate that the CMAQ model is capable of reproducing the distribution of atmospheric SO_2 and sulfate aerosols. Sulfate aerosols play an important role in the tropospheric radiation scattering, so I evaluated the reconstructed atmospheric AODs based on the CMAQ results (Figure 6.3). Good correlation (*r = 0.85*) was observed, but the CMAQ model substantially underestimated the atmospheric AODs by ~50% (*slope = 0.45*, *intercept = -0.16*).

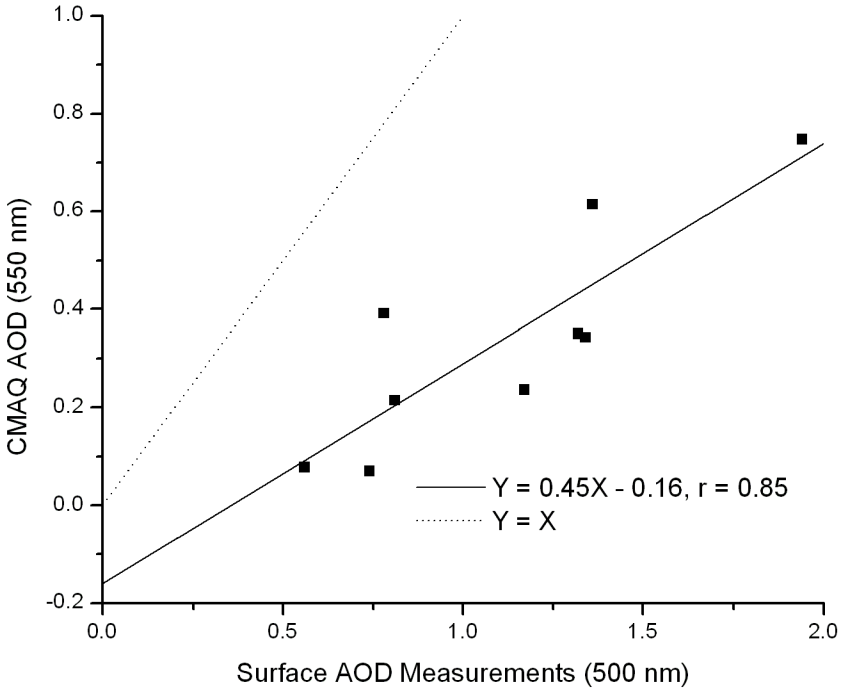

Figure 6.3 Comparison of AODs from surface sunphotometer measurements and CMAQ simulations. Black line presents the linear regression; dot line presents the 1:1 line.

Possible explanations of the CMAQ underestimation included: 1) insufficient sample size of AOD measurements observed by the handheld sunphotometer, 2) INTEX-B emission inventory, which was utilized as emissions for CMAQ simulations, did not include information on dust emissions. In China, atmospheric dust accounts for a signification portion of atmospheric aerosols especially in spring [*Dickerson et al.*, 2007; *Wang et al.*, 2004; *Xin et al.*, 2005; *Zhang et al.*, 2003]. To verify the possible underestimation of atmospheric AOD by the CMAQ model, more research is needed in future. For instance, the dust aerosols are simulated by global models such as GOCART, which can provide atmospheric AOD information to supplement the CMAQ simulations.

6.3 Evaluation of CMAQ simulated aerosols over central and eastern China

As discussed above, the CMAQ model demonstrated fair performance on atmospheric aerosol simulations in comparison to surface sunphotometer measurements and MODIS observations. Still, limited *in situ* measurements at one single site can not provide sufficient data to evaluate the CMAQ simulations over a large area. A similar approach for evaluating the OMI SO_2 products is applied here: the simulations over the coarse domain (Figure 5.1) are evaluated with the co-located MODIS aerosol products. The coarse domain, with ~4.6×10^6 km^2, covered most of the industrialized region and population in China, so the simulations provide an estimate of total anthropogenic aerosols. To reduce the daily uncertainties of daily MODIS aerosol products, the model simulations and satellite products were averaged from 03/28/2008 to 04/26/2008. AODs

were re-constructed based on the CMAQ-RM method [*Malm et al.*, 1994], and $PM_{2.5}$ column masses were calculated as the integral of fine particle mass through vertical columns. MODIS aerosol products were mapped to the coarse model, and the comparisons were plotted in Figure 6.4. CMAQ simulations captured the hot spots of MODIS AOD and column mass in the Sichuan Basin and northern China, but missed the maximum in the YRD region. Figure 6.5 presents the map of monthly mean Angstrom Exponent from MODIS aerosol products. Low AE values were observed spreading from

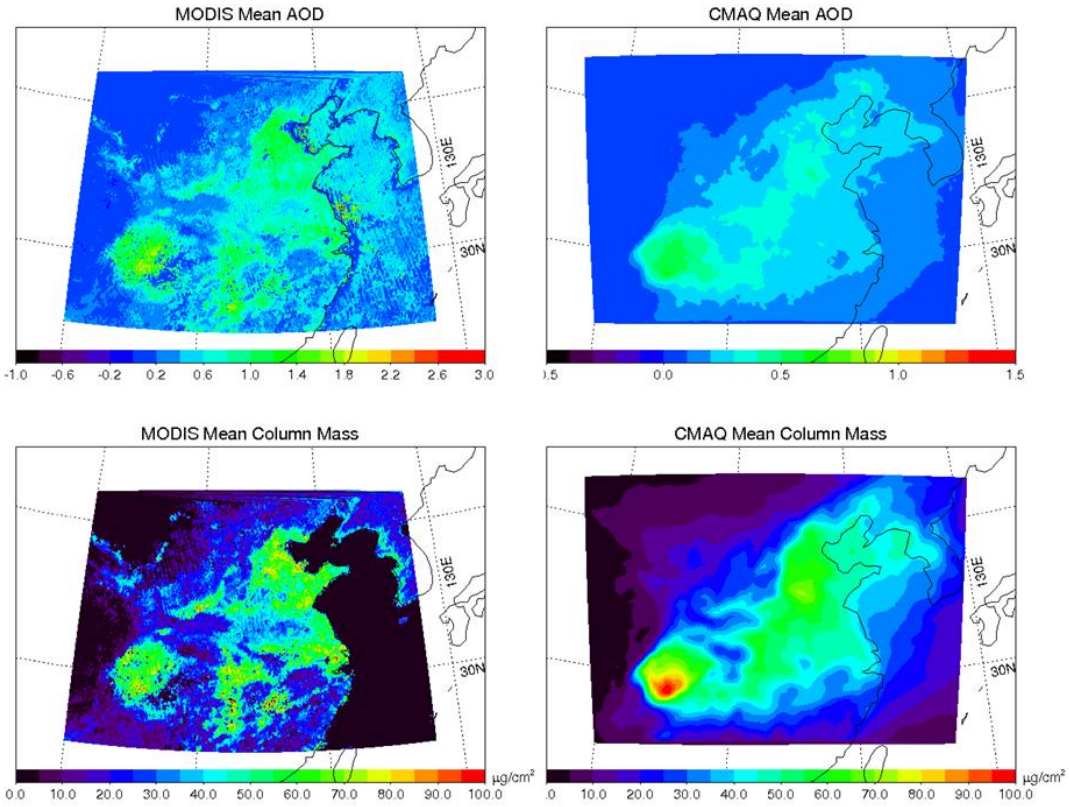

Figure 6.4 Monthly mean AOD and $PM_{2.5}$ column mass maps from MODIS aerosol products and CMAQ simulations. Left column: MODIS AOD (top) and $PM_{2.5}$ column mass (bottom) in units of μg/cm^2; right column CMAQ AOD (top) and $PM_{2.5}$ column mass (bottom).

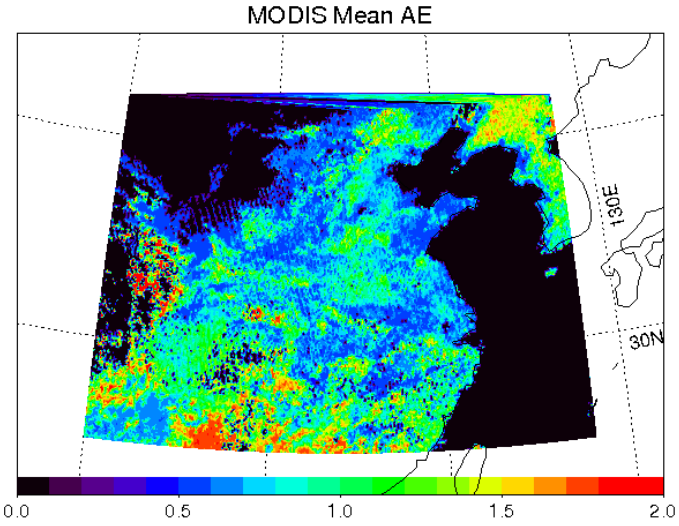

Figure 6.5 Monthly mean Angstrom Exponent (466/645 nm) map from MODIS.

northern China like Beijing to southeast China like the YRD region, suggesting the existence of dust aerosols. In these high AE regions, especially over the Shandong peninsula (around 36.5 ºN, 120.0 ºE) and on the east coast of China, the CMAQ simulated AODs were substantially lower than the MODIS AOD measurements. This underestimation of CMAQ could be explained by the missing dust in the simulations. Based on the comparison between MODIS and CMAQ $PM_{2.5}$ column masses, the CMAQ simulations captured the hot spots of particulate matter in the Sichuan basin and north China, while CMAQ overestimated the aerosol column masses over the whole coarse domain.

In summary, CMAQ underestimated the MODIS AODs and overestimated the MODIS $PM_{2.5}$ column masses. Based on Figure 6.4, MODIS used different algorithms to retrieve $PM_{2.5}$ column mass and AOD over land and over ocean, so in this study, only MODIS aerosol products over the land were selected. Figure 6.6 (left) presents the

scatter plot of column masses versus AOD measurements, suggesting that MODIS presented higher AOD value than the CMAQ-RM method for the same amount of $PM_{2.5}$ column mass. The CMAQ/MODIS ratios are plotted in Figure 6.6 (right), revealing that MODIS greatly overestimated the AOD value (MODIS to CMAQ AOD ratio around 10) when the $PM_{2.5}$ column mass values were comparable (MODIS to CMAQ mass ratio around 1). Therefore the MODIS algorithm for retrieving $PM_{2.5}$ column mass had systematic low bias compared with the CMAQ-RM algorithm developed based on the IMPORVE network observations. To quantify the over-prediction, I analyzed the MODIS-CMAQ differences in Figure 6.7 and presented the summary of statistics in Table 6.1. It is found that the mean AOD difference between MODIS and CMAQ is about 0.25, close the value obtained in a similar study over the U.S. [*Roy et al.*, 2007]. On the other hand, the mean $PM_{2.5}$ column mass difference (MODIS-CMAQ) is close to zero (about -3.0 μg/cm^2), with mean values of 33.6 μg/cm^2

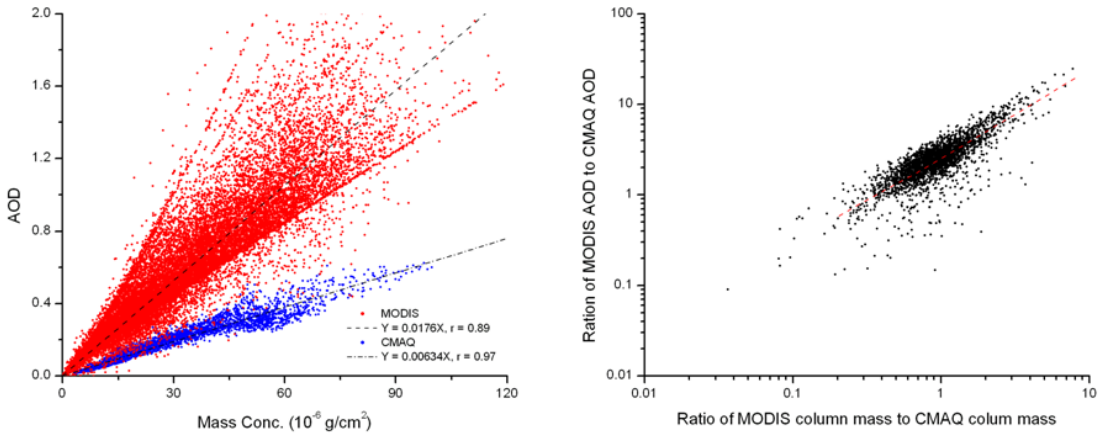

Figure 6.6 Scatter plot of AOD and $PM_{2.5}$ column mass. Left: AOD versus column mass (μg/cm^2); right: comparison of AOD ratio (MODIS/CMAQ) and column mass ratio (MODIS/CMAQ) in logarithmic scales.

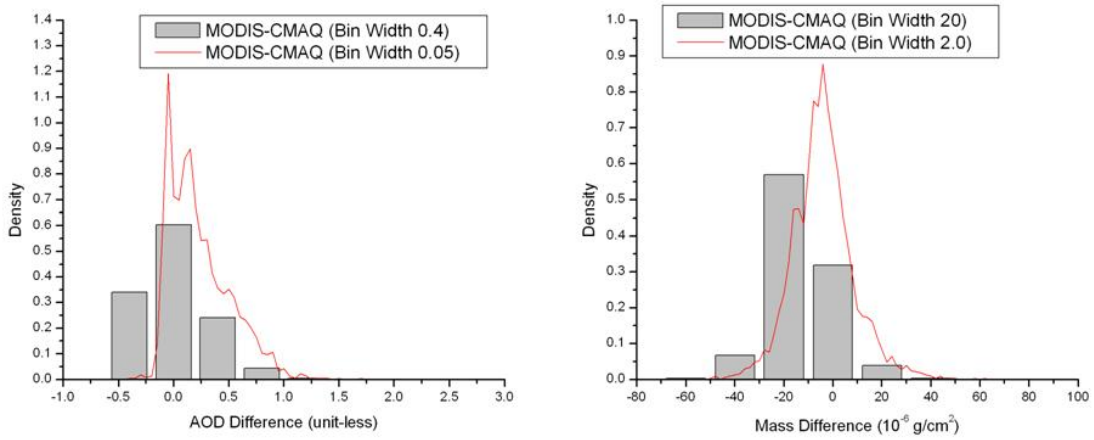

Figure 6.7 Histograms of MODIS-CMAQ AOD and $PM_{2.5}$ column mass differences. The density values with finer bin (red) width are multiplied by 10 for better visualization.

Table 6.1 Statistical analysis of differences (MODIS-CMAQ) of AOD and $PM_{2.5}$ column mass.

	ΔAOD (unitless)		*ΔMass* (μg/cm^2)	
Parameter	Mean	Median	Mean	Median
MODIS-CMAQ	0.26	0.19	-3.1	-3.5

observed by MODIS. These results indicate that the CMAQ simulations have good agreement with the MODIS retrievals of $PM_{2.5}$ column mass, but the reconstructed AODs had large discrepancies.

6.4 Conclusions and Discussion

During the EAST-AIRC aircraft campaign, a handheld sunphotometer was deployed at Xinzheng Meteorological Observatory, and AOD measurements at five

wavelengths were conducted during the EOS Aura satellite overpass time. Spaceborne observations of atmospheric aerosols were obtained from the MODIS instrument aboard the EOS Aqua satellite. The comparison of sunphotometer and MODIS AODs indicated that MODIS underestimated the AODs by ~30%. I calculated the Angstrom exponents (440/500 nm) based on the sunphotometer observations (466/645 nm) and compared them with the MODIS AE values. Both AE measurements demonstrated the occasional existence of dust aerosols over Henan province. On the days with large AE values (MODIS AE higher than 1.0), the mean MODIS AOD and $PM_{2.5}$ column mass were 1.08 and 47.0 $\mu g/cm^2$ respectively, suggesting heavy anthropogenic aerosol loadings in springtime China. I also reconstructed AODs from the CMAQ aerosols simulations based on the CMAQ-RM algorithm. The comparison between CMAQ AODs and sunphotometer observations demonstrated good agreement but the CMAQ simulations underestimated the AOD by ~50% with a systematic low bias. The discrepancies between the *in situ* observations and the numerical simulations could be explained by: 1) insufficient sunphotometer observations collected during the EAST-AIRC aircraft campaign, which caused large uncertainties in the evaluation; 2) the CMAQ model did not include the simulation on the atmospheric dust aerosols, while atmospheric dust accounts for a crucial part in the total AOD over China.

To take advantage of the large dataset from the MODIS products and CMAQ simulations, I applied them to a large area, the coarse domain covering central and eastern China. Monthly mean AOD and $PM_{2.5}$ column mass were calculated based on the CMAQ simulations, and the MODIS aerosol products were sampled over the same domain. The CMAQ model successfully captured the hot spots of both AOD and $PM_{2.5}$

column mass, especially over the Sichuan basin and north China, but missed the maximum in the coastline and YRD region. Over the same regions, low AE events were observed, suggesting that the CMAQ underestimation could be caused by the dust aerosols. Even though CMAQ reproduced the spatial distribution of aerosols, the absolute values of AOD and $PM_{2.5}$ column mass showed significant discrepancies with respect to the MODIS aerosol products. Scatter plots of AOD versus $PM_{2.5}$ column mass revealed that the MODIS algorithm for retrieving aerosol column mass had systematic difference compared with the CMAQ-RM algorithm, which was developed on the IMPROVE network observations in the U.S. Statistical analysis demonstrated that over the land, CMAQ systematically underestimated AOD by ~0.3 with respect to MODIS products, close to results from the U.S. [*Roy et al.*, 2007]. But the discrepancy between the CMAQ $PM_{2.5}$ column masses and MODIS products was small, i.e., CMAQ reproduced the $PM_{2.5}$ column masses with respect to MODIS products. Therefore, on the same amounts of aerosol column masses, the CMAQ-RM algorithm systematically under-predicted the AOD compared with the MODIS products. This discrepancy might be caused by the different aerosol properties in China, such as chemical composition and size distribution, while the CMAQ-RM method was developed based on IMPROVE network observations in the U.S.

Chapter 7. Conclusions and future work

7.1 Summary of results

In this study, I investigated air pollution in the eastern U.S. and in central China. The study on the U.S. focused on the long-term trends of air pollution observed from the UMD aircraft. The column contents of ambient CO and O_3 in the lowest 1500 m showed good correlation, with a decreasing trend of ~20.0 DU/decade and ~2.0 DU/decade respectively, which equals to ~800 ppb/decade and ~15 ppb/decade decrease at the surface. Unlike regional CO and O_3 pollution, ambient SO_2 exists more in the form of isolated plumes in the troposphere, and the column contents were significantly influenced by the location and time of the research flights. The Maryland Healthy Air Act reduced by up to 90% Maryland power plant SO_2 emissions, and a 30~40% decrease of SO_2 column contents was observed after the Healthy Air Act was fully implemented (2009 and before compared to 2010-2011). But at the same time, AODs observed during the same flights only decreased ~10% after 2010, indicating that the SO_2 pollution is mainly a local problem, while aerosol pollution is more regional for the eastern U.S. states.

Aircraft observe air pollution above the ground level, which provides a unique opportunity to study the long-range transport of air pollutants. The states upwind of the DC-Baltimore region (PA, OH and WV) have large numbers of tall smokestacks for their power plants, which emit pollutants into the FT. USEPA's CEMS program continuously

monitored these point sources, and the CEMS data from 1997 to 2011 demonstrate a significant decrease of NO_x and SO_2. The long-term trend of CEMS NO_x emissions shows a sharp decrease after the EPA NO_x SIP call (2003-2004), and the EPA AQS surface observation confirmed this sharp decrease.

My study on the NO_x emissions from point sources indicates that the increasing NO_x emission with the increasing ambient temperature contributed about half of the CPF values observed in the eastern U.S. SO_2 data demonstrated a gradual decrease for these states. A clustering technique based on the NOAA HYSPLIT back trajectory calculations demonstrated that the transport from OH and PA has significant impacts on the MD air pollution.

Air pollution in central China was investigated in a comprehensive case study on sulfur compounds through aircraft measurements, satellite observations, and numerical simulations. Spatial and temporal distributions of ambient SO_2 were measured from the aircraft, and real-time OMI SO_2 products were utilized as forecasting tool. The ambient mean SO_2 concentration decreased from ~7 ppb near the surface to ~1 ppb at 1800 m altitude, with an effective scale height of ~800 m. During the campaign isolated SO_2 plumes were observed in the FT, and HYSPLIT back trajectory calculations showed long-range transport processes. I calculated the SO_2 column contents and compared them with the co-located OMI SO_2 retrievals including operational OMISO2 products (BRD algorithm) and research ISF algorithm. The OMISO2 products demonstrated good correlation but systematic low bias (-0.40 DU) and substantial underestimation (~50%) were observed. The new ISF algorithm showed comparable correlation, lesser bias, and better performance (only ~15% underestimate). This study showed the feasibility of

replacing the BRD algorithm with the improved ISF algorithm. I also estimated the mean SO_2 column over the aircraft campaign area, and monthly mean OMISO2 PBL column showed better performance after averaging over longer times and larger areas.

To evaluate the sulfur budget including the export of sulfur compounds, I conducted a month-long simulation using the CMAQ model, driven by the WRF meteorological model and the NASA INTEX-B emission inventory. Improvements of the CMAQ model were carried out to correct the SO_2 dry deposition velocity and calculate the horizontal advection of air pollutants. The correction of SO_2 mesophyll resistance improved the simulation of SO_2 dry deposition velocity, closer to the value observed from field experiments. Reasonable agreement was obtained between the *in situ* SO_2 column contents with CMAQ simulations ($r = 0.62$, $slope = 1.33$), but faster mixing in the lower atmosphere in the CMAQ simulations was observed. Then I applied the numerical simulations and OMI SO_2 PBL products over central and eastern China, and found that CMAQ successfully reproduced the hot spots in the OMI SO_2 column map, with ~30% underestimation of SO_2 loadings (54 kT from CMAQ versus 42 kT from OMI). Based on the calculation of horizontal advection, it was found that 35-61% of the anthropogenic sulfur emissions were transported downwind (exported), and the overall lifetime of SO_2 was estimated as 38 ± 7 hrs in April over China.

During the EAST-AIRC aircraft campaign, surface observations of AODs were collected coincident with the Aqua MODIS over pass time. The comparison of sunphotometer and MODIS AODs showed that MODIS underestimated the AODs by ~30%. Angstrom exponent data from sunphotometer and MODIS both demonstrated the existence of dust aerosols during the field campaign. On the cloud-free and dust-free

days, the average MODIS AOD (550 nm) and $PM_{2.5}$ column mass were 1.08 and 47.0 $\mu g/cm^2$, indicating high anthropogenic aerosol loadings. I also reconstructed the AODs from the aerosols simulated by CMAQ using the CMAQ-RM algorithm, and observed good correlation between the sunphotometer measurements and CMAQ simulations but ~50% underestimation and systematic low bias by the CMAQ model. These discrepancies could be caused by insufficient sample size of surface sunphotometer measurements, so the large amount of MODIS data and CMAQ simulations over central and eastern China were utilized. CMAQ successfully captured the spatial distribution of AODs and $PM_{2.5}$ column mass observed by the MODIS instrument. Quantitatively, CMAQ showed a systematic underestimation (-0.3) of AOD with respect to MODIS AOD observations. The CMAQ-RM algorithm was established from the long-term observations of the IMPROVE network in the U.S., while the chemical composition and aerosol properties are different in China.

7.2 Recommendations for future work

In the first part of this dissertation, I discussed the long-term trend of air pollution in the eastern U.S. based on the aircraft measurements and USEPA CEMS emissions. The preliminary results showed that the upwind CEMS emissions had significant effects on the air pollution in the downwind region, especially pollutant concentrations aloft. Normally ~90% of CO and ~50% NO_x, important precursors for O_3 pollution, are emitted by mobile sources (on-road and non-road vehicles) in the eastern U.S. In this study,

annual mobile emissions from USEPA NEI inventory were used to track the long-term trend, but seasonal and diurnal variations of mobile emissions were not available. During the O_3 season, both point and mobile emissions are highly influenced by the meteorology such as ambient temperature; the dispersion and transport of air pollutants are also controlled by the meteorology and atmospheric circulation. In future research, numerical model such as SMOKE can be used to generate four-dimensional emission data to study the long-term emission trends of mobile sources with seasonal and diurnal variability. These model simulations will be also useful to study the sharp decrease of surface NO_x decrease after the USEPA SIP call.

Under the climate change, it is important to study the climate penalty factor (CPF) for O_3 production. Using the high resolution data of CEMS NO_x emissions, a preliminary analysis demonstrates that the dependence of NO_x emissions on ambient temperature decreased in the last 15 years. The O_3 photochemistry in the Mid-Atlantic region is NO_x-sensitive, so the decrease of NO_x emissions with respect to ambient temperature will reduce the CPF value. Previous study reported that the CPF has been decreased from ~3.2 ppbv/℃ prior to 2002 and ~2.2 ppbv/℃ after 2002 [*Bloomer et al.*, 2009]. As discussed above, future research should focus on the variations of mobile emissions with temperature change. Combining point emissions and mobile emissions, the contribution of NO_x reduction to the total CPF can be further explored, based on the same approach applied in section 3.5.2.

In the second part of this dissertation, I investigated tropospheric sulfur chemistry through a combination of aircraft measurements, satellite observations, and CMAQ simulations over China. Future research could include:

1) Improve the ISF algorithm in order to replace the operational OMI SO_2 product. Isolated SO_2 plumes in the FT were observed both over central China and the Mid-Atlantic, and the ISF algorithm will take them into account. Aerosols were also observed co-located with SO_2 in the troposphere by both aircraft flights in the U.S. and China, and the ISF algorithm can incorporate their effects for better performance.

2) The NASA INTEX-B emission inventory proved useful to the numerical simulations of air quality over China in this dissertation. But this emission inventory is established based on the emissions of 2006, and large changes occurred after 2006 [*Fioletov et al.*, 2011; *Witte et al.*, 2009] caused by the clean air measures for 2008 Beijing Olympics and the economic downturn. These significant changes in anthropogenic emissions could be observed by a satellite such as the OMI instrument. For accurate simulations, an updated emission inventory for China or East Asia is needed in the future, and the technique developed in this dissertation can act as a useful tool to evaluate the new emission data.

3) Preliminary analysis of the aerosols simulated by CMAQ showed good agreement with the MODIS aerosol product, but further investigations are needed. First, to compensate for the missing dust in CMAQ, global models such as GOCART or GEOS-Chem should be employed to provide information on dust aerosols such as dust AOD and mass. Second, long-term surface observations such as AERONET deployed in China can be utilized to evaluate CMAQ simulations to take advantage of these month-long simulation results. Third, additional field campaigns on aerosol composition and optical characteristics are necessary in future to investigate the aerosol properties in China, so that a better algorithm such as CMAQ-RM can be

established for the reconstruction of AODs based on the simulated aerosol species and concentrations.

Appendix I Savitzky-Golay Smoothing

Savitzky-Golay smoothing is an improved algorithm to perform the least-square techniques. In this approach the least-square value of a given point is computed as a weighted combination of itself and *m* points on either side, therefore a moving (*2m+1* points) least-squares fit across the data [*Savitzky and Golay*, 1964]. Savitzky-Golay smoothing tends to preserve features of the data such as maxima and minima, which are usually flattened by adjacent moving averaging.

The algorithm of Savitzky-Golay smoothing involves utilization of pre-set weighting coefficients (A_{-n}, $A_{-(n-1)}$…, A_{n-1}, A). The values of weighting coefficients are determined by the filter width and polynomial degree, and coefficients (http://www.chem.uoa.gr/applets/appletsmooth/appl_smooth2.html) of typical "quadratic smooth" are in Table AI.1. So the smoothed data $(y_k)_s$ can be expressed in:

$$(y_k)_s = \frac{\sum_{i=-N}^{N} A_i y_{k+i}}{\sum_{i=-N}^{N} A_i} \qquad \text{(Equation AI.1)}$$

Table AI.1 Weighting coefficients of "quadratic Savitzky-Golay Smoothing".

Filter Width	Data position (*i*)								
(*2n+1*)	-4	-3	-2	-1	0	1	2	3	4
9	-21	24	39	54	59	54	39	24	-21
7		-2	3	6	7	6	3	-2	
5			-3	12	17	12	-3		

Appendix II Case studies on the emission rate of air pollutants from different type of power plants

The EPA CEMS program were continuously monitoring the NO_x and SO_2 emissions from the point sources, and the 1997 to 2011 data of MD, OH, PA, VA, and WV were utilized in this study. The CEMS dataset also included simultaneous measurements of CO_2, heat input and gross load in hourly and daily values, so I could evaluate the long-term trend of emissions of air pollutant to track the efficacy of regulation on the these point sources. In this study, the values of $\frac{dE_{NO_x}}{dE_{CO_2}}$ and $\frac{dE_{SO_2}}{dE_{CO_2}}$ in JJA are calculated to investigate the additional NO_x/SO_2 mass released through burning of fossil fuel per one unit mass of CO_2. There are three types of electric generating units (EGUs) commonly in use: 1) base-load EGUs running all year-around except a short time for maintenance; 2) intermediate, load-following EGUs running specifically for expected enhanced power demand such as air conditioning in warm weather; 3) peaking units running temporarily to compensate for a deficit of electric demand, for instance under heat waves in the summer. The type 1 and 2 EGUs are usually coal-fired or oil-fired boilers with steam turbines, often equipped with sophisticated scrubbers to remove NO_x and SO_2. These steam turbines need time to adjust their power output, and can not change the gross load instantaneously. The short time power demand, i.e., peak demand, is met by the peaking units, normally gas turbines burning natural gas or oil. Gas turbines can kick in quickly with the demand of the electrical grid. The characteristics of SO_2 and NO_x emissions of a given power plant are determined by the type of fuel used and the efficiency of scrubber. Here I conducted a case study on three individual power

plants (Table AII.1 and Figure AII.1) and tested their performance in JJA during the past few years.

Table AII.1 Characteristics of Brand Shores, Brunot Island, and Rocksprings stations.

Name	Location	Lat	Lon	Notes
Brandon Shores	Glen Burnie, MD	39.18	-76.53	coal-fired boiler with steam turbine, renovated in 2002, and 2007-2010
Brunot Island	Pittsburg, PA	40.46	-80.04	oil-fired simple cycle peaking units, scrubbed added in 2002
Rock Springs	Rock Springs, MD	39.72	-76.15	natural gas turbine, built in 2003 with scrubber

The Brandon Shores generating station was first modified in 2002 through adding NO_x scrubber, and then renovated in 2007-2010 to comply with the Healthy Air Act. Figure AII.2 presents the linear fit ($Y = A + BX$, r as correlation) of 2000 and 2009 data. It is observed that in 2000, both NO_x and SO_2 emissions were highly correlated with the amount of coal burning (i.e., CO_2 emissions), but by 2009, NO_x emissions had been reduced significantly and scattered high values were observed. This demonstrated that the NO_x scrubber worked effectively, and fuel consumption (CO_2 emissions) is no longer a good predictor of NO_x emissions. The trends of linear regression slope (B) and correlation (r) in Brand Shores generating station are presented in Figure AII.3. The trend of $\frac{dE_{NO_x}}{dE_{CO_2}}$ shows a sharp decrease after 2002, the EPA NO_x SIP call, decreasing to a low value around zero. This shows that the NO_x scrubber was highly effective to remove

39.18139, -76.53777
© 2012 Google
Google

40.4638, -80.044
Brunots Island
Brunot Island
© 2012 Google
©2010 Google

Figure AII.1 Google Earth images of Brand Shores, Brunot Island, and Rock Springs generating stations. (BS: top, BI: middle, RS: bottom).

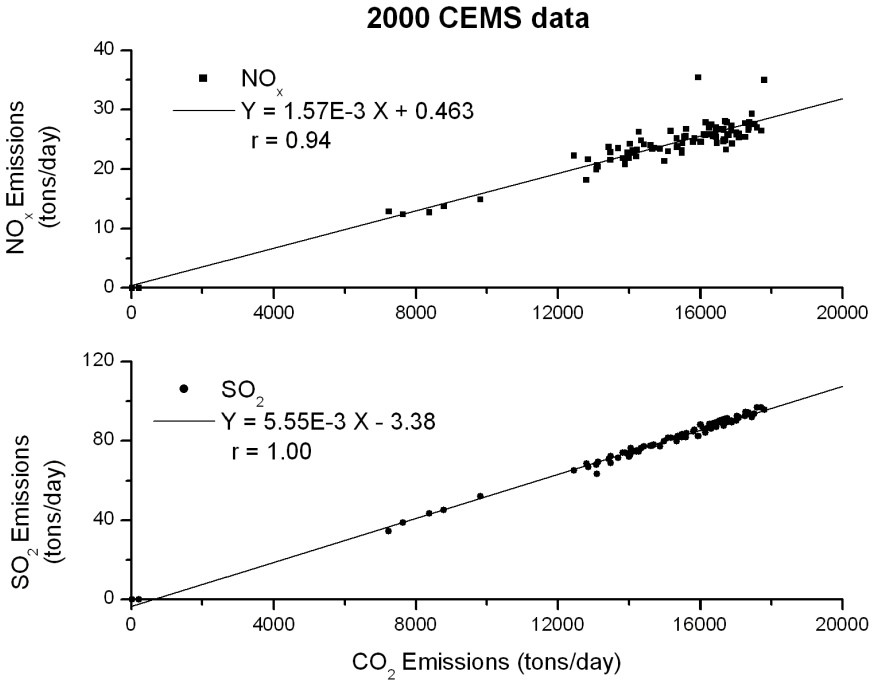

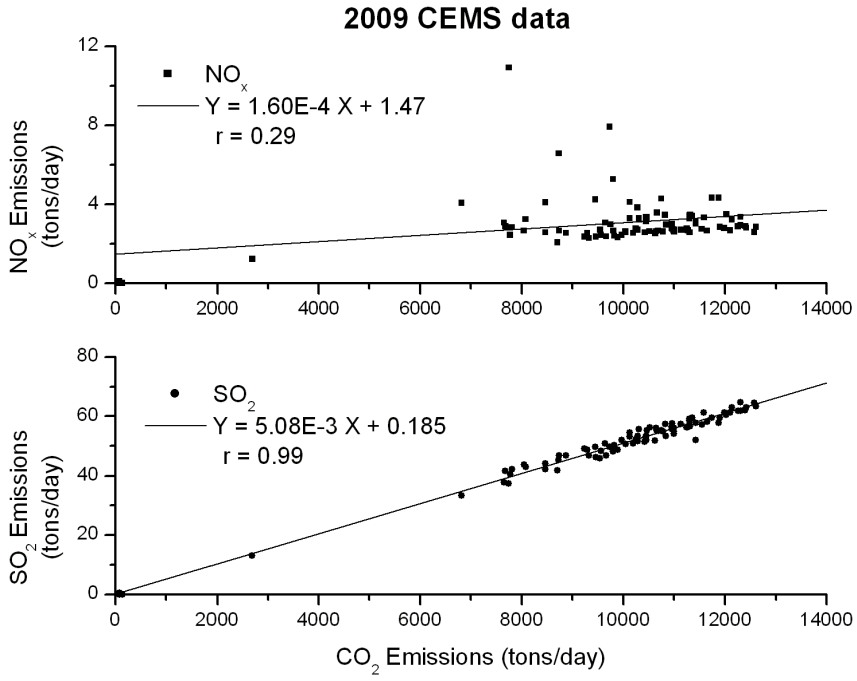

Figure AII.2 Scatter plot and linear regression of NO_x and CO_2 emissions of Brandon Shores generating station during JJA in 2000 (top) and 2009 (bottom).

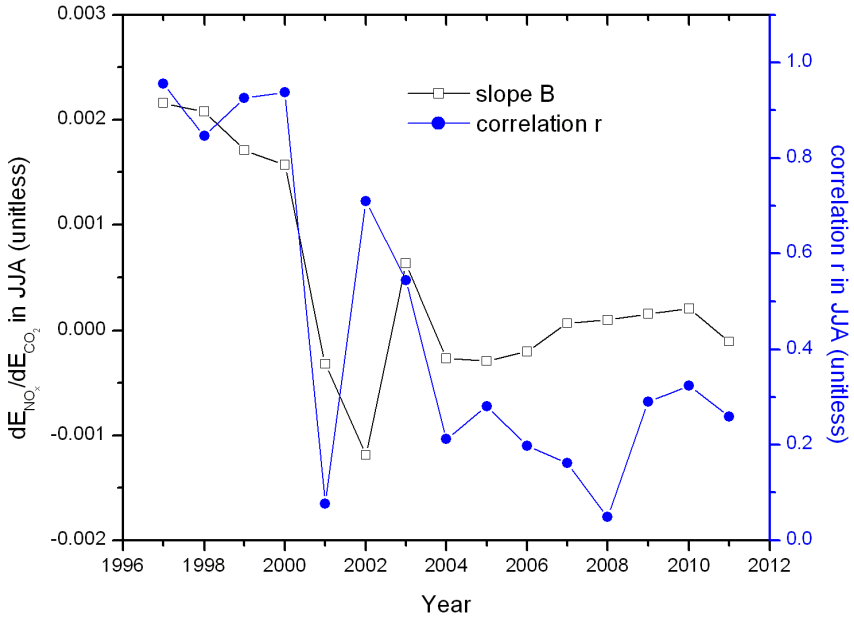

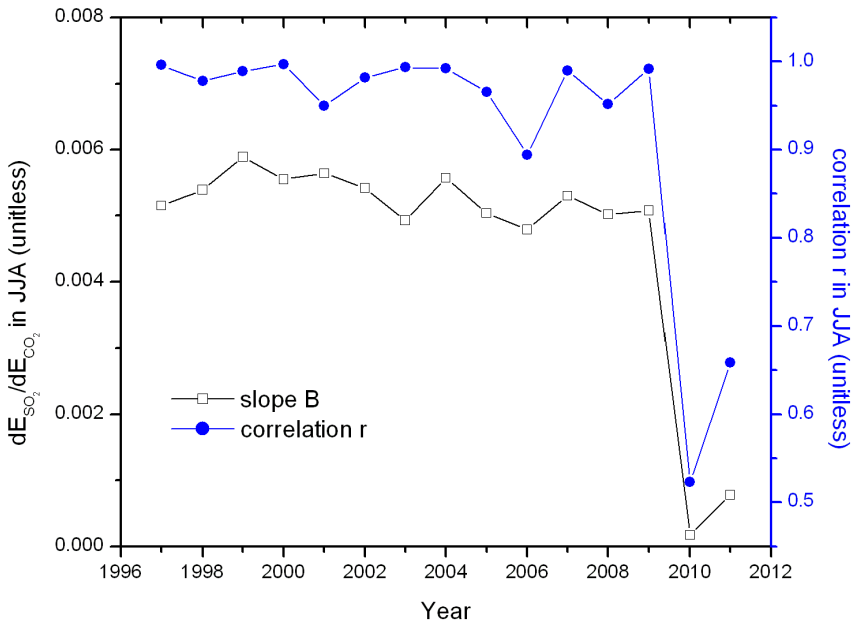

Figure AII.3 Trend of slope of air pollutant emissions versus CO_2 emissions of Brand Shores generating station in JJA (top: NO_x vs. CO_2, bottom: SO_2 vs CO_2).

almost all NO_x generated. The value of $\frac{dE_{SO_2}}{dE_{CO_2}}$ remained the ~0.005 until 2010, when it decreased to ~0.001. The magnitudes of these large decreases are ~100% for $\frac{dE_{NO_x}}{dE_{CO_2}}$ and ~90% for $\frac{dE_{SO_2}}{dE_{CO_2}}$.

Similar approaches were applied to Brunot Island generating station, which was renovated in 2002. The linear regressions of NO_x and SO_2 emissions versus CO_2 emissions are presented in Figure AII.4. Compared with the coal-fired EGU, this oil-fired peaking unit emitted much less SO_2 per unit mass of CO_2 emissions. And the rate

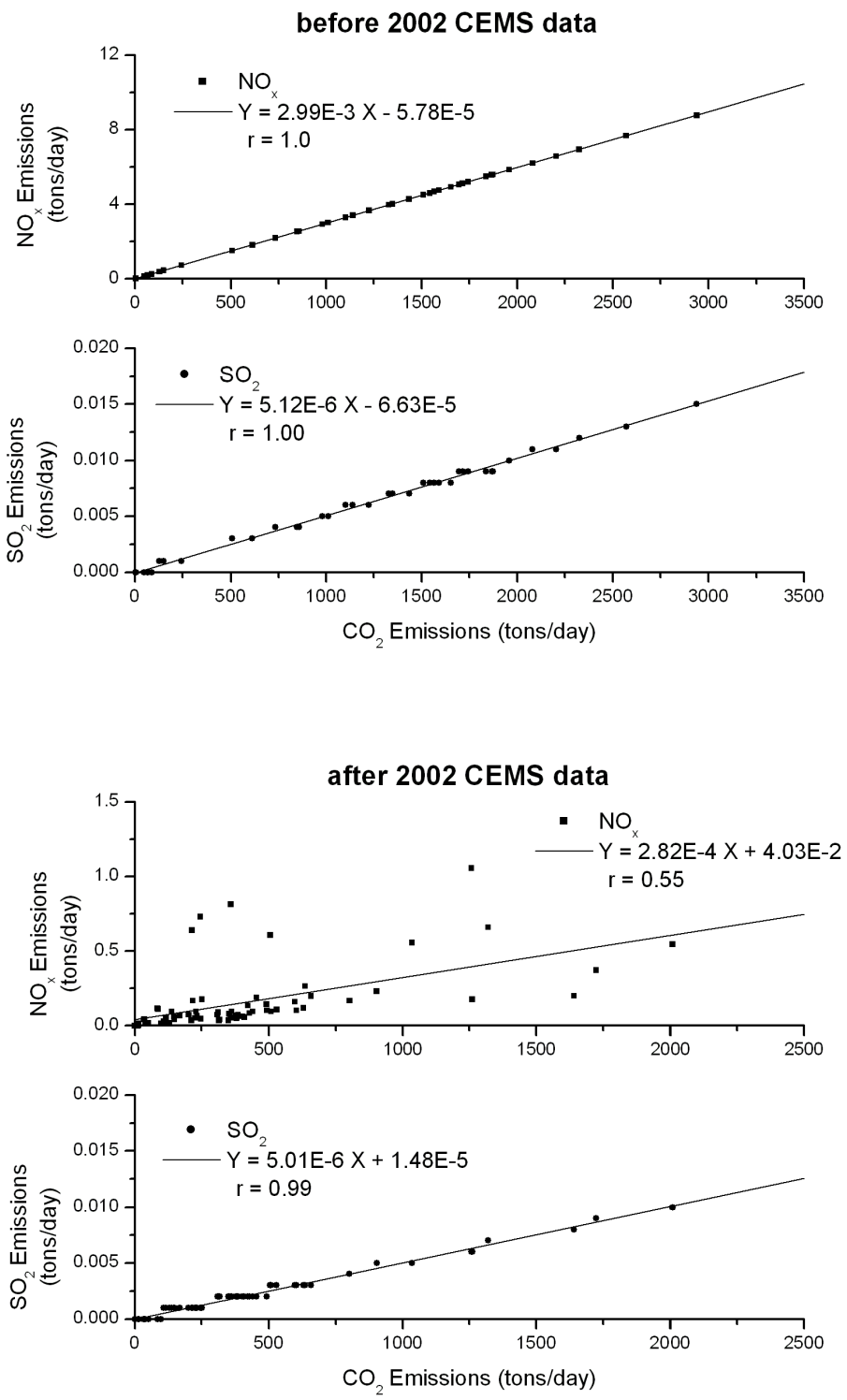

Figure AII.4 Scatter plot and linear regression of NO_x and CO_2 emissions of Brunot Island generating station in JJA before 2002 and after 2002.

of NO_x emissions per unit mass of CO_2 emissions decreased ~90% with installation of NO_x scrubber. The $\frac{dE_{NO_x}}{dE_{CO_2}}$ and $\frac{dE_{SO_2}}{dE_{CO_2}}$ of natural gas turbines in the Rock Springs peaking unit shows the similar results, low SO_2 emissions and high NO_x emissions per unit mass of CO_2 emissions (Figure AII.5). The summary of $\frac{dE_{NO_x}}{dE_{CO_2}}$ and $\frac{dE_{SO_2}}{dE_{CO_2}}$ of these three power plants is presented in Table AII.2. On the SO_2 emissions, coal-fired power plants can reduce the SO_2 emission rate by ~90% (5.0×10^{-3} to 5.0×10^{-4}) through scrubbing sulfur, but still have an emission rate (5.0×10^{-4}) two order of magnitude higher than the usage of heavy oil and natural gas (5.0×10^{-6}), because there is significant amount of sulfur in the coal while the sulfur content is negligible in heavy oil and natural

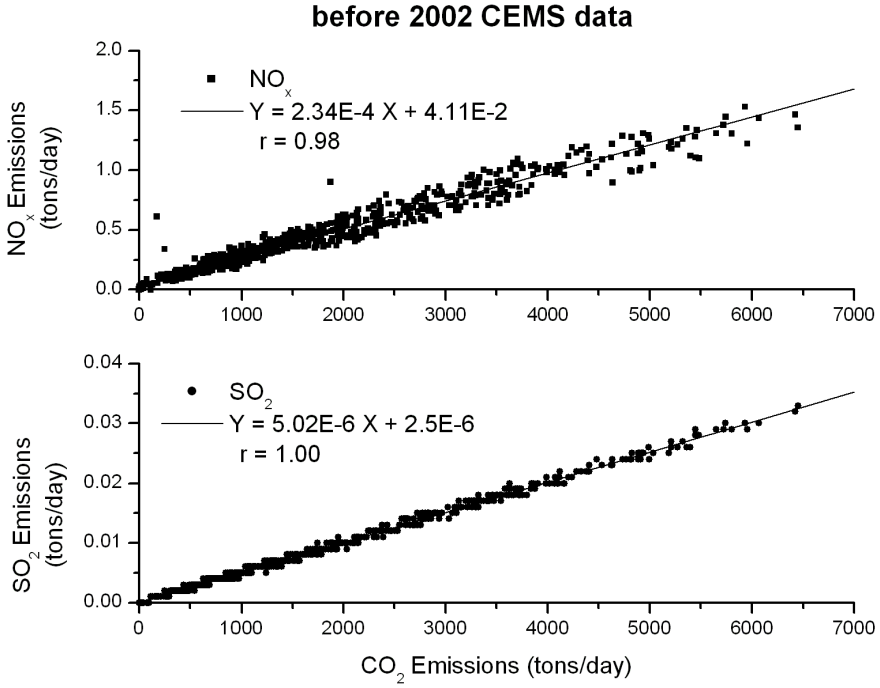

Figure AII.5 Scatter plot and linear regression of NO_x and CO_2 emissions of Rock Springs generating station in JJA.

gas. On the emission of NO_x, without a scrubber, the NO_x emission rates from coal-fired power plants and oil-fired peaking units are comparable. The scrubbers in coal-fired power plants are extremely effective removing almost all NO_x emissions produced, while

Table AII.2 Summary of NO_x and SO_2 emission rate per unit mass of CO_2.

Power Plants	Type	Facility	NO_x/CO_2	SO_2/CO_2
Brandon Shores	coal-fired boiler	no scrubber	2.50E-03	5.00E-03
		with scrubber	~0.0	5.00E-04
Brunot Island	oil-fired peaking unit	no scrubber	3.00E-03	5.00E-06
		with scrubber	7.00E-04	5.00E-06
Rocksprings	nature gas turbine	with scrubber	2.40E-04	5.00E-06

peaking units using both heavy oil and natural gas emit more NO_x, one order of magnitude higher.

I also conducted the similar analysis on the $\frac{dE_{NO_x}}{dE_{CO_2}}$ and $\frac{dE_{SO_2}}{dE_{CO_2}}$ for the five states near the DC-Baltimore area. The trends of values are presented in Figure AII.6 and Figure AII.7. Both NO_x and SO_2 emissions were highly correlated to CO_2 emissions in the five states, except for WV where the renovations were conducted during summer. On the state levels, the value of $\frac{dE_{NO_x}}{dE_{CO_2}}$ decreased from ~3.0×10^{-3} to ~1.0×10^{-3}, and the value of $\frac{dE_{SO_2}}{dE_{CO_2}}$ decreased from ~7.0×10^{-3} to ~3.0×10^{-3}, suggesting great strides on scrubbing air pollutants have been made. I also observed the abrupt change of $\frac{dE_{SO_2}}{dE_{CO_2}}$

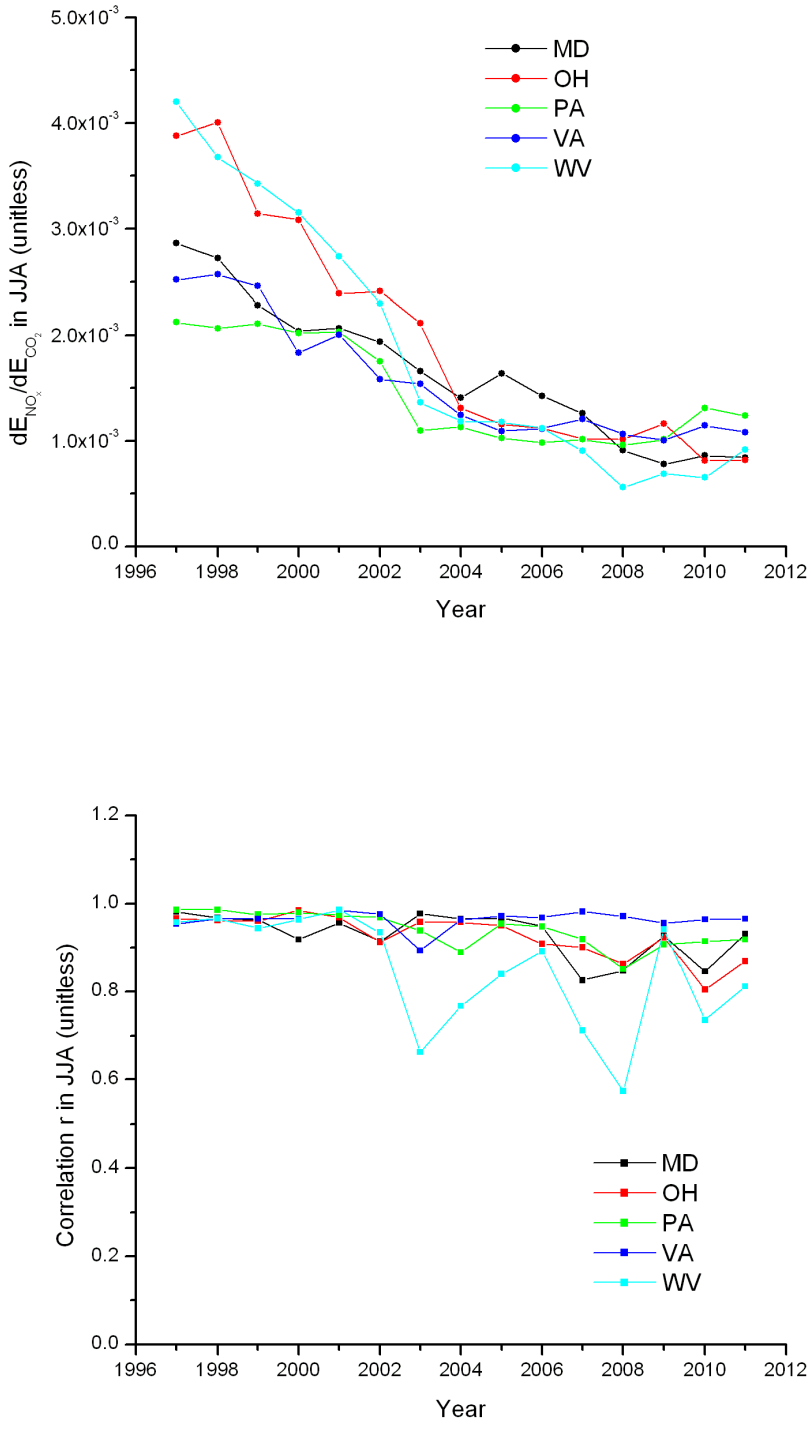

Figure AII.6 Trends of linear regression analysis on CEMS NO_x data in MD/OH/PA/VA/WV during JJA (top: slope, bottom: correlation).

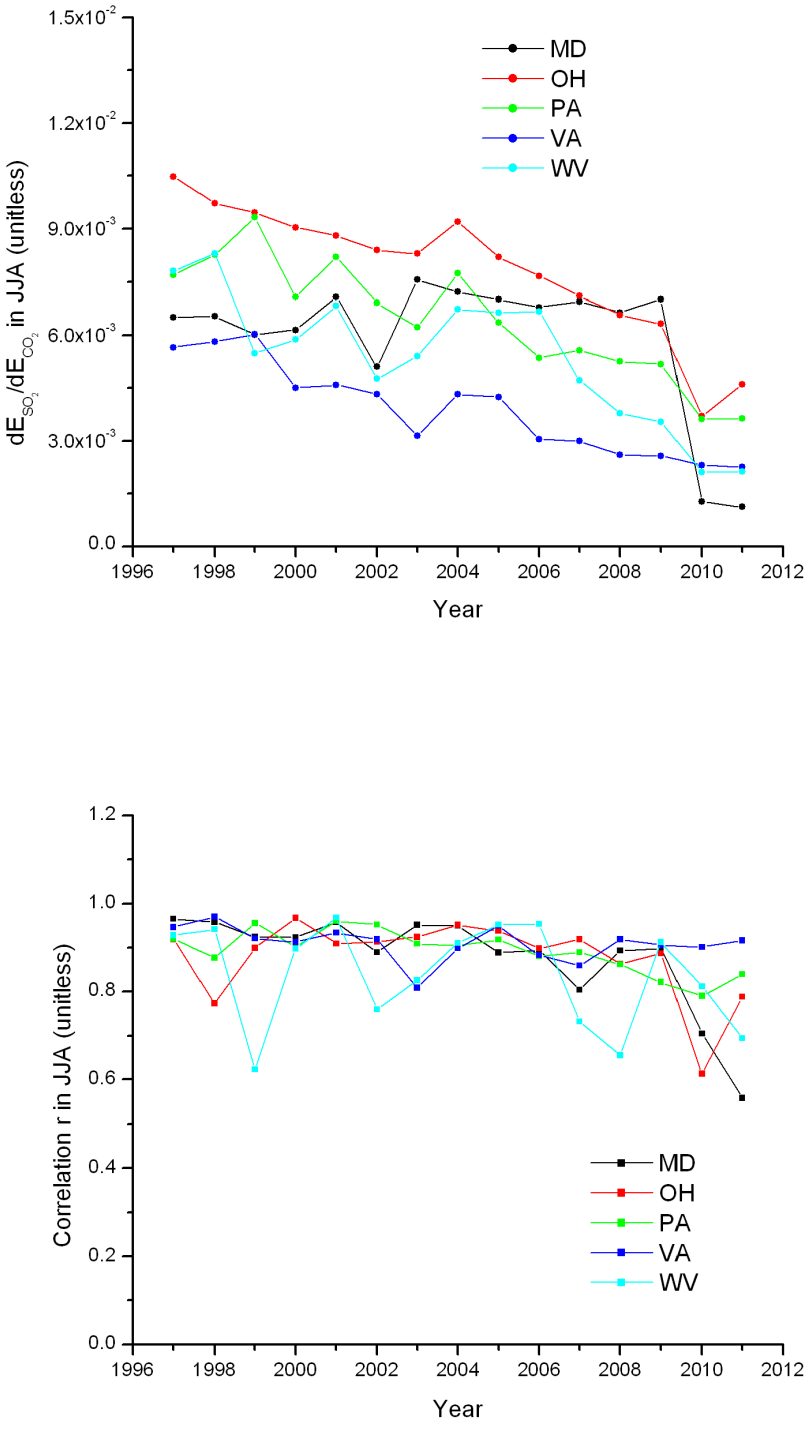

Figure AII.7 Trends of linear regression analysis on CEMS SO_2 data in MD/OH/PA/VA/WV during JJA (top: slope, bottom: correlation).

from MD after 2009, from ~9.0 $\times 10^{-3}$ to ~1.0 $\times 10^{-3}$; apparently caused by the local Healthy Air Act. This legislation brought MD's SO_2 emissions rate from the highest to the lowest ranking in the five states. The MD case demonstrated the extent to which SO_2 emission could be reduced with local regulations.

Appendix III NOAA HYSPLIT back trajectories of SO_2 plumes in the FT observed during the EAST-AIRC aircraft campaign

Figure AIII.1 Observations and back trajectories of Plume 1 in Table 4.3.

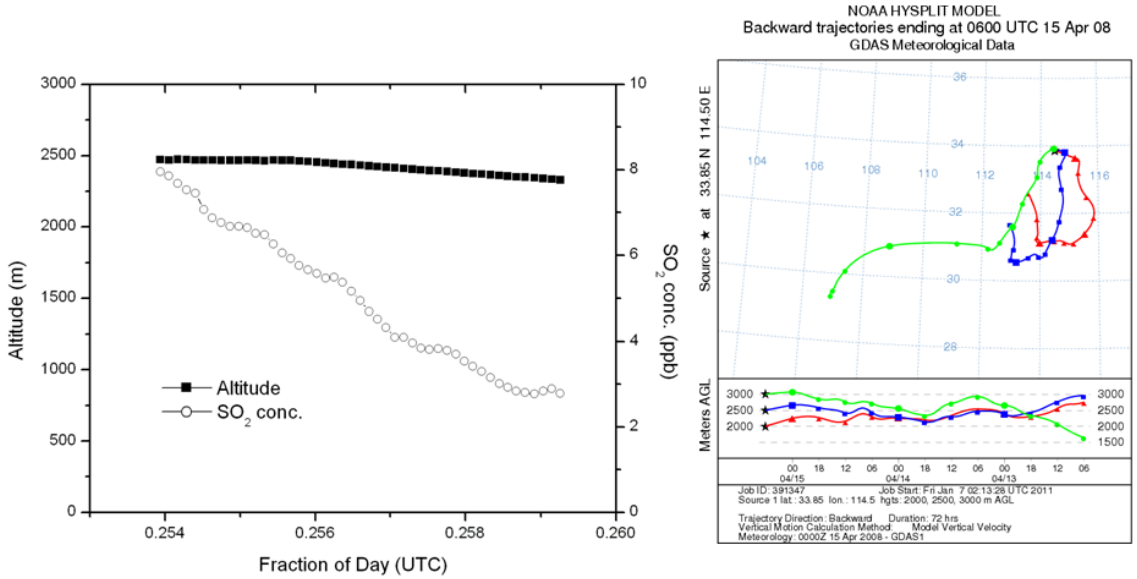

Figure AIII.2 Observations and back trajectory of Plume 2 in Table 4.3.

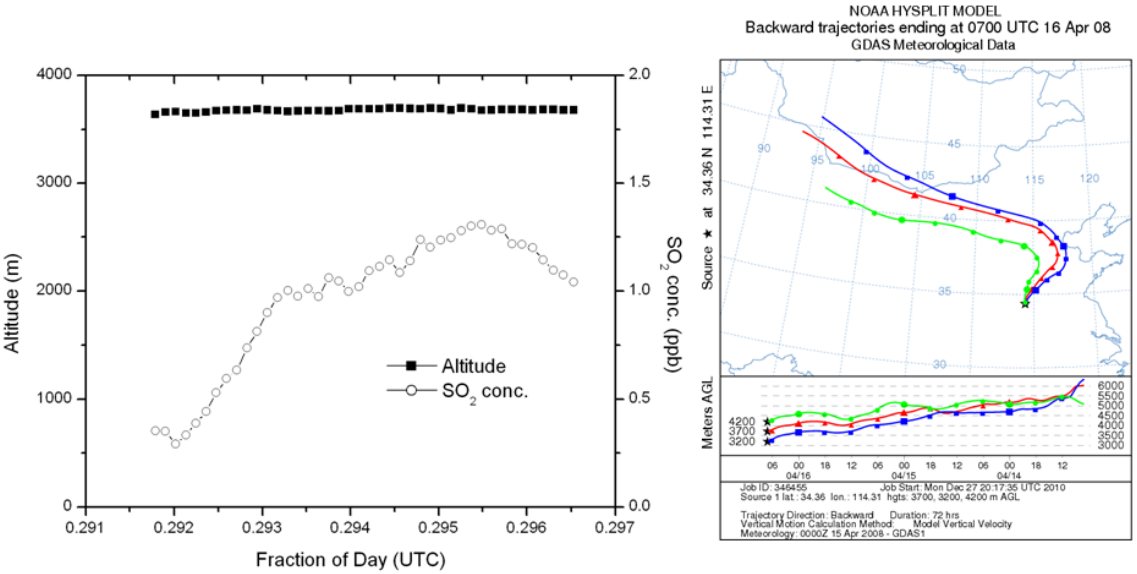

Figure AIII.3 Observations and back trajectory of Plume 4 in Table 4.3.

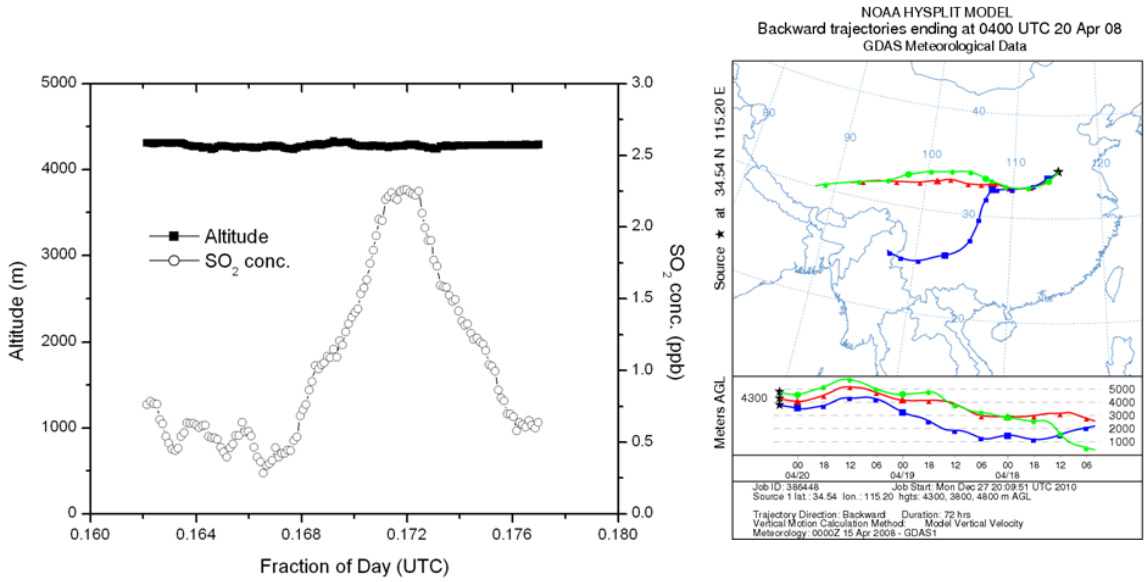

Figure AIII.4 Observations and back trajectory of Plume 5 in Table 4.3.

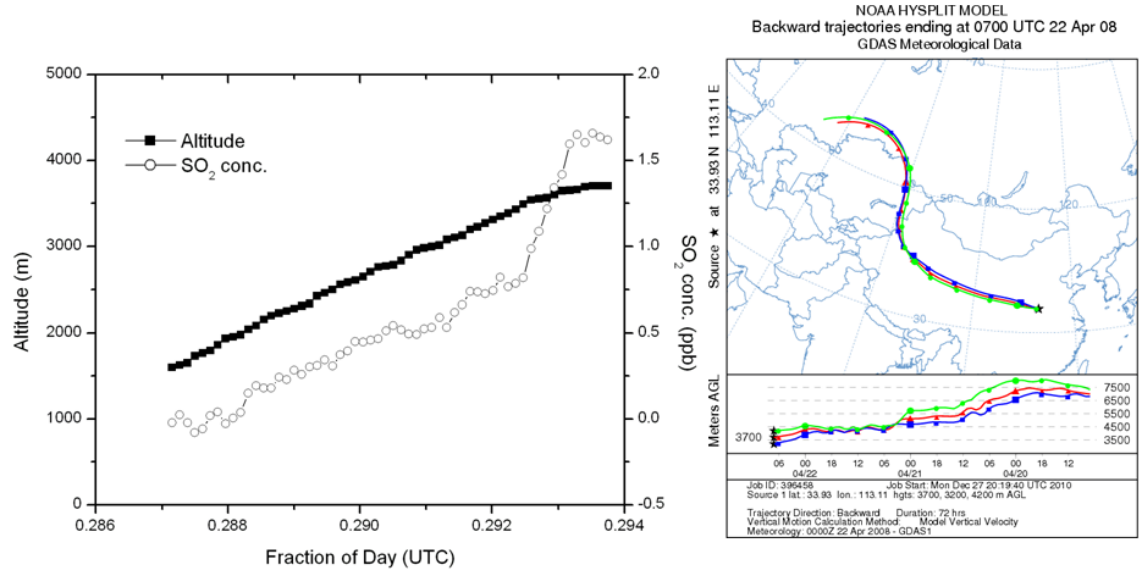

Figure AIII.5 HYSPLIT forward trajectory of plume 3 in Table 4.3.

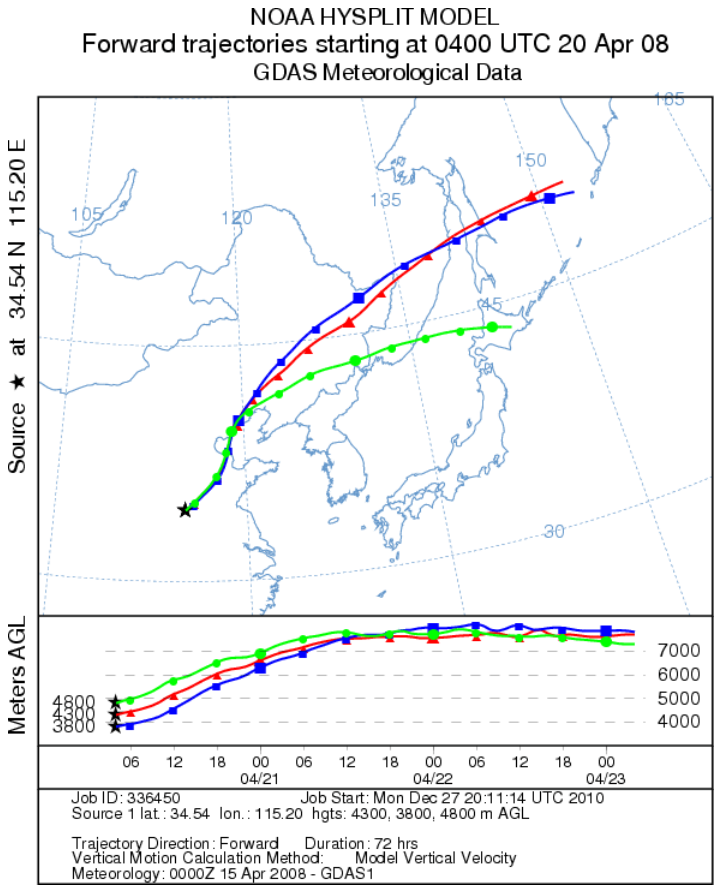

Appendix IV Validation of OMISO2 PBL products vs. the integrated EAST-AIRC SO_2 column contents

Figure AIV.1 Evaluation of *in situ* measurements vs. the co-located OMISO2 PBL products. The dotted line represents the Y = X (1:1) line. X and Y error bars describe the uncertainties of aircraft observations and OMI PBL column estimates. Solid line is linear regression passing through zero.

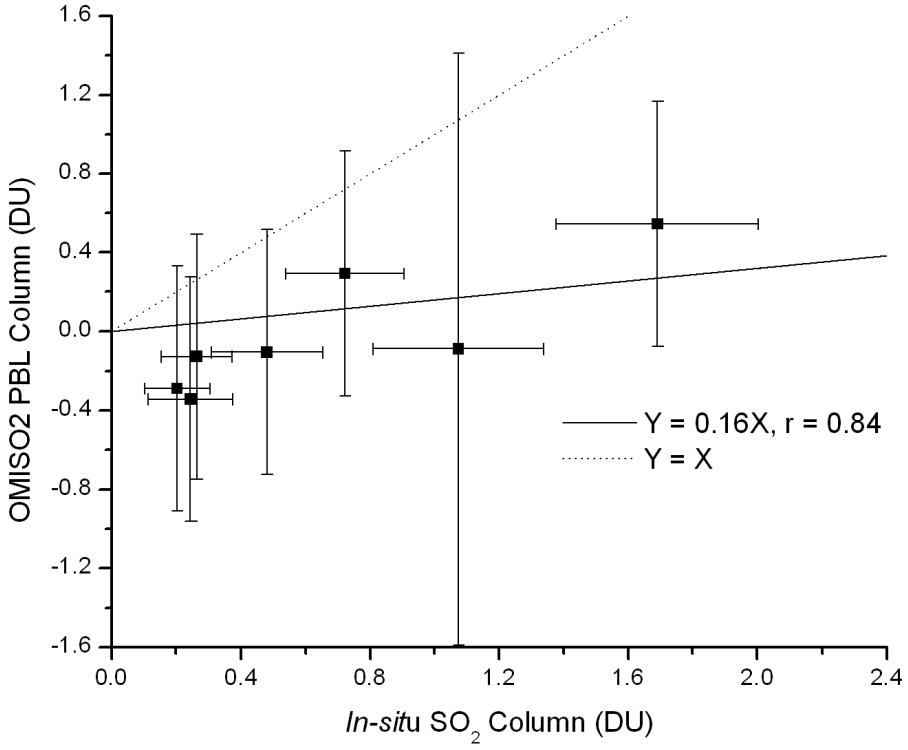

Appendix V. Evaluation of the WRF simulation

I evaluated the WRF outputs with respect to *in situ* observation of meteorological fields. In Figure AV.1, the sea level pressure (SLP) of WRF is compared with the surface analysis of East Asia ((http://web.kma.go.kr/eng/weather/images/analysischart.jsp) from Korea Meteorological Administration (KMA) on April 18, 2008. The location of high pressure system over the East China Sea and low pressure over southwestern China is captured well by the WRF simulation.

To verify the long-time accuracy, I selected the city Zhengzhou, a megacity in the central of my nested domain, and collected historic meteorological observations from wundergournd.com (http://www.wunderground.com/global/stations/57083.html) for the month-long campaign. The comparison of the surface observation and WRF simulation is illustrated in Figure AV.2 with a linear regression analysis, showing that the WRF model underestimates these parameters. It is worth noting that the weather station is located in the urban area of Zhengzhou city with the microsccale meteorology such as urban heat island effects [*Zhang et al.*, 2009a], while the nested domain only has 10 km resolution, which is too coarse to capture these local effects.

The sounding data (http://weather.uwyo.edu/upperair/seasia.html) of Zhengzhou station (113.67 °E, 34.76 °N) were used to evaluate the corresponding WRF variables (Figure AIV.3) at UTC 0 (local time 8 am), April 18, 2008. They demonstrate that WRF can re-construct the meteorological field accurately, and drive the CMAQ model precisely. The input FNL data only have $1^{o} \times 1^{o}$ horizontal resolution

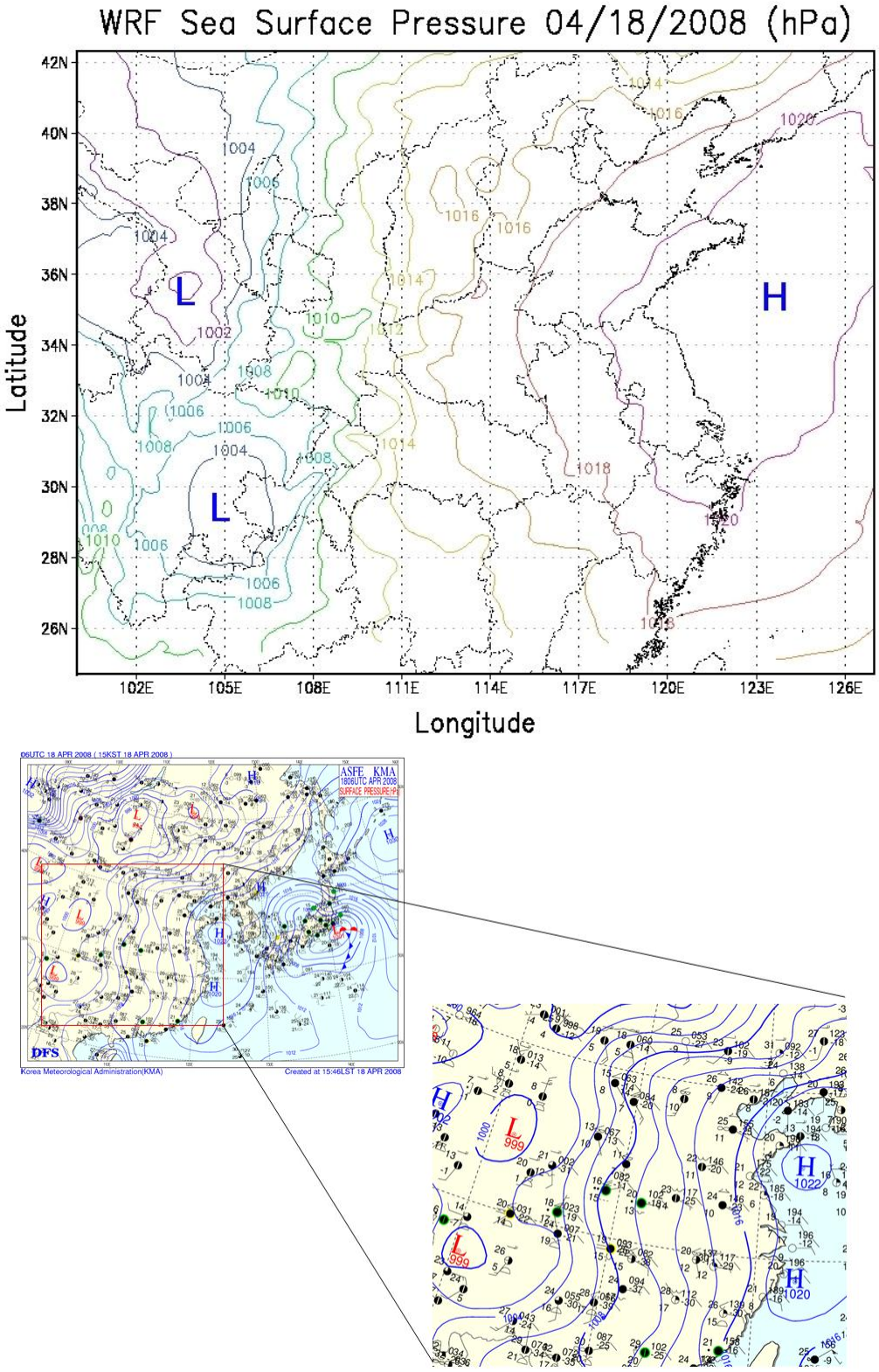

Figure AV.1 Evaluation of WRF SLP (upper panel) and KMA surface analysis (lower panel) in 04/18/2008.

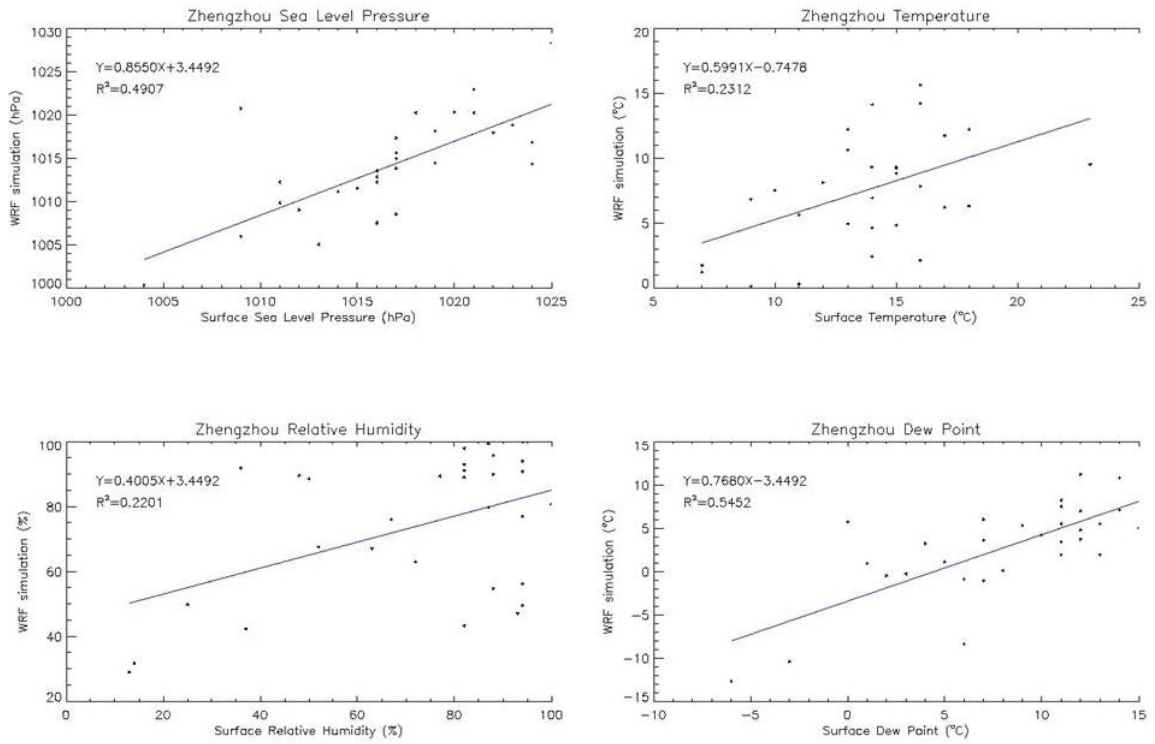

Figure AV.2 Evaluation of meteorological observations from WRF and Zhengzhou city.

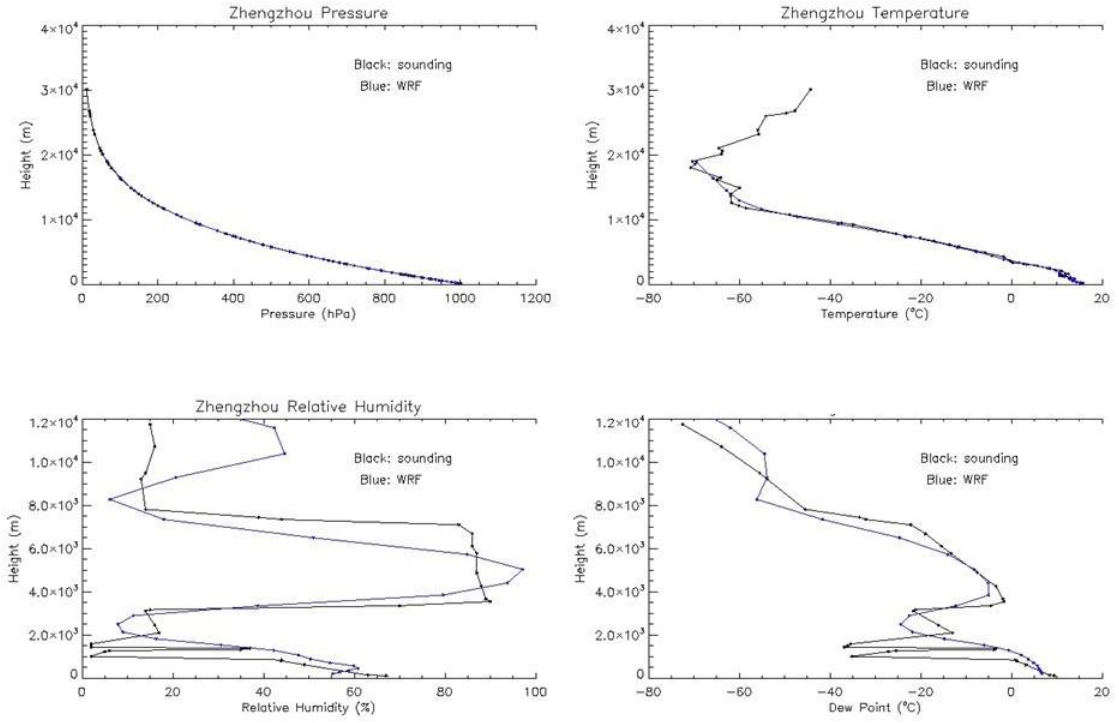

Figure AV.3 Comparison of WRF meteorological data and sounding observations (UTC 00, 04/18/2008).

(111.2 km × 111.2 km on mid-altitude), and after processed by nested WRF runs the final products (10 km × 10 km) agrees well with the sounding records.

Appendix VI. Analyses of the SO_2 dry deposition calculated by MCIP and CMAQ

The SO_2 dry deposition velocity and rate from NoMR_HPPM and MR_HPPM runs are analyzed here, with case studies on 04/05/2008 (sunny day) and 04/18/2008 (cloudy day). The deposition velocity of SO_2 from two MCIP runs is calculated (Figure AVI.1), to show the difference between the base case without mesophyll resistance and the case with mesophyll resistance. The MR_HPPM run decreased the SO_2 deposition velocity by 0.15-0.2 cm/s for April 4 and 0.35-0.5 cm/s for April 18 respectively. The deposition velocity has been reduced by up to 30-60% in the central and eastern domain, yielding the value ~1.0 cm /s for 04/05 and less than 0.5 cm/s for 04/18. At the same time, the deposition velocity is increased by 30-50 % in the western domain with the absolute values less than 0.05 cm/s. There values are much close to the real measurements conducted in China.

Actual dry deposition amounts are calculated by the CMAQ model (Figure AVI.2), these depend not only on SO_2 deposition velocity but also ion other factors such as land use, PBL height, topography, and pollutant concentration. So the SO_2 dry deposition varies depending on locations. In the case of April 5, the SO_2 dry deposition rate increases 0-10% in the west and southeast of the domain, and decreases 30-50% in the center and northeast of the domain. In the case of April 18, the SO_2 dry deposition rate increases less than 10% in the west of the domain and decreases 40-60% in the center of the domain. Both cases have the same pattern of dry deposition change of with respect to locations. The terrain height of the domain is depicted in Figure AVI.3. It is observed that the modification of mesophyll resistance tends to increase the SO_2 dry deposition in the mountainous region and drastically decrease the

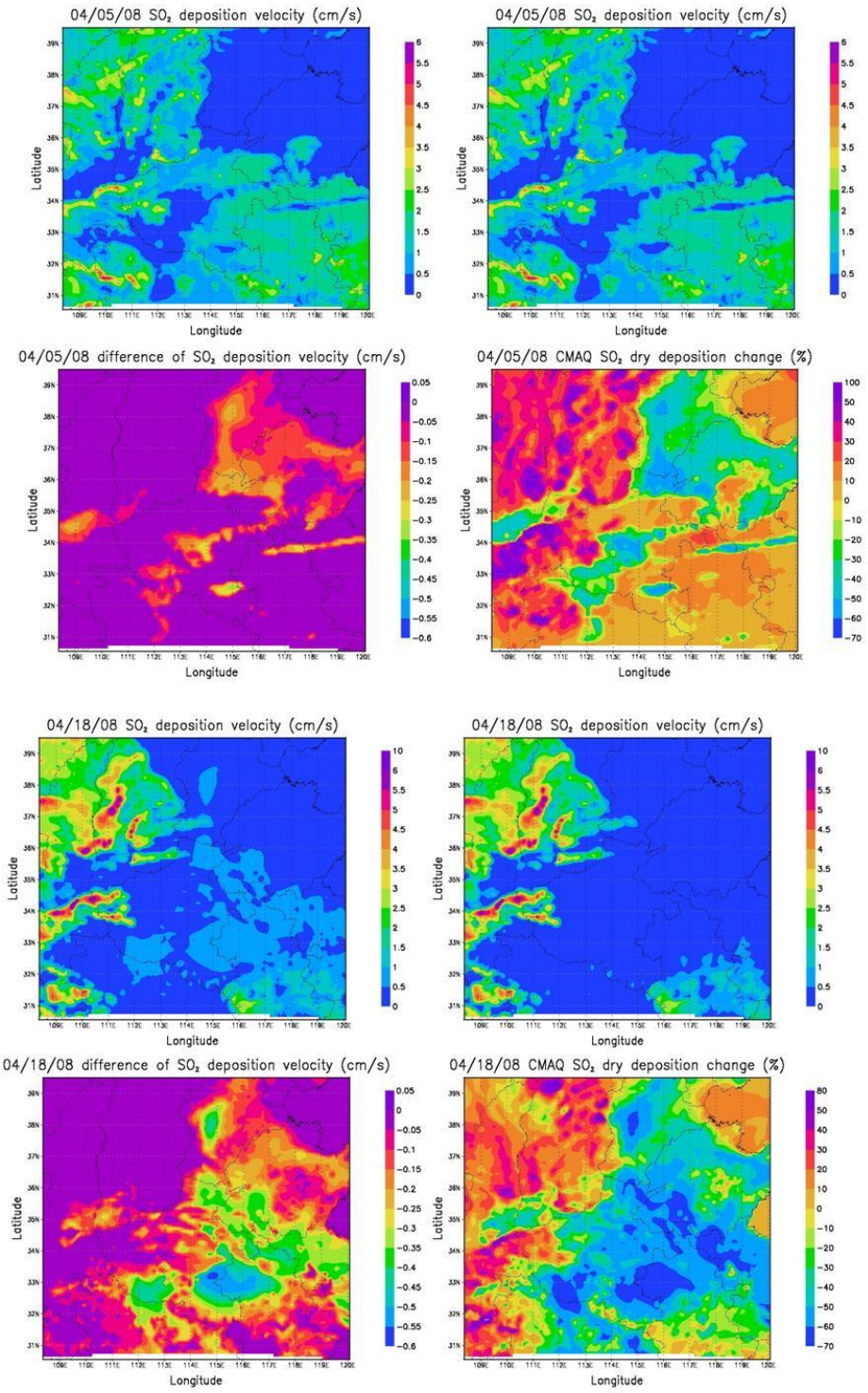

Figure AVI.1 SO_2 dry deposition velocity map of 04/05/2008 (upper panel) and 04/18/2008 (lower panel). In each panel, the left/right up represents the dry deposition velocity without/with MR; the left/right bottom show the absolute/relative change.

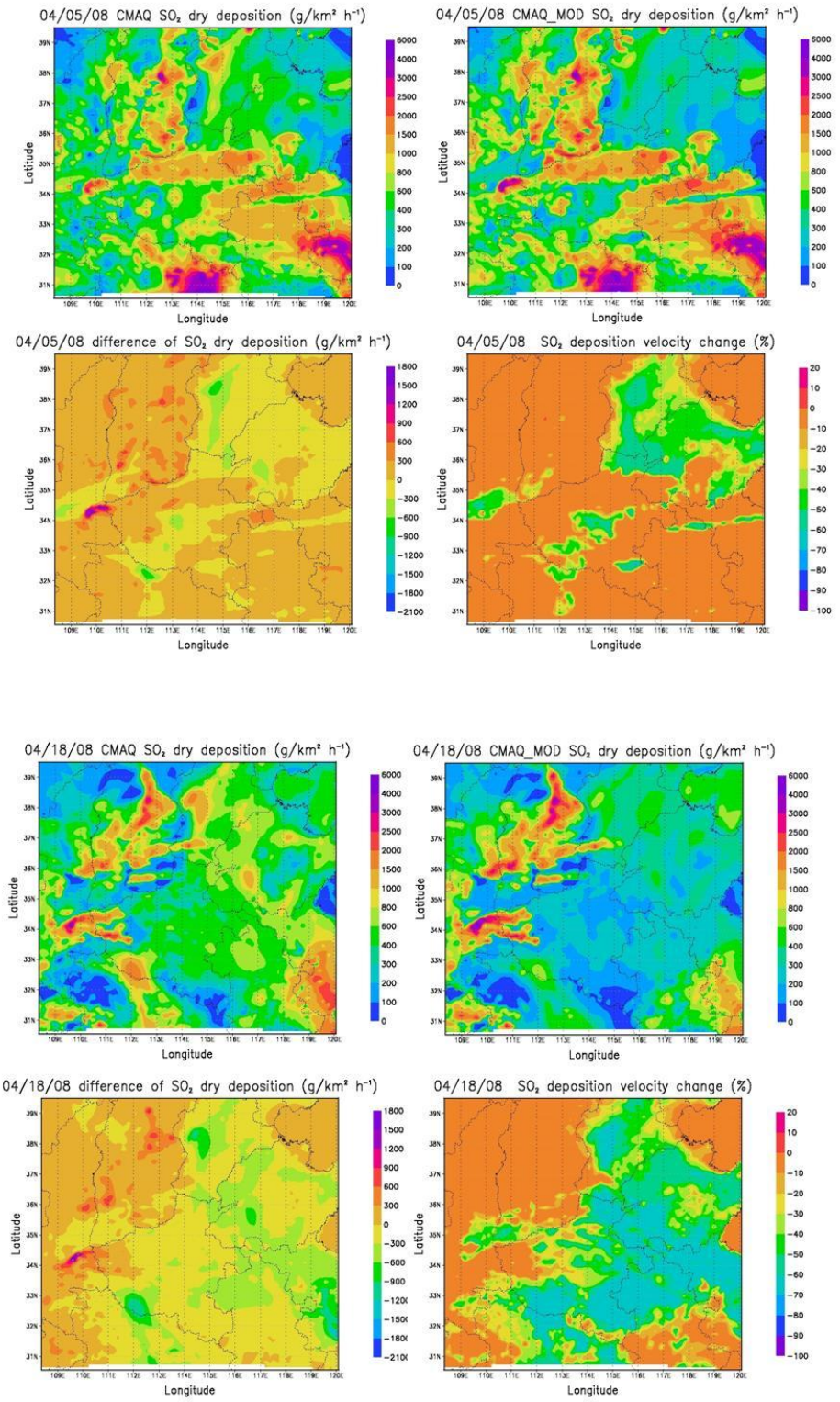

Figure AVI.2 SO_2 dry deposition flux map of 04/05/2008 (upper panel) and 04/18/2008 (lower panel). In each panel, the left/right up represents the dry deposition flux without/with MR; the left/right bottom show the absolute/relative change.

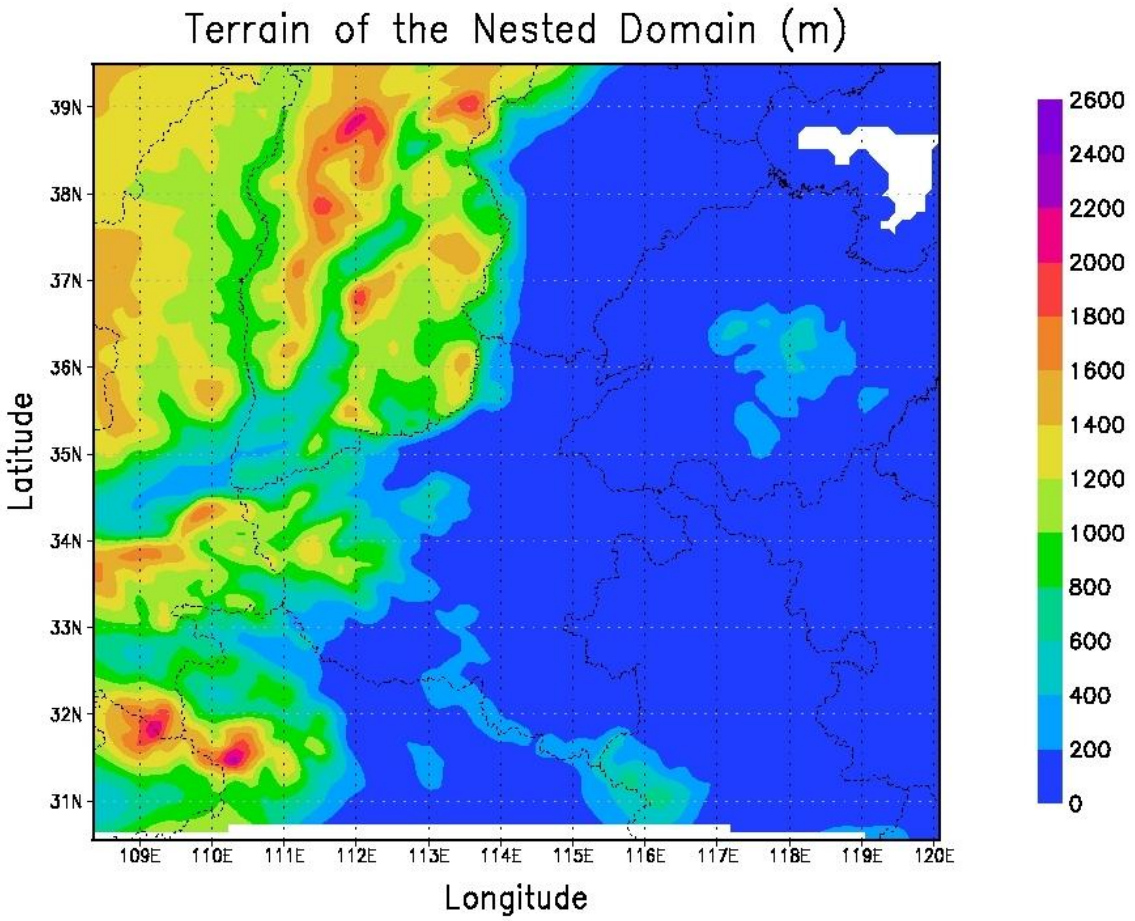

Figure AVI.3 Terrain height of the nested domain.

rate on the plains. This is possible due to greater vegetation coverage on the plains than on the mountains, and the more plants have higher resistance effects to SO_2 reducing the SO_2 dry deposition.

In conclusion, the modification of SO_2 mesophyll resistance to the CMAQ models has great effects on the SO_2 deposition velocity and dry deposition. For plains with high vegetation, the SO_2 deposition velocity has been decreased up to 60%, while over the mountainous region with less vegetation the SO_2 increases slightly. The accurate SO_2 dry deposition greatly benefits the calculation of sulfur-compound balance.

Appendix VII. Discussion on the SO_2 lifetime due to sinks and chemistry

To investigate the details of SO_2 chemistry, I also calculated the life time with respect to specific sinks such as dry and wet deposition of SO_2. The monthly average wet deposition was trivial for this month with the value several orders lower than the emission, while the average dry deposition rate is 1.46×10^{-3} mol/km^2 s, which results in life time of 73.69 hours (3 days) and equals to 34.02% of the emission flux. This is higher than the dry deposition, ~ 30% measured in U.S. [*Wesely and Hicks*, 2000].

Apart from dry deposition, SO_2 remaining in the atmosphere will be oxidized to sulfur-compounds such as H_2SO_4 and ammonium sulfate. Therefore I should take into account both gas phase OH oxidization and aqueous phase H_2O_2 oxidization. The rate constant k for the reaction (1) can be calculated as: $k = \frac{7.4 \times 10^{11}}{1 + \frac{237}{p}}$ (cm^3 mol^{-1} s^{-1}) where p is the pressure in mmHg, or $k = \frac{1.229 \times 10^{-12}}{1 + \frac{237 \times 1.33}{p}}$ where p is the pressure in hPa [*Paraskevopoulos et al.*, 1983]. I focus on the OH reaction in the lower atmosphere (altitude less than 2000 m), where the mean value is 1.80×10^6 molecules/cm^3, and the mean rate constant k is 9.09×10^{-13} cm^3 molecules^{-1} s^{-1}. The lifetime for the pseudo-first order reaction is defined as: $\tau = \frac{1}{k'} = \frac{1}{k[OH]}$, and the value is 140 hours (~ 5.8 days).

The aqueous H_2O_2 oxidization is hard to be parameterized because it involves the complicated process of dissolving SO_2 into water droplets. Here I simply compared the absolute concentration of H_2O_2 and SO_2 at two altitudes (500m and 1500m) for

04/05/2008 and 04/18/2008 (Figure AVII.1). The weather of 04/05 was controlled by high pressure systems, sunny and cloud-free; while the weather pattern of 04/18 was influenced by a passing frontal system the day before, so it had moderate cloud coverage and humidity. In the central of our nest domain, the case of 04/05 had high SO_2 concentration of 10 ppbv within the PBL (500 m) and 6 ppbv in the free troposphere (1500 m), while the case of 04/18 had low SO_2 concentration of 6 ppbv and 2 ppbv respectively. On the other hand, H_2O_2 has the opposite trend of vertical distribution, because H_2O_2 production relies on the UV photon flux that does not effectively penetrate into the low atmosphere. In the case of April 5, 0.2 ppbv and 0.8 ppbv H_2O_2 were found at 500 m and 1500 m respectively, while in the cloudy April 18, 0.6 ppbv and 0.8 ppbv H_2O_2 were observed. The higher H_2O_2 concentration in April 18 was produced by high humidity providing sufficient H_2O vapor. The opposite vertical trends of SO_2 and H_2O_2 decreased the influence of H_2O_2 oxidization, because most of the SO_2 was constrained within the PBL. Therefore, in a typical sunny day without cloud, the H_2O_2 oxidization had a trivial contribution to the total SO_2 loss, and in a cloudy day with sufficient atmospheric water content, the H_2O_2 chemistry accounted for at most 10% of the SO_2 loss. In short, it is difficult to quantify the effect of H_2O_2 due to the complex physics and chemistry, but the H_2O_2 chemistry dominates in the case of April 18 500m and the H_2O_2 concentration is anti-correlated with the SO_2 concentration. The aqueous oxidization of SO_2 occurs in the cloud, and better numerical simulations of the clouds are essential to get the chemistry right.

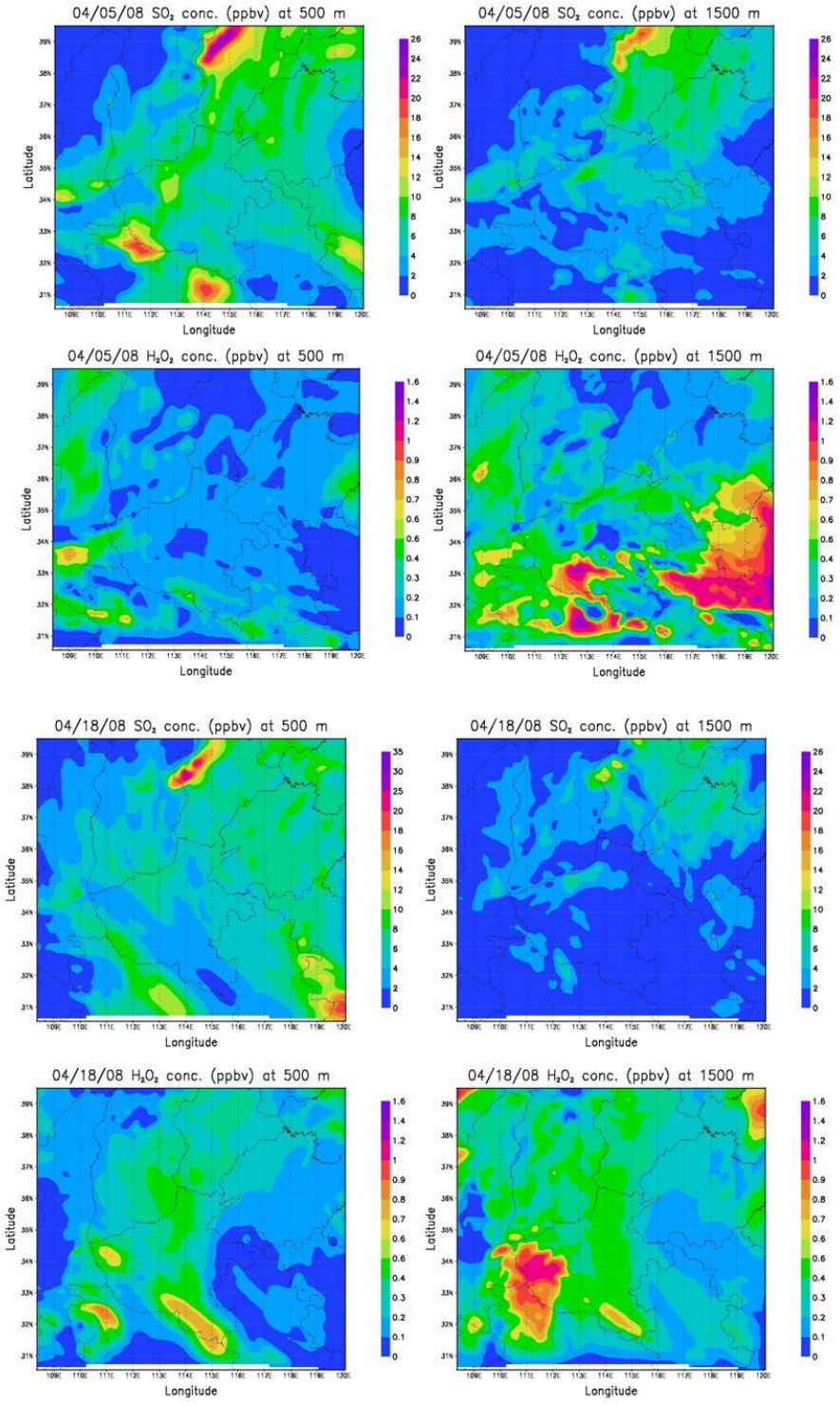

Figure AVII.1 H_2O_2 and SO_2 concentrations from the CMAQ simulation (upper panel, 04/05/2008; lower panel, 04/18/2008).

Column contents of sulfate aerosols were computed for this campaign, and the average value was 16.1 kg S/km^2. From the discussion above, the SO_2 left in atmosphere is 7.8 kg S/km^2 sulfur. If we assume that all the SO_2 was oxidized to sulfate aerosols with 100% conversion efficiency within one day, daily it would produce 2.4 kg/km^2 sulfate, which was much more than the sulfate content. The low conversion rate was also confirmed by the slow oxidization of OH and H_2O_2. Therefore, these results inferred to the possibility that SO_2 could be transported out of the domain without being attacked by oxidants.

On the other hand, the sulfate content also should be balanced by sources and sinks. The direct mean sulfate emission (688 g/km^2) was trivial compared with the mean sulfate content; proving the major source was SO_2 oxidization. The mean daily losses due to dry deposition and wet deposition were 7.0 kg/km^2 and 1.9 kg/km^2 respectively. It was reasonable, in the real world the major sink of sulfate is wet deposition. The life time due to the total deposition was 43 hours (1.8 days), which was much shorter than the typical lifetime in southeast China (3.6 days) [*Barth and Church*, 1999; *Li et al.*, 2010]. Similar to SO_2, sulfate is advected out of the domain.

In summary, the simply box model calculation demonstrated that the sulfur content was not balanced based with local sources and sinks. Therefore, it is important to take the horizontal advection into account, while they are not incorporated in the CMAQ model. It revealed the necessity of developing the CMAQ model to improve the SO_2 evaluation.

Appendix VIII Advection of SO_2 and sulfate aerosols

The daily data are calculated by averaging advection for 30 days. The positive/negative signs indicate the flow into/out of the domain respectively. The strong positive signals near the surface in Eastern boundary (near 31 ℃N) are related to the strong sulfur emissions near Shanghai in the YRD region. Analyses showed that the advection through the Eastern and Northern boundary of the nested domain.

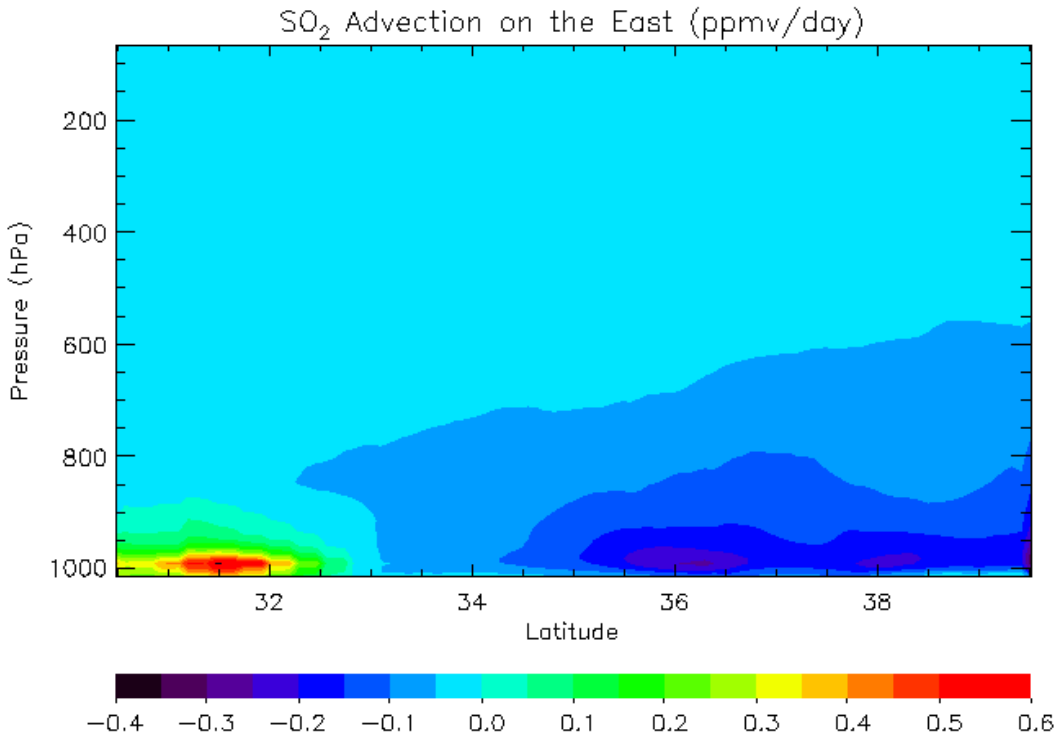

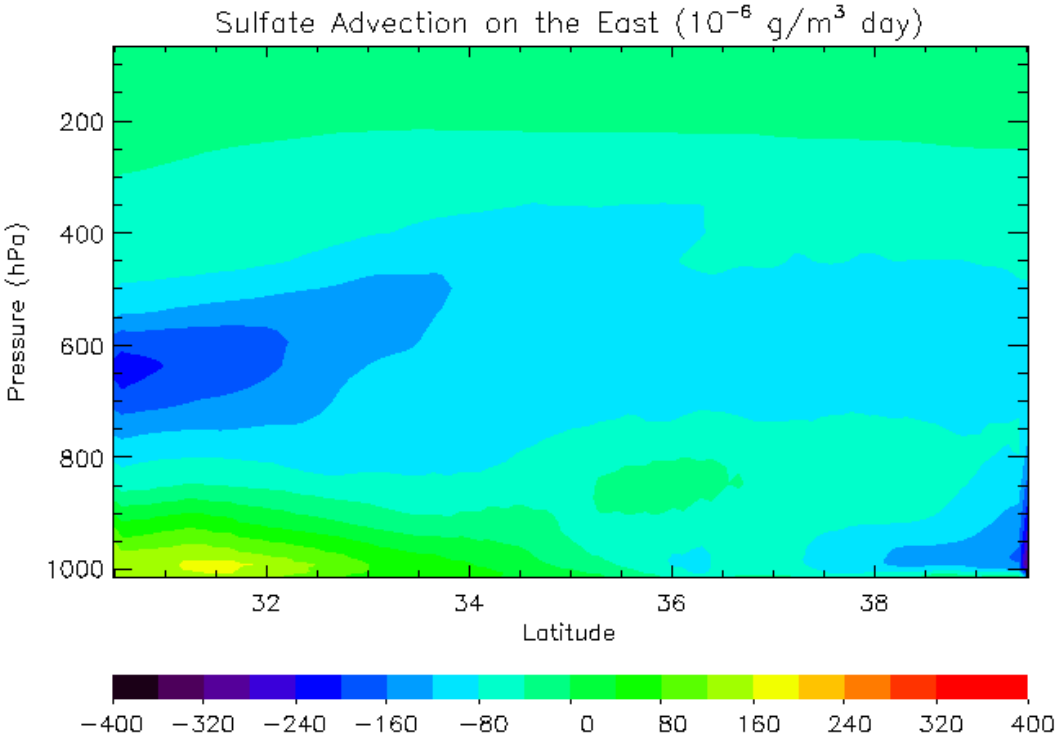
Sulfate Advection on the East (10^{-6} g/m^3 day)
Pressure (hPa)
200
400
600
800
1000
32
34
36
38
Latitude
−400
−320
−240
−160
−80
0
80
160
240
320
400

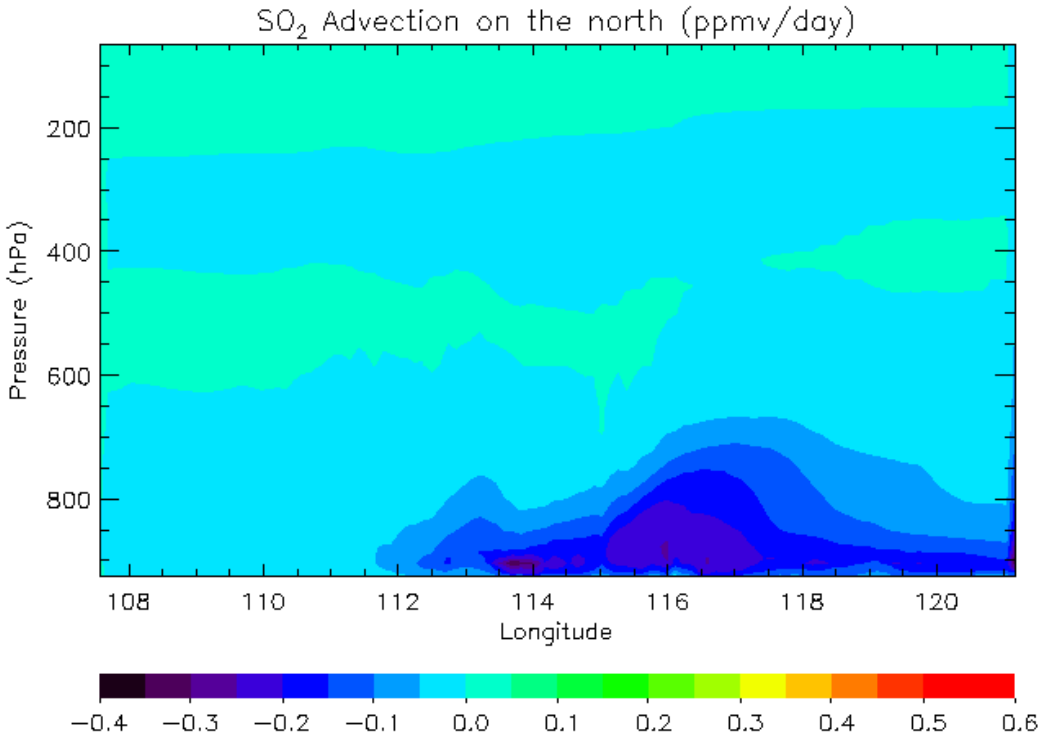
SO_2 Advection on the north (ppmv/day)
Pressure (hPa)
200
400
600
800
108
110
112
114
116
118
120
Longitude
−0.4
−0.3
−0.2
−0.1
0.0
0.1
0.2
0.3
0.4
0.5
0.6

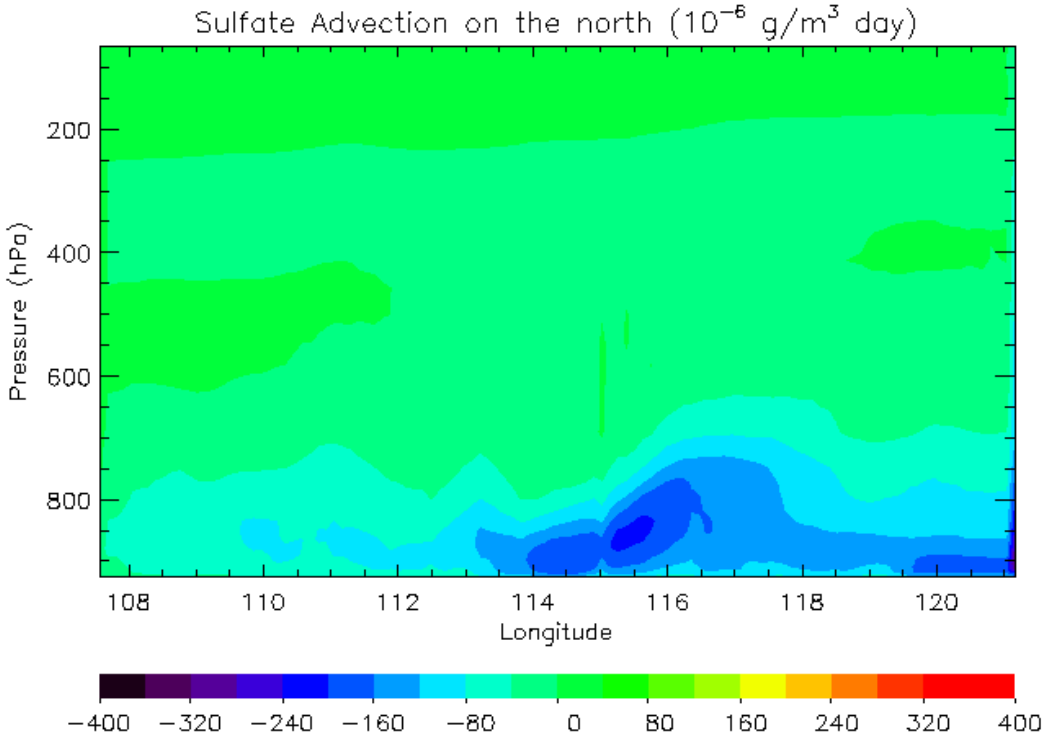

Figure AVIII.1 SO_2 and sulfate advections in and out of the nested domain.

Bibliography

Albrecht, B. A. (1989), AEROSOLS, CLOUD MICROPHYSICS, AND FRACTIONAL CLOUDINESS, *Science*, *245*(4923), 1227-1230.

Anderson, H. R. (2009), Air pollution and mortality: A history, *Atmospheric Environment*, *43*(1), 142-152.

Anderson, J., et al. (2000), Halogen occultation experiment confirmation of stratospheric chlorine decreases in accordance with the Montreal Protocol, *Journal of Geophysical Research-Atmospheres*, *105*(D4), 4483-4490.

Anderson, J. G., et al. (1989), OZONE DESTRUCTION BY CHLORINE RADICALS WITHIN THE ANTARCTIC VORTEX - THE SPATIAL AND TEMPORAL EVOLUTION OF CLO-O3 ANTICORRELATION BASED ON INSITU ER-2 DATA, *Journal of Geophysical Research-Atmospheres*, *94*(D9), 11465-11479.

Anderson, J. G., et al. (1991), FREE-RADICALS WITHIN THE ANTARCTIC VORTEX - THE ROLE OF CFCS IN ANTARCTIC OZONE LOSS, *Science*, *251*(4989), 39-46.

Anderson, T. L., et al. (1996), Performance characteristics of a high-sensitivity, three-wavelength, total scatter/backscatter nephelometer, *Journal of Atmospheric and Oceanic Technology*, *13*(5), 967-986.

Barrie, L. A., et al. (1981), THE INFLUENCE OF MID-LATITUDINAL POLLUTION SOURCES ON HAZE IN THE CANADIAN ARCTIC, *Atmospheric Environment*, *15*(8), 1407-1419.

Barrie, L. A., et al. (2001), A comparison of large-scale atmospheric sulphate aerosol models (COSAM): overview and highlights, *Tellus Series B-Chemical and Physical Meteorology*, *53*(5), 615-645.

Barth, M. C., and A. T. Church (1999), Regional and global distributions and lifetimes of sulfate aerosols from Mexico city and southeast China, *Journal of Geophysical Research-Atmospheres*, *104*(D23), 30231-30239.

Bates, D. R., and M. Nicolet (1950), THE PHOTOCHEMISTRY OF ATMOSPHERIC WATER VAPOR, *Journal of Geophysical Research*, *55*(3), 301-327.

Bates, D. R. (1984), RAYLEIGH-SCATTERING BY AIR, *Planet Space Sci.*, *32*(6), 785-790.

Bell, M. L., and D. L. Davis (2001), Reassessment of the lethal London fog of 1952: Novel indicators of acute and chronic consequences of acute exposure to air pollution, *Environmental Health Perspectives*, *109*, 389-394.

Berglen, T. F., et al. (2004), A global model of the coupled sulfur/oxidant chemistry in the troposphere: The sulfur cycle, *Journal of Geophysical Research-Atmospheres*, *109*(D19), 27.

Bloomer, B. J., et al. (2009), Observed relationships of ozone air pollution with temperature and emissions, *Geophysical Research Letters*, *36*.

Bloomer, B. J., et al. (2010), Changes in seasonal and diurnal cycles of ozone and temperature in the eastern US, *Atmospheric Environment*, *44*(21-22), 2543-2551.

Bluth, G. J. S., et al. (1992), GLOBAL TRACKING OF THE SO2 CLOUDS FROM THE JUNE, 1991 MOUNT-PINATUBO ERUPTIONS, *Geophysical Research Letters*, *19*(2), 151-154.

Bluth, G. J. S., et al. (1993), THE CONTRIBUTION OF EXPLOSIVE VOLCANISM TO GLOBAL ATMOSPHERIC SULFUR-DIOXIDE CONCENTRATIONS, *Nature*, *366*(6453), 327-329.
Bovensmann, H., et al. (1999), SCIAMACHY: Mission objectives and measurement modes, *Journal of the Atmospheric Sciences*, *56*(2), 127-150.
Brasseur, G. P., et al. (1998), MOZART, a global chemical transport model for ozone and related chemical tracers 1. Model description, *Journal of Geophysical Research-Atmospheres*, *103*(D21), 28265-28289.
Bromba, M. U. A., and H. Ziegler (1981), APPLICATION HINTS FOR SAVITZKY-GOLAY DIGITAL SMOOTHING FILTERS, *Anal. Chem.*, *53*(11), 1583-1586.
Brook, R. D., et al. (2004), Air pollution and cardiovascular disease - A statement for healthcare professionals from the expert panel on population and prevention science of the American Heart Association, *Circulation*, *109*(21), 2655-2671.
Burrows, J. P., et al. (1999), The global ozone monitoring experiment (GOME): Mission concept and first scientific results, *Journal of the Atmospheric Sciences*, *56*(2), 151-175.
Byun, D., and K. L. Schere (2006), Review of the governing equations, computational algorithms, and other components of the models-3 Community Multiscale Air Quality (CMAQ) modeling system, *Appl. Mech. Rev.*, *59*(1-6), 51-77.
Byun, D. W., and J. E. Ching (1999), Science algorithm of the EPA Models-3 Community Multi-scale Air Quanlity (CMAQ) modeling system. Chap. 12, *U.S. Environmental Protection Agency, Research Triangle Park, NC, EPA/600/R-99/030*.
Byun, D. W., et al. (2007), Chapter 12, Meteorology-Chemistry Interface Processor (MCIP) for Models-3 Community Multiscale Air Quality (CMAQ) Modeling System, *U.S. EPA, CMAQ Science Documentation*, available at http://www.epa.gov/AMD/CMAQ/ch12.pdf.
Calvert, J. G., and W. R. Stockwell (1984), Mechanism and Rates of the Gas Phase Oxidations of Sulfur Dioxides and Nitrogen Oxides in the Atmosphere, *Acid Precipitation Series, Butterworth, Stoneham MA*, *3*, 1-62.
Camalier, L., et al. (2007), The effects of meteorology on ozone in urban areas and their use in assessing ozone trends, *Atmospheric Environment*, *41*(33), 7127-7137.
Carn, S. A., et al. (2007), Sulfur dioxide emissions from Peruvian copper smelters detected by the Ozone Monitoring Instrument, *Geophysical Research Letters*, *34*(9).
Carn, S. A., et al. (2009), Tracking volcanic sulfur dioxide clouds for aviation hazard mitigation, *Natural Hazards*, *51*(2), 325-343.
Castellanos, P. (2009), Analysis of Air Quality with Numerical Simulations (CMAQ), and Observations of Trace Gases, *PhD Dissertation, University of Maryland, College Park*.
Castellanos, P., et al. (2009), The sensitivity of modeled ozone to the temporal distribution of point, area, and mobile source emissions in the eastern United States, *Atmospheric Environment*, *43*(30), 4603-4611.
Castellanos, P., et al. (2011), Ozone, oxides of nitrogen, and carbon monoxide during pollution events over the eastern United States: An evaluation of emissions and vertical mixing, *Journal of Geophysical Research-Atmospheres*, *116*, 16.
CESY (2005), Energy Statistical Yearbook in 2005, *China Statistic Press*.
Chan, C. K., and X. Yao (2008), Air pollution in mega cities in China, *Atmospheric Environment*, *42*(1), 1-42.

Chang, D., et al. (2009), Visibility trends in six megacities in China 1973-2007, *Atmospheric Research*, *94*(2), 161-167.
Chapman, S. (1930), A theory of upper atmospheric ozone, *Mem. Roy. Meteorol. Soc. 3*, 103-125.
Che, H. Z., et al. (2007), Horizontal visibility trends in China 1981-2005, *Geophysical Research Letters*, *34*(24), 5.
Chen, B. H., et al. (2011), Air Pollution and Health Studies in China-Policy Implications, *J. Air Waste Manage. Assoc.*, *61*(11), 1292-1299.
Chin, M., et al. (1996), A global three-dimensional model of tropospheric sulfate, *Journal of Geophysical Research-Atmospheres*, *101*(D13), 18667-18690.
Chin, M., et al. (2000a), Atmospheric sulfur cycle simulated in the global model GOCART: Model description and global properties, *Journal of Geophysical Research-Atmospheres*, *105*(D20), 24671-24687.
Chin, M., et al. (2000b), Atmospheric sulfur cycle simulated in the global model GOCART: Comparison with field observations and regional budgets, *Journal of Geophysical Research-Atmospheres*, *105*(D20), 24689-24712.
Clarke, J. F., et al. (1997), Dry deposition calculations for the clean air status and trends network, *Atmospheric Environment*, *31*(21), 3667-3678.
CMAS (2007), CMAQ v4.6 Operational Guidance Document, *Community Modeling and Analysis System (CMAS), University of North Carolina at Chapel Hill*.
Costabile, F., et al. (2006), A preliminary assessment of major air pollutants in the city of Suzhou, China, *Atmospheric Environment*, *40*(33), 6380-6395.
Crutzen, P. J. (1970), INFLUENCE OF NITROGEN OXIDES ON ATMOSPHERIC OZONE CONTENT, *Q. J. R. Meteorol. Soc.*, *96*(408), 320-&.
DeBell, L. J., et al. (2004), Asian dust storm events of spring 2001 and associated pollutants observed in New England by the Atmospheric Investigation, Regional Modeling, Analysis and Prediction (AIRMAP) monitoring network, *Journal of Geophysical Research-Atmospheres*, *109*(D1), 16.
Deng, X. J., et al. (2008), Long-term trend of visibility and its characterizations in the Pearl River Delta (PRD) region, China, *Atmospheric Environment*, *42*(7), 1424-1435.
Dennis, R. L., et al. (1996), The next generation of integrated air quality modeling: EPA's Models-3, *Atmospheric Environment*, *30*(12), 1925-1938.
Dickerson, R. R., and A. C. Delany (1988), Modification of a commercial gas filter correlation CO detector for enhanced sensitivity, *Journal of Atmospheric and Oceanic Technology*, *5*, 424-431.
Dickerson, R. R., et al. (1995), LARGE-SCALE POLLUTION OF THE ATMOSPHERE OVER THE REMOTE ATLANTIC-OCEAN - EVIDENCE FROM BERMUDA, *Journal of Geophysical Research-Atmospheres*, *100*(D5), 8945-8952.
Dickerson, R. R., et al. (2007), Aircraft observations of dust and pollutants over northeast China: Insight into the meteorological mechanisms of transport, *Journal of Geophysical Research-Atmospheres*, *112*(D24).
Doddridge, B. G., et al. (1998), Ground-based and airborne observations of carbon monoxide during NASA measurements of air pollution from satellite (MAPS) missions SRL-1 and SRL-2, *Journal of Geophysical Research-Atmospheres*, *103*(D15), 19305-19316.

Dunlea, E. J., et al. (2009), Evolution of Asian aerosols during transpacific transport in INTEX-B, *Atmospheric Chemistry and Physics*, *9*(19), 7257-7287.
Eisinger, M., and J. P. Burrows (1998), Tropospheric sulfur dioxide observed by the ERS-2 GOME instrument, *Geophysical Research Letters*, *25*(22), 4177-4180.
Ek, M. B., et al. (2003), Implementation of Noah land surface model advances in the National Centers for Environmental Prediction operational mesoscale Eta model, *Journal of Geophysical Research-Atmospheres*, *108*(D22), 16.
EPA, U. S. (2004), Air Quality Criteria for Particulate Matter (Final Report, Oct 2004), *U.S. Environmental Protection Agency, Washington, DC. , EPA 600/P-99/002aF-bF*.
EPA, U. S. (2006), Air quality criteria for ozone and related photochemical oxidants, Environ. Prot. Agency, , Research Triangle Park, N.C.
EPA, U. S. (2011), The benefits and costs of the Clean Air Act from 1990 to 2020, USEPA Office of Air and Radiation, Washington, DC.
Farman, J. C., et al. (1985), LARGE LOSSES OF TOTAL OZONE IN ANTARCTICA REVEAL SEASONAL CLOX/NOX INTERACTION, *Nature*, *315*(6016), 207-210.
Feichter, J., et al. (1996), Simulation of the tropospheric sulfur cycle in a global climate model, *Atmospheric Environment*, *30*(10-11), 1693-1707.
Finlayson-Pitts, B. J., and J. N. Pitts (1999), *Chemistry of the Upper and Lower Atmosphere*, 1st ed., Academic Press, UK.
Fioletov, V. E., et al. (2011), Estimation of SO2 emissions using OMI retrievals, *Geophysical Research Letters*, *in press*.
G.A.O. (2011), Information on Tall Smokestacks and their Contribution to Interstate Transport of Air Pollution, United States Government Accountability Office (GAO), Washginton D.C.
Geng, F. H., et al. (2009), Aircraft measurements of O-3, NOx, CO, VOCs, and SO2 in the Yangtze River Delta region, *Atmospheric Environment*, *43*(3), 584-593.
Gorry, P. A. (1990), GENERAL LEAST-SQUARES SMOOTHING AND DIFFERENTIATION BY THE CONVOLUTION (SAVITZKY-GOLAY) METHOD, *Anal. Chem.*, *62*(6), 570-573.
Haagensmit, A. J. (1952), CHEMISTRY AND PHYSIOLOGY OF LOS-ANGELES SMOG, *Industrial and Engineering Chemistry*, *44*(6), 1342-1346.
Haagensmit, A. J., and M. M. Fox (1956), OZONE FORMATION IN PHOTOCHEMICAL OXIDATION OF ORGANIC SUBSTANCES, *Industrial and Engineering Chemistry*, *48*(9), 1484-1487.
Haerter, J. O., et al. (2009), Parametric uncertainty effects on aerosol radiative forcing, *Geophysical Research Letters*, *36*.
Hains, J. C. (2007), A Chemical Climatology of Lower Tropospheric Trace Gases and Aerosols over the Mid-Atlantic Region, *PhD Dissertation, University of Maryland, College Park*.
Hains, J. C., et al. (2008), Origins of chemical pollution derived from Mid-Atlantic aircraft profiles using a clustering technique, *Atmospheric Environment*, *42*(8), 1727-1741.
Hand, J. L., and W. C. Malm (2007), Review of aerosol mass scattering efficiencies from ground-based measurements since 1990, *Journal of Geophysical Research-Atmospheres*, *112*(D18), 24.

Hansen, J. E., and L. D. Travis (1974), LIGHT-SCATTERING IN PLANETARY ATMOSPHERES, *Space Sci. Rev.*, *16*(4), 527-610.
Hao, J. M., et al. (2000), Designation of acid rain and SO2 control zones and control policies in China, *Journal of Environmental Science and Health Part a-Toxic/Hazardous Substances & Environmental Engineering*, *35*(10), 1901-1914.
Haywood, J., and O. Boucher (2000), Estimates of the direct and indirect radiative forcing due to tropospheric aerosols: A review, *Reviews of Geophysics*, *38*(4), 513-543.
He, K. B., et al. (2001), The characteristics of PM2.5 in Beijing, China, *Atmospheric Environment*, *35*(29), 4959-4970.
He, K. B., et al. (2002), Urban air pollution in China: Current status, characteristics, and progress, *Annu. Rev. Energ. Environ.*, *27*, 397-431.
Hirsch, A. I., et al. (1996), Seasonal variation of the ozone production efficiency per unit NOx at Harvard Forest, Massachusetts, *Journal of Geophysical Research-Atmospheres*, *101*(D7), 12659-12666.
Hong, S.-Y., and J.-O. Lim (2006), The WRF single-moment 6-class microphysics scheme (WSM6), *J. Korean Meteor. Soc.*, *42*, 129-151.
Hsu, N. C., et al. (2004), Aerosol properties over bright-reflecting source regions, *Ieee Transactions on Geoscience and Remote Sensing*, *42*(3), 557-569.
Hu, H., et al. (2010), Air Pollution and Control in Different Areas of China, *Crit. Rev. Environ. Sci. Technol.*, *40*(6), 452-518.
Huebert, B. J., et al. (2004), PELTI: Measuring the passing efficiency of an airborne low turbulence aerosol inlet, *Aerosol Science and Technology*, *38*(8), 803-826.
Husar, R. B., et al. (2001), Asian dust events of April 1998, *Journal of Geophysical Research-Atmospheres*, *106*(D16), 18317-18330.
Igarashi, Y., et al. (2006), Seasonal variations in SO2 plume transport over Japan: Observations at the summit of Mt. Fuji from winter to summer, *Atmospheric Environment*, *40*(36), 7018-7033.
IPCC (2007), Climate Change 2007: The Physical Science Basis., *Contribution of Working Group I to the Fourth Assessment Report (AR4) of the Intergovernmental Panel on Climate Change*, 996 pp.
Jacob, D. J. (2000), Heterogeneous chemistry and tropospheric ozone, *Atmospheric Environment*, *34*(12-14), 2131-2159.
Jacob, D. J., and D. A. Winner (2009), Effect of climate change on air quality, *Atmospheric Environment*, *43*(1), 51-63.
Jaffe, D., et al. (1999), Transport of Asian air pollution to North America, *Geophysical Research Letters*, *26*(6), 711-714.
Johnston, H. (1971), REDUCTION OF STRATOSPHERIC OZONE BY NITROGEN OXIDE CATALYSTS FROM SUPERSONIC TRANSPORT EXHAUST, *Science*, *173*(3996), 517-&.
Kahl, J. D., et al. (1989), Intercomparison of three long-range trajectory models applied to Arctic haze, *Tellus Series B-Chemical and Physical Meteorology*, *41*(5), 524-536.
Kain, J. S. (2004), The Kain-Fritsch convective parameterization: An update, *Journal of Applied Meteorology*, *43*(1), 170-181.
Kan, H. D., et al. (2010), Short-term association between sulfur dioxide and daily mortality: The Public Health and Air Pollution in Asia (PAPA) study, *Environ. Res.*, *110*(3), 258-264.

Kaufman, Y. J., et al. (1997), Operational remote sensing of tropospheric aerosol over land from EOS moderate resolution imaging spectroradiometer, *Journal of Geophysical Research-Atmospheres*, *102*(D14), 17051-17067.
Kim, B. G., et al. (2001), Transport of SO2 and aerosol over the Yellow sea, *Atmospheric Environment*, *35*(4), 727-737.
King, M. D., et al. (2003), Cloud and aerosol properties, precipitable water, and profiles of temperature and water vapor from MODIS, *Ieee Transactions on Geoscience and Remote Sensing*, *41*(2), 442-458.
Kleinman, L. I. (2000), Ozone process insights from field experiments - part II: Observation-based analysis for ozone production, *Atmospheric Environment*, *34*(12-14), 2023-2033.
Kleinman, L. I., et al. (2002), Ozone production efficiency in an urban area, *Journal of Geophysical Research-Atmospheres*, *107*(D23), 12.
Koch, D., et al. (1999), Tropospheric sulfur simulation and sulfate direct radiative forcing in the Goddard Institute for Space Studies general circulation model, *Journal of Geophysical Research-Atmospheres*, *104*(D19), 23799-23822.
Koike, M., et al. (2003), Export of anthropogenic reactive nitrogen and sulfur compounds from the East Asia region in spring, *Journal of Geophysical Research-Atmospheres*, *108*(D20).
Krotkov, N. A., et al. (2006), Band residual difference algorithm for retrieval of SO2 from the aura Ozone Monitoring Instrument (OMI), *Ieee Transactions on Geoscience and Remote Sensing*, *44*(5), 1259-1266.
Krotkov, N. A., et al. (2008), Validation of SO2 retrievals from the Ozone Monitoring Instrument over NE China, *Journal of Geophysical Research-Atmospheres*, *113*(D16).
Krueger, A. J. (1983), SIGHTING OF EL-CHICHON SULFUR-DIOXIDE CLOUDS WITH THE NIMBUS-7 TOTAL OZONE MAPPING SPECTROMETER, *Science*, *220*(4604), 1377-1379.
Krueger, A. J., et al. (1995), VOLCANIC SULFUR-DIOXIDE MEASUREMENTS FROM THE TOTAL OZONE MAPPING SPECTROMETER INSTRUMENTS, *Journal of Geophysical Research-Atmospheres*, *100*(D7), 14057-14076.
Langner, J., and H. Rodhe (1991), A GLOBAL 3-DIMENSIONAL MODEL OF THE TROPOSPHERIC SULFUR CYCLE, *Journal of Atmospheric Chemistry*, *13*(3), 225-263.
Larssen, T., et al. (2006), Acid rain in China, *Environmental Science & Technology*, *40*(2), 418-425.
Lee, C., et al. (2009), Retrieval of vertical columns of sulfur dioxide from SCIAMACHY and OMI: Air mass factor algorithm development, validation, and error analysis, *Journal of Geophysical Research-Atmospheres*, *114*.
Lee, C., et al. (2011), SO2 emissions and lifetimes: Estimates from inverse modeling using in situ and global, space-based (SCIAMACHY and OMI) observations, *Journal of Geophysical Research-Atmospheres*, *116*, 13.
Levelt, P. F., et al. (2006), Science objectives of the Ozone Monitoring Instrument, *Ieee Transactions on Geoscience and Remote Sensing*, *44*(5), 1199-1208.
Levy, R., et al. (2009), Algorithm for remote sensing of tropospheric aerosol over dark targets from MODIS, *supporting material for MOD04/MYD04*, *NASA/GSFC*,(http://modis-atmos.gsfc.nasa.gov/_docs/ATBD_MOD04_C005_rev2.pdf), 1.

Levy, R. C., et al. (2007), Second-generation operational algorithm: Retrieval of aerosol properties over land from inversion of Moderate Resolution Imaging Spectroradiometer spectral reflectance, *Journal of Geophysical Research-Atmospheres*, *112*(D13), 21.
Levy, R. C., et al. (2010), Global evaluation of the Collection 5 MODIS dark-target aerosol products over land, *Atmospheric Chemistry and Physics*, *10*(21), 10399-10420.
Li, C., et al. (2007a), In situ measurements of trace gases and aerosol optical properties at a rural site in northern China during East Asian Study of Tropospheric Aerosols: An International Regional Experiment 2005, *Journal of Geophysical Research-Atmospheres*, *112*(D22).
Li, C., et al. (2010), Transport and evolution of a pollution plume from northern China: A satellite-based case study, *Journal of Geophysical Research-Atmospheres*, *115*.
Li, Z. Q., et al. (2007b), Preface to special section on east Asian studies of tropospheric aerosols: An international regional experiment (EAST-AIRE), *Journal of Geophysical Research-Atmospheres*, *112*(D22), 10.
Li, Z. Q., et al. (2011), East Asian Studies of Tropospheric Aerosols and their Impact on Regional Climate (EAST-AIRC): An overview, *Journal of Geophysical Research-Atmospheres*, *116*, 15.
Lin, M., et al. (2008a), Long-range transport of acidifying substances in east Asia - Part II - Source-receptor relationships, *Atmospheric Environment*, *42*(24), 5956-5967.
Lin, M. Y., et al. (2008b), Long-range transport of acidifying substances in East Asia - Part I - Model evaluation and sensitivity studies, *Atmospheric Environment*, *42*(24), 5939-5955.
Lin, W. L., et al. (2012), Characteristics and recent trends of sulfur dioxide at urban, rural, and background sites in North China: Effectiveness of control measures, *Journal of Environmental Sciences-China*, *24*(1), 34-49.
Lin, X., et al. (1988), ON THE NONLINEARITY OF THE TROPOSPHERIC OZONE PRODUCTION, *Journal of Geophysical Research-Atmospheres*, *93*(D12), 15879-15888.
Liu, S. C., et al. (1987), OZONE PRODUCTION IN THE RURAL TROPOSPHERE AND THE IMPLICATIONS FOR REGIONAL AND GLOBAL OZONE DISTRIBUTIONS, *Journal of Geophysical Research-Atmospheres*, *92*(D4), 4191-4207.
Liu, X. H., et al. (2010a), Understanding of regional air pollution over China using CMAQ, part I performance evaluation and seasonal variation, *Atmospheric Environment*, *44*(20), 2415-2426.
Liu, X. H., et al. (2010b), Understanding of regional air pollution over China using CMAQ, part II. Process analysis and sensitivity of ozone and particulate matter to precursor emissions, *Atmospheric Environment*, *44*(30), 3719-3727.
Lohmann, U., and J. Feichter (2005), Global indirect aerosol effects: a review, *Atmospheric Chemistry and Physics*, *5*, 715-737.
Loughner, C. (2011), Impacts of fair-weather cumulus clouds, bay breezes, and landuse on urban air quality and climate, *PhD Dissertation, University of Maryland, College Park*.
Loughner, C. P., et al. (2011), Impact of fair-weather cumulus clouds and the Chesapeake Bay breeze on pollutant transport and transformation, *Atmospheric Environment*, *45*(24), 4060-4072.
Lu, Z., et al. (2010), Sulfur dioxide emissions in China and sulfur trends in East Asia since 2000, *Atmospheric Chemistry and Physics*, *10*(13), 6311-6331.

Luke, W. T. (1997), Evaluation of a commercial pulsed fluorescence detector for the measurement of low-level SO2 concentrations during the gas-phase sulfur intercomparison experiment, *Journal of Geophysical Research-Atmospheres*, *102*(D13), 16255-16265.
Malm, W. C., et al. (1994), SPATIAL AND SEASONAL TRENDS IN PARTICLE CONCENTRATION AND OPTICAL EXTINCTION IN THE UNITED-STATES, *Journal of Geophysical Research-Atmospheres*, *99*(D1), 1347-1370.
Matsui, H., et al. (2009), Spatial and temporal variations of aerosols around Beijing in summer 2006: Model evaluation and source apportionment, *Journal of Geophysical Research-Atmospheres*, *114*, 22.
Matsui, H., et al. (2010), Spatial and temporal variations of aerosols around Beijing in summer 2006: 2. Local and column aerosol optical properties, *Journal of Geophysical Research-Atmospheres*, *115*, 20.
McNaughton, C. S., et al. (2007), Results from the DC-8 Inlet Characterization Experiment (DICE): Airborne versus surface sampling of mineral dust and sea salt aerosols, *Aerosol Science and Technology*, *41*(2), 136-159.
Meng, Z. Y., et al. (2010), Ambient sulfur dioxide, nitrogen dioxide, and ammonia at ten background and rural sites in China during 2007-2008, *Atmospheric Environment*, *44*(21-22), 2625-2631.
Mi, W., et al. (2007), Evaluation of the moderate resolution Imaging spectroradiometer aerosol products at two aerosol robotic network stations in china, *Journal of Geophysical Research-Atmospheres*, *112*(D22), 14.
Mokdad, A. H., et al. (2004), Actual causes of death in the United States, 2000, *JAMA-J. Am. Med. Assoc.*, *291*(10), 1238-1245.
Molina, M. J., and F. S. Rowland (1974), STRATOSPHERIC SINK FOR CHLOROFLUOROMETHANES - CHLORINE ATOMIC-CATALYSED DESTRUCTION OF OZONE, *Nature*, *249*(5460), 810-812.
Morgenstern, O., et al. (2008), The world avoided by the Montreal Protocol, *Geophysical Research Letters*, *35*(16).
Mozurkewich, M. (1993), THE DISSOCIATION-CONSTANT OF AMMONIUM-NITRATE AND ITS DEPENDENCE ON TEMPERATURE, RELATIVE-HUMIDITY AND PARTICLE-SIZE, *Atmospheric Environment Part a-General Topics*, *27*(2), 261-270.
Muller, J. F., and G. Brasseur (1995), IMAGES - A 3-DIMENSIONAL CHEMICAL-TRANSPORT MODEL OF THE GLOBAL TROPOSPHERE, *Journal of Geophysical Research-Atmospheres*, *100*(D8), 16445-16490.
NCAR (2010), Weather Research and Forecasting, ARW version 3 Modeling System's User Guide, *Mesoscale & Microscale Meteorology Division, National Center for Atmospheric Research*.
Nunnermacker, L. J., et al. (2000), NOy lifetimes and O-3 production efficiencies in urban and power plant plumes: Analysis of field data, *Journal of Geophysical Research-Atmospheres*, *105*(D7), 9165-9176.
Nunnermacker, L. J., et al. (2008), Aircraft and ground-based measurements of hydroperoxides during the 2006 MILAGRO field campaign, *Atmospheric Chemistry and Physics*, *8*(24), 7619-7636.

Okuda, T., et al. (2011), The impact of the pollution control measures for the 2008 Beijing Olympic Games on the chemical composition of aerosols, *Atmospheric Environment*, *45*(16), 2789-2794.
Otte, T. L. (2008), The impact of nudging in the meteorological model for retrospective air quality simulations. Part I: Evaluation against national observation networks, *J. Appl. Meteorol. Climatol.*, *47*(7), 1853-1867.
Paraskevopoulos, G., et al. (1983), RATES OF OH RADICAL REACTIONS - THE REACTION OH+SO2+N2, *Chemical Physics Letters*, *100*(1), 83-87.
Peled, R. (2011), Air pollution exposure: Who is at high risk?, *Atmospheric Environment*, *45*(10), 1781-1785.
Pfanz, H., et al. (1987), MESOPHYLL RESISTANCES TO SO2 FLUXES INTO LEAVES, *Plant Physiol.*, *85*(4), 922-927.
Pham, M., et al. (1995), A three-dimensional study of the tropospheric sulfur cycle, *Journal of Geophysical Research-Atmospheres*, *100*(D12), 26061-26092.
Prospero, J. M., et al. (2003), Long-term record of nss-sulfate and nitrate in aerosols on Midway Island, 1981-2000: Evidence of increased (now decreasing?) anthropogenic emissions from Asia, *Journal of Geophysical Research-Atmospheres*, *108*(D1), 11.
Quinn, P. K., et al. (2007), Arctic haze: current trends and knowledge gaps, *Tellus Series B-Chemical and Physical Meteorology*, *59*(1), 99-114.
Rahn, K. A., et al. (1977), ASIAN SOURCE OF ARCTIC HAZE BANDS, *Nature*, *268*(5622), 713-715.
Ramanathan, V., et al. (1987), CLIMATE-CHEMICAL INTERACTIONS AND EFFECTS OF CHANGING ATMOSPHERIC TRACE GASES, *Reviews of Geophysics*, *25*(7), 1441-1482.
Remer, L. A., et al. (1997), Urban/industrial aerosol: Ground-based Sun/sky radiometer and airborne in situ measurements, *Journal of Geophysical Research-Atmospheres*, *102*(D14), 16849-16859.
Remer, L. A., et al. (2005), The MODIS aerosol algorithm, products, and validation, *Journal of the Atmospheric Sciences*, *62*(4), 947-973.
Rotman, D. A., et al. (2004), IMPACT, the LLNL 3-D global atmospheric chemical transport model for the combined troposphere and stratosphere: Model description and analysis of ozone and other trace gases, *Journal of Geophysical Research-Atmospheres*, *109*(D4).
Rowland, F. S., and M. J. Molina (1975), CHLOROFLUOROMETHANES IN ENVIRONMENT, *Reviews of Geophysics*, *13*(1), 1-35.
Roy, B., et al. (2007), A comparison of CMAQ-based aerosol properties with IMPROVE, MODIS, and AERONET data, *Journal of Geophysical Research-Atmospheres*, *112*(D14), 17.
Ryan, W. F., et al. (1998), Pollutant transport during a regional O-3 episode in the mid-Atlantic states, *J. Air Waste Manage. Assoc.*, *48*(9), 786-797.
Salawitch, R. J., et al. (1989), DENITRIFICATION IN THE ANTARCTIC STRATOSPHERE, *Nature*, *339*(6225), 525-527.
Savitzky, A., and M. J. E. Golay (1964), SMOOTHING + DIFFERENTIATION OF DATA BY SIMPLIFIED LEAST SQUARES PROCEDURES, *Anal. Chem.*, *36*(8), 1627-&.

Schleicher, N., et al. (2011), The effect of mitigation measures on size distributed mass concentrations of atmospheric particles and black carbon concentrations during the Olympic Summer Games 2008 in Beijing, *Science of the Total Environment*, *412*, 185-193.
Schlesinger, R. B., and F. Cassee (2003), Atmospheric secondary inorganic particulate matter: The toxicological perspective as a basis for health effects risk assessment, *Inhal. Toxicol.*, *15*(3), 197-235.
Seidel, D. J., et al. (2010), Estimating climatological planetary boundary layer heights from radiosonde observations: Comparison of methods and uncertainty analysis, *Journal of Geophysical Research-Atmospheres*, *115*, 15.
Seinfeld, J. H. (1986), *Atmospheric Chemistry and Physics of Air Pollution*, 1st ed., John Wiley & Sons, Inc.
Seinfeld, J. H. (2004), Air pollution: A half century of progress, *Aiche J.*, *50*(6), 1096-1108.
Seinfeld, J. H., and S. N. Pandis (2006), *Atmospheric Chemistry and Physics: From Air Pollution to Climate Change*, 2nd ed., John Wiley & Sons, Inc.
Seinfeld, J. H. e. a. (1991), *Rethinking the Ozone Problem in Urban and Regional Air Pollution*, National Academics Press, Washingtong, DC.
Shaw, G. E. (1995), The arctic haze phenomenon, *Bulletin of the American Meteorological Society*, *76*(12), 2403-2413.
Shen, J. L., et al. (2010), Impacts of Pollution Controls on Air Quality in Beijing during the 2008 Olympic Games, *J. Environ. Qual.*, *40*(1), 37-45.
Shen, Z. X., et al. (2007), Chemical composition and source characterization of spring aerosol over Horqin sand land in northeastern China, *Journal of Geophysical Research-Atmospheres*, *112*(D14).
Shon, Z. H., et al. (2008), Characteristics of the NO-NO(2)-O(3) system in different chemical regimes during the MIRAGE-Mex field campaign, *Atmospheric Chemistry and Physics*, *8*(23), 7153-7164.
Sillman, S. (1995), THE USE OF NOY, H2O2, AND HNO3 AS INDICATORS FOR OZONE-NOX-HYDROCARBON SENSITIVITY IN URBAN LOCATIONS, *Journal of Geophysical Research-Atmospheres*, *100*(D7), 14175-14188.
Smith, R. I., et al. (1989), THE STATISTICS OF PHYTOTOXIC AIR-POLLUTANTS, *J. R. Stat. Soc. Ser. A-Stat. Soc.*, *152*, 183-198.
Smith, S. J., et al. (2011), Anthropogenic sulfur dioxide emissions: 1850-2005, *Atmospheric Chemistry and Physics*, *11*(3), 1101-1116.
Solomon, S., et al. (1986), ON THE DEPLETION OF ANTARCTIC OZONE, *Nature*, *321*(6072), 755-758.
Sorimachi, A., et al. (2003), Measurements of sulfur dioxide and ozone dry deposition over short vegetation in northern China - A preliminary study, *Atmospheric Environment*, *37*(22), 3157-3166.
Sorimachi, A., and K. Sakamoto (2007), Laboratory measurement of the dry deposition of sulfur dioxide onto northern Chinese soil samples, *Atmospheric Environment*, *41*(13), 2862-2869.
Stier, P., et al. (2007), Aerosol absorption and radiative forcing, *Atmospheric Chemistry and Physics*, *7*(19), 5237-5261.

Stockwell, W. R., et al. (1990), THE 2ND GENERATION REGIONAL ACID DEPOSITION MODEL CHEMICAL MECHANISM FOR REGIONAL AIR-QUALITY MODELING, *Journal of Geophysical Research-Atmospheres*, *95*(D10), 16343-16367.
Stohl, A., et al. (1995), INTERPOLATION ERRORS IN WIND FIELDS AS A FUNCTION OF SPATIAL AND TEMPORAL RESOLUTION AND THEIR IMPACT ON DIFFERENT TYPES OF KINEMATIC TRAJECTORIES, *Journal of Applied Meteorology*, *34*(10), 2149-2165.
Stohl, A. (1998), Computation, accuracy and applications of trajectories - A review and bibliography, *Atmospheric Environment*, *32*(6), 947-966.
Streets, D. G., et al. (2003), An inventory of gaseous and primary aerosol emissions in Asia in the year 2000, *Journal of Geophysical Research-Atmospheres*, *108*(D21), 23.
Stunder, B. J. B. (1996), An assessment of the quality of forecast trajectories, *Journal of Applied Meteorology*, *35*(8), 1319-1331.
Sun, Y., et al. (2009), Measurement of the vertical profile of atmospheric SO2 during the heating period in Beijing on days of high air pollution, *Atmospheric Environment*, *43*(2), 468-472.
Sunyer, J. (2001), Urban air pollution and chronic obstructive pulmonary disease: a review, *European Respiratory Journal*, *17*(5), 1024-1033.
Tan, Q., et al. (2002), Budget and export of anthropogenic SOx from East Asia during continental outflow conditions, *Journal of Geophysical Research-Atmospheres*, *107*(D13), 18.
Taubman, B. F., et al. (2004a), Airborne characterization of the chemical, optical, and meteorological properties, and origins of a combined ozone-haze episode over the eastern United States, *Journal of the Atmospheric Sciences*, *61*(14), 1781-1793.
Taubman, B. F., et al. (2004b), Smoke over haze: Aircraft observations of chemical and optical properties and the effects on heating rates and stability, *Journal of Geophysical Research-Atmospheres*, *109*(D2).
Taubman, B. F., et al. (2006), Aircraft vertical profiles of trace gas and aerosol pollution over the mid-Atlantic United States: Statistics and meteorological cluster analysis, *Journal of Geophysical Research-Atmospheres*, *111*(D10).
Tebrake, W. H. (1975), AIR-POLLUTION AND FUEL CRISES IN PREINDUSTRIAL LONDON, 1250-1650, *Technol. Cult.*, *16*(3), 337-359.
TEI (2004a), Model 49C UV Photometric O3 Analyzer, instruction manual.
TEI (2004b), *Model 48C NDIR Gas Filter Correction CO analyzer, Instruction Manual*.
TEI (2004c), *Model 43C Trace Level Pulsed Fluorescence SO2 analyzer, Instruction Manual*.
Thompson, G. E., et al. (2006), A new bulk microphysical parameterization for WRF $ MM5. Preprints, *Seventh Weather Research and Forecasting User's Workshop*, Boulder, CO, NCAR, 5.3.
Tsai, Y. I., and C. L. Chen (2006), Characterization of Asian dust storm and non-Asian dust storm PM2.5 aerosol in southern Taiwan, *Atmospheric Environment*, *40*(25), 4734-4750.
TSI (1997), *Model 3550/3560 Series Integrating Nephelometer, Instruction Mannual*.
Tu, F. H., et al. (2004), Long-range transport of sulfur dioxide in the central Pacific, *Journal of Geophysical Research-Atmospheres*, *109*(D15), 19.

Twomey, S. (1977), INFLUENCE OF POLLUTION ON SHORTWAVE ALBEDO OF CLOUDS, *Journal of the Atmospheric Sciences*, *34*(7), 1149-1152.
Van de Hulst, H. C. (1957), *Light Scattering by Small Particles*, Wiley, New York.
van Donkelaar, A., et al. (2008), Analysis of aircraft and satellite measurements from the Intercontinental Chemical Transport Experiment (INTEX-B) to quantify long-range transport of East Asian sulfur to Canada, *Atmospheric Chemistry and Physics*, *8*(11), 2999-3014.
Walcek, C. J., and H. H. Yuan (1995), CALCULATED INFLUENCE OF TEMPERATURE-RELATED FACTORS ON OZONE FORMATION RATES IN THE LOWER TROPOSPHERE, *Journal of Applied Meteorology*, *34*(5), 1056-1069.
Wang, L. T., et al. (2010a), Assessment of air quality benefits from national air pollution control policies in China. Part II: Evaluation of air quality predictions and air quality benefits assessment, *Atmospheric Environment*, *44*(28), 3449-3457.
Wang, L. T., et al. (2010b), Assessment of air quality benefits from national air pollution control policies in China. Part I: Background, emission scenarios and evaluation of meteorological predictions, *Atmospheric Environment*, *44*(28), 3442-3448.
Wang, S. X., et al. (2010c), Quantifying the Air Pollutants Emission Reduction during the 2008 Olympic Games in Beijing, *Environmental Science & Technology*, *44*(7), 2490-2496.
Wang, W., et al. (2008), Aircraft measurements of gaseous pollutants and particulate matter over Pearl River Delta in China, *Atmospheric Environment*, *42*(25), 6187-6202.
Wang, X. M., et al. (2004), Modern dust storms in China: an overview, *J. Arid. Environ.*, *58*(4), 559-574.
Wang, X. M., et al. (2010d), Has the Three Norths Forest Shelterbelt Program solved the desertification and dust storm problems in arid and semiarid China?, *J. Arid. Environ.*, *74*(1), 13-22.
Wang, Y., et al. (1998), Nitric oxide production by simulated lightning: Dependence on current, energy, and pressure, *Journal of Geophysical Research-Atmospheres*, *103*(D15), 19149-19159.
Watson, J. G. (2002), Visibility: Science and regulation, *J. Air Waste Manage. Assoc.*, *52*(6), 628-713.
Wayne, R. P. (2000), *Chemistry of Atmospheres*, 3rd ed., Oxford University Press.
Wesely, M. L., and B. B. Hicks (2000), A review of the current status of knowledge on dry deposition, *Atmospheric Environment*, *34*(12-14), 2261-2282.
Winner, W., et al. (1986), *Sulfur Dioxide and Vegetation: Physiology, Ecology, and Policy issues*, First ed., Standford University Press.
Wise, E. K., and A. C. Comrie (2005), Meteorologically adjusted urban air quality trends in the Southwestern United States, *Atmospheric Environment*, *39*(16), 2969-2980.
Witte, J. C., et al. (2009), Satellite observations of changes in air quality during the 2008 Beijing Olympics and Paralympics, *Geophysical Research Letters*, *36*, 6.
Wood, E. C., et al. (2009), A case study of ozone production, nitrogen oxides, and the radical budget in Mexico City, *Atmospheric Chemistry and Physics*, *9*(7), 2499-2516.
Xin, J. Y., et al. (2005), Optical properties and size distribution of dust aerosols over the Tengger Desert in Northern China, *Atmospheric Environment*, *39*(32), 5971-5978.

Xin, J. Y., et al. (2007), Aerosol optical depth (AOD) and Angstrom exponent of aerosols observed by the Chinese Sun Hazemeter Network from August 2004 to September 2005, *Journal of Geophysical Research-Atmospheres*, *112*(D5), 13.
Xue, L. K., et al. (2010), Aircraft measurements of the vertical distribution of sulfur dioxide and aerosol scattering coefficient in China, *Atmospheric Environment*, *44*(2), 278-282.
Yang, F., et al. (2011), Characteristics of PM(2.5) speciation in representative megacities and across China, *Atmospheric Chemistry and Physics*, *11*(11), 5207-5219.
Yang, K., et al. (2007), Retrieval of large volcanic SO2 columns from the Aura Ozone Monitoring Instrument: Comparison and limitations, *Journal of Geophysical Research-Atmospheres*, *112*(D24).
Yang, K., et al. (2009a), Improving retrieval of volcanic sulfur dioxide from backscattered UV satellite observations, *Geophysical Research Letters*, *36*.
Yang, K., et al. (2009b), Estimating the altitude of volcanic sulfur dioxide plumes from space borne hyper-spectral UV measurements, *Geophysical Research Letters*, *36*.
Yang, K., et al. (2010), Direct retrieval of sulfur dioxide amount and altitude from spaceborne hyperspectral UV measurements: Theory and application, *Journal of Geophysical Research-Atmospheres*, *115*, 15.
Yang, L. (2012), Beijing kicks off PM2.5 measure of air quality, in *http://news.xinhuanet.com/english/china/2012-01/21/c_131372324.htm*, edited, XinHuaNet, Beijing.
Yumimoto, K., et al. (2010), Summertime trans-Pacific transport of Asian dust, *Geophysical Research Letters*, *37*, 7.
Zhang, D. L., et al. (2009a), Upstream urbanization exacerbates urban heat island effects, *Geophysical Research Letters*, *36*.
Zhang, D. Z., et al. (2003), Mixture state of individual Asian dust particles at a coastal site of Qingdao, China, *Atmospheric Environment*, *37*(28), 3895-3901.
Zhang, Q., et al. (2009b), Asian emissions in 2006 for the NASA INTEX-B mission, *Atmospheric Chemistry and Physics*, *9*(14), 5131-5153.
Zhang, Y. H., et al. (2008), Regional Integrated Experiments on Air Quality over Pearl River Delta 2004 (PRIDE-PRD2004): Overview, *Atmospheric Environment*, *42*(25), 6157-6173.
Zheng, M., et al. (2005), Seasonal trends in PM2.5 source contributions in Beijing, China, *Atmospheric Environment*, *39*(22), 3967-3976.